The Electron-Scattering Reaction in the Sudbury Neutrino Observatory

by

Christopher James Jillings

A thesis submitted to the Department of Physics
in conformity with the requirements for
the degree of Doctor of Philosophy

Queen's University
Kingston, Ontario, Canada
July, 1999

to Anne and Dominique

Statement of Originality

The work presented in this thesis is the author's own and is original except where noted here. All use of other's work is appropriately cited in the text.

The Sudbury Neutrino Observatory is a large complicated instrument designed to study many phenomena. The associated data analysis and simulation tools are correspondingly complicated. Thus not all the work described here is the author's own. The introductory chapter is a description of the status of the field at the time this work was done. It is, therefore, a survey of other's work. The theory chapter is a description of the theory of the sun, neutrinos, and neutrino interactions with matter. It is a description of other's work. I performed the calculations of interaction-rates in chapter 2.

The third chapter describes the SNO detector in general. I worked for 4 months on the construction of the acrylic vessel, for approximately 2 months on the degassing system for the heavy water, for 1 year on the SNO manipulator system. My work on the manipulator system is described in the appendix. I provided 4 significant code modules for the calibration-control program `manip`. The primary authors of `manip` are P.J. Harvey and T.J. Radcliffe.

The fifth chapter starts with a discussion of simulations of the detector. The SNO Monte Carlo and Analysis System (SNOMAN) was written by many collaboration members. I am not an author of the code. The event reconstruction algorithms used in SNOMAN were developed by others in the collaboration. However, I developed the method of using the elastic fitter and the parameters to control it in a way not suggested by the algorithm's author. I ran all the simulations in the chapter. The analysis of the output of the simulation and interpretation of results is mine.

Chapter 6 develops a calibration technique to understand angular resolution. I developed the analysis with helpful suggestions from colleagues. Those suggestions are cited where appropriate. I performed the analyses in chapter 7.

The data analysis and methodology described in chapter 8 is entirely my own. Another graduate student at Queen's University, Andre Hamer, studied the same data for the ^{16}N calibration at airfill and we had several useful discussions. His analysis used a different technique to separate the events in which the ^{16}N gamma-rays interacted in the acrylic from those that did not. I used the SNOMAN program and a useful suite of tools which Mark Boulay, a graduate-student colleague, developed.

Acknowledgements

I would like to thank my advisor, Professor A.B. McDonald, for his thoughtful guidance throughout the course of my studies. I can not in a few sentences describe all he has done for me but I have particularly appreciated his ability to get at the essence of an issue, his willingness to make time to discuss my work, his positive outlook, and his understanding of my priorities.

Professor Aksel Hallin supervised my activities in the calibration group. He always viewed the work cheerfully and with a sense of humour. Professor Barry Robertson, head of my committee, had an open door and on many occasions helped with a fresh perspective.

The graduate students at Queen's are a great group with which to work. Thanks in particular to Richard Ford, Andre Hamer, Mark Boulay, Bryce Moffat, Lorne Erhardt, Ed Korpach, Matthieu Dayon and Keith Rose. I would like to thank Chuck Hearnes, Alvin Bell, Aubert Perrera, Bob Stevenson, and Philip Hart for their help with mechanical and electrical aspects of the calibration systems. I had the opportunity to work with several talented researchers at Queen's. Peter Skensved, Fraser Duncan, Emmanuel Bonvin, Tom Radcliffe, Henry Lee, and Phil Harvey taught me a great deal.

All the members of the SNO collaboration deserve my thanks. I would like to single out Nick West, Tony Noble, and Josh Klein.

Hugh Evans did a great deal to make working and living in Sudbury easier. Norm Bodson and Hardy Seifert organized many of my activities on site. I would like to thank them and my underground supervisors for many favours. My thanks go to the INCO staff at Creighton mine and Copper Cliff and the United Steel Workers of America Local 6500.

Dan Deptuck and Ray Kuntz helped achieve a personal goal.

The one person whom I would like to thank most is Anne. It would not have been possible to do this work without her help, love, and encouragement. She took on many extra burdens to allow me to work both at Queen's and on site and I am very grateful.

Abstract

The Sudbury Neutrino Observatory (SNO) is a 1000-tonne heavy-water Čerenkov detector designed to measure the flux and energy spectrum of electron-type solar neutrinos and the total flux of all flavours of solar neutrinos as well as neutrinos from other astrophysical sources.

The angular resolution (the ability to measure the direction of recoil electrons from neutrino interactions with the heavy water) of the SNO detector has been studied in detail using Monte Carlo simulations. The factors affecting angular resolution, including the passage of electrons through water, the optical quality of detector components, and event reconstruction, are considered. The systematic uncertainty in angular resolution contributed by these factors is calculated. An analytic function which accurately describes the angular response of the SNO detector is presented.

A method using a 6.13 MeV gamma-ray source to verify that the Monte Carlo calculations of angular resolution are correct is presented. The reconstructed direction for those events which reconstruct far from the source is compared to a measure of the initial direction of the gamma ray. The initial direction is taken to be the vector from the known location of the source to the reconstructed location of the event. Techniques to reduce the effect of misreconstruction of position are discussed.

The impact of the angular resolution on the extraction of the electron-scattering (ES) signal is presented. Three simple analyses which use only directional information to extract the ES signal are presented. The statistical and systematic uncertainties are discussed in detail. The impact of the calibration on the ES extraction is discussed.

Early detector data and calibrations are discussed with particular emphasis on use of the ^{16}N source before water was added to the detector and on gamma rays striking the water surface at partial fill. The behavior of the algorithms for reconstruction of direction during partial fill is presented.

Contents

List of Figures

List of Tables

List of Acronyms and Abbreviations

ADC	analog-to-digital converter
ASYNC	asynchromous
CC	charged-current
CNO	Carbon-Nitrogen-Oxygen (chain of nuclear reactions)
DOS	MicroSoft's MS DOS operating system
EGS4	Electron-Gamma Shower computer code (version 4)
ES	neutrino-electron elastic scattering
ESUM	energy sum (total integrated charge in one event)
EXT	external
GTID	global trigger identification
hep	$^3\mathrm{He} + p \longrightarrow {}^4\mathrm{He} + e^+ + \nu_e$
INCO	The International Nickel Company
LG	low-gain (refers to a PMT)
MSW	Mikeyev-Smirnov-Wolfenstein (matter-enhanced neutrino oscillations)
NC	neutral-current
NCD	neutral current detector (^{3}He-filled proportional counter)
NHIT	number of PMTs with anode signal above threshold
OWL	outward-looking (refers to a PMT)
pep	$p + e + p \longrightarrow d + \nu_e$
PGT	pulsed global trigger
PMT	photomultipler tube
pp	proton-proton (chain of nuclear reactions)
PSUP	photomultiplier tube support structure

SM	standard model of electro-weak interactions
SNO	The Sudbury Neutrino Observatory
SNOMAN	SNO Monte Carlo and Analysis code
SNU	solar neutrino unit (10^{-36} interactions per target per second)
SSM	standard solar model
SYNC	synchronous
TAC	time-to-analog converter
UVT	ultra-violet transmitting

Chapter 1

Introduction

The Sudbury Neutrino Observatory (SNO) is a one-kilotonne heavy-water Čerenkov detector located 6800 feet underground at INCO's Creighton mine near Sudbury, Ontario, Canada[Ch85, Ew$^+$87]. A principal goal of the detector is to resolve the long-standing *solar neutrino problem* — the number of electron neutrinos detected in five experiments performed to date can not be reconciled with each other, models of the sun, and the standard model of particle physics.

The solar-neutrino fluxes and energy spectra are calculated in solar models [BTM98, BP98]. According to these models, several nuclear reactions produce these neutrinos with various energies, up to approximately 16 MeV. The study of solar neutrinos is unique in that it allows the observer to study the core of the sun, where the energy generation takes place.

SNO measures recoil electrons and free neutrons from three kinds of neutrino interactions in heavy water. Neutrino-electron elastic scattering (ES) is one of the reactions. This reaction has sensitivity to all flavours of neutrinos and can, therefore, in conjunction with the charged-current (CC) disintegration of the deuteron (which is sensitive only to electron-flavour neutrinos) provide evidence of oscillation of solar neutrinos from the electron flavour, in which they are created, to muon or tau flavours. In the ES reaction, the recoil electron is directed almost parallel to the incident neutrino. This makes the direction of the recoil electrons the most important variable for the extraction of the ES signal from the data set. Thus the ability of SNO to measure the direction of recoil electrons is important to the analysis of the electron-scattering reaction. Understanding the directional sensitivity, its uncertainty, and the uncertainty this contributes to the extraction of the ES signal is the principal goal of this work.

1.1 The Solar Neutrinos

The sun produces neutrinos from many nuclear reactions in its core. Models of the sun (of which a description is presented in the next chapter) predict fluxes of solar neutrinos. Figure 1.1 shows the neutrino spectra from [BP98].

1.2 Experiments to Date

Five experiments have been performed to study these neutrinos. The experiments differ in energy threshold and therefore measure neutrinos from different reactions. This allows the determination of the fluxes of neutrinos from individual reactions in the sun rather than just a sum over all reactions.

The first was the Homestake experiment, performed by R. Davis Jr. and colleagues in the Homestake gold mine in South Dakota[CDD$^+$98]. (Neutrino experiments are performed underground to have shielding from cosmic-ray backgrounds.) This experiment uses ^{37}Cl to detect neutrinos with the absorption reaction $\nu_e + {}^{37}\mathrm{Cl} \rightarrow e^- + {}^{37}\mathrm{Ar}$. The threshold for this reaction, 0.814 MeV, causes the counting to be dominated by neutrinos from the beta decay of ^{8}B and electron capture on ^{7}Be.

The chlorine is in a sealed tank of (liquid) perchloroethylene. The argon atoms created by the reaction are flushed from the tank periodically and then trapped in small proportional counters which detect their beta decay back to chlorine. Data from 1970 to 1994 ([CDD$^+$98]) yield a neutrino capture rate of $2.56 \pm 0.16(\mathrm{stat}) \pm 0.16(\mathrm{syst}) \times 10^{-36}(\mathrm{target\ atom})^{-1}(\mathrm{second})^{-1}$. This is in clear disagreement with predictions of solar models, $7.7^{+1.2}_{-1.0}$ SNU [BP98] and 7.18 [BTM98] SNU. The unit, interactions per 10^{36} target atoms per second, is given the shorthand notation, SNU, for solar neutrino unit.

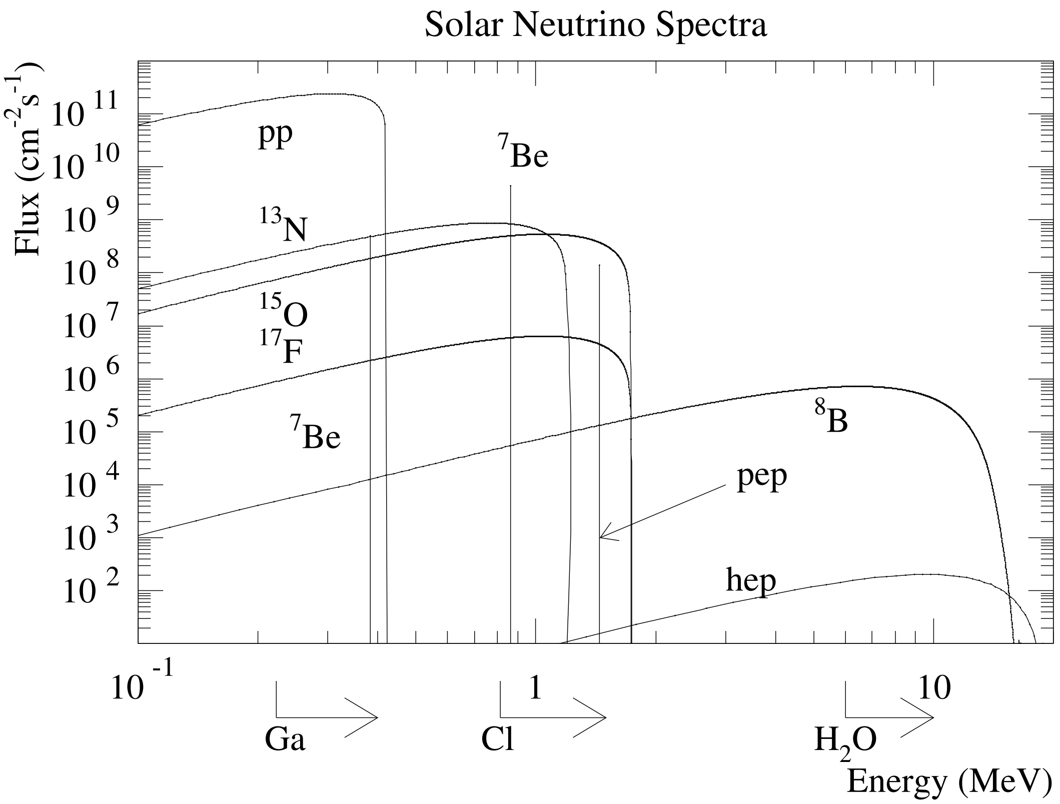

Figure 1.1: The energy spectra of solar neutrinos. The units for the continuum sources are $\mathrm{cm}^{-2}\mathrm{s}^{-1}\mathrm{MeV}^{-1}$. The units for the line sources are $\mathrm{cm}^{-2}\mathrm{s}^{-1}$. Curves labelled with an isotope refer to the beta decay of or electron capture by that isotope. The symbol pp refers to the reaction $p + p \longrightarrow d + e^{+} + \nu_e$; pep, $p + e^{-} + p \longrightarrow d + \nu_e$; and hep, $^{3}\mathrm{He} + p \longrightarrow {}^{4}\mathrm{He} + e^{+} + \nu_e$. The arrows underneath the frame indicate the threshold for Gallium, Chlorine, and Water Čerenkov experiments.

The Kamiokande experiment was located in the Kamioka zinc mine in Japan. It was a light-water Čerenkov detector and thus gave real-time information about the neutrino flux. The neutrinos were detected with elastic neutrino-electron scattering. The recoil electron from this process is of sufficient energy to produce Čerenkov light as it travels in the water. The energy threshold, 7 to 9 MeV, is larger than the Homestake experiment. It was sensitive only to neutrinos from the beta decay of ^{8}B. (There is a possibility that there is a significant contribution from hep neutrinos. This point is currently controversial and is discussed in section 2.1.2.) It also measured fewer neutrinos than expected, a flux of $2.80 \pm 0.19\,(\mathrm{stat}) \pm 0.33\,(\mathrm{syst})\ \times 10^6\mathrm{cm}^{-2}\mathrm{s}^{-1}$, a rate between 49% and 64% of predictions of standard solar models [Ka96].

The Kamiokande experiment has been superseded by Super-Kamiokande, a much larger detector with a corresponding increase in event rate. The energy threshold is 6.5 MeV for the recoil electron. The first 504 days of live time yielded a capture rate of $2.44 \pm 0.06\,(\mathrm{stat})\ ^{+0.09}_{-0.07}\,(\mathrm{syst})\ \times 10^6\mathrm{cm}^{-2}\mathrm{s}^{-1}$ [Su98a, Su98b]. Another goal of the upgraded detector is to obtain sufficient statistical accuracy to measure the energy spectrum of recoil electrons from the elastic-scattering reaction.

There are two experiments that use gallium to detect solar neutrinos with the reaction $\nu_e + {}^{71}\mathrm{Ga} \rightarrow e^- + {}^{71}\mathrm{Ge}$. The threshold for this reaction is 0.223 MeV, which makes it sensitive to the most fundamental of all reactions in the sun, $p + p \rightarrow d + e^+ + \nu_e$. The product,^{71}Ge, is radioactive and decays with a half life of 11.43 days [HR85].

The GALLEX experiment [GA92] was located in the Gran Sasso underground laboratory in Italy. It used 30.3 tonnes of gallium in a $GaCl_3$-HCl solution. The standard solar model predicts a capture rate of 129^{+8}_{-6}SNU [BP98]. The rate from [BTM98] is 127 SNU. Data from approximately 4.5 year's live time have been analyzed and the result is $76.4 \pm 6.7\,(\mathrm{stat})\ ^{+8}_{-7}(\mathrm{syst})$ SNU [GA96, GA97].

SAGE, the Russian-American Gallium Experiment [SA94], is located underground at Baksan in southern Russia. It uses 57 tonnes of liquid pure gallium of which 39.6% is ^{71}Ga. The rate predicted by standard solar models is the same as for GALLEX. The latest SAGE result is $69.9\ ^{+8.0}_{-7.7}\,(\mathrm{stat})\ ^{+3.9}_{-4.1}\,(\mathrm{syst})$ SNU [SA97].

When a global analysis is done of all the experiments they are found to be inconsistent with each other, the standard solar model and the standard model of electroweak interactions. Several authors have analyzed the data [HL97, FLM+97, BKS98]. One method of performing an analysis independent of a solar model is to analyze the data in terms of the fluxes from each reaction that produces solar neutrinos. One can write the total flux as a linear combination of the individual fluxes. The three types of experiment have different sensitivities to the individual fluxes because they have different energy thresholds. The water-Čerenkov experiments are sensitive to the ^{8}B flux. The Homestake experiment is sensitive to ^{7}Be and CNO fluxes and the ^{8}B flux. (CNO refers to the sum of the ^{13}N, ^{16}O, and ^{17}F fluxes. The CNO cycle is discussed in the next chapter.) The gallium experiments are sensitive to the sum of the pp and pep fluxes, ^{7}Be and CNO fluxes, and ^{8}B flux. Thus, the solar neutrino spectrum has been broken into three sets of fluxes: the ^{8}B flux, the ^{7}Be and CNO fluxes, and the pp and pep fluxes. The contribution of each of these three groups of fluxes to each experiment is calculated from the experimental data. No solution can be found which fits all the data. In fact, these analyses indicate a negative flux of ^{7}Be and CNO neutrinos [HR96]. Furthermore, if any one type of experiment is rejected (chlorine, water Čerenkov, or gallium) the remaining data still do not fit the standard solar models.

1.3 Proposed Solutions to the Solar Neutrino Problem

Non-standard solar models have been considered and even radical changes in solar model (arbitrarily dropping the core temperature, arbitrarily changing nuclear-reaction cross sections, or eliminating reactions) can not fit the data. On their own, non-standard models do not seem to supply a satisfactory explanation.

One attractive possibility is the proposed phenomena of neutrino oscillations, the lepton-flavour violating conversion of ν_e to ν_μ or ν_τ. The nuclear reactions in the sun produce only electron-flavour neutrinos. If at least one flavour is massive and if the weak neutrino eigenstates are linear combinations of the mass eigenstates, then neutrino flavour oscillations will occur. The chlorine and gallium experiments are sensitive only to the electron flavour of neutrinos while the light-water Čerenkov detectors are also sensitive primarily to the electron flavour with approximately 16%

sensitivity to muon and tau flavours. Thus, oscillation of electron neutrinos into muon or tau neutrinos could account for the deficit in the experimental data.

Flavour oscillations can occur in vacuum or can be enhanced by neutrino interactions with electrons in the sun or earth. The matter-enhanced oscillations, or Mikeyev-Smirnov-Wolfenstein (MSW) effect [Wo78, MS85, Be86, Pa86], fit current data well [HL97, FLM+97, BKS98]. Neutrino oscillation theories, depending on parameter choice, allow the probability of oscillation to be dependent on the neutrino energy. This is necessary for fits to the current data because the deficit in the number of neutrinos observed varies with the energy threshold of the experiments.

1.4 Evidence for Atmospheric Neutrino Oscillations

The Super-Kamiokande collaboration has reported results which they state to be evidence of neutrino oscillations of cosmic-ray induced atmospheric neutrinos [Su98c]. These neutrinos have energies of approximately 1 to 10 GeV. Vacuum oscillations from muon flavour to tau flavour are favoured. The oscillation parameters are $\sin^2 2\theta > 0.82$ and $5 \times 10^{-4} < \delta m^2 < 6 \times 10^{-3}\mathrm{eV}^2$ at the 90% confidence level. At the American Physical Society Centennial meeting in Atlanta, Georgia in March 1999, the Super-Kamiokande collaboration reported analysis of more data. This analysis gave $39 < \theta < 45$ (degrees) and $2 \times 10^{-3} < \delta m^2 < 5 \times 10^{-3}$ (eV^2) at the 68% confidence level [To99]. This compelling and exciting result emphasizes the need to look for oscillations of solar neutrinos.

1.5 The Sudbury Neutrino Observatory

To study neutrino oscillations, a detector is needed which is sensitive to all flavours. A heavy-water Čerenkov detector is ideal [Ch85, Ew+87] because the following three reactions give it that sensitivity.

CC $\quad \nu_e + d \longrightarrow p + p + e^-$

NC $\quad \nu_{e,\mu,\tau} + d \longrightarrow p + n + \nu_{e,\mu,\tau}$

ES $\quad \nu_{e,\mu,\tau} + e^- \longrightarrow \nu_{e,\mu,\tau} + e^-$

The relativistic electrons produced by the charged-current (CC) and electron-scattering (ES) reactions emit Čerenkov light which is detected by an array of photomultiplier tubes, or PMTs. The free neutron created in the neutral current (NC) reaction can be captured by a nucleus producing gamma rays which yield relativistic electrons via Compton scattering or can be detected with independent neutron detectors. The threshold for detecting these reactions (neutrino energy greater than approximately 6.5 MeV for the CC and ES reaction and 2.2 MeV for the NC reaction) is sufficiently high that only neutrinos from the beta decay of ^{8}B will be measured.

The first reaction, the charged-current, is only sensitive to electron neutrinos. The neutral-current reaction, is equally sensitive to all non-sterile neutrino flavours. Thus a comparison of the rates of these two reactions shows if electron neutrinos originating in the sun have undergone flavour change before reaching the detector.

The third reaction, the electron scattering or ES, is sensitive to muon and tau neutrinos, but with a cross section approximately 6 times smaller than for electron neutrinos. Also, the cross section for elastic scattering, even for electron neutrinos, is smaller than that for the NC reaction. Nonetheless, the comparison of this reaction with the CC reaction provides a measure of the muon and tau neutrino flux, albeit with reduced sensitivity. Therefore, the electron-scattering reaction in SNO can be a useful tool in resolving the solar neutrino problem.

1.6 Plan

Chapter 2 presents an account of solar models, neutrino propagation, and detection in SNO. Analyses of experimental data to date are presented with limits on acceptable parameters. Chapter 3 is a general description of the SNO detector and its fundamental calibrations. Chapter 4 presents, in broad terms, the analysis procedure for SNO data. Chapter 5 is a discussion of angular resolution as studied in the Monte Carlo. A calibration method for the angular resolution is presented in chapter 6. Chapter 7 discussed the extraction of the ES signal from the data with emphasis on the directionality of recoil electrons relative to the sun. Systematic uncertainties are considered. Chapter 8 is a discussion of some of the early calibration and data runs of the SNO detector, taken before and during the filling of the detector with light and heavy water. Chapter 9 presents conclusions from the present work. Appendix A is a presentation of some of the apparatus of the calibration system.

Chapter 2

Theoretical Background

This chapter develops theory on which neutrino physics and the SNO measurements are based. It considers neutrino production in the sun, transport of neutrinos from the solar interior to the earth, cross-sections for the various reactions by which SNO detects neutrinos, and behavior of the resulting relativistic electrons in heavy water. In particular, neutrino flavour oscillations in vacuum and in matter are considered. Uncertainties in the theoretical predictions are discussed. The ability of the SNO detector to detect or measure neutrino oscillations is discussed.

2.1 Solar Models, Neutrino Predictions and Uncertainties

The evolution of the sun can be modeled numerically. So-called standard solar models (SSMs) are based on a few simple assumptions [TDF$^+$93, BPW95]. First, the energy generation within the sun is nuclear and only nuclear reactions change the composition of the sun. Second, the sun is assumed to be a non-rotating spherical object with a negligible internal magnetic field. Third, the sun is in hydrostatic equilibrium — the gravitational weight is exactly balanced by pressure (This is only true until the current source of nuclear fuel is expended. Then the weight causes a contraction, heating the core of the sun. This "ignites" the next source of nuclear fuel and a new hydrostatic equilibrium is then reached.) Fourth, the sun is assumed to be in thermal equilibrium. The transfer of heat is through photon diffusion or convective motions and the rates of these processes determine the temperature gradient at a given radius.

Several important solar parameters can be measured. They are [Ba89] the photon luminosity (3.86×10^{33} erg/s), mass (1.99×10^{33} g), radius (6.96×10^{10} cm), oblateness ($R_{\mathrm{equatorial}}/R_{\mathrm{polar}}-1 \leq 2\times10^{-5}$), and age ($\simeq 4.55\times10^9$ years). The initial elemental abundances are found by studying the solar photosphere and meteorites [TDF+93]. The exception is helium; the initial elemental abundance of helium is determined from solar models.

Solar model calculations are iterated until they correctly calculate the values of these parameters. All other properties of the sun (including neutrino production rates) are predictions of the models.

2.1.1 Nuclear Reactions in the Sun and Neutrino Production

The basic source of solar energy is the process

$$4p \longrightarrow {}^4\mathrm{He} + 2e^- + \mathrm{neutrinos} + \mathrm{energy} \tag{2.1}$$

where here, energy refers to the Q-value minus the energy taken by neutrinos. This energy is that part of the total which provides heat to the core of the sun.

The pp-chain, which models predict [TDF+93, BPW95] produces 98% of the sun's energy, is shown in figure 2.1. The CNO-cycle, which produces the remainder of the energy, is the following simpler set of reactions.

$$\begin{aligned}
{}^{12}\mathrm{C} + p &\longrightarrow {}^{13}\mathrm{N} + \gamma \\
{}^{13}\mathrm{N} &\longrightarrow {}^{13}\mathrm{C} + e^+ + \nu_e \\
{}^{13}\mathrm{C} + p &\longrightarrow {}^{14}\mathrm{N} + \gamma \\
{}^{14}\mathrm{N} + p &\longrightarrow {}^{15}\mathrm{O} + \gamma \\
{}^{15}\mathrm{O} &\longrightarrow {}^{15}\mathrm{N} + e^+ + \nu_e \\
{}^{15}\mathrm{N} + p &\longrightarrow {}^{12}\mathrm{C} + \alpha
\end{aligned}$$

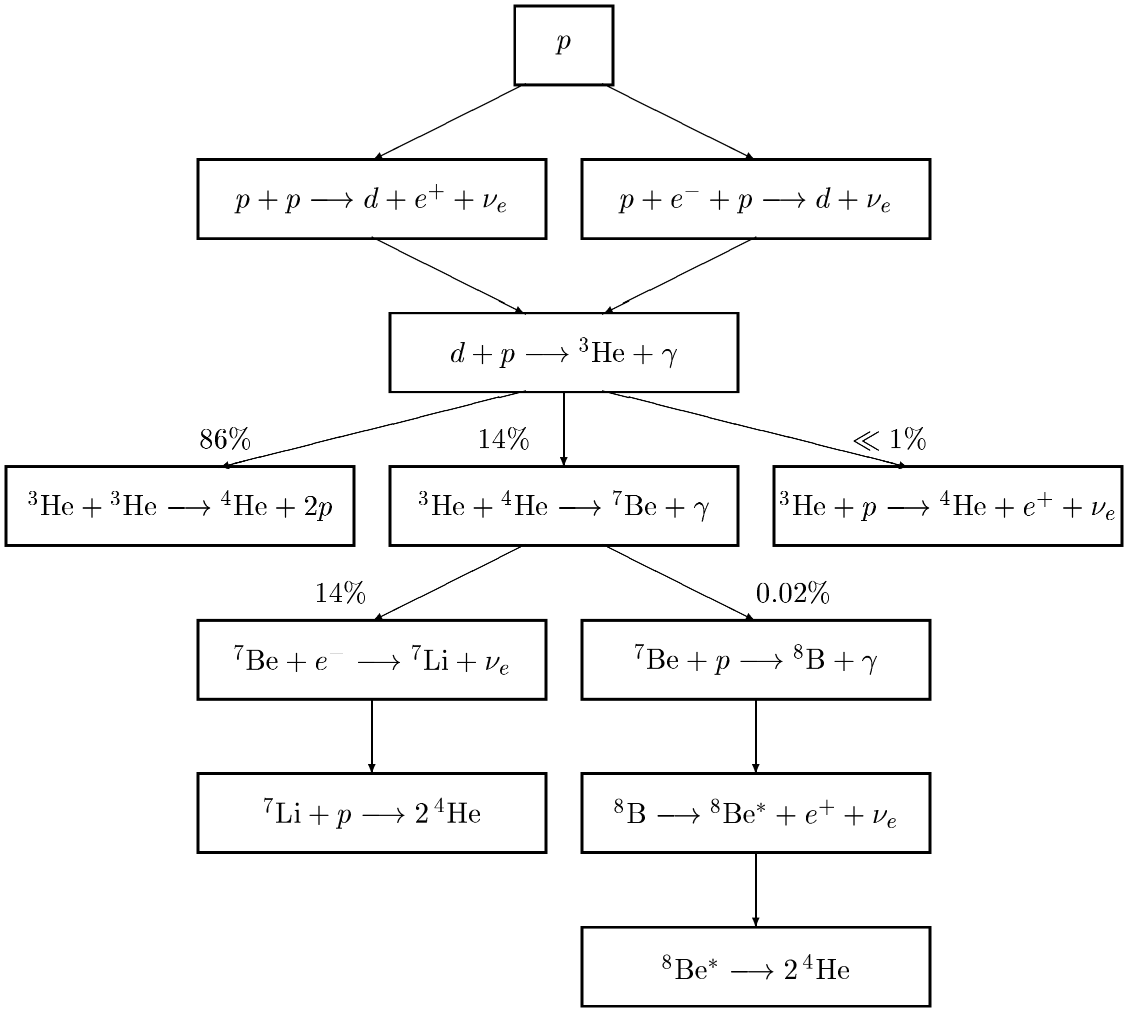

Figure 2.1: The pp chain of reactions by which the sun converts 4 protons to an alpha particle. The percentages give the relative number of cycles going through each branch [TDF+93].

Solar models predict the rates of these nuclear reactions. From this the flux of neutrinos from each reaction are calculated. The results from [BP98] are shown in table 2.1. The results from [BTM98] are quoted differently. This group quotes the neutrino fluxes integrated with the total neutrino absorption cross sections for radiochemical experiments and then gives the flux of ^{8}B neutrinos for calculating rates in water Čerenkov detectors. (This group does not state uncertainties on its results.) Similar results are available for [BP98] and are presented in table 2.2.

The neutrino spectrum for each reaction is shown in figure 1.1. The shapes of the individual spectra were taken from [Ba89, BLA$^+$96, BPW95, Ba97]. The amplitude of each spectrum was taken from [BP98]. All three reactions (CC, NC, and ES) by which SNO detects neutrinos will have an energy threshold sufficiently high that SNO will be sensitive only to ^{8}B and hep neutrinos. It is important to note that the uncertainties in the fluxes do not affect the shape of the neutrino spectra. The shapes are determined only by nuclear physics. Doppler broadening of the neutrino energies is negligible at solar energies.

The shape of the energy spectrum of neutrinos from the decay of ^{8}B is complicated by the final-state nuclear wave function. The decay is to a broad band of states in ^{8}Be*, which decays to 2 alpha particles. A review of the data of the spectrum of alpha particles has been carried out [BLA$^+$96]. This allowed the authors to calculate the neutrino energy spectrum and assign an uncertainty in the shape caused by uncertainty in the alpha data. Figure 2.2 shows the best fit spectrum and curves at $\pm 3\sigma$ confidence limits.

2.1.2 Uncertainties in Neutrino Fluxes

There is large uncertainty in some of these fluxes, including the ^{8}B flux. The source of this uncertainly in the ^{8}B flux [TDF$^+$93, BP98] comes from three main sources: uncertainty in the radiative opacity, uncertainty in the ^{7}Be(p,γ) cross section, and uncertainty in ^{3}He-^{4}He cross section. A table of uncertainties is shown for the Bahcall-Pinsonneault model in table 2.3.

The radiative opacity is a measure of how much the material in the sun prevents the radiative transfer of energy from the core to the surface. It affects, therefore, the temperature gradient in the

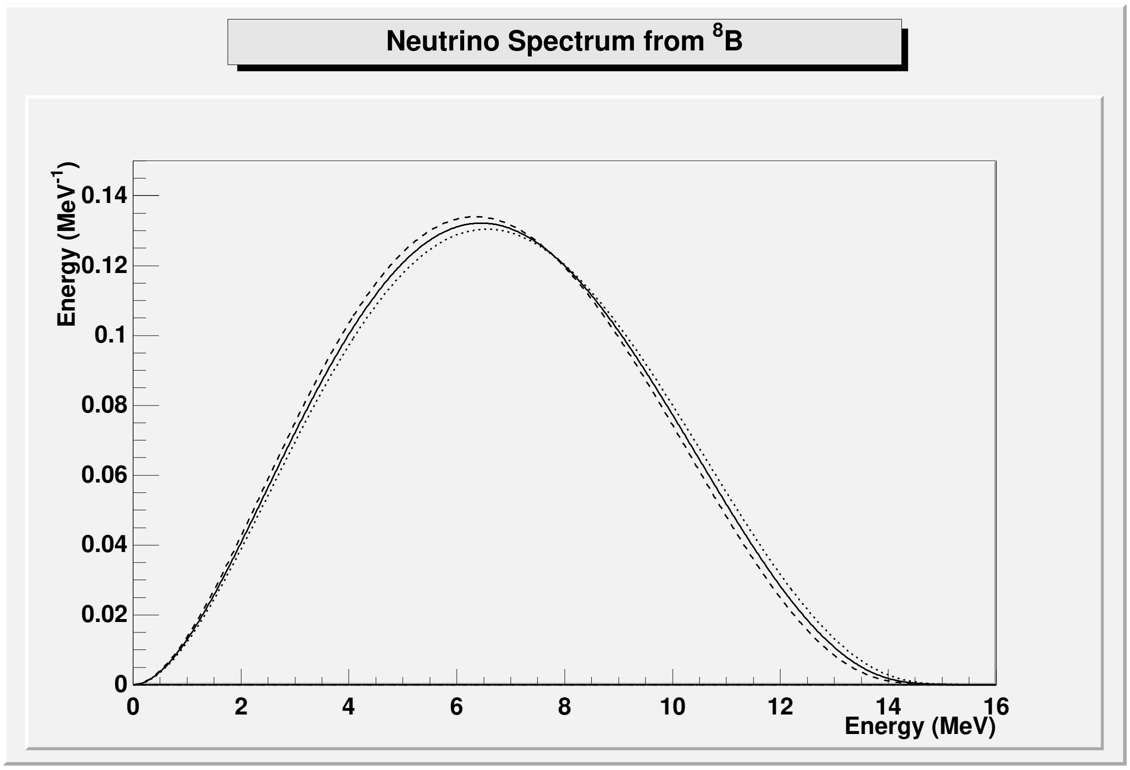

Figure 2.2: The energy spectrum and uncertainty for neutrinos from the decay of ^{8}B. The best fit curve according to [BLA^{+}96] is the solid line. The dashed lines represent $\pm 3\sigma$ uncertainty in the shape.

Predicted Neutrino Fluxes ($cm^{-2}s^{-1}$)	
Reaction	BP98
pp chain	
pp	$(5.94 \pm 1\%) \times 10^{10}$
pep	$(1.39 \pm 1\%) \times 10^{8}$
hep	2.1×10^{3}
^{7}Be	$(4.8 \pm 9\%) \times 10^{10}$
^{8}B	$(5.15^{+19\%}_{-14\%}) \times 10^{6}$
CNO cycle	
^{13}N	$(6.05^{+19\%}_{-13\%}) \times 10^{8}$
^{15}O	$(5.32^{+22\%}_{-15\%}) \times 10^{8}$
^{17}F	$(6.33^{+12\%}_{-11\%}) \times 10^{6}$

Table 2.1: The fluxes of neutrinos from each reaction according the models of [BP98]

Predicted Interaction Rates (SNU)		
Reaction	[BP98]	[BTM98]
Gallium	129^{+8}_{-6}	127
Chlorine	$7.7^{+1.2}_{-1.0}$	7.18
Neutrino Flux 10^{6} $cm^{2}s^{-1}$		
^{8}B	$(5.15^{+19\%}_{-14\%})$	4.82

Table 2.2: The fluxes of neutrinos integrated with the total neutrino absorption cross section for the models of [BP98] and [BTM98] for the radiochemical experiments. Also shown is the flux of ^{8}B neutrinos.

Contributions to fractional unc. in ^{8}B ν flux.	
Source of uncertainty	frac. unc.
Cross section of ^{3}He^{4}He reaction	0.075
Cross section of ^{7}Be(p,γ)^{8}B reaction	0.105
Opacity: calculation	0.05
Opacity: primordial Z/X	0.042
Diffusion	0.04
Cross Section of pp reaction	0.040
Cross section of ^{3}He^{3}He reaction	0.021
Solar age	0.006
Total	$+0.19\ -0.14$

Table 2.3: The fractional uncertainy in the flux of neutrinos from the ^{8}B reaction from each source of uncertainty. There are two components to the uncertainty in the opacity: uncertainty in the calculation itself and uncertainty in the ratio Z/X which is an input to the opacity calculation.

sun and because the surface temperature in the model must agree with the measured value, radiative opacity affects the temperature in the core. The nuclear reactions occur in the core and their rates are temperature dependent; thus opacity has a large effect on neutrino fluxes. Radiative opacity is difficult to calculate because it depends strongly on the heavy-element abundances (defined as elements with $Z \geq 3$.) Turck-Chièze and co-workers[TDF+93] state that the heavy elements, which contribute 2% to the mass of the sun, contribute 40% of the total opacity in the central part of the sun and 90% in the intermediate region. Even given identical inputs (the composition, density, and temperature) the calculational technique for determining the opacity can affect the result. This point is discussed in detail in both [BP98] and [BTM98].

The ^{8}B neutrino flux depends directly on the ^{7}Be(p,γ) cross section, which is known only within a large uncertainty despite many experiments. Recently a re-examination of this and other nuclear reaction rates was carried out at a workshop [AAB+98]. At this workshop, it was agreed that the experimental result of Filipone and coworkers [FED+83] was most dependable. This is the value that had been used previously by Turck-Chièze and Lopes [TDF+93, TDF+93]. Prior to this meeting, Bahcall and Pinsonneault [BPW95] used a higher value. The models from Bahcall and Pinsonneault [BP98] use the value from Filipone and co-workers.

One should note that despite the different choice of cross section, the neutrino-flux results from Bahcall and coworkers [BPW95, Ba89] (without helium and heavy element diffusion) agree within uncertainty with those of Turck-Chièze, Lopes, and co-workers. Both groups[TDF+93, BPW95] were careful to point out that if they use the same input parameters, the neutrino fluxes they calculate agree exactly.

The question of the flux of hep neutrinos is currently controversial. The flux of these neutrinos as predicted by standard solar models is sufficiently small that they can be ignored.

It is possible that the flux of hep neutrinos is underestimated in solar models by a large factor (approximately 20) and that hep neutrinos do contribute significantly to the flux measured by Kamiokande [BK98]. The uncertainty in flux arises from a large uncertainty in the cross section for the reaction. Because hep neutrinos are on a small branch of the pp chain, the rate of this reaction can be increased without affecting other reactions.

There is a hint in the data from the Super-Kamiokande experiment ([Su98a]) that there is an excess of high-energy events. The Super-Kamiokande collaboration points out that at the high-energy tail of the energy spectrum "uncertainties in the absolute energy scale and resolution can have large effects." [Su98a] They also note in the same paragraph that the rise in the energy spectrum "is difficult to be explained by these experimental uncertainties." Whether the discrepancy is due to a subtle systematic effect or is due to a real physical process is currently unclear.

Helium and heavy element diffusion have only recently been incorporated in solar models. In this process helium and heavy elements diffuse down towards the center of the sun under the influence of gravity. This affects the elemental abundance as a function of radius which affects the equation of state and the opacity.

Solar models also predict the density profile of the sun. The result [BPW95] is presented in figure 2.3. Note that the electron number density is approximately log-linear over much of the range.

2.1.3 Helio-Seismology: An Independent Test of Solar Models

Solar models have recently been given an independent observational test. Several experiments, both satellite-borne and ground-based have measured pressure oscillations on the solar surface. These observations of sound waves in the sun allow comparison of the sound speed as a function of radius as calculated by models to sound speeds inferred from the data. As well, the sound speed near the surface of the sun allows determination of the helium mass-fraction at the surface. There are two clear conclusions [BTM98, BP98]. First, diffusion of helium must be included to match the helium mass fraction at the surface. Second, standard solar models agree well with the data whereas non-standard models do not. Indeed, the models which fit the data best are standard models with diffusion.

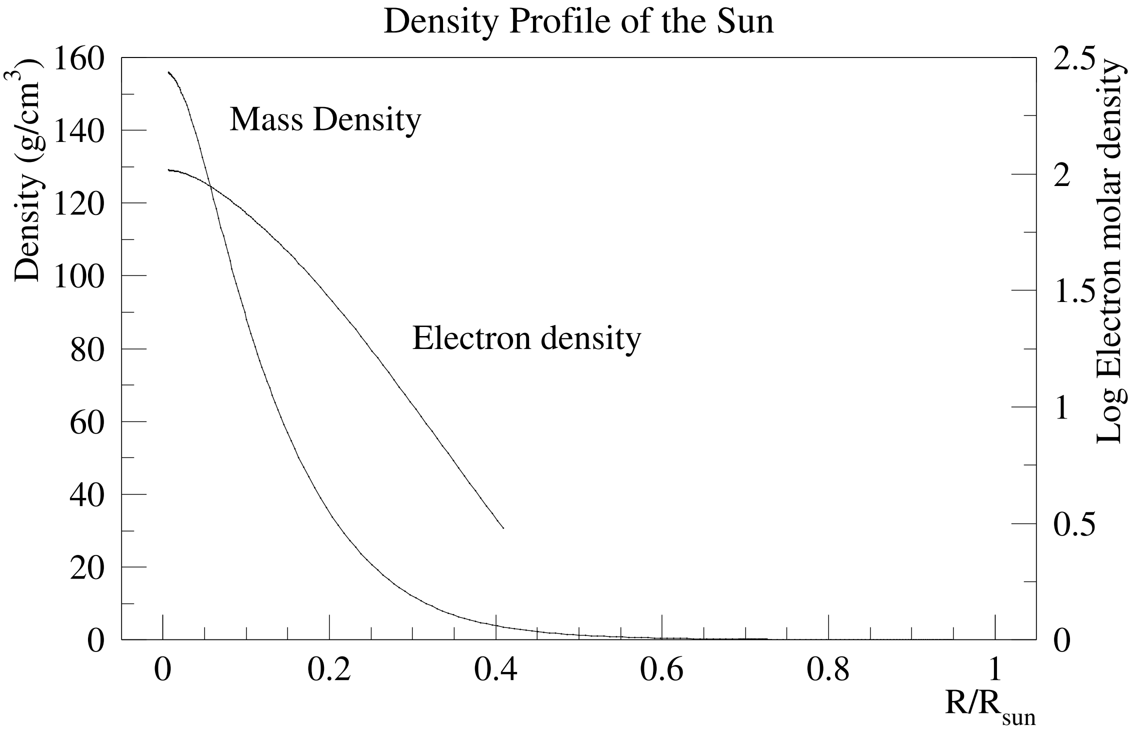

Figure 2.3: The density profile of the sun from [BPW95].

2.2 Neutrino Transport From Creation To the Earth

In the standard model (SM) of particle physics, neutrinos of all flavours are massless and have no magnetic moment. In this case, the neutrinos detected on earth would be completely unaffected by their propagation from the sun. (Gravitational red-shift of the neutrinos as they escape the sun's gravitational potential well is negligibly small.)

Granting at least one flavour of neutrino a mass is an extension to the SM, but a simple one. If, furthermore, we assume that the eigenstates of the neutrino mass matrix are not the same as the weak-interaction eigenstates, then it is possible for neutrinos to oscillate between flavours in the vacuum between the sun and the earth.

If we want to consider the effects of neutrino masses, we must study the neutrino wave equation.

Neutrinos are fermions and thus obey the Dirac equation. However, for ultra-relativistic neutrinos the spin structure is not important to propagation. Eliminating the spin structure from the Dirac equation yields the Klein-Gordon equation, regardless of whether neutrinos are Dirac or Majorana particles [KP89]. The Klein-Gordon equation is further simplified by considering only radially-outward-going particles. Also, if one approximates that the three mass states have identical three-momenta, then the second derivative term in the Klein-Gordon equation contributes a constant (therefore irrelevant) phase factor. We can write [KP89]

$$\frac{m^2}{p}|\nu >= i\frac{d}{dt}|\nu > \tag{2.2}$$

From this equation we can write the time-evolution of the neutrino in the mass basis. The results derived here will be done assuming two neutrino species: electron and muon. The equations are similar to, and illustrate the concepts of, the more rigorously correct equations with three neutrino species. There are situations where the two-flavour approach is inadequate for solar neutrinos. These are discussed in the text.

2.2.1 Vacuum Oscillations

The solution to the wave equation in vacuum is

$$\begin{pmatrix} \nu_1(t) \\ \nu_2(t) \end{pmatrix} = \begin{pmatrix} e^{-\imath E_1 t} & 0 \\ 0 & e^{-\imath E_2 t} \end{pmatrix} \begin{pmatrix} \nu_1(0) \\ \nu_2(0) \end{pmatrix} \tag{2.3}$$

The states detected and created are eigenstates of the weak-interactions so a rotation matrix characterized by angle θ is used to convert between the mass and weak-interaction basis. The survival probability is the probability that an electron neutrino created in the sun is still an electron neutrino when it reaches the earth. Is is defined as $P(\nu_e \longrightarrow \nu_e) = (< \nu_e|\nu_e >)^2$. Applying this to the above equation results in

$$P(\nu_e \longrightarrow \nu_e) = \left[\begin{pmatrix} 1 & 0 \end{pmatrix} \begin{pmatrix} \cos\theta & \sin\theta \\ -\sin\theta & \cos\theta \end{pmatrix} \begin{pmatrix} e^{-\imath E_1 t} & 0 \\ 0 & e^{-\imath E_2 t} \end{pmatrix} \begin{pmatrix} \cos\theta & -\sin\theta \\ \sin\theta & \cos\theta \end{pmatrix} \begin{pmatrix} 1 \\ 0 \end{pmatrix} \right]^2 \tag{2.4}$$

which simplifies to

$$P(\nu_e \longrightarrow \nu_e) = 1 - \frac{1}{2}\sin^2 2\theta \times [1 - \cos(E_2 - E_1)t] \tag{2.5}$$

This equation is useful. It allows a definition of the length scale of the problem, the so-called vacuum-oscillation length,

$$\lambda = \frac{p}{\pi}(m_2^2 - m_1^2) \tag{2.6}$$

$$\lambda = \frac{4\pi \mathrm{E}}{\Delta m^2} \tag{2.7}$$

where $\Delta m^2 \equiv m_2^2 - m_1^2$.

If the production of neutrinos in the sun occurs over distances larger than λ, or if the solar neutrino sources are not mono-chromatic, the phase term in equation 2.5 averages out leaving

$$P(\nu_e \longrightarrow \nu_e) = 1 - \frac{1}{2}\sin^2 2\theta \tag{2.8}$$

While the two-flavour description for vacuum oscillations is simple and illustrates the fundamental concepts, for solar neutrinos it is necessary to incorporate all three flavours. Indeed, if the number of flavours is given by N, the reduction in electron-neutrino flux has a maximum value of 1/N [Ba89]. For solar neutrinos, a reduction of 1/2 is not sufficient to explain the solar neutrino problem and N = 3, which is allowed as there are three neutrino types, is necessary to explain the deficit in the Homestake data. The main drawback of the vacuum-oscillation scenario is that the reduction in flux is independent of energy and energy dependence in needed to reconcile the results of all three experiments.

2.2.2 Effects of Matter

The oscillation effects are more complicated when the effects of matter are considered. The electron neutrinos feel a charged-current interaction with the electrons in the matter that muon or tau neutrinos do not. This "forward scattering" gives an induced mass to the electron neutrino. It is important to note that the potential, $V = \sqrt{2}G_F N_e$, where G_F is the Fermi constant and N_e

is the electron number density, is linear in the Fermi constant, and is therefore much larger than the scattering cross-sections which are quadratic in G_F. Thus, while the probability of a neutrino scattering in the sum is small, the potential is not necessarily small.

The wave equation in the weak-interaction basis becomes

$$-i\frac{d}{dt}|\nu_\alpha >= \frac{1}{2p}M^2|\nu_\alpha > \tag{2.9}$$

with

$$M^2 = U\begin{pmatrix} m_1^2 & 0 \\ 0 & m_2^2 \end{pmatrix}U^\dagger + \begin{pmatrix} A & 0 \\ 0 & 0 \end{pmatrix} \tag{2.10}$$

with $A = 2\sqrt{2}G_F N_e E$.

Similar to the vacuum case, we define a rotation matrix, U_m, to transfer from the weak-interaction basis to the mass basis, this time characterized by the angle θ_m. When the wave equation (2.9) is diagonalized, a relationship between θ_m, θ, Δm^2, and A is found.

$$\tan 2\theta_m = \frac{\Delta m^2 \sin 2\theta}{-A + \Delta m^2 \cos 2\theta} \tag{2.11}$$

The diagonalized mass matrix can be defined.

$$U_m^\dagger M^2 U_m \equiv \begin{pmatrix} M_1^2 & 0 \\ 0 & M_2^2 \end{pmatrix} \tag{2.12}$$

The eigenvalues are

$$M_{2,1}^2 = \left(m_1^2 + m_2^2 + A \pm [(A - \Delta m^2 \cos 2\theta)^2 + (\Delta m^2 \sin 2\theta)^2]^{1/2}\right)/2 \tag{2.13}$$

This has two important features. While θ is restricted to the region $0 \leq \theta < \pi/4$, θ_m can vary from 0 to $\pi/2$ and there is a resonance at $A = \Delta m^2 \cos 2\theta$ where mixing is maximal.

2.2.3 Solving the Wave Equation in Matter

The wave equation can be written as follows.

$$\imath\frac{d}{dx}\begin{pmatrix} \nu_e \\ \nu_\mu \end{pmatrix} = \frac{1}{2E}U_m\begin{pmatrix} M_1^2 & 0 \\ 0 & M_2^2 \end{pmatrix}\begin{pmatrix} \nu_1 \\ \nu_2 \end{pmatrix} \tag{2.14}$$

where U_m is a function of density and therefore radial position in the sun. (The derivative on the left-hand side of the equation is written with respect to position because the neutrino travels at approximately the speed of light and thus the derivative with respect to time is proportional to a derivative with respect to position.) Writing this completely in the mass basis and neglecting a diagonal phase factor yields

$$\imath \frac{d}{dx}\left(\begin{array}{c}\nu_1\\ \nu_2\end{array}\right)=\left(\begin{array}{cc}-(M_2^2-M_1^2)/4E & -\imath d\theta_m/dx\\ \imath d\theta_m/dx & (M_2^2-M_1^2)/4E\end{array}\right)\left(\begin{array}{c}\nu_1\\ \nu_2\end{array}\right) \tag{2.15}$$

It is convenient to define two length scales analogous to the vacuum-oscillation length defined in equation 2.7. They are the induced-mass length, λ_0, and the mass-oscillation wavelength, λ_m.

$$\lambda_0 \equiv 4\pi E/A \tag{2.16}$$

$$\lambda_m \equiv 4\pi E/(M_2^2-M_1^2) \tag{2.17}$$

With equation 2.15 the wave equation can be solved easily if the *adiabatic approximation* is made. The adiabatic approximation states that the density changes in the sun are long on the length scale of λ_m or, more precisely,

$$\left|\frac{1}{N_e}\frac{dN_e}{dx}\right| \ll \frac{1}{\sin 2\theta}\frac{2\pi}{\lambda_m}\frac{\lambda\lambda_0}{\lambda_m^2} \tag{2.18}$$

If this condition is true, then the off-diagonal terms in equation 2.15 can be dropped. In this case, then, the propagation is diagonal in the mass basis. One need only know the mixing at the point the neutrino was created and detected to work out the probability that the neutrino, created as a ν_e, is detected as a ν_e. If one assumes detection at approximately vacuum and creation at a mixing angle θ_m, then

$$P(\nu_e \to \nu_e) = \frac{1}{2}\left(1+\cos 2\theta \cos 2\theta_m\right) \tag{2.19}$$

The adiabatic formula is useful and accurate for many values of θ and Δm^2, but not for all. Therefore, a correction term is needed to take into account the off-diagonal terms in equation 2.15. This correction is needed in a narrow region near the resonance, where the adiabatic requirement is most strict. Away from this region, adiabatic propagation is still accurate. The physical picture is neutrino creation at high density where the adiabatic equation holds; propagation towards the resonance, where, briefly, the off-diagonal terms become comparable to the diagonal terms; and adiabatic propagation through the rest of the sun and into vacuum. Put differently, the mass eigenvalues, which are affected by the solar density and thus the location of the neutrinos within the sun, can become almost degenerate at the resonance point. If they are nearly degenerate, a "level-crossing" can occur and there can be tunneling between the mass eigenstates.

The mathematical methods to solve this problem were developed in 1932 by Landau, Zener, and Stueckelberg in the context of magnetic levels of electrons in atomic collisions. Parke [Pa86] applied this to neutrino propagation and obtained the following, now called the Parke formula:

$$P(\nu_e \to \nu_e) = \frac{1}{2} + \left(\frac{1}{2} - P_c\right) \cos 2\theta \cos 2\theta_m \tag{2.20}$$

The term, P_c is the correction term and depends on the derivative of the density profile near resonance. For solar neutrino applications, P_c can be written as

$$P_c = e^{-\pi\gamma(1-\tan\theta)/2} \tag{2.21}$$

with

$$\gamma = \frac{\Delta m^2 \sin^2 2\theta}{2E \cos 2\theta |dN_e/dx|} \tag{2.22}$$

with the derivative evaluated at resonance.

It is important to note that this applies only if the non-adiabatic propagation of the neutrino is near the resonance. This will not be true for large mixing angles. More sophisticated functions for P_c can be derived to account for these conditions. The reader is referred to equation 2.58 and table III in the review by Kuo and Pantaleone [KP89]. For solar neutrino oscillation analysis for the parameter range near the best-fit MSW solutions to current data, the Parke formula with P_c defined above is accurate.

2.2.4 The Number of Neutrino Species

For MSW analysis, it is important to understand when the two-flavour analysis is appropriate and when a three-flavour analysis is required. A two-flavour description is valid if two conditions are met. First, the three-flavour oscillation must break up into 3 independent two-flavour oscillations. This will occur as long as no two neutrino masses are degenerate or nearly degenerate. Second, during neutrino propagation from the core to the edge of the sun there must be only one resonance [KP89]. This condition will hold if the neutrino masses are hierarchical: if $|m_2^2 - m_1^2| \ll |m_3^2 - m_2^2|$. This may be borne out by the data [FLM$^+$97].

2.3 Experimental Constraints on Oscillations

Using the solar model in [BPW95], Hata and Langacker have performed global fits to the data using various oscillation models [HL97]. They find the following 2 sets of parameters for an MSW analysis: The "small angle" solution has $\sin^2 2\theta = 8.2\times10^{-3}$ and $\Delta m^2 = 5.1\times10^{-6}(\mathrm{eV})^2$ with $\chi^2(7\mathrm{dof}) = 5.9$. The "large angle" solution has $\sin^2 2\theta = 0.63$ and $\Delta m^2 = 1.6 \times 10^{-5}(\mathrm{eV})^2$ with $\chi^2(7\mathrm{dof}) = 6.3$. For a vacuum oscillation analysis, they find three good fits with similar parameters. The best is $\sin^2 2\theta = 0.90$ and $\Delta m^2 = 6.6 \times 10^{-11}(\mathrm{eV})^2$ with $\chi^2(9\mathrm{dof}) = 9.9$. The other two $\sin^2 2\theta = 0.83$ and $\Delta m^2 = 7.9 \times 10^{-11}(\mathrm{eV})^2$ with $\chi^2(9\mathrm{dof}) = 11.4$ and $\sin^2 2\theta = 1.0$ and $\Delta m^2 = 5.2 \times 10^{-11}(\mathrm{eV})^2$ with $\chi^2(9\mathrm{dof}) = 11.9$. While these parameters look similar, the 95%-confidence-level regions around these local minimum are disjoint from each other.

An analysis by Bahcall, Krastev, and Smirnov [BKS98] using the most recent solar model calculations fit to the rates from all experiments and the zenith-angle distribution and electron recoil spectrum from Super Kamiokande arrives at a best fit small-angle MSW solution of $\sin^2 2\theta = 5.5 \times 10^{-3}$, $\Delta m^2 = 5.4 \times 10^{-6}(\mathrm{eV})^2$, and $\chi^2 = 37.2$ for 26 degrees of freedom. The best-fit vacuum oscillation scenario has $\sin^2 2\theta = 0.75$, $\Delta m^2 = 6.5 \times 10^{-11}(\mathrm{eV})^2$ and $\chi^2 = 28.4$ for 18 degrees of freedom.

The analysis by Bahcall, Krastev, and Smirnov finds an acceptable fit to the data for a large-angle solution if the ^{8}B flux is taken as a *free* parameter. (In the analysis discussed above the flux was fixed; they do not discuss a case where the ^{8}B flux is allowed to vary but also included in the calculation of χ^2.) The large-angle solution found is $\sin^2 2\theta = 0.57$, $\Delta m^2 = 1.6 \times 10^-5 (\mathrm{eV})^2$, and a reduced value of χ^2 of 0.91.

If the fits are performed using only the average event rates for each experiment, then the results of [BKS98] become $\sin^2 2\theta = 6 \times 10^{-3}$ and $\Delta m^2 = 5.4 \times 10^{-6} (\mathrm{eV})^2$ for the small-angle solution and $\sin^2 2\theta = 0.76$ and $\Delta m^2 = 1.8 \times 10^{-5} (\mathrm{eV})^2$ for the large-angle solution.

2.4 Interaction Rates in the Detector

The theory developed so far yields the neutrino flux at the earth. The cross sections for neutrino interactions with heavy water are needed to calculate reaction rates in SNO. There are three important reactions: the charged current (CC), the electron scattering (ES), and the neutral current (NC) interaction.

2.4.1 The Charged-Current Reaction

The charged-current interaction,

$$\nu_e + d \longrightarrow p + p + e^- \tag{2.23}$$

is only sensitive to electron neutrinos. The charged-current breakup of the deuteron at solar neutrino energies can be calculated accurately using the effective range approximation [BL96] if the recoil energies of the two protons in the two-proton center of mass system and the total momentum of the two-proton final state are considered. Calculations of the differential cross section with respect to out-going electron energy using this simple technique are in excellent agreement with more detailed calculations. This calculation underestimates the total cross section by approximately 5%, independent of neutrino energy, in comparison with the more-detailed calculations.

These more sophisticated calculations use realistic nucleon Hamiltonians and wave functions. However, it is important to include corrections to take into account exchange-current effects even at solar energies. (Exchange current operators are many-body operators which correct for neglected hadronic degrees in freedom in the nucleon wave functions. An example is the presence of virtual pions induced by the weak interaction.) If such effects are not taken into account, as they were not in the calculation of Ying, Haxton, and Henley [YHH82], the total cross section is under-estimated by approximately 5% [KN94].

Kubodera and Nozawa report two independent calculations that include all the corrections known to be important (carried out by Kohyama and Kubodera and by Doi and Kubodera, both unpublished) and get answers in agreement to 2%. The results of the Kohyama and Kubodera calculation are tabulated in [KN94]. A 5% uncertainty is assigned to these results.

Recently, calculations of the radiative corrections to the CC cross-section were performed. They are typically of order 2% [To98].

There are three important features of the cross section from the experimental point of view. First, the total cross section increases with energy approximately as the square of the neutrino energy. Figure 2.4 shows the total CC cross section as a function of neutrino energy from [KN94].

Second, the electron energy is correlated with the neutrino energy. Figure 2.5 shows the differential charged-current cross section with respect to energy for an 8 MeV neutrino. Figure 2.6 shows the the recoil electron energy spectrum integrated over the ^{8}B neutrino flux.

The third important feature is the angular relation between the neutrino and electron. Because the CC reaction is to first order a pure Gamow-Teller process, the angular distribution between the two goes as $1 - \frac{\beta}{3}\cos\theta$ [CB83]. For electrons above a few MeV, $\beta \simeq 1$ and the angular distribution is constant with twice as many electrons directed back towards the sun as away from it. This slope is reduced slightly by higher order corrections [KN94].

2.4.2 The Electron-Scattering Interaction

The electron-scattering interaction,

$$\nu_x + e \longrightarrow \nu_x + e \tag{2.24}$$

is sensitive to all flavours of neutrinos although the cross section for electron neutrinos is approximately 6 times larger than that for muon or tau neutrinos.

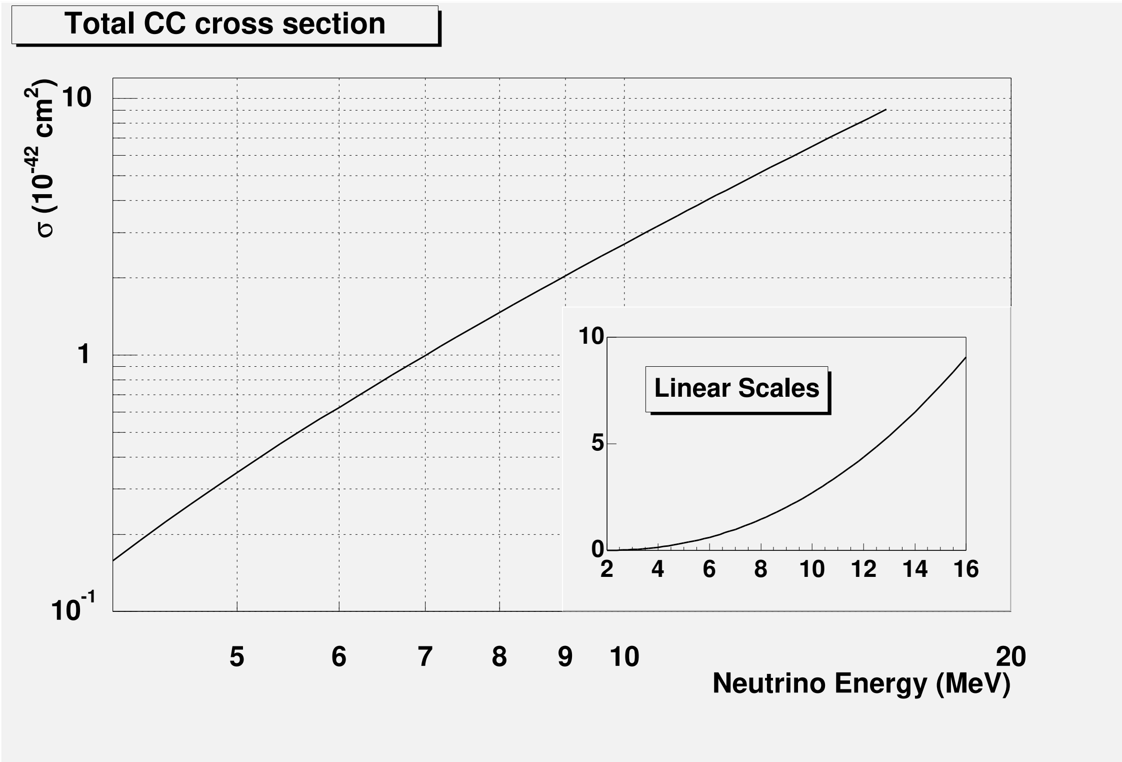

Figure 2.4: The total charged-current cross section is plotted as a function of neutrino energy. The large plot has logarithmic scales on the ordinate and abscissa. The inlaid plot has linear scales with the same units.

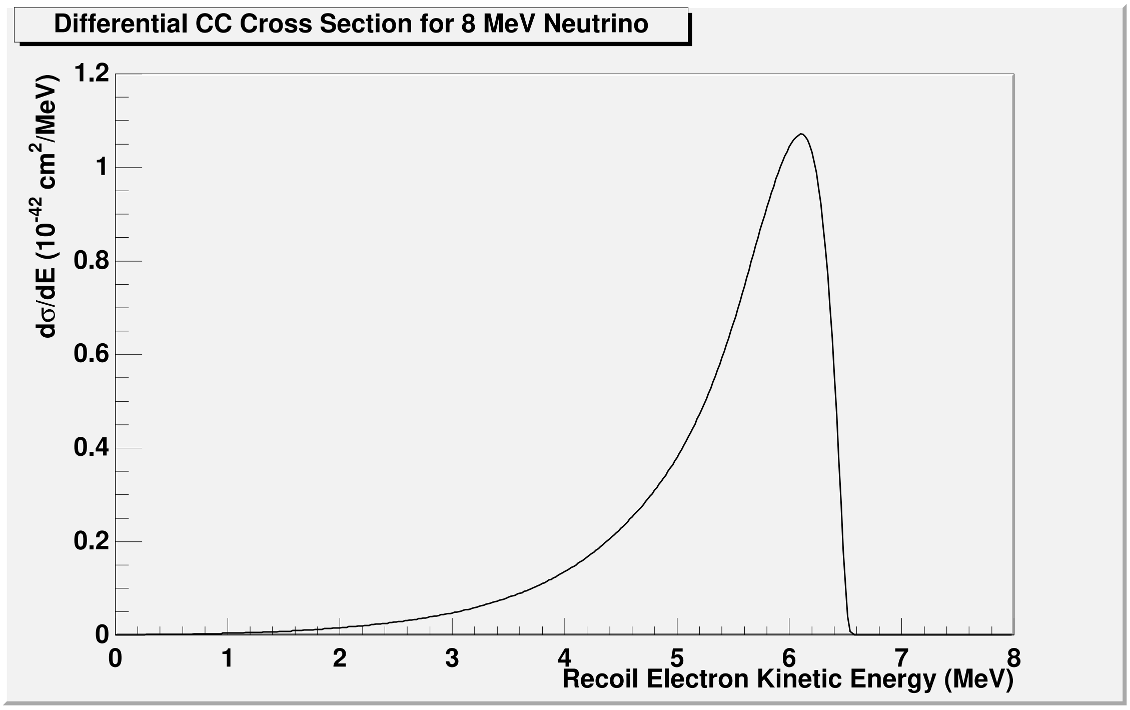

Figure 2.5: The differential charged-current cross section with respect to electron recoil energy for 8 MeV neutrinos.

The cross section for a neutrino of energy q scattering and producing a recoil electron with kinetic energy, T, is [Ba89]

$$\frac{d\sigma}{dT} = \frac{2G_F^2 m_e^3}{\pi\hbar^4}\left[g_L^2 + g_R^2(1-T/q)^2 - g_L g_R(Tm_e/q^2)\right] \tag{2.25}$$

The coefficients are $g_L = \pm 1/2 + sin^2\theta_W$ and $g_R = sin^2\theta_W$ with the positive sign for $\nu_e e^-$ scattering and the negative sign for $\nu_{\mu,\tau} e^-$ scattering. The Weinberg angle, θ_W, is given by $\sin\theta_W = 0.23124(24)$ [Pa98]. Unlike the CC case, the electron recoil energy distribution for a given neutrino energy is almost flat. If this cross section is integrated over the neutrino spectrum from the ^{8}B beta decay, the electron energy spectrum for this reaction is obtained. It is shown in figure 2.6.

Calculations of the radiative corrections were carried out and found to reduce the cross section by approximately 2% on average. The effect is as large as 4% at the highest electron recoil energies in the solar neutrino spectrum [BKS95]. The uncertainty in the cross section after these corrections are made is less than 1%.

Also important is the relationship between the neutrino energy, q, the electron kinetic energy, T, and the angle between the outgoing electron and the incident neutrino,

$$\cos^2\theta = \frac{T/m_e(1+q/m_e)^2}{(T/m_e+2)q^2/m_e^2} \tag{2.26}$$

where only positive values of $\cos\theta$ are physical. This equation shows that for $T, q \gg m_e$ the cosine is almost exactly one. If one considers electrons with a kinetic energy of 4.5 MeV or more, this condition holds true and the electrons are directed along the neutrino incident direction. The neutrino incident direction is very well defined by the location of the sun and the detector and thus the notation used in the rest of the text is $\cos\theta_{\text{sun}}$. This angular information will prove critical in extracting the ES signal from the data.

2.4.3 The Neutral-Current Reaction

The reaction

$$\nu_x + d \longrightarrow \nu_x + p + n \tag{2.27}$$

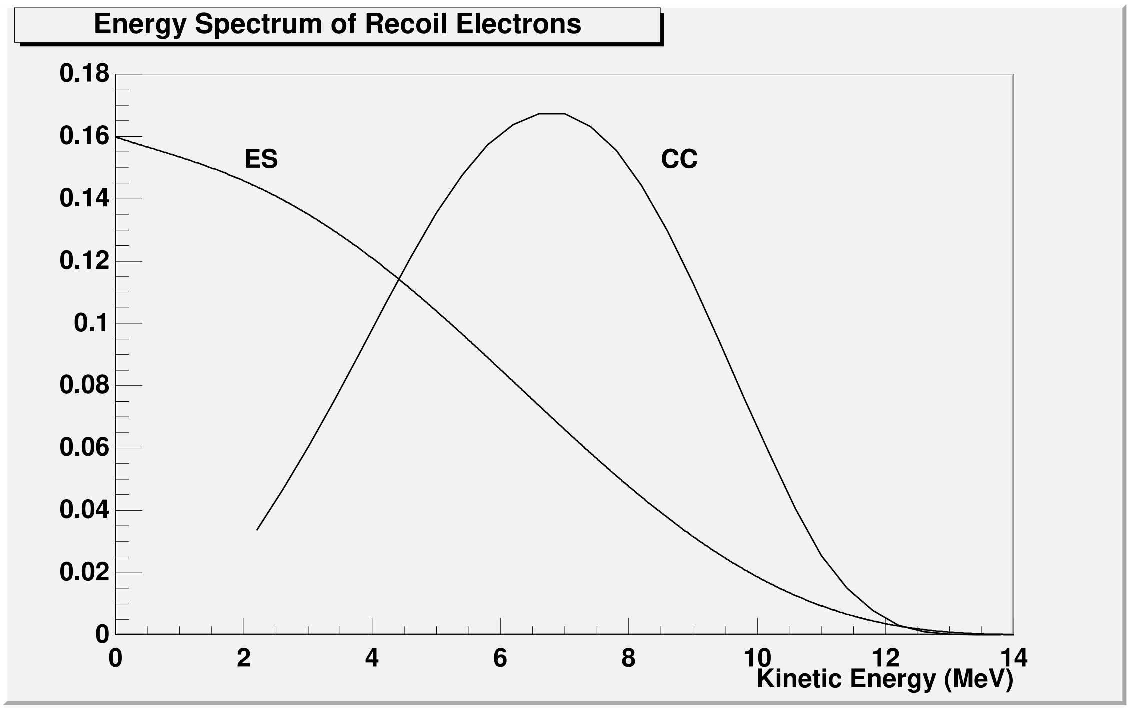

Figure 2.6: The energy spectrum for the electron-scattering (ES) and charged-current (CC) reactions integrated over the ^{8}B beta spectrum. The spectra are normalized to unit area. The CC spectrum is only shown for electron energies above 2 MeV.

yields a free neutron which must then be detected. With pure heavy water in the vessel, the only method by which a neutron can be observed is by detecting the 6.2 MeV gamma ray resulting from capture on the deuteron. Because the thermal neutron capture cross section on a deuteron is only 0.521 millibarns compared to 0.335 barns on hydrogen [GK76] and because the thermal-neutron diffusion length is approximately 120 cm [SW98], the probability that a neutron captures on a deuteron in the heavy water is less than the probability of capture on hydrogen in the acrylic vessel or light water. Only approximately 20% of free neutrons from the reaction will produce a 6.2 MeV gamma ray. (The 2.2 MeV gamma ray liberated when a neutron captures on hydrogen becomes a component of the low-energy background discussed in the next chapter.)

The uncertainty in the total cross section for the NC reaction is similar to that for the CC reaction. However, the ratio of the two cross-sections has a smaller uncertainty, approximately 2%, because many of the uncertainties cancel [KN94]. This is important because SNO will measure the ratio of the NC to the CC rate.

There are two other methods to detect neutrons [Ew$^+$87, BDH$^+$92]. One is the addition of $MgCl_2$ to the heavy water. The cross section for capture on ^{35}Cl is 41.8 barns [GK76]. There is a resulting gamma cascade liberating 8.581 MeV. The probability a neutron is captured on a ^{35}Cl nucleus in the heavy water is approximately unity.

The second method uses neutral-current detectors, or NCDs. The NCDs are an array of ^{3}He-filled proportional counters which detect the proton from the (n,p) reaction on the ^{3}He. The array is approximately 50% efficient in detecting neutrons and has only a small effect on detector optics.

2.4.4 The Rates

Using neutrino fluxes and energy spectra, the Parke formula, and the cross sections, it is possible to calculate the event rates per year for various scenarios. The formulae to do so are

$$\mathrm{N_{ES}} = \mathrm{N_e N_\nu} \mathcal{S} \int_{5\mathrm{MeV}}^{\infty} dE_e \int_0^{\infty} dE_\nu \phi_\nu \left(\mathrm{P}_e \frac{d\sigma(\nu_e)}{dE_e} + (1 - \mathrm{P}_e) \frac{d\sigma(\nu_\mu)}{dE_e} \right) \tag{2.28}$$

and

$$\mathrm{N_{CC}} = \mathrm{N_D N_\nu} \mathcal{S} \int_{5\mathrm{MeV}}^{\infty} dE_e \int_0^{\infty} dE_\nu \phi_\nu \mathrm{P}_e \frac{d\sigma(\mathrm{CC})}{dE_e} \tag{2.29}$$

where $\mathrm{N_{ES}}$ and $\mathrm{N_{CC}}$ are the number of events for each reaction in one year; $\mathrm{N_e}$ and $\mathrm{N_D}$ are the number of electrons and deuterium nuclei respectively; N_ν is the total neutrino flux per second; $\mathcal{S}$ is the number of seconds in one year; ϕ_ν is the normalized neutrino flux as a function of neutrino energy; P_e is the probability that an electron neutrino generated in the sun is still an electron neutrino at the detector; $d\sigma(\nu_e)/dE_e$ is the differential cross section for electron scattering by electron neutrinos of energy E_ν; $d\sigma(\nu_\mu)/dE_e$ is the differential cross section for electron scattering by muon neutrinos of energy E_ν; and $d\sigma(\mathrm{CC})/dE_e$ is the differential charged-current cross section. A threshold of 5 MeV has been imposed on the recoil electron. The shorthand notation ν_μ has been used to represent a muon or tau-type neutrino.

Calculations were performed for two scenarios, the small-angle and large-angle best fits to average event rates in all experiments from the analysis in [BKS98]. The small-angle solution is $\Delta m^2 = 5.4 \times 10^{-6}\mathrm{eV}^2$ and $\sin^2 2\theta = 6.0 \times 10^{-3}$. Figure 2.7 shows several spectra from the calculation. The neutrino survival probability is plotted as a function of neutrino energy. The top-right plot shown the neutrino spectra at the detector. The curve labelled "all" is the full undistorted ^{8}B flux normalized to unit area. The electron and muon-neutrino components to this flux are shown also. The average energy of the electron-neutrino spectrum is shifted upwards because the survival probability is higher at higher energies. This is important because the total CC cross section increases as energy squared. The bottom-left plot shows the recoil-electron energy spectrum for the CC reaction. The units are electrons per MeV for a live time of one-year for 1000 tonnes of heavy water. The bottom-right plot shows the electron-recoil spectrum for the ES reaction from ν_e and ν_μ neutrinos individually as well as the sum of the two.

A similar figure (2.8) is shown for the large-angle solution in [BKS98]. This calculation has $\Delta m^2 = 1.8 \times 10^{-5}\mathrm{eV}^2$ and $\sin^2 2\theta = 0.76$. Note that the survival probability for electron neutrinos is only 28% and is not a function of neutrino energy.

The final results are given in table 2.4.4. What is important here is the ratio of the rates: ES/CC.

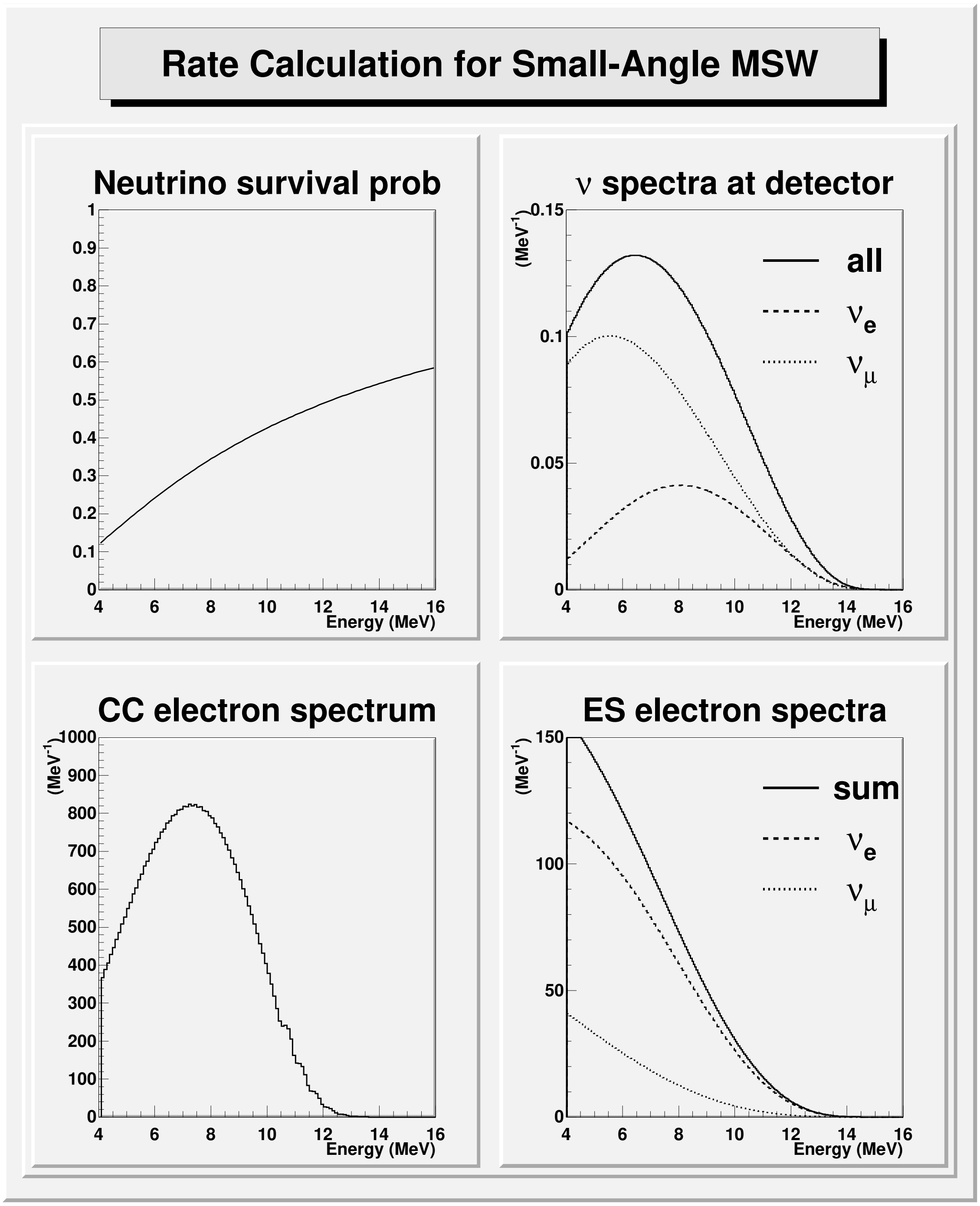

Figure 2.7: Spectra are shown for the calculation of event rates for the small-angle solution. The electron spectra have units of events per MeV per year of data for 1000 tonnes of heavy water. The spectra are described in the text.

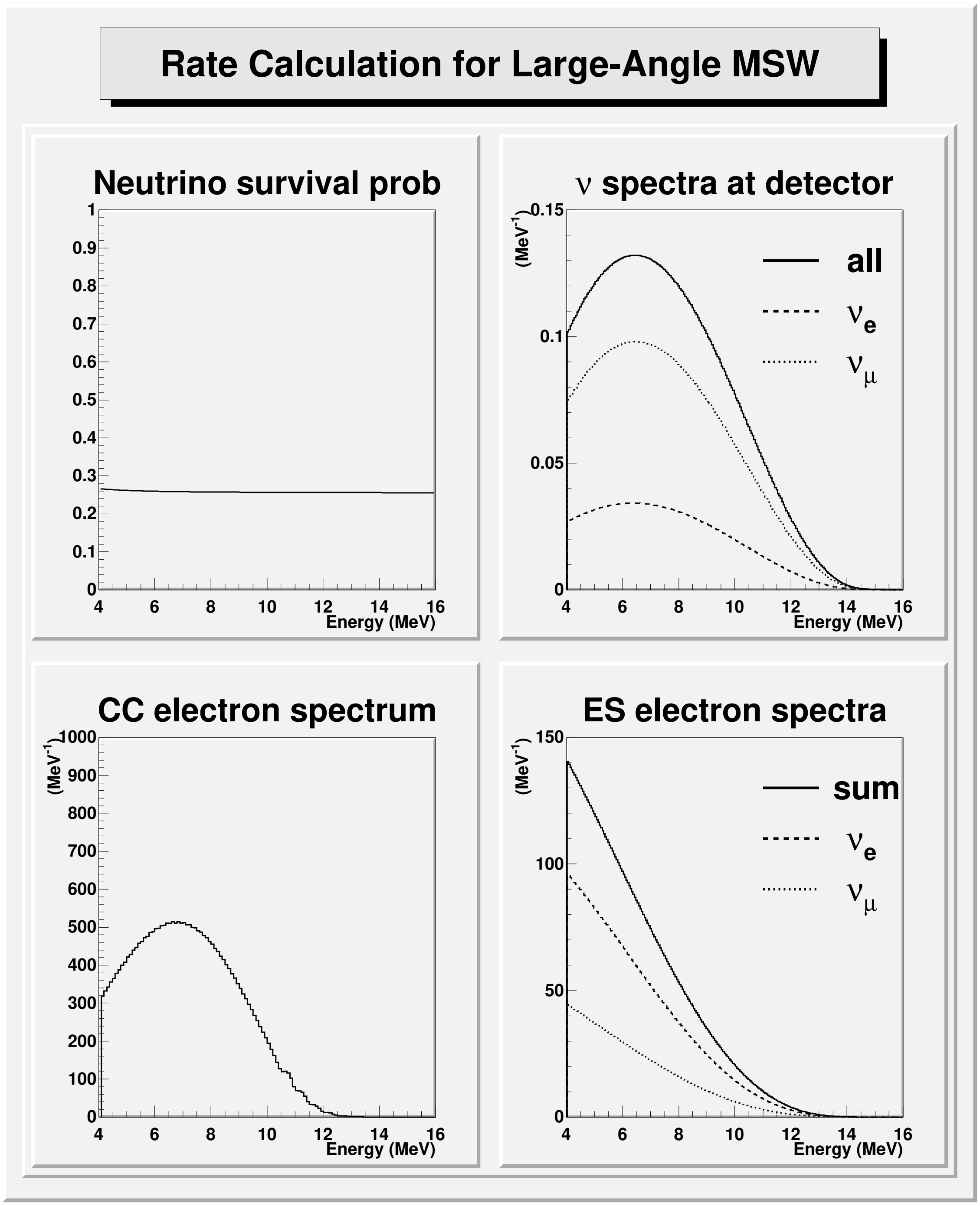

Figure 2.8: Spectra are shown for the calculation of event rates for the large-angle solution. The electron spectra have units of events per MeV per year of data for 1000 tonnes heavy water. The spectra are described in the text.

This ratio has no uncertainty from the absolute neutrino flux, N_ν. Therefore, this measurement is a model-independent test of neutrino oscillations if there are no oscillations to sterile neutrinos. The ratio for the favoured small-angle solution is 20% different than that for a scenario with no oscillations. This suggests that the statistical uncertainty on the measurement should be smaller than 5% to differentiate the small-angle solution from the reduced-flux model. A 5% statistical uncertainty suggests a minimum of 400 ES events are needed to make this measurement. Given the calculated rates, this measurement requires approximately one year of data.

The rates for the large-angle MSW deserve some comment. The large-angle MSW solutions do not give as good a fit to the experiments performed to date as the small-angle solution if the fits use a solar model. One reason for this is apparent in the table. The rate of ES interactions for the large-angle solution is well below that suggested by the Super-Kamiokande data. Most reviews of the data [BKS98, HL97] do indicate that the quality of fit for the large-angle solution is not nearly as good as the small-angle solution. To bring the electron-scattering rate for the large-angle MSW scenario up to that measured by the Super-Kamiokande experiment, the ^{8}B flux must be increased by 27%. The uncertainty in [BP98] is $+19\%$ -14%. The required increase is 1.5σ.

The difference between the large-angle and reduced-flux hypothesis is 7σ (statistical uncertainty only) for a data sample from one year. If this model is correct, a comparison of the ES to CC rate in SNO will be able to clearly differentiate this model from the reduced-flux case and provide solid evidence of solar-neutrino oscillations.

The statistical uncertainties used to estimate the significance of the difference between oscillation scenarios and the reduced flux case are calculated as the square root of the number of ES events. There will, of course, be uncertainties from the extraction of the ES signal from the total data set and many systematic uncertainties. These are discussed throughout the course of this work.

2.5 Electron Transport in Water and Čerenkov Light

The recoil electrons from solar neutrino interactions in the heavy water and background from radioactive decays are relativistic. That is to say the electrons have kinetic energies of 1 to 15 MeV

Event Rates above 5 MeV year^{-1}			
	Reduced Flux	Small Angle MSW	Large Angle MSW
ES	457	468	359
CC	4495	3828	2457
Ratio	0.102	0.122	0.147

Table 2.4: Event rates for various scenarios. The small-mixing-angle and large-mixing-angle solution parameters are from [BKS98] with only the event rates considered. (See section 2.3.) The event rate for the reduced-flux case was calculated based on the measured flux from [Su98b].

and thus have $\beta \equiv v/c \simeq 1$. The electrons lose energy by collisions with electrons in the water, they are Coulomb-scattered by nuclei, and, as long as they are sufficiently energetic, emit Čerenkov radiation. All neutrino measurements in SNO are in fact measurements of the Čerenkov radiation. (The exception to this is the ^{3}He proportional counters which will be used to detect neutrons.)

Čerenkov radiation is emitted whenever a charged particle travels faster than the phase velocity of light in a medium. The emission of the radiation is a coherent response of the medium to the electric field created by the passing particle.

Čerenkov radiation is emitted at a particular angle relative to the path of the particle according to the formula [Ja75]

$$\cos\theta = 1/n\beta \tag{2.30}$$

where $\beta = v/c$ and n is the index of refraction.

The number of photons produced per unit track length, x, as a function of wavelength, λ, is given by [Pa94]

$$\frac{d^2N}{dxd\lambda} = \frac{2\pi\alpha}{\lambda^2}\left(1 - \frac{1}{\beta^2 n^2(\lambda)}\right) \tag{2.31}$$

where α is the fine structure constant and n is the index of refraction of the medium. If one makes the approximation that the index of refraction is independent of wavelength, then the dependence on wavelength is $1/\lambda^2$. This shows that more photons are emitted in the blue and ultraviolet than in the red part of the spectrum. This equation depends on the electron energy only weakly via the term $\beta^2 n^2$. Since the value of β changes only very slightly for most of the energy range of interest, the amount of Čerenkov radiation emitted by an electron depends only on the path length of the electron.

The path length of the electron is determined by the rate of energy loss, $-dE/dx$, due to interactions with atomic electrons in the water. The theory of energy loss is discussed by Jackson [Ja75] and in the Particle Data Book [Pa94]. A thorough description, complete with many references to original works can be found in the *EGS4 Code System* Manual [NHR85].

The mean rate of energy loss is given by the Bethe-Bloch equation

$$-\frac{dE}{dx} = \frac{4\pi N_A r_e^2 m_e c^2 Z}{A} \frac{1}{\beta^2} \left[\frac{1}{2} \ln \frac{2 m_e c^2 \beta^2 \gamma^2 T_{\text{max}}}{I^2} - \beta^2 - \frac{\delta}{2} \right] \tag{2.32}$$

where N_A is Avogadro's number, $r_e = e^2/4\pi\epsilon_0 c^2$ is the classical electron radius, T_{max} is the maximum energy which can be transfered in a single collision, and I is the ionization potential of the medium. The term, $\delta/2$, represents the energy lost to Čerenkov radiation.

The key feature of this equation is that the dependence on energy is via the quantity β, except in the logarithm where there is a term proportional to γ^2. Thus energy loss is approximately independent of energy above energies of 1.5 MeV. Thus the total path length of an electron is proportional to its original energy. This coupled with the fact that the Čerenkov output depends only on path length leads to a critical result for SNO. The total output of Čerenkov light is proportional to the electron energy. It is this that allows water-Čerenkov detectors to measure electron energies. Figure 2.9 shows the energy loss and the relative Čerenkov output per unit path length. This figure shows the constancy of the values above 1.5 MeV and their rapid change below 1.5 MeV.

The distribution of light produced is also affected by the electron transport in the water. Equation 2.30 gives the angular distribution of light relative to the electron path, but the electron is deflected as it travels in water, mostly by Coulomb scattering from nuclei. There will be occasional large angle scatters, which can be treated as discrete interactions within a model of the detector. However, there will be many small deflections as the electron travels, and these can not be treated

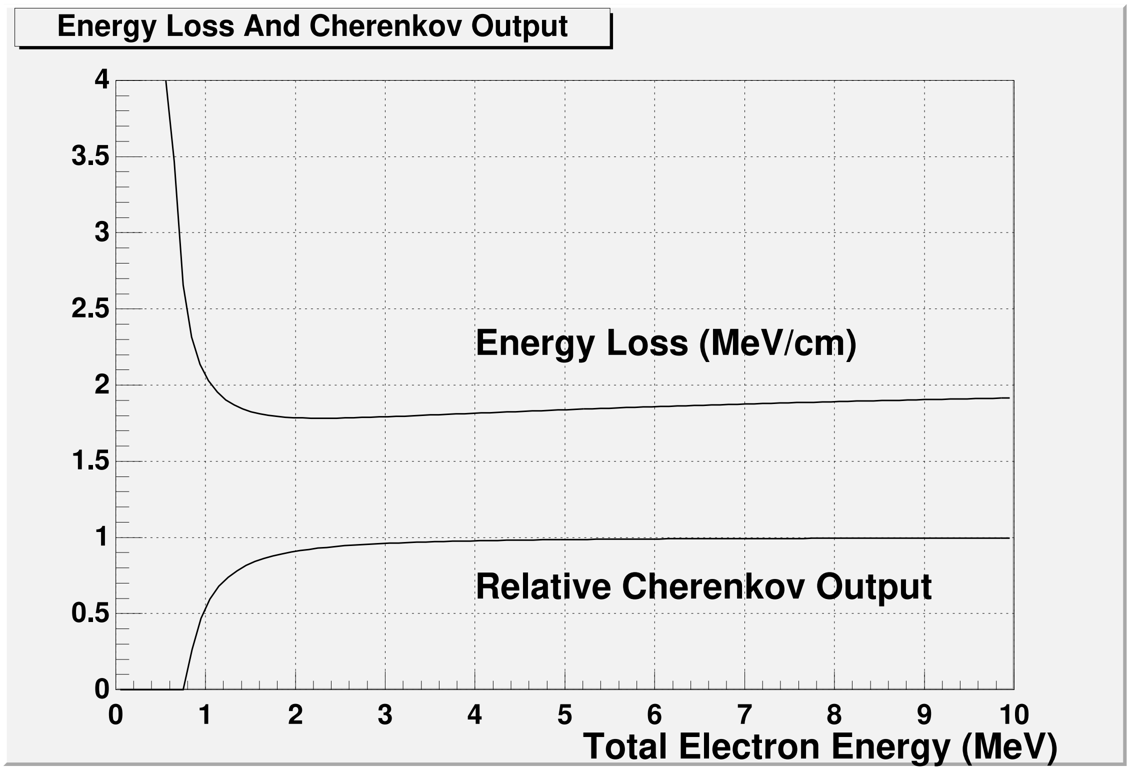

Figure 2.9: The energy loss for electrons in water and the relative Čerenkov output per unit path length as a function of total electron energy. The Čerenkov output is normalized to 1 at high energy. The constancy of these values above 1 MeV is clear and shows that the total Čerenkov production will be a linear function of electron energy.

discretely.

The scattering can be treated using Molière's theory of multiple-scattering, a statistical theory. It has been described in several reviews, [NHR85, Pa94, Be53, Sc63] and Molière's original paper (written in German) [Mo48].

An electron, having traversed a slab of material of thickness, s, will have traveled a distance $t > s$ and will have been scattered through an angle Θ. The value of Θ can be related to a reduced angle θ, which does not depend on the material or electron energy, and two terms which do depend on the material and electron energy.

$$\Theta = \chi_c \mathrm{B}^{1/2} \theta \tag{2.33}$$

The formulae for the probability density function, *pdf*, $f(\theta)$ are complicated, but amount to a Gaussian distribution with small corrections so that at large angles the distribution goes over to the Rutherford law. The Gaussian part is [NHR85]

$$f(\theta) = 2e^{-\theta^2} \tag{2.34}$$

The term, B, is a function of the total path length of the electron during the step, t (measured in centimeters), the material via b_c (= 7529 for heavy and light water), and weakly on the energy via β^2. Its physical meaning comes from its relationship to the mean number of single small-angle scatters, Ω_0, that occur along the path.

$$\mathrm{B} - \ln \mathrm{B} = \ln \frac{\mathrm{b}_c t}{\beta^2} \equiv \ln \Omega_0 \tag{2.35}$$

Because the theory is statistical, the mean number of scatters must be large for the theory to be accurate. Molière suggested $\Omega_0 > 20$. This implies $\mathrm{B} > 4.5$.

The third term, χ_c, shows the dependence on electron energy.

$$\chi_c = \frac{\chi_{cc}\sqrt{(}t)}{E_{MS}\beta^2} \tag{2.36}$$

where χ_{cc} depends only on the material and E_{MS} is the total energy of the electron in MeV. For (heavy or light) water $\chi_{cc} = 0.814$ [NHR85].

Putting the three terms together shows that the scattering is through smaller angles at higher electron energies. Thus higher energy electrons (12 to 15 MeV) can be expected to travel farther than lower energy (5 to 8 MeV) electrons before scattering appreciably. Therefore, it is easier to measure the original direction of an electron accurately at higher energies than at lower energies.

Consider an electron with total energy of 3.511 MeV moving 0.04 cm. The value of B is 8 which is greater than the Molière limit of 4.5. Then $\Theta = 0.109\theta$. Taking the Gaussian part of the pdf for θ, we find a Gaussian distribution in Θ with a standard deviation of 0.077 radians or 4.4 degrees. An electron with a total energy of 6.511 MeV taking the same step will have $\Theta = 0.06\theta$ and will thus have a standard deviation of 0.042 radians or 2.43 degrees.

Of course an electron must travel farther than this one step and the angles will be added in three dimensions. How this is handled in numerical simulations of the detector and how the Čerenkov light generation is simulated will be discussed in chapter 3.

But even without detailed simulations this calculation can be seen as imposing a fundamental limit on the ability to resolve the angle between a candidate event and the sun because the electron direction is intrinsically variable on the order of tens of degrees during its path. This is especially important for the ES signal because the recoil electron is directed away from the sun and this directionality is key to extracting the ES from the data. Thus these formula impose a fundamental systematic limit on the ability to extract the ES signal.

Chapter 3

The Sudbury Neutrino Observatory Detector

This chapter describes the Sudbury Neutrino Observatory (SNO) detector and some of its fundamental energy calibrations. The Monte Carlo simulation and data analysis program, SNOMAN, is discussed.

The SNO detector design was driven by three principal criteria: the need for low background from cosmic radiation, the need for low backgrounds from sources within the detector, and the efficient detection of Čerenkov light.

3.1 The Detector

To remove almost all cosmic-ray backgrounds, the SNO detector is located at the 6800-foot level of INCO's Creighton mine near Sudbury, Ontario, Canada. The rock above the detector allows only approximately 50 muons a day to penetrate to the detector. The rock surrounding the detector is Norite.

The detector is shown in figure 3.1. One kilotonne of heavy water is in a spherical acrylic vessel with a chimney. The acrylic vessel has a diameter of twelve meters and is approximately 5.5 to 6 cm thick. Outside the vessel is a volume of ultra-pure light water which helps support the vessel and acts as shielding preventing gamma rays and neutrons from the rock from entering the heavy water. In the light water volume there is a geodesic dome of diameter 17 meters holding 9522 photomultiplier tubes (PMTs) each pointing to the center of the heavy water volume. The 20 cm diameter PMTs each have a reflector to increase the geometrical area of the geodesic dome sensitive to light. Sixty-six of the 9522 PMTs have a signal from the last dynode as well as the anode providing a low-gain (LG) signal. On the outside of the geodesic dome there are 91 outward-looking PMTs (OWL PMTs). The detector is in a barrel-shaped cavity, 22 meters in diameter and approximately 30 meters high. The cavity is lined with polyurethane coating to inhibit the diffusion of radioactive ^{222}Rn from the rock into the cavity. There is a nitrogen cover-gas system to keep radon-loaded mine air from coming in contact with the water. The electronics and calibration hardware are on a deck directly above the water volume. There is a series of penetrations from the deck into the heavy-water and light-water volumes to allow insertion and removal of calibration sources.

3.1.1 The Heavy Water

The water systems (both heavy and light) are described in detail in [NSWG96]. The heavy water must have a low radioactive contamination. The uranium chain element ^{214}Bi and the thorium chain element ^{208}Tl are of particular concern because they both produce a gamma ray with sufficient energy to photo-disintegrate the deuteron. Approximately 1 in 500 ^{208}Tl decays and 1 in 2000 ^{214}Bi decays will do so [Ew$^+$87]. The resulting free neutrons mimic the neutral-current signal. To keep the rate of free neutrons from this background at one-tenth the rate from solar neutrinos, the heavy water must have a contamination less than 3×10^{-15} g/g ^{232}Th and 1×10^{-14} g/g ^{238}U. In these units the limit means the amount of thallium and bismuth in the water must be less than the amount that would be in the water if the water contained uranium and thorium in the given quantity and the entire decay chains were in equilibrium.

The bismuth and thallium backgrounds are also important when the decay does not create a free neutron. This is because these decays release more electromagnetic energy than any other background in the detector. The amount of contamination from these two elements, particularly

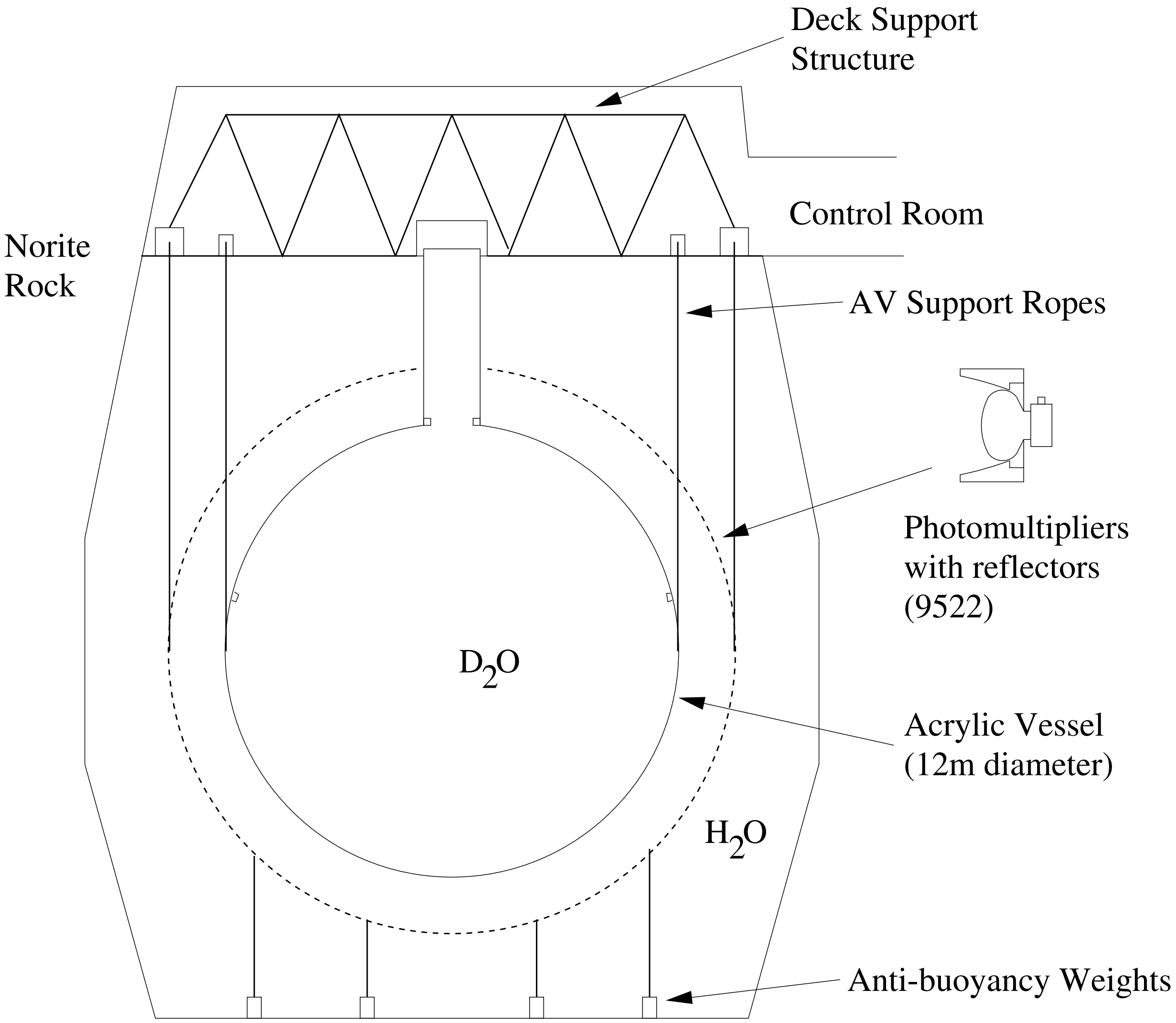

Figure 3.1: A schematic view of the SNO detector showing the heavy water, acrylic vessel, light water, photomultiplier tubes and rock wall.

the thallium, sets the energy threshold for analysis of solar neutrinos.

The heavy water must be filtered on arrival, and perhaps continuously, during operation. There are several systems to remove uranium, thorium, radium, lead, and potassium including seeded ultra-filtration (using DTiO), reverse osmosis, and MnO_x filters. The concentrate from these systems can be assayed to measure the levels of contamination. In addition there is a radon-removal system. The "Liqui-Cell" by Hoechst-Celanese is based on a membrane which passes dissolved gases but not water.

Because the heavy-water is so clean it will have low attenuation of optical photons and Rayleigh scattering. The attenuation and scattering lengths must be calibrated.

3.1.2 The Acrylic Vessel

The purpose of the vessel is simply to contain the heavy water. It is made from ultraviolet-transmitting (UVT) acrylic so the Čerenkov light is not attenuated too much as it traverses the vessel from the heavy water to the PMTs. Even so, at low wavelength, the acrylic is the largest source of absorption [Fo98]. The attenuation co-efficient for wavelengths less than 300 nm is approximately 1.7 cm^{-1}. The attenuation co-efficient drops to less than 0.1 cm^{-1} at a wavelength of approximately 340 nm. The acrylic vessel must also have low contamination. The limit is 10^{-12} g/g Uranium and Thorium. This is a much higher concentration than is required for the water because there is much less total mass of acrylic than water.

3.1.3 The Light Water

The light water also has very strict requirements for cleanliness. The bismuth and thallium are again the principal concern. Because the Čerenkov light from decays in the light water can reach the PMTs without being attenuated by the acrylic, these decays appear more energetic in the light water than in the heavy water. Given that some events in the light water will mis-reconstruct into the heavy water volume, the energy threshold is affected by contamination in the light water. Similar to the heavy water, there is a series of filters and monitoring hardware to remove contamination from the light water and to measure the residual levels.

The light-water originates from the INCO supply and is, by the requirements of SNO, highly contaminated. In particular, iron is a concern. Therefore a polymer is injected to complex the iron for removal by subsequent filters. The water is then passed through multi-media filters, a ten-micron filter, activated charcoal, a softener, a three-micron filter, and a reverse-osmosis unit. The water from the reverse osmosis is clean enough for injection into the main purification loop.

The first step in the main purification loop is an ultraviolet lamp system (185 nm) to break up large organic molecules for removal by the next stage, ion exchange columns. The output of the ion-exchange columns is water with a resistivity of 18.3 MΩ·cm. The water is then passed to a vacuum-degassing system which extracts over 95% of the radon in the water. The water is then passed to another set of ultraviolet lamps (254 nm) to kill bacteria. The water is then passed through a one-micron filter to remove particulates, through a chiller to lower its temperature to 10 degrees Celsius, and finally into the detector.

3.1.4 The Photomultiplier Tubes

The photomultiplier tubes are 20 cm Hammamatsu R1408 PMTs. They were extensively tested for noise rate, timing resolution, and relative quantum efficiency before being accepted for use in SNO [JFH+96]. The photocathode of each PMT is surrounded by a reflector designed to trap light that would otherwise have missed the PMT [DGJ+96]. This gives a large increase in the photocathode "coverage" (that fraction of the detector sensitive to light) with no increase in noise rate. The concentrators were designed such that any light entering the reflector within 56 degrees of the PMT axis will be reflected to the photocathode.

The mean timing resolution was 1.5 ns with an RMS deviation of 0.08 ns. The mean noise rate during testing (at 20 degrees Celsius) was 2300 counts above threshold a second. The PMTs in SNO will be kept at 10 degrees Celsius, resulting in a reduced noise rate. The importance of the noise rate can be seen by calculating the mean number of noise signals that will occur in a 400 ns time period (the approximate time window in which signals will be accepted for an event.) The mean number is $\bar{n} = N_{\mathrm{PMT}} \cdot 400 \times 10^{-9}$ s $\cdot R_{\mathrm{noise}} \times 10^3$ signals/s, where N_{PMT} is the number of PMTs and R_{noise}, the noise rate in kHz. If we approximate $N_{\mathrm{PMT}} \simeq 10000$, then the formula reduces to $\bar{n} = 4R_{\mathrm{noise}}$. Thus for a mean PMT noise rate of 1 kiloHertz, the number of noise signals in the event will be given approximately by a Poisson distribution with a mean of 4.

PMTs are a source of background because the glass bulbs contain contamination. This effect was ameliorated by choosing low-radioactivity glass. However, PMTs are still the source of the largest number of background decays. The majority of these decays produce very little light and events from PMT radioactivity reconstruct mostly outside of the acrylic vessel. There remains a small tail of events with tens of PMTs hit that reconstructs inside the acrylic vessel. While this tail is small, the raw number of decays is large. Simulation study is thus computationally expensive and difficult.

3.1.5 Deck and Electronics

Above the detector, but still within the cavity is the "deck". There is a series of penetrations through the deck that can be opened to insert calibration sources into either the heavy water or light water volume.

The electronics is a sophisticated system designed not only for solar neutrino counting but also to detect a supernova at the core of the Milky Way galaxy. Each PMT has independently controlled high voltage and threshold. Eight PMTs are connected to card which contains a discriminator, a time-to-amplitude converter (TAC) and 4 sets of 16 capacitors for each PMT. One set of capacitors stores the amplitude of the TAC output, the other three sets store the integrated charge of the PMT anode signal. There are 3 charge capacitors to measure the charge 3 different ways: High-Gain Long Integrate stores the amplified charge integrated over a period of approximately 150 ns. High-Gain Short Integrate stores the amplified charge over a time period just long enough to include the full PMT anode signal (approximately 60 ns). Low-Gain Long Integrate stores the charge from a low-gain amplification; its purpose is to provide a meaningful charge measurement for those signals whose high-gain charge is above the range of the analog-to-digital converter (ADC). Solar neutrinos are not expected to yield such signals.

There is a 16-fold redundancy in the capacitors to enable SNO to collect complete data in case of a supernova at the core of the Milky Way galaxy. In that case, there will be a short burst of events at high rate. The front-end electronics is fast enough to handle such a burst, but the ADC converter and read-out electronics is not. The front-end electronics can handle 16 hits on each PMT without data loss before requiring readout.

There are many triggers for the electronics, but they fall into four main categories: NHIT, ESUM, OWL and external. An NHIT trigger fires if a certain (programmable) number of PMTs give signals within a certain time window. There are three NHIT triggers with a 100 ns window and two with a 20 ns window. The 20 ns trigger window is not wide enough for regular data taking; it is used only for some background studies. The three 100 ns NHIT triggers allow for three thresholds to be used simultaneously. The lowest-threshold trigger can be "pre-scaled" so only a programmable fraction of the triggers will cause an event. This is useful for low-NHIT studies where the event rate is higher than the read out and data acquisition can handle.

An ESUM trigger uses an analog sum of the charge in all PMTs. If it is above a certain threshold, the trigger is activated. Thus an ESUM trigger will fire if there is only one PMT signal, if that PMT's signal is sufficiently large. There are two ESUM triggers, both with programmable thresholds. There are three OWL triggers. They fire if certain conditions are met in the outward-looking PMTs. One is an NHIT trigger and the other two are ESUM triggers. The OWL triggers are completely independent of the triggers for the normal, inward-looking PMTs.

The fourth class of trigger is very important for calibration. These are the external (EXT) triggers. External triggers, as the name suggest, are triggers generated by a source other than the detector itself. Several calibration sources supply external triggers which are used to tag the event as a calibration event and to ensure that all calibration data gets read out, independent of the settings of other triggers. External triggers can be asynchronous (EXT-ASYNC) or synchronous (EXT-SYNC). An asynchronous trigger is generated in the detector as soon as the signal is received by the trigger logic. A synchronous external trigger generates a trigger on the first "tick" of the of 50 MHz clock in the electronics after arrival of the signal at the trigger logic. A special kind of external trigger is the pulsed global trigger, or PGT. It is used to generate a trigger at regular programmable time intervals. It, therefore, can be used to study the random noise in the detector. It is very useful in determining the PMT noise rate.

3.2 Calibration

The electronics calibration comprises finding the pedestals and the slopes of the ADCs for each electronics channel. The electronics contains systems to activate the read-out of channels at the same time as a global trigger is generated. This allows the electronics channels to be sampled with no input signal and thus yields pedestals. The time slopes can be measured by adjusting the delay between the activating the channels and generating the global trigger. The charge slopes can be measured with a charge injection circuit that places a known amount of charge on the front-end electronics for each channel.

The calibration of the response of the SNO detector to physics signals is carried out with two sources: the "laserball" and the ^{16}N source. The purpose of the laserball is optical calibration. The ^{16}N source provides a 6.13 MeV gamma-ray and yields an absolute energy calibration.

3.2.1 Optical Calibration

The laserball light originates from a pulsed nitrogen laser. The wavelength is 337 nm and the pulse width is less than 1 ns. A system of mirrors on motorized mounts can, if desired, direct the light to one of a series of dyes to select a longer wavelength. The light is then passed through computer-controlled attenuation to select a particular intensity of light. This light is passed into a bundle of optical fibres 100 feet long which leads the light to the diffusing ball. The diffusing ball has a nearly isotropic light output [Fo98].

The laserball system has many critical uses: calibrating time offsets of the PMTs, calibrating the charge-verses-time walk of the PMTs and discriminators on the front-end electronics, and measuring attenuation of heavy water, acrylic, and light water at various wavelengths. The laserball data gives a complete relative calibration of the detector. It yields the response of the detector as a function of position within the detector, both in the heavy and light water.

3.2.2 Absolute Energy Calibration

The optical calibration does not give information about the amount of light detected per MeV of energy deposited. This is accomplished with the ^{16}N source. ^{16}N beta decays with a 26% branch to the ground state of ^{16}O. There is a a 68% branch to an excited state of ^{16}O resulting in a prompt 6.1304 MeV gamma ray. A 4.9% branch results in a prompt 7.1169 MeV gamma ray. The remaining 1.1% result in 1 or 2 prompt gamma rays with a total energy of 8.87 MeV. The source is constructed such that beta particles can not leave the source but gamma rays can.

The inner volume of the source is a cylinder of radius 4.78 cm and height 14.64 cm. This "decay volume" is surrounded by a cylinder of plastic scintillator 0.3 cm thick. The scintillator is surrounded by a stainless steel can of wall thickness 0.635 cm. Electrons in the energy range of 1 to 10 MeV lose energy at a rate of approximately 1.5 to 2 MeV $g^{-1}cm^2$. Because the density of stainless steel is approximately 8 g cm^{-3}, electrons lose energy at a rate of 12 to 16 MeV cm^{-1} in stainless steel. Thus the stainless steel does not allow most electrons to escape the source even in the case of beta decay to the ground state where the endpoint is 10.4 MeV. The electrons that do leak out of the source have low energy. For the case where the ^{16}N decays to an excited state of ^{16}O resulting in a gamma ray, the highest beta energy is 4.29 MeV which is easily stopped by the stainless steel.

There is a tail of low energy gamma rays from the source from Bremsstrahlung radiation electron from decay to the ground state and from Compton scattering of the 6.13 and 7.1 MeV gamma rays in the stainless steel. In a simulation of 10000 ^{16}N decays, there were 362 gamma rays with energy between 3 and 6.12 MeV which entered the heavy water around the source. The effect of the low energy tail on the use of the source for energy calibration is discussed in detail in [Ha99].

The radioactive nitrogen is made from the reaction ^{16}O (n,p)^{16}N by passing CO_2 gas through a region of high neutron flux created with a commercial d-t generator [Ha99]. The gas is circulated through conduits towards the SNO detector, into a decay chamber and back out. Because the ratio of volume of the decay chamber to the gas conduit lines is very large and because ^{16}N has a lifetime of only 7.13 seconds, most of the decays occur in the chamber. The chamber contains a plastic scintillator and a 2 inch PMT which detects the electron from the beta-decay of ^{16}N to ^{16}O*. This signal is used to tag the subsequent gamma decay of the ^{16}O*. The beta decay to the ground state is also detected so the tag also yields triggers when no energy is visible to the detector.

Through Monte Carlo study, the relationship between the amount of light expected from a gamma ray and an electron can be determined. Thus the ^{16}N source gives the absolute energy calibration. In principle, only one energy value is needed because the amount of Čerenkov light produced is a linear function of electron energy. However as the electron or gamma energy increases, the probability of a single PMT detecting 2 photons increases. Thus while the Čerenkov production is linear, the total number of PMTs hit is not. A high-energy gamma-ray source ($E_{\gamma} = 19.8$MeV) has been developed to study this effect [Po98]. A lower-energy gamma source [Dr99] using ^{22}Na will be particularly useful in understanding the response of the detector to the low-energy background wall from thallium and bismuth contamination.

This ^{16}N source also gives the energy resolution of the detector. The width of the response of the detector, or more precisely, the variation in the number of PMTs detecting light, is measured when the calibration is performed.

With these calibrations performed and the appropriate results used as inputs, the Monte Carlo can be expected to yield the correct relationship between electron energy, the number of PMTs hit detecting light (NHIT) and the position and direction of the event.

3.3 The SNOMAN Monte Carlo

3.3.1 The Program

The SNO Monte Carlo and Analysis software package, or SNOMAN, is a collaboration-written Fortran 77 program. It uses the CERN Program Library, CERNLIB, and the ZEBRA memory manager also from CERN [Ce].

Monte Carlo simulations are necessary to understand the detector data and calibrations because of the complexity and number of physical processes involved in events. An event simulation starts with the "creation" of one or more particles: electrons, positrons, muons, gamma rays or optical photons. Nuclear decays are handled by choosing a decay mode (according to the branching ratio) and simulating the beta and gamma rays emitted in that mode. Alpha decays are not handled by the code because SNO is not sensitive to them.

The transport of electrons, positrons, and gamma ray is performed with the EGS4 code system [NHR85]. EGS4 uses Molière scattering theory in its calculations but allows for user control over how this is done. SNOMAN uses the ESTEPE algorithm [NHR85]. In this algorithm electrons are transported in straight-line steps of a length that gives a certain fractional energy loss. The distance that higher-energy electrons are transported in each step is greater than that for lower-energy electrons. From the discussion in section 2.5 this is appropriate because the direction for a high energy electron changes less than a low energy electron over a constant step.

There are a couple of requirements that must be met. If the step sizes are too large, the electron simulations will be inaccurate because details smaller than the step length will be lost. Conversely, the steps must be large enough that the Molière criterion, $\Omega_0 > 20$ hold for all relevant energies. SNOMAN uses a step length of 3% energy loss per step by default.

Čerenkov light generation is not included in the EGS4 package. Therefore, collaboration-written code was used to simulate Čerenkov generation. The number, wavelengths, and directions of the photons must match the Čerenkov formulae. The only source of ambiguity is in equation 2.30 that specifies the direction of the light relative to the direction of the electron. The difficulty lies in determining the electron direction. If the Čerenkov light is emitted along each electron step relative to the electron direction at the start of each step, then the distribution of light generated by the Monte Carlo will be inaccurate and will depend on the step length. It is necessary to interpolate between the electron direction at the start of the step and the end of the step. This interpolation is an approximation because the simulation only "knows" these two directions. SNOMAN generates

Čerenkov light at equal probability along the step and performs a linear interpolation between the direction at the start and end of the electron step.

Once the optical photons are generated, they are transported. The optical transport includes reflection and refraction at surfaces, diffuse scattering and transmission at surfaces, Rayleigh scattering and absorption in media, and, of course, absorption and detection by the PMTs.

3.3.2 Results from Early Simulations

The simulation can be used to generate the detector response to neutrino signals and backgrounds once its parameters have been set according to calibrations. Preliminary simulations can be carried out using the best estimates from component evaluation during the construction and testing phases of the detector. A series of such simulations were performed. The NHIT distributions for ES, CC, NC, and several backgrounds are plotted in figure 3.2.

A few features are clear. The background rises sharply near 40 PMTs hit. It is dominant below 40 hits but small above 40 hits. The photo-disintegration of the deuteron by the 2.6 MeV gamma ray from ^{208}Tl is included in the background. The number of thallium decays in the heavy water corresponds to 3×10^{15} g/g Thorium [NSWG96]. (The unit g/g is defined in section 3.1.1.) A plot can also be made of the fitted direction with respect to the sun. The plot is shown in figure 3.3.

The distribution of events with respect to the sun shows that the ES events are sharply peaked near $\cos\theta_{\text{sun}} = 1$. This makes clear that understanding the angular resolution of the detector events will be critical to extracting the ES signal.

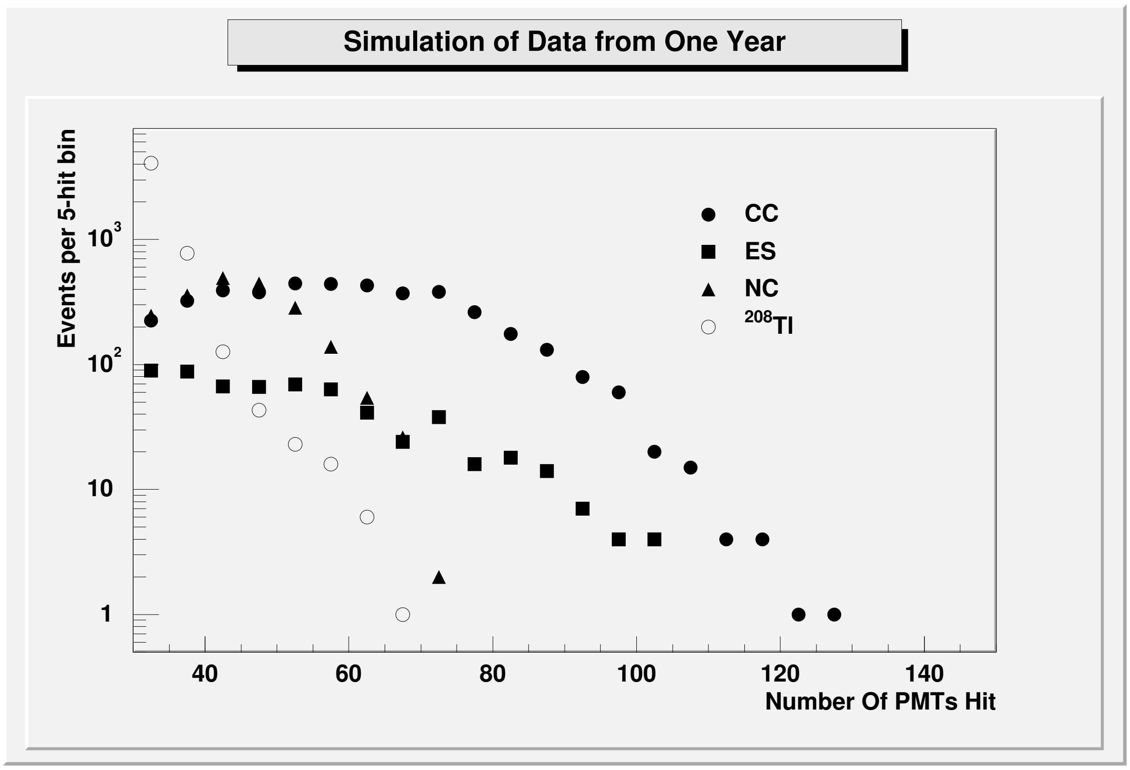

Figure 3.2: A spectrum of NHIT for simulation. The various components are plotted separately. The bin width is 5 NHIT.

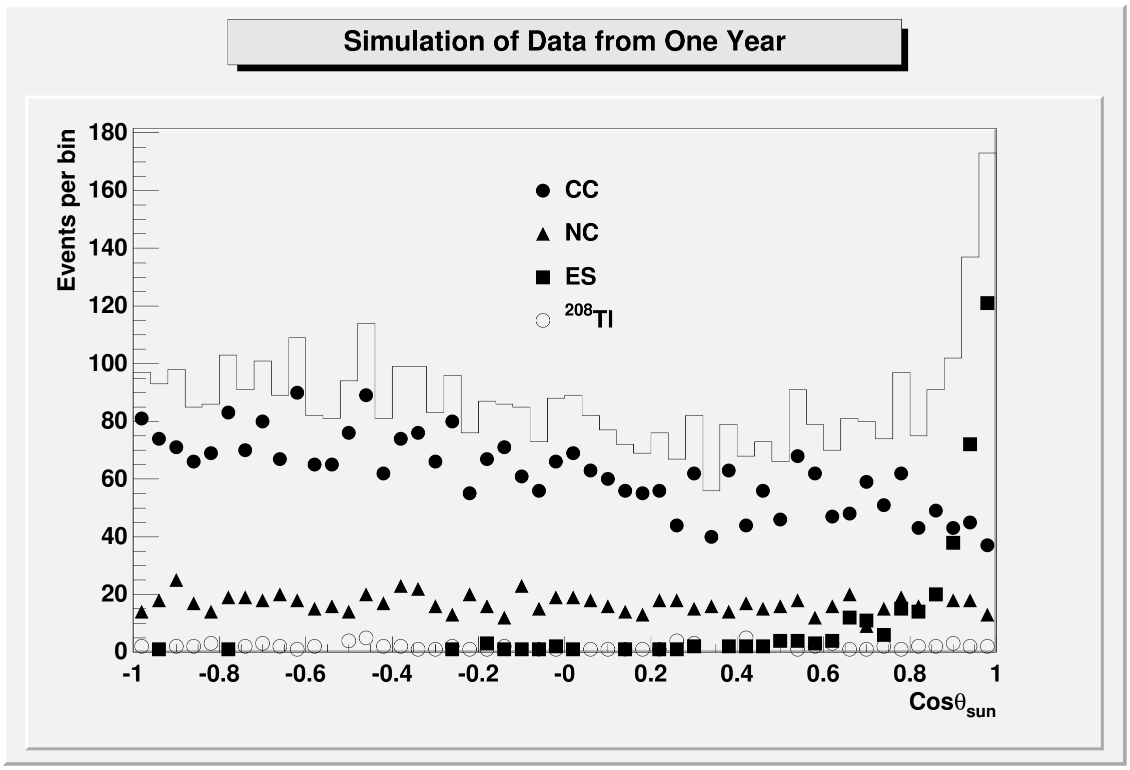

Figure 3.3: Angular distributions from simulation. The various components are plotted separately. The histogram is the sum of all signals. A threshold of NHIT ≥ 45 was imposed.

Chapter 4

Data Analysis for Neutrinos

This chapter presents a brief overview of how data will be analyzed to extract the solar-neutrino signals. There are four main steps in analysis that will be discussed in sequence. First, there are the fundamental calibrations to define all the parameters required in the Monte Carlo. Second, there are the calibrations that over-constrain the Monte Carlo and allow the systematic errors in the Monte Carlo to be quantified. Third, the detector individual events must be reconstructed to determine their position, direction, and an estimate of their energy. Fourth, the results of the third step must be compared to the Monte Carlo simulations of different physics scenarios to determine the physics implications of the data.

4.1 Step 1: Fundamental Calibration

There are many fundamental calibrations. The electronics and PMT calibrations must be performed first. The slopes of the TACs are measured with a precision timed pulser. The time offsets of all the PMTs must be measured with the laserball at the center of the detector — this ensures the arrival time of signals at the front end of the electronics can be reliably compared between PMTs. The charge pedestals are measured by triggering electronics channels independent of any light source in the detector. The charge slopes of the channels are determined by taking single-photoelectron spectra with the laserball. Because the electronics uses leading-edge discriminators, the "walk" of the discriminator signals as a function of signal amplitude are calibrated using the laserball with different light intensities.

The second stage of the fundamental calibrations is to determine the optical properties of the detector. The laserball calibration is performed at several positions within the detector at several wavelengths to determine the optical attenuation and scattering lengths for the heavy water, acrylic, and light water. This calibration also determines the relative efficiencies of the PMTs. Once the optical calibrations have been performed, the relative calibration of the detector is complete.

The third stage is to determine the absolute energy scale of the detector. This is performed by placing the ^{16}N source at the center of the detector. Because the ^{16}N source provides a known amount of electromagnetic energy, it calibrates the number of PMTs hit per unit of gamma-ray energy. The average quantum efficiency of the PMTs can be adjusted to best match the data. This must be done by comparing the calibration with Monte Carlo simulation. In principle this will not depend on the method of event reconstruction as long as the calibration and Monte Carlo are handled the same way. If the measured PMT efficiency depends on the analysis method used, this dependence must be well understood and the data and calibration must be analyzed identically.

The noise rates of the PMTs can be measured using PGT events and then used as parameters in the Monte Carlo.

Once this procedure has been carried out, the Monte Carlo is completely constrained. The Monte Carlo will use the EGS4 system and collaboration-written optical-photon codes to simulate the detector response to electrons, positrons and gamma rays.

4.2 Step 2: Monte Carlo Verification

Further calibrations determine if the Monte Carlo is correct. The first part of this procedure is to perform the ^{16}N calibrations at various locations in the detector to ensure that the geometrical effects as defined by the optical calibration correctly predict the variation in detector response to the ^{16}N source as a function of position.

Furthermore, a higher-energy and a lower-energy gamma-ray source will be used to verify that the Monte Carlo is accurate over the energy range of interest. The high-energy gamma-ray source is particularly important for understanding the response of the detector when there is a significant probability that a single PMT will detect two photons from the same event. When this occurs, there is a reduction in the ratio of NHIT to energy. The Monte Carlo must correctly predict this.

The Monte Carlo also performs neutron transport and it is necessary to ensure that these custom-written codes give the correct result. This transport code has been compared to detailed analytical calculations of neutron-diffusion with excellent agreement [SW98]. Calibration with a neutron source will also be performed to verify these calculations.

When the Monte Carlo verification has been done, there will be an understanding not only of the response of the detector to neutrinos but also of of the systematic errors in the Monte Carlo. The systematic errors can be estimated from the discrepancy between the Monte Carlo and calibration. They will be necessary in step 4 of the analysis.

4.3 Step 3: Processing Data and Reconstructing Events

Data reduction is the process of taking events (a list of PMTs that fired, the charges they measured, and the times at which they fired) and determining a few simple parameters: the location, direction, and a measure of the energy of the event. Data reduction will be performed identically on both Monte Carlo and detector data.

The first step is to remove unwanted events from the data sample. For a solar-neutrino analysis, this would involve cutting out events from physics signals such as muons and anomalous signals from, for example, "flashing" PMTs [Ko98].

The second step in this process is reconstructing (or "fitting") the selected event to determine its location and direction. The next step is using the fitted location and an understanding of the gross optical and geometrical effects of the detector to obtain a measure of the energy of the event. For example, some events are such that most photons must pass through a long path length in the acrylic to reach the PMTs. Because the acrylic has high attenuation at low wavelength, these events yield less light than an average event. Using knowledge of the detector optics, it is possible to incorporate these effects [Fo98, Ha99] in the analysis of individual events. The function which accomplishes this, $\mathcal{C}$, would also be used to correct for events occurring with a different number of channels turned on, if for example, some channels were disconnected for maintenance. The function can also be used to remove known biases in the event reconstruction (an example is "fitter pull" discussed at the end of section 5.1.2). Written symbolically, the function $\mathcal{C}$ transforms raw event information and the initial event reconstruction into the best estimates of the event energy, position, and direction:

$$\mathcal{C}(\text{NHIT}, \vec{x}_{\text{fit}}, \vec{u}_{\text{fit}}, \text{number of active channels}, \text{optical parameters} \longrightarrow E', \vec{x}', \vec{u}') \tag{4.1}$$

where the subscript "fit" refers to values from the fitter. The primed variables are the best estimates, given all available information. The vectors $\vec{x}$ and $\vec{u}$ refer to the position and direction of the event. The energy of the event is denoted by E.

The result of the data reduction of a series of events is a multi-dimensional histogram. The variables in the histogram will be (at least) energy or NHIT, $\cos\theta_{\text{sun}}$, and reconstructed radius. Each of these variables helps in one or more aspect of separating the NC, the CC, and the ES signal.

4.4 Step 4: Extracting Physics Information

This result of this step is the goal of the experiment. It attempts to answer questions like "Do neutrinos oscillate?"and "What oscillation parameters best fit the data?". The most direct way to do this is to use physics scenarios as input to the Monte Carlo and generate a series of events that yield what the detector would have measured given that physics input. These events are reduced exactly as the real data were reduced in step 3. A chi-square or log-likelihood comparison can be made of the histograms from the simulation and the data. The best-fit choice of parameters for various scenarios can be found along with the statistical errors.

The second part of this process is to analyze the effect of systematic uncertainty on the measurement. The systematic uncertainties were derived in step 2 with the Monte Carlo verification.

The parameters in the Monte Carlo can be varied according to their uncertainty to see what effect this has on the analysis. This yields the systematic uncertainty in the physics analysis.

4.5 Analyzing to Extract the Electron-Scattering Signal

The analysis above extracts as much information as possible for all signals. The discussion now turns to specific parts of the process that are most relevant to determining the elastic-scattering signal and comparing it with the charged-current signal.

Each variable of the NHIT/energy – $\cos\theta_{\text{sun}}$ – radius histogram will be considered independently. The energy spectrum for ES and CC events are fairly similar above 5 MeV (see figure 2.6). The energy spectrum will not easily separate the ES from the CC. The radial distribution of ES events will be very similar to that for CC inside the acrylic vessel where both CC and ES events will occur isotropically. The ES rate is isotropic over the entire light and heavy water volumes whereas CC events are generated only in the heavy water. There will be some information to be gained by looking for ES events in the light water. Extending the radius of the analysis region from 600 to 700 centimeters increases the interaction rate by 59%.

The variable which most differentiates the ES signal from other signals in the detector is $\cos\theta_{\text{sun}}$. The recoil electrons are directed almost parallel to the incident neutrino direction in the energy range of interest. Thus it is the ability of SNO to measure accurately the direction of recoil electrons that will determine how well the ES signal can be extracted.

The detector response is best determined by the Monte Carlo, once it has been calibrated, verified, and quantitative estimates of systematic errors have been deduced. In the following discussion, the detector response will be approximated as an analytic function. The reason for this is to understand clearly what is important and what can, to good approximation, be neglected. This intuitive understanding will allow the final analysis to be cross-checked. Starting with equations 2.29 for the CC reaction and equation 2.28 for the ES reaction, it is possible to write

$$\frac{d^3N}{dE' d\cos\theta'_{\text{sun}} dR'} = \mathcal{N}\int_0^\infty dE_\nu \phi_\nu \left(\mathrm{P}_e \frac{d^2\sigma(\nu_e)}{dE_e d\cos\theta_{\text{sun}}} + (1-\mathrm{P}_e)\frac{d^2\sigma(\nu_\mu)}{dE_e d\cos\theta_{\text{sun}}}\right) \tag{4.2}$$

$$\otimes\mathcal{P}(E, \cos\theta_{\mathrm{sun}}, R, \rightarrow E', \cos\theta'_{\mathrm{sun}}, R')$$

where $\otimes$ means convolution and $\mathcal{P}$ is the probability that a recoil electron of energy E, of direction relative to the sun $\cos\theta_{\mathrm{sun}}$, at radius R reconstructs at E', $\cos\theta'_{\mathrm{sun}}$, and R'. (That is to say the variables with the prime are measured variables and the variables without the prime are the actual values.) $\mathcal{N}$ is a normalization accounting for the number of targets for the reaction, the total neutrino flux, and the live-time of the detector.

The discussion in the following chapters will touch on matters in all steps of the analysis. First a Monte Carlo study of angular resolution, the ability of SNO to measure directions, is presented. This study asks what physics processes and detector properties affect the angular resolution. An analytic function for the angular part of $\mathcal{P}$ is described. Once the angular resolution is understood it is possible to define what analysis and calibration effort is needed to deduce the angular resolution with the minimum statistical and systematic uncertainty. Also discussed is how the uncertainty in the fundamental calibration (step 1) affects the angular resolution and how the reconstruction of each event (step 3) affects the angular resolution. The discussion then turns to how the Monte Carlo can be verified in the calibration (step 2). Then how all these steps affect the data analysis of step 4 is described.

Chapter 5

Monte Carlo Study of Angular Resolution

5.1 Event Reconstruction

Before an ensemble of events can be analyzed, it is necessary to understand how individual events are reconstructed. This event reconstruction is a major component of step 3 of the analysis. The information that can be used is the times that the PMTs in each event detected a signal, the amplitude of that signal, and perhaps the trigger from a calibration source.

5.1.1 Methods

The goal of event reconstruction is to determine the time, location, and direction of an event. (The direction of the event is the best estimate of the initial direction of travel of the electron or gamma ray.) Because electrons travel only a few centimeters at relativistic speeds, the Čerenkov light for an electron can be assumed to come from a point source at one instant in time. The location and time can be reconstructed using the time each PMT was hit. The time for the $\imath^{\text{th}}$ PMT to be hit, $t_\imath$ is

$$t_\imath = t_{\text{fit}} + |\vec{x}_\imath - \vec{x}_{\text{fit}}|/(c/n) \tag{5.1}$$

where t_{fit} is the reconstructed time of the event, x_i is the location of the PMT, x_{fit} is the reconstructed position of the event and c/n is the speed of light in water.

It is then possible to define the residual for this PMT as

$$R_i = t_i - t_{\text{fit}} - |\vec{x}_i - \vec{x}_{\text{fit}}|/(c/n) \tag{5.2}$$

A minimization can be performed on $\chi^2 = \Sigma R_i^2/\sigma_i^2$ to determine the event location. The quantity, σ_i is the 1-sigma width in the PMT timing resolution including the effect of the reflectors. It will be measured with laserball calibration. A reconstruction algorithm that minimizes this χ^2 is called a *time fitter*. As discussed in section 3.1.4, there will be approximately 4 PMT noise signals included in an event that are uncorrelated with the physics of the event. Also, some Čerenkov light generated will be scattered and this will result in a PMT signal that is "out of time" relative to the light that went directly from the electron to a PMT. Both noise signals and scattered light skew the event reconstruction and must be eliminated. To do this, the time fitter is called for several passes for each event with each pass putting a tighter acceptance window on the residual. Thus badly out-of-time PMTs should be rejected. It is essential that the final time window not be too tight or the fit will lose accuracy from rejecting PMTs that should be included. A width of two to three σ is appropriate. In the Monte Carlo, the PMT timing jitter is 1.6 ns. (The values after calibrations will vary from PMT to PMT and will reflect the results of calibration.) The window used for the discussion in this chapter is $\pm$4ns.

Another method to determine the event position is the "quad" fitter. A quad point, (x, y, z, t), is found analytically from 4 hit PMTs. A cloud of quad points is made by looping over all possible combinations of 4 PMTs. The fitted vertex is taken to be the region of highest density of quad points. This fitter is enormously computationally expensive. For an event with NHIT of N, there are N-choose-4 possible quad points and, therefore, that many 4×4 matrix equations to solve. Thus only a small fraction of the quad points, chosen randomly, are determined. Because most PMT hits are in-time, the vast majority of quad points are clustered around the real vertex. The quad points containing out of time light will be far from the real vertex. Therefore, the region of highest density of quad points is relatively unaffected by the out-of-time PMTs. Thus the quad fitter has better noise immunity than the time fitter. The extra precision gained will be useful in the discussion of calibration of angular resolution.

There are several ways to determine the event direction. The simplest is to take the mean direction from the reconstructed vertex, $\vec{x}_{\text{fit}}$, to the hit PMTs, $\vec{x}_\imath$, which fall within the final acceptance time window of the fitter. This method benefits from being computationally fast.

A second method is to use the vertex from the time fitter and fit a cone to the hit PMTs. Again, this method needs a method to reject PMTs. The noise PMTs are rejected *a priori* by the position reconstruction. However, multiple-scattering of the electron as it travels in the water reduces the directional information in the event but does not affect the time residuals. To properly fit a cone, the light emitted after the electron has significantly scattered must be removed from the fit.

The algorithm to remove this light was provided by collaboration member, S. Brice, who implemented a cone-finding algorithm into a simulated-annealing minimization technique [Br95]. The cone has its vertex at the reconstructed event position and has a half angle of 41 degrees. The orientation of the cone which best fits the data is found. To perform a fit, a residual is needed for each PMT. The residual, $M_\imath$, is given as the sine squared of the angle, ϕ, between the cone and the vector from the vertex to the PMT. The weight for each PMT must be known in the fit. It is given by

$$V_\imath = \frac{1}{1 + e^{-(\lambda - M_\imath)/T}} \tag{5.3}$$

Two terms deserve comment. The term, λ, sets the range of angle for good PMTs. The term, T, is the *temperature*. It controls the relationship between the weight and λ. If $T >> \lambda$, then the weight is almost independent of $M_\imath$. If, however, $T \to 0$, then the weight will be unity if $M_\imath < \lambda$ and zero if $M_\imath > \lambda$. If the PMT is behind the cone, the weight is always set to 0.

Simulated annealing is a method whereby early in the minimization process, the acceptance windows are set very loosely (the temperature is set high and thus the weights are approximately equal for all PMTs) and as the minimization proceeds, the window becomes steadily tighter (the temperature is lowered and thus PMTs off the reconstructed cone have substantially reduced weights).

The implementation of the simulated annealing uses a gradient-step minimization. At each step, the temperature is decreased a certain fractional amount until the final temperature is reached. Then the fit continues reducing the step size a certain fractional amount until convergence at a minimum.

Each step in the minimization is computationally expensive and there are many steps in each fit. Thus this method is much slower than the time fitter. This reconstruction technique is called the elastic fitter because the the "elasticity" in the weighting formula with change in temperature.

The elastic fitter is complicated by the number of parameters it uses; the most important are λ, the initial temperature, the final temperature, the rate of decrease of temperature and the step size of the two angles defining the orientation of the cone. The range of acceptable residuals at low temperature ($T \ll \lambda$) should allow a significant amount of width about the cone. A value of 0.08 rad^2, corresponding to 16 degrees, is used.

The final temperature must be less than λ in order that the weights at the end of the fit strongly favour PMTs close to the cone. A value of 0.03 is used. The initial temperature should be sufficiently high that an angular deviation of 30 or 40 degrees is given weight larger than 0.1 or 0.2. The value can be found by substituting the values above into equation 5.3. The initial temperature used is 0.5 rad^2. The temperature gradient must not be too high or the fit will "cool" too quickly allowing the fit to get trapped in a local minimum. Each step in the gradient step search has the temperature reduced by a factor, η. If this factor is close to one, the search will proceed slowly because it will take more steps to reach the final temperature but it is less likely to be trapped in a local minimum. $\eta > 0.98$ works best and the value used here is 0.995. The step size in angle is 0.01 radians for both theta and phi. Once the fit has reached minimum temperature, both step sizes are reduced by a constant factor of 0.985 each step until the fit converges.

5.1.2 Angular Resolution and Reconstruction Algorithm

To study the effect of the event-reconstruction algorithm, a simulation of 20000 electrons of 7 MeV kinetic energy was performed. The electrons were started at the center of the detector and given an initial direction distributed isotropically. Plots were made of the dot product between the fitted direction, $\vec{u}_{\text{fit}}$, and the initial direction, $\vec{u}$, for the electrons. Plotting the dot product, or $\cos\theta$, ensures that an isotropic distribution is represented as a flat distribution in the histogram. Two values of $\cos\theta$ are marked on each plot, $\cos\theta_{80}$, and $\cos\theta_{50}$. These are defined such that 80% (50%) of the events lie between $\cos\theta_{80}$ ($\cos\theta_{50}$) and 1. These quantities provide a convenient method for quantifying the angular resolution. The uncertainty in $\cos\theta_{80}$ (and $\cos\theta_{50}$) is found using the formula from binomial statistics, $\sigma = \sqrt{Np(1-p)}$ where $p = 0.8$ for $\cos\theta_{80}$ and N is the total number of counts in the histogram. This σ is the standard deviation of the number of counts above $\cos\theta_{80}$. The uncertainty in $\cos\theta_{80}$, $\Delta\cos\theta_{80}$, is found by finding the value of $\Delta\cos\theta_{80}$ such that the integral of the angular distribution from $\cos\theta_{80}$ to $\cos\theta_{80} + \Delta\cos\theta_{80}$ is σ. The same procedure is used for $\cos\theta_{50}$ except $p = 0.5$.

Figure 5.1 show the angular distributions for the time and elastic fitters. The elastic fitter is clearly superior. However, both will continue to be used. The time fitter, while the less precise, is computationally fast, necessary as a starting guess for the elastic fitter, and benefits from simplicity which is useful for analysis of early data.

Because the elastic fitter contains many parameters, it is important to show that the reconstruction is stable against changes in these parameters. Table 5.1 shows the values of $\cos\theta_{80}$ and $\cos\theta_{50}$ obtained when different parameters were used. Only one parameter was changed at a time. The fitter was applied to an identical set of events in all cases.

5.1.3 Quality of Fit for Position and Direction

The Monte-Carlo studies also show an important anti-correlation between the accuracy of the reconstruction of position and direction. Consider an electron at the origin traveling in the negative z-direction. If the electron path is relatively straight, most of the light will be in a cone about the negative z-axis. This tightly constrains the position in the x and y directions, but gives little constraint in the z-direction. However, because the pattern of PMT hits is cone-like, the direction is easily reconstructed by either the time or elastic fitter. Conversely, if the electron path is particu-

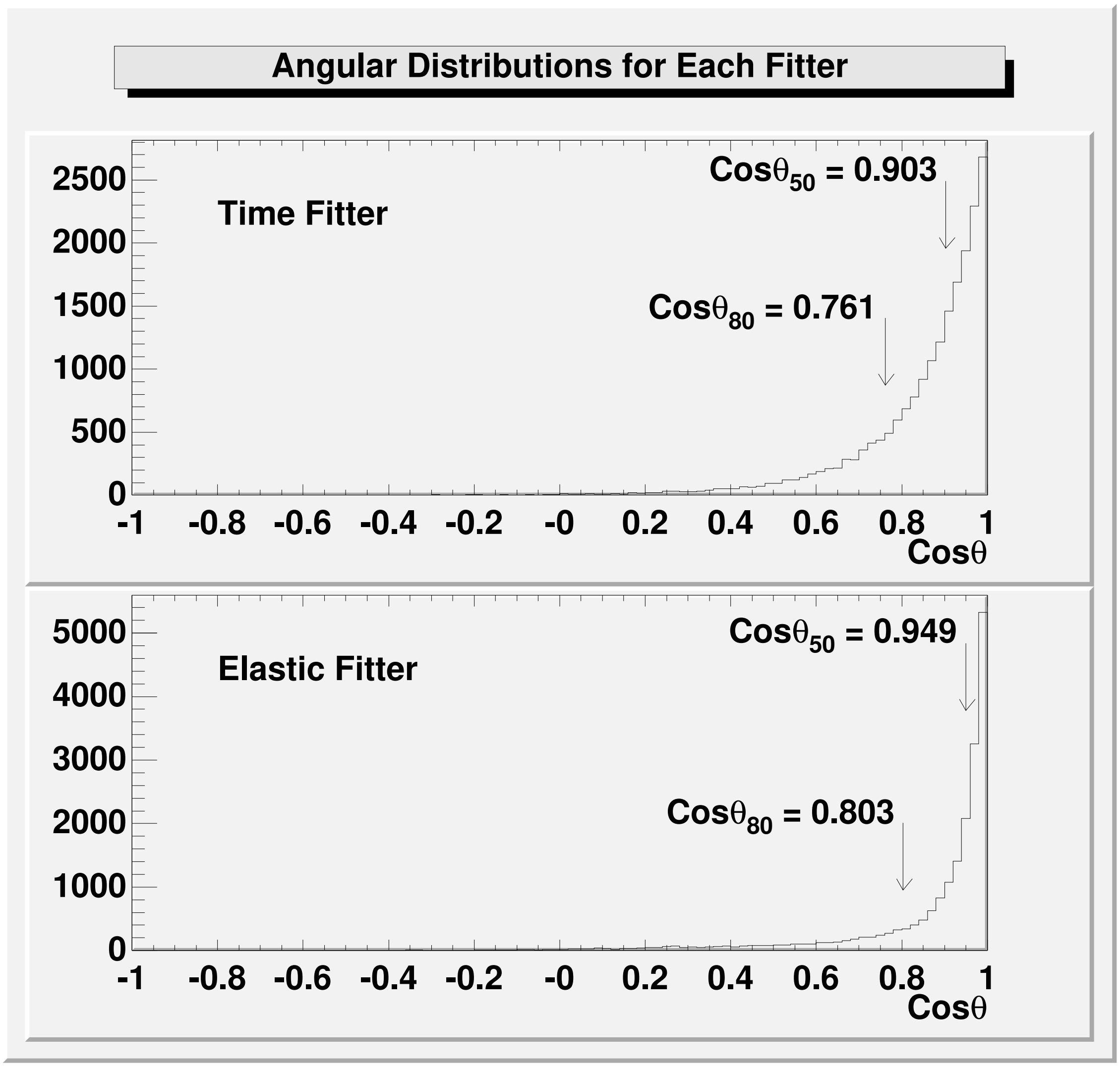

Figure 5.1: The angular distributions for a simulation of 20000 electrons (7 MeV kinetic energy) at the center of the detector water with an isotropic direction.

Angular Resolution and Fitter Parameters				
	Default	Test	$\cos\theta_{80}$	$\cos\theta_{50}$
default values			**0.803**	**0.949**
Initial T	0.5	0.25	0.799	0.951
Final T	0.03	0.015	0.795	0.953
T grad	0.995	0.99	0.799	0.951
T grad	0.995	0.98	0.797	0.949
λ	0.08	0.12	0.803	0.951
θ, ϕ step	0.01	0.02	0.799	0.953
step grad	0.985	0.97	0.799	0.953
			± 0.003	± 0.001

Table 5.1: The effect of elastic-fitter parameters on reconstruction. The second column shows the default values of the parameters. The third column shows the value used to test the effect of parameter change. The following columns show $\cos\theta_{80}$ and $\cos\theta_{50}$ respectively for the case of changed parameter. Only one parameter was changed from the default value in each run. The uncertainty at the bottom of the table are the uncertainty in each entry in that column calculated according to the method described in section 5.1.2. The bold-faced entries show the values when all the parameters were at their default value.

larly contorted, the PMT hits will not be on a cone. The off-cone light constrains the reconstruction of position, but gives misleading information about the initial direction of the electron. This anti-correlation is not caused by the reconstructed position affecting the reconstruction of direction — the root cause is the pattern of PMT hits.

The simulation of 7 MeV electrons at the origin is used to show this effect. First the resolution of the position fit is shown in figure 5.2. The misreconstruction in position is shown as two components. The first component is the misreconstruction perpendicular to the initial direction of travel of the electron. The second component is the misreconstruction parallel to the direction of travel. They are plotted separately.

To study this effect, the position fit was divided into two groups. A "good" position reconstruction meant the parallel component of the position fit was within 40 cm of the actual vertex. A "poor" position reconstruction denotes a parallel component greater than 40 cm from the origin. It is clear from figure 5.3 that there is a large difference between the two distributions.

The reconstruction of direction depends on knowing the position of the event. Thus misreconstructing the position could directly impact the direction fit. To determine the size of this effect, the elastic fitter was applied to a similar simulation except the position used in the direction fit was not the reconstructed position but rather the generated position of the electron in the Monte Carlo. The value of $\cos\theta_{80}$ was unchanged and $\cos\theta_{50}$ was improved by only 0.004. This means that that misreconstruction of the position of the event by tens of centimeters does not cause a significant shift in the direction reconstruction. The difference in the angular resolution for good and poor position fits can not be caused by the misreconstruction of position.

(The plot of position resolution shows an interesting effect not related to the direction fitting. The reconstructed position is systematically "pulled" along the electron's direction of travel. This is a geometrical effect caused by photons scattered through a small angle. These photons when detected are slightly late. Late PMT hits inside the Čerenkov cone push the fitter backward while late hits outside the cone pull the fitter forward. Because there are more PMTs outside the cone than in, the net effect is a pull forward.)

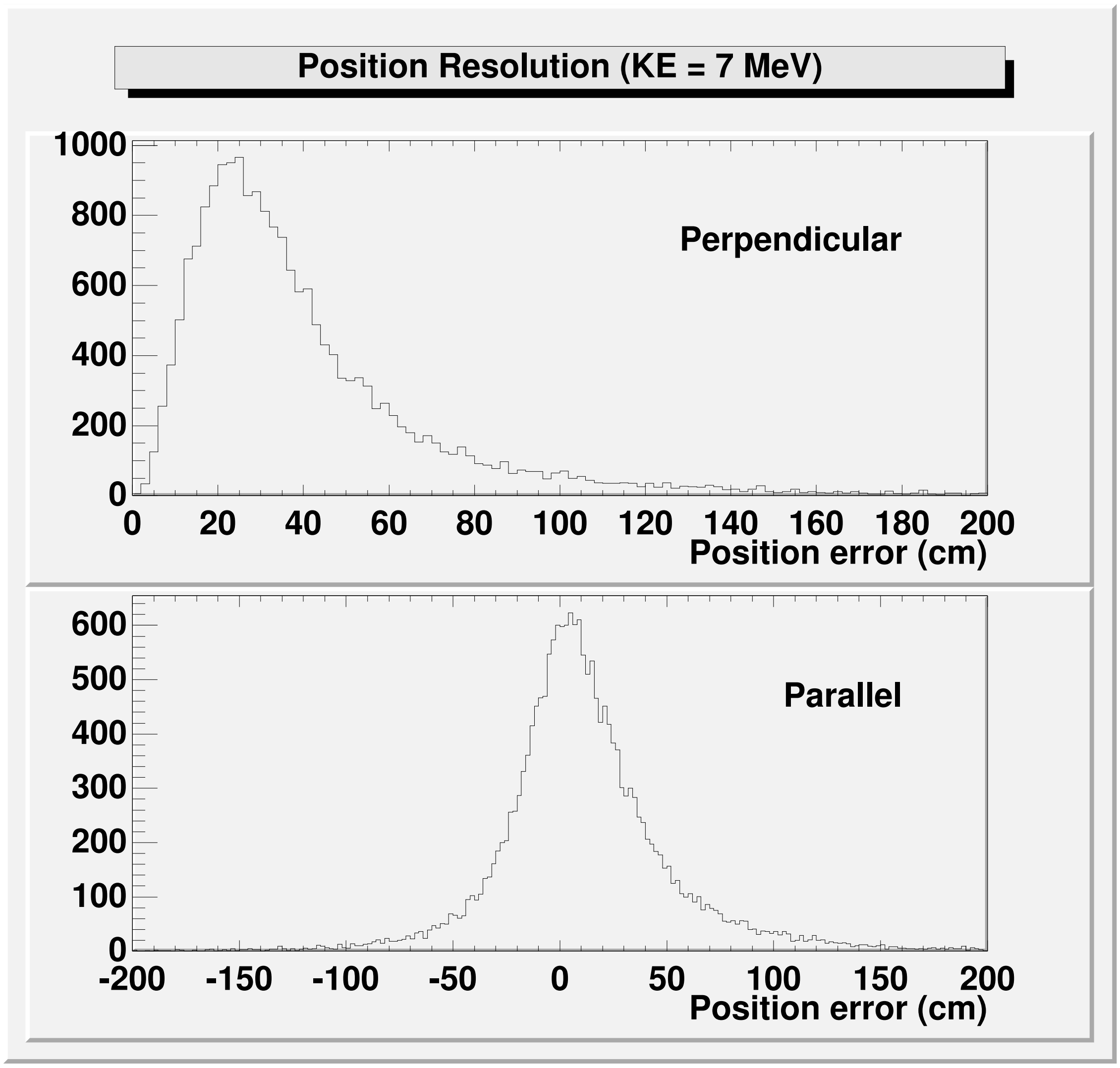

Figure 5.2: The resolution in the position resolution of 7 MeV electrons at the center of the detector. The plot labelled parallel is the component of the fitted position parallel to the initial direction of the electron. The plot labelled perpendicular shows the magnitude of the component perpendicular to the initial direction.

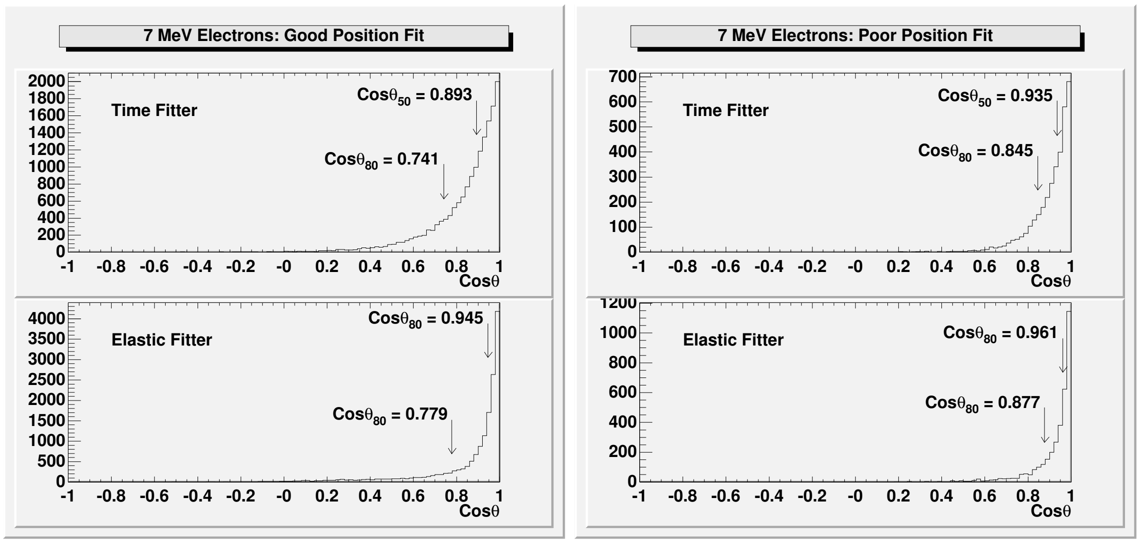

Figure 5.3: The angular distributions are plotted for 7 MeV (kinetic) electrons at the center of the detector. Those events whose reconstructed accuracy is better than 40 cm along the initial direction of the electron are described as "good" position fits. If the accuracy is less than 40 cm, the fit is described as "poor".

5.2 Electron Energy

The angular resolution of SNO improves dramatically as electron energy is increased. Figure 5.4 shows the angular distributions for both fitters at 4 different energies. The value of $\cos\theta_{80}$ for the elastic fitter improves from 0.771 at 6 MeV to 0.895 at 12 MeV. (All energies, except where noted, are kinetic energies.)

There are three reasons why the angular resolution would improve as the electron energy increases. The first and simplest reason is that as the energy increases, so does NHIT. Increased NHIT improves the statistical accuracy of the reconstruction. The second reason is that the amount of scattering of an electron is a function its energy. Molière multiple-scattering theory states that high energy electrons are deflected less for a given path length than low-energy electrons. This means that high-energy electrons travel "straighter longer" than low-energy electrons making the direction easier to measure. The third reason is the Moller-scattering and Bremsstrahlung cross sections decrease as electron energy increases. The probability that Moller scattering or Bremsstrahlung would significantly deflect the electron early in its path is smaller for high-energy electrons. Moller scattering and Bremsstrahlung have a smaller effect than multiple scattering but they do have an interesting consequence discussed in section 5.2.3.

5.2.1 Increase in NHIT

To evaluate the effect of an increase in NHIT on the angular resolution independent of all other effects, a series of 5 simulations of 7 MeV electrons at the center of the detector was run with the quantum efficiency of the PMTs scaled over a range of values from 80% to 120% of nominal. (The probability of an optical photon, of wavelength 400 nm, absorbed by the photocathode producing an anode signal is approximately 19% at the nominal value in the Monte Carlo.) The values of $\cos\theta_{80}$ and $\cos\theta_{50}$ for both fitters are shown in figure 5.5 plotted as a function of the mean value of NHIT for the simulation. The axis on the top of the plot labels the quantum efficiency of the PMTs. The dependence on the quantum efficiency of the PMTs is small. The improvement in angular resolution with increase in energy must be due to other factors.

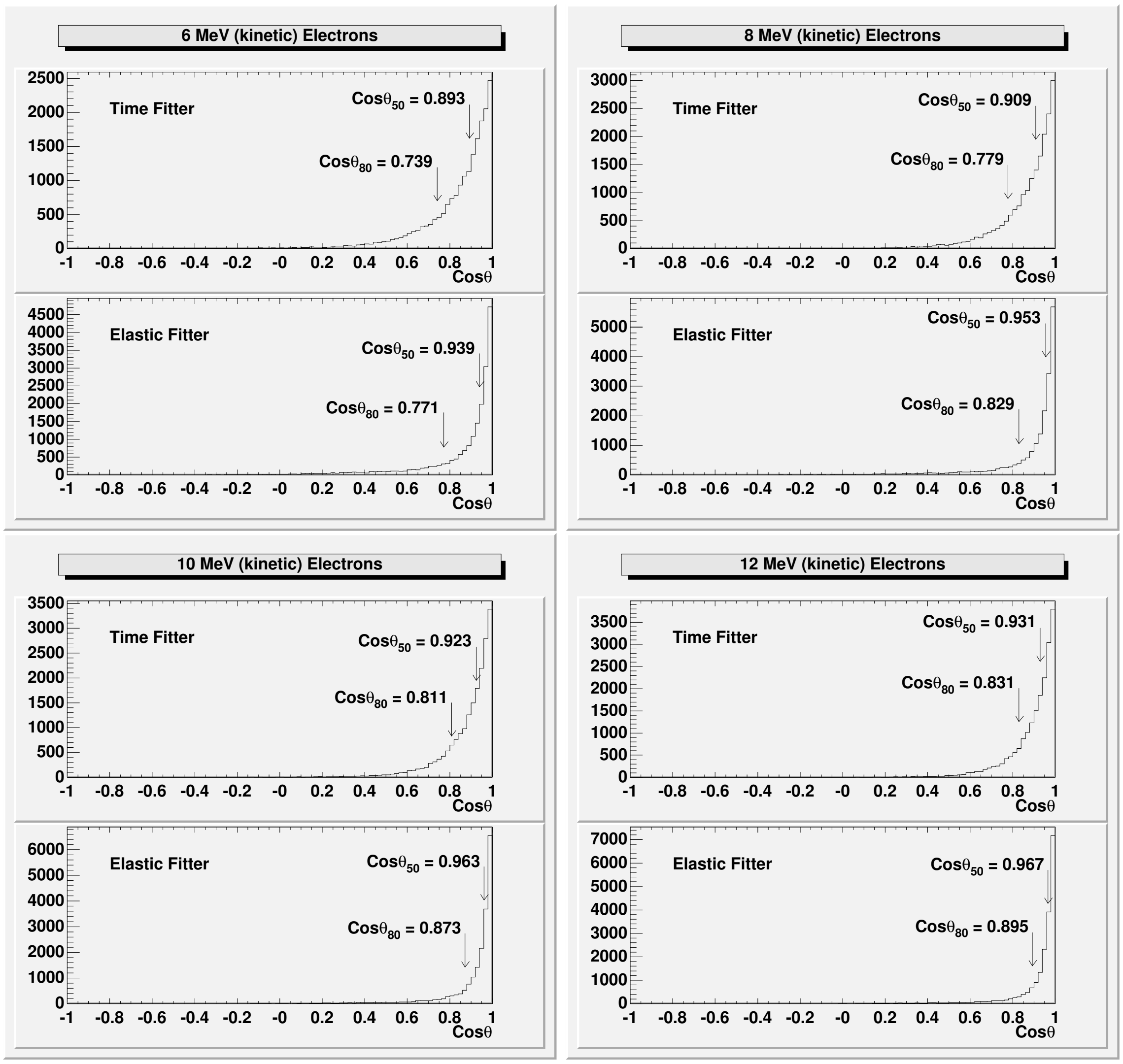

Figure 5.4: The angular distributions for simulations of 20000 electrons at four different energies are presented. The electrons were generated at the center of the detector with directions sampled isotropically. The angular resolution improves markedly with increased energy.

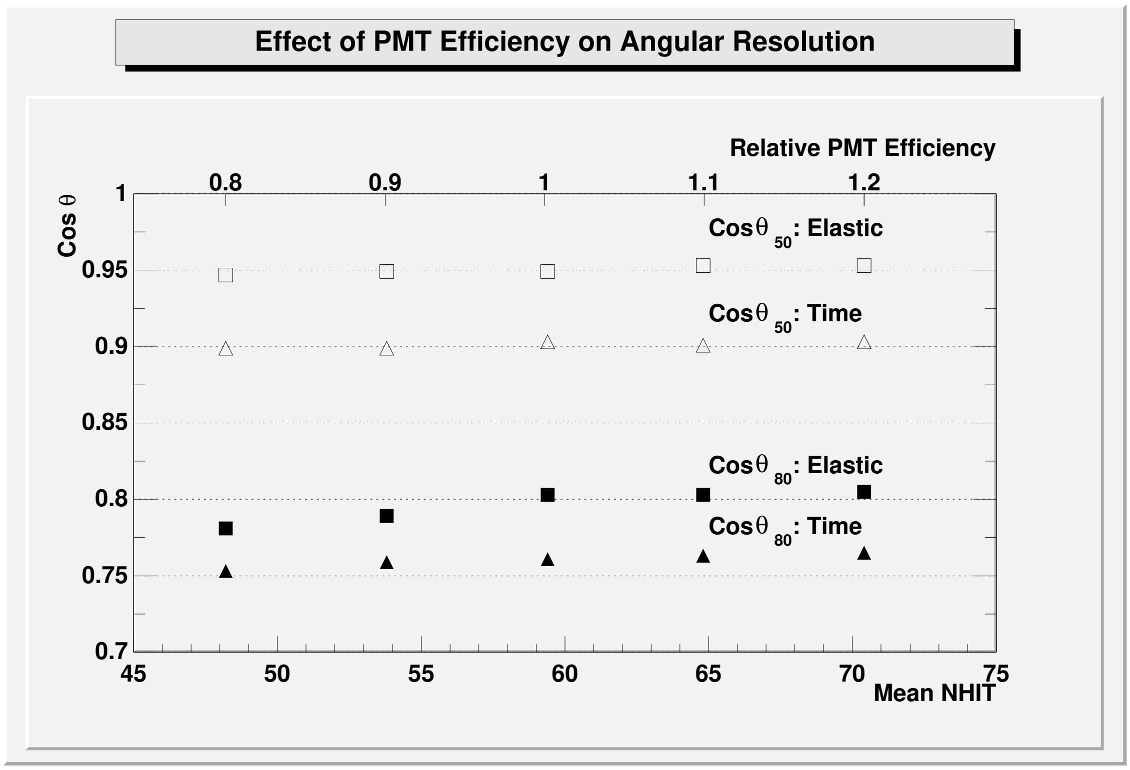

Figure 5.5: The angular resolution is shown for a series of runs with the absolute quantum efficiency of the PMTs at 0.8, 0.9, 1.0, 1.1, and 1.2 times nominal. The efficiency (relative to nominal) is shown on the upper x-axis. The variable plotted on the lower x-axis is the mean NHIT obtained at that particular efficiency.

5.2.2 Multiple Scattering

The direction of an event as determined by the time fitter is found by averaging the vectors from the reconstructed vertex to the hit PMTs. To isolate the effects of electron transport, the direction of each event was found by averaging the direction vectors of all the Čerenkov photons generated. The average direction of Čerenkov photon generation can be compared with the initial direction of the electron to produce an angular distribution. Studying the pattern of Čerenkov light generated rather than the PMT hits removes the effect of detector optics, finite PMT efficiency, and finite position resolution.

Simulations were performed of 6 and 12 MeV electrons in the heavy water. Angular distributions found by studying the pattern of the generated light were compared with the distributions of figure 5.4 which show the angular distributions found by fitting the PMT hits.

Figures 5.6 and 5.7 show the comparison. All histograms were normalized to a total area of 1 count.

Two key things are clear from visual inspection of the plots. First, the direction fit of the Čerenkov production and and the Čerenkov detection are similar. Second, the angular resolution for Čerenkov production is slightly better than for detection. A quantitative comparison of the angular resolution in the two cases for both energies is presented in table 5.2.

The conclusion from this is clear: electron transport dominates the angular distributions. The distributions resulting from Čerenkov production and those resulting from *all* detector processes as modeled by the Monte Carlo are strikingly similar. The electron transport and Čerenkov production cannot be improved upon by the experimenter. The only method by which the experimenter can improve the angular resolution is to find the best possible method to reconstruct the direction of events.

The strong impact of multiple scattering on angular resolution can be seen intuitively from the formulae in section 2.5. The mean scattering angle for a fixed track length is inversely proportional to electron energy. For a 12 MeV electron, for example, the Čerenkov light emitted contains the good directional information while the electron is being slowed to 8 MeV, the moderate directional

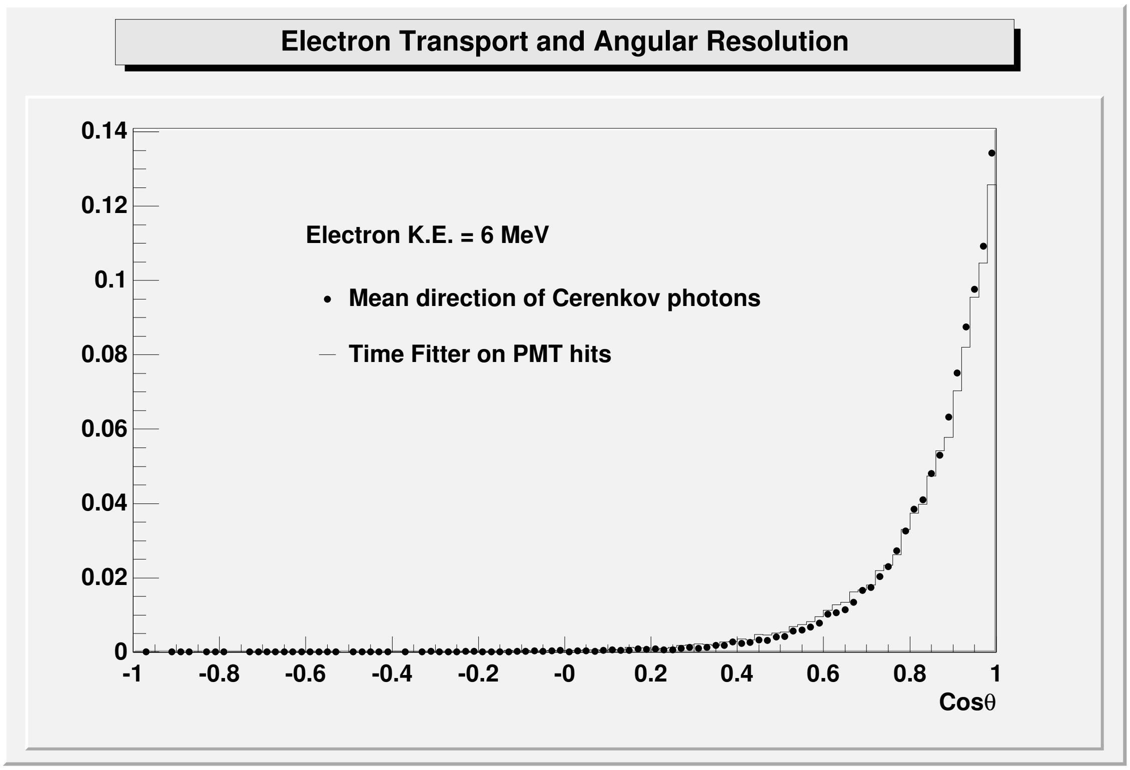

Figure 5.6: The angular distribution for 6 MeV electrons is plotted as a histogram. The angular distribution found by applying the time fitter direction-reconstruction algorithm to the Čerenkov production is shown as the points. The plot of production of light isolates the effect of electron transport on angular resolution while the plot of Čerenkov detection (PMT hits) includes *all* detector effects modeled in the Monte Carlo including the finite resolution of the position resolution.

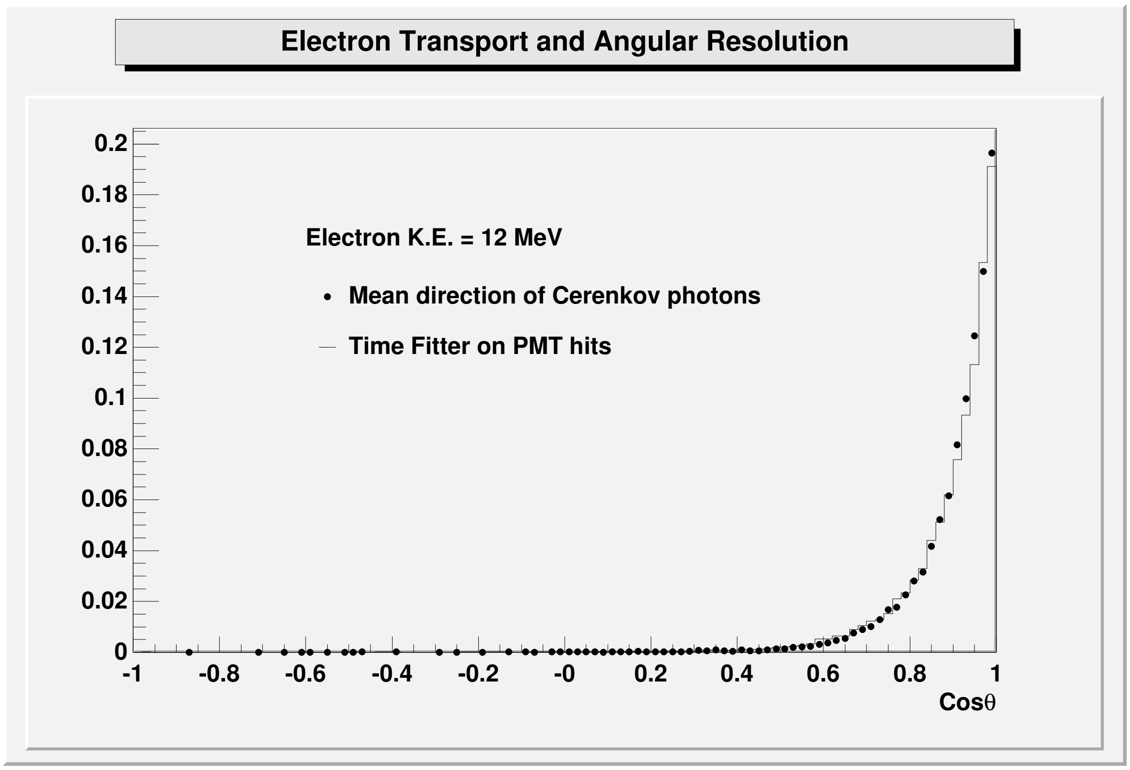

Figure 5.7: The angular distribution for 12 MeV electrons are plotted as a histogram. The angular distribution found by applying the time fitter direction-reconstruction algorithm to the Čerenkov production is shown as the points. The plot of production of light isolates the effect of electron transport on angular resolution while the plot of Čerenkov detection (PMT hits) includes *all* detector effects modeled in the Monte Carlo including the finite resolution of the position resolution.

Angular Resolution of Čerenkov Production and Detection			
		$\cos\theta_{80}$	$\cos\theta_{50}$
6 MeV	Production	0.761	0.901
	Detection	0.739	0.893
12 MeV	Production	0.843	0.935
	Detection	0.831	0.931

Table 5.2: The values of $\cos\theta_{80}$ and $\cos\theta_{50}$ are shown for the time fitter for 6 and 12 MeV electrons. The time fitter was applied to both the Čerenkov detection (ie a normally fitted event including all effects of the detector and position reconstruction) and and to the Čerenkov production (the direction cosines of all emitted Čerenkov photons are averaged for each event and compared to the initial electron direction.) The angular resolution is only slightly poorer for the fit to the hit PMTs.

information while being slowed to 4 MeV, and the poor directional information while being slowed the final 4 MeV. Taken on average, the directional information for a 12 MeV electron must be better than that for an 8 MeV electron which in turn must be better than that for a 4 MeV electron. Higher-energy electrons, on average, travel straighter for a longer fraction of their total track than lower-energy electrons. Thus the direction information is better for higher-energy electrons.

The (simple) argument above can be quantified to give the scaling of the change in angular resolution with energy. The scattering angle of an electron after a short track is distributed according to a Gaussian with a sigma that scales as $1/E$, where E is the total electron energy. The sigma for the Gaussian of step i can be written $\sigma_i = \Sigma/E_i$, if the step length is constant for all steps.

Initially the electron has energy $\mathcal{E}$ and has not scattered. After 1 step the electron has scattered (on average) through an angle $\Sigma/\mathcal{E}$. During the second step, the electron is scattered through an angle $\Sigma/(\mathcal{E} - \Delta E)$, where ΔE is the energy lost during the previous step. The average angle for the scattering through both steps together is given by σ, with

$$\sigma^2 = \sigma_1^2 + \sigma_2^2 = \Sigma^2 \left(\frac{1}{\mathcal{E}^2} + \frac{1}{(\mathcal{E} - \Delta E)^2} \right) \tag{5.4}$$

As more steps are included, the sum expands to include them. Once many steps are included the sum can be written as an integral and the mean angle of scatter for an electron of initial energy $\mathcal{E}$ at energy E can be calculated with

$$\sigma^2 = \Sigma^2 \int_E^{\mathcal{E}} \frac{dE'}{E'^2} = \frac{1}{E} - \frac{1}{\mathcal{E}} \tag{5.5}$$

where E' is the variable of integration.

The average angle of the electron during its path can be calculated. The average value of a function $f(x)$ between two values x_1 and x_2 is $\int_{x_1}^{x_2} f(x)dx/(x_2 - x_1)$. Thus the average angle, $\bar{\sigma}$, of the electron over the course of its path is

$$\bar{\sigma} = \frac{\Sigma}{\mathcal{E} - E_{\text{low}}} \int_{E_{\text{low}}}^{\mathcal{E}} (1/E' - 1/\mathcal{E})^{1/2} dE' \tag{5.6}$$

where, again, E' is the variable of integration.

The remaining issue is the value of E_{low}. The rate of Čerenkov emission below 1 MeV starts falling quickly and the rate of energy loss increases rapidly for energies below 1 MeV. Therefore, the integral is computed with $E_{\text{low}} = 1\text{MeV}$.

By evaluating the integral for various values of $\mathcal{E}$, the scaling of angular resolution with energy can be found. The value of Σ was set such that the mean angle for electrons with initial energy of 6.511 MeV is 1.

The comparison of this model with the simulation requires that the mean value of θ for the time fitter be found. (The time fitter uses the average direction from the reconstructed position to the PMTs to obtain the direction and is thus more directly comparable to the model than the elastic fitter.) The mean angles (in degrees) for total electron energies of 12.511, 10.511, 8.511, and 6.511 are 23.6, 25.1, 27.1, and 29.6. To compare with the model, the angles were also scaled such that the angle for 6.511 MeV electrons was 1. (Angular distributions with respect to θ not $\cos\theta$ were used to find the mean because the arc-cosine of the mean of $\cos\theta$ is not the same as the mean value of θ.) Figure 5.8 shows the result of the simple model as a function of total electron energy as a curve with the results from the 4 simulations shown as the points.

There is reasonable agreement between the simple model and the detailed simulations. This discussion does not prove that the fine details of the simulation of Molière scattering are correct. What it does show is that a simple model of Molière scattering behaves similarly with respect to energy as the detailed calculations of the Monte Carlo.

5.2.3 Angular Resolution at Fixed Energy and PMT Efficiency

A high-statistics simulation of 7 MeV electrons was performed. Figure 5.9 shows the NHIT spectrum obtained and the angular distributions for three subranges of the NHIT spectrum. The angular resolution worsens slightly as NHIT increases. This is contrary to the expectation of statistical effects.

This can be explained by considering the electron track length. Those electrons which emit more light have a longer track. Thus the electron has a longer path on which to be scattered and emit more light off the cone. Furthermore, the cross-sections for production of δ-rays and soft Bremsstrahlung increase at low energy. Thus these processes reduce the light output preferentially at the end of the track where the direction of the electron is least likely to be parallel to the direction at the start of the track. This effect tends to cancel out the statistical effect discussed in section 5.2.1.

5.2.4 Fitter Performance as a Function of Energy

The elastic fitter attempts to fit a cone to the hit PMTs. For higher energy events this is a good model. For some low energy events, the PMT hit patterns do not show a well defined cone. The elastic fitter at low energies loses accuracy. Figure 5.10 shows the vales of $\cos\theta_{80}$ for both fitters as a function of electron kinetic energy. The elastic fitter, clearly superior to the time fitter above 6 MeV, is only equally good at 5 MeV and worse below 5 MeV.

It is interesting that this does *not* hold for $\cos\theta_{50}$; the elastic fitter is better than the time

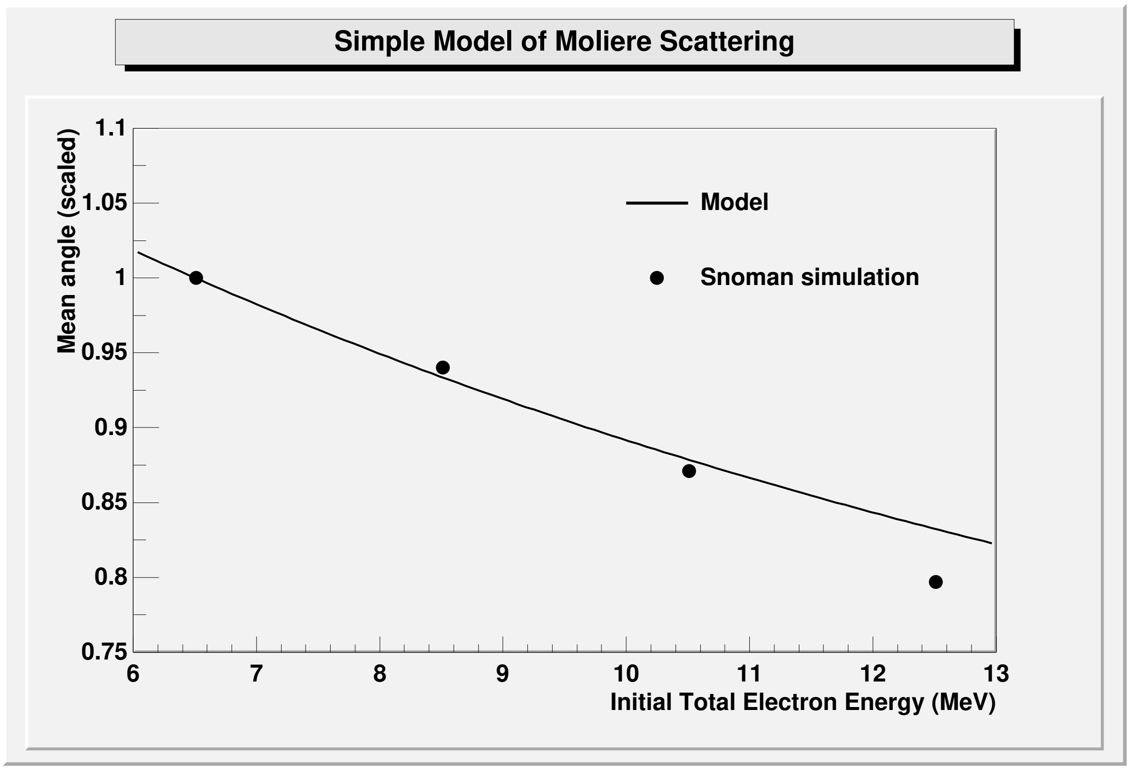

Figure 5.8: A comparison of the simple model of Molière scattering and the result from SNOMAN simulation is presented. The quantity plotted for the model is the mean angle of the electron as it emits Čerenkov light scaled to 1 at 6.511 MeV. The points are the mean value of θ found from the angular distributions from the simulation at four energies. The variable plotted on the x-axis is the total electron energy.

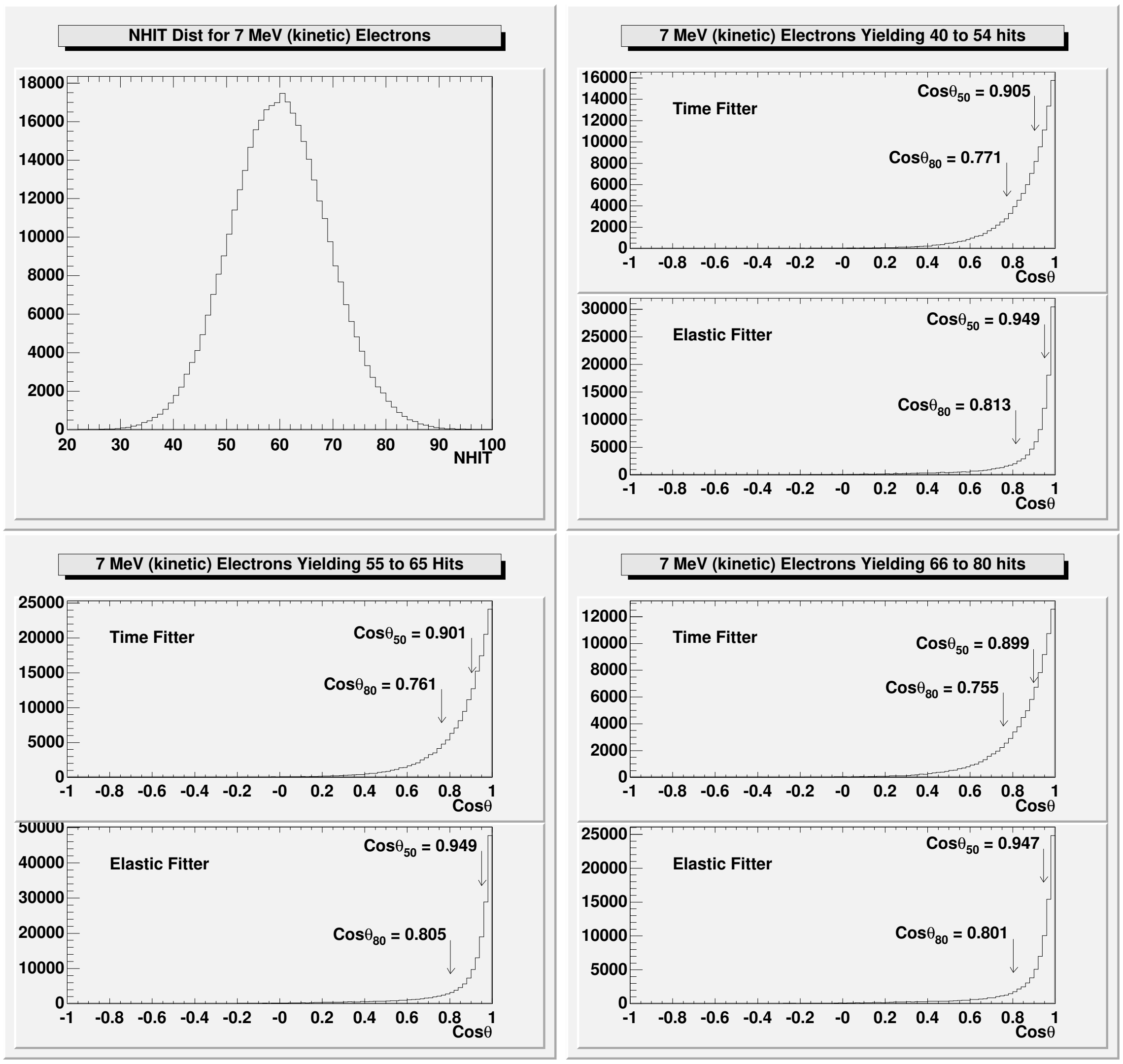

Figure 5.9: The angular distributions for a high-statistics simulation of electrons at the center of the detector. The first plot shows the distribution in NHIT. The following plots show the angular distributions for different ranges of NHIT.

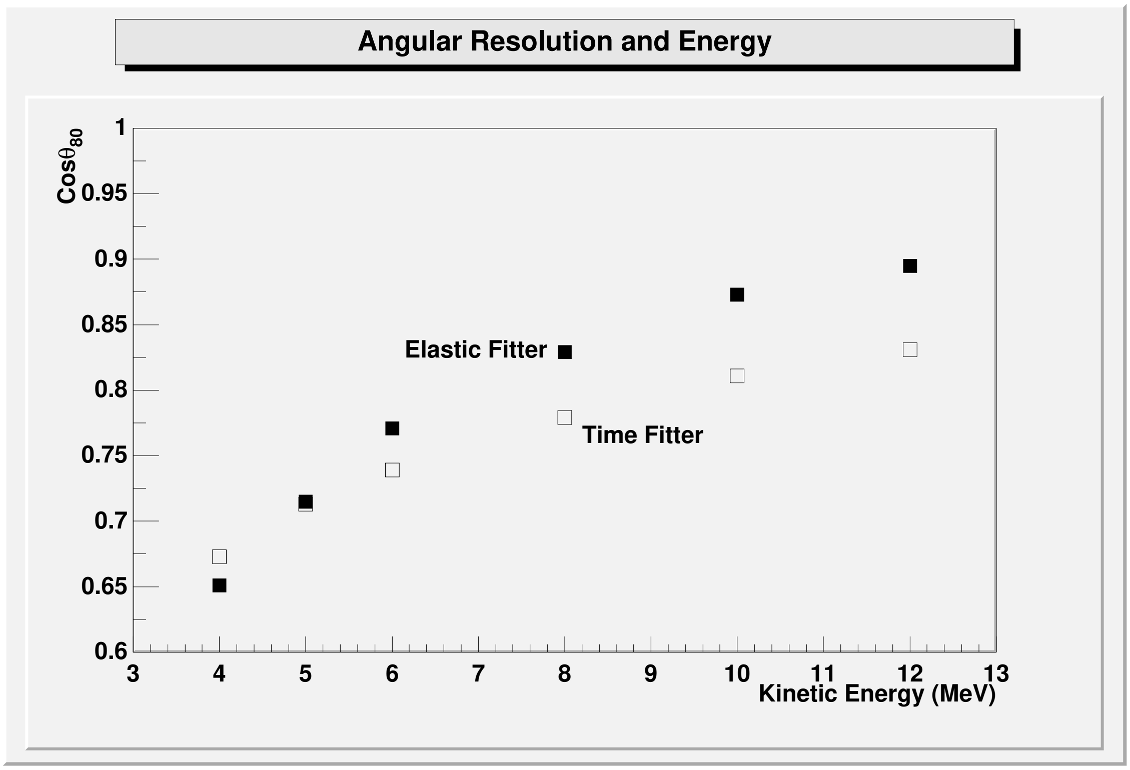

Figure 5.10: The value of $\cos\theta_{80}$ is plotted for both fitters as a function of energy. At high energies the elastic fitter is clearly superior but at low energies its accuracy drops markedly.

fitter even at 4 MeV. This suggests that a large fraction (on order half) of the events at low energy reconstruct well to a cone but a significant fraction (on order 20%) do not.

5.2.5 Application to the Detector Response Function

Two conclusions are clear. First, the angular resolution is a strong function of the energy of the electron. Second, the energy part and the angular part of the detector-response function are decoupled. The directional response of 7 MeV electrons which reconstruct with an energy of 8 MeV is very similar to that of 7 MeV electrons which reconstruct at 6 MeV. The convolution over the energy and angular parts of $\mathcal{P}$ can be treated as 2 one-dimensional convolutions rather than 1 two-dimensional convolution. Because the angular response is a function of the real, not the measured electron energy, the convolution in the directional response must be performed first.

5.3 Detector Optics and Position and Direction of the Event

The data presented so far have been for simulations of electrons generated at the center of the detector. This ensures that there are no gross geometrical or optical differences between events, except for the presence of the chimney of the acrylic vessel. These optical and geometrical effects are now considered.

The optical properties of SNO, in particular the Rayleigh-scattering and attenuation lengths of the water and acrylic, will be measured using the laserball calibration source (step 1 of the analysis). The extinction lengths will be measured with a 14% uncertainty for the heavy water and the acrylic and a 100% uncertainty for the light water [Fo98]. Extinction refers to loss of direct light by either scattering or attenuation. (For an event at any location and direction in the heavy-water volume there is a strong correlation between the path length in the acrylic and light water. Because the acrylic extinction is much larger than that of the light water, the acrylic extinction dominates. The light water has a large relative uncertainty because its effect is small.)

Simulations of 7 MeV electrons at the center of the detector were performed with different optical properties: the Rayleigh-scattering and attenuation probabilities used were one-half and double the default values for the heavy water, the light water and the acrylic. Only one parameter was changed at a time. The resulting values of $\cos\theta_{80}$ and $\cos\theta_{50}$ are shown in table 5.3. There are no clear changes in angular resolution with optical quality of any media with the exception of acrylic attenuation. For events in the center of the detector, increasing the acrylic attenuation is like reducing the efficiency of the PMTs. Thus one would expect a slight decline in angular resolution. It is more pronounced for acrylic attenuation than for heavy- or light-water attenuation because the acrylic attenuates more light. Thus doubling its attenuation has a larger effect on NHIT.

The effect of the acrylic is more pronounced near the acrylic vessel. This is so because the Čerenkov cone can intersect the vessel obliquely. Thus light on some part of the cone must travel through much more acrylic than other parts of the cone. A simulation identical to that of the 7 MeV electrons was performed except that the electrons were distributed uniformly in a sphere of radius 7 meters about the center of the detector. The initial direction was chosen randomly. Four sets of plots were made: the first two included electrons generated between 2 and 4 meters from the origin directed in and out; the second two looked at electrons generated between 5 and 6 meters directed in and out. *In* (*Out*) is defined such that the generated direction is within 45 degrees of the vector pointing radially in (out) from the generated position. The distributions are shown in figure 5.11. At low radius, there is little difference between in and out as a simple examination of the geometry would suggest. (In the limit of the radius going to zero there is no distinction between in and out.) There is a large difference between inward and outward going electrons at high radius.

The discussion of inward-going and outward-going events has neglected half of the data. Two more classes were studied. These are events whose direction vector is between 45 degrees and 90 degrees of the radial vector and those whose direction vector is between 90 and 145 degrees of the radial vector. (These could be described as “slightly out” and “slightly in”.) The angular distributions for both of these sets of events are similar to the inward-going events.

These results raise the question of whether there is a systematic shift in the reconstruction of direction caused by detector geometry. This might occur, for example, if the geometry of the detector and the event cause light on one “side” of the Čerenkov cone to be attenuated more than

Angular Resolution and Optics						
			Time Fitter		Elastic Fitter	
			$\cos\theta_{80}$	$\cos\theta_{50}$	$\cos\theta_{80}$	$\cos\theta_{50}$
default values			**0.761**	**0.903**	**0.803**	**0.949**
Heavy water	Attenuation	doubled	0.763	0.903	0.797	0.949
		halved	0.759	0.903	0.801	0.951
	Rayleigh scat	doubled	0.755	0.901	0.789	0.949
		halved	0.763	0.905	0.797	0.951
Light water	Attenuation	doubled	0.765	0.903	0.797	0.949
		halved	0.763	0.903	0.795	0.951
	Rayleigh scat	doubled	0.763	0.903	0.793	0.951
		halved	0.759	0.903	0.793	0.951
Acrylic	Attenuation	doubled	0.761	0.901	0.785	0.949
		halved	0.765	0.905	0.807	0.953
	Rayleigh scat	doubled	0.765	0.903	0.799	0.951
		halved	0.767	0.903	0.795	0.951
			±0.002	±0.001	±0.003	±0.001

Table 5.3: The effect of varying the optical properties of the heavy water, light water and acrylic angular resolution. There is no effect at this level of statistical accuracy. The default values are in bold face at the top of the table. The uncertainties at the bottom of the table are the uncertainty on each measurement in that column.

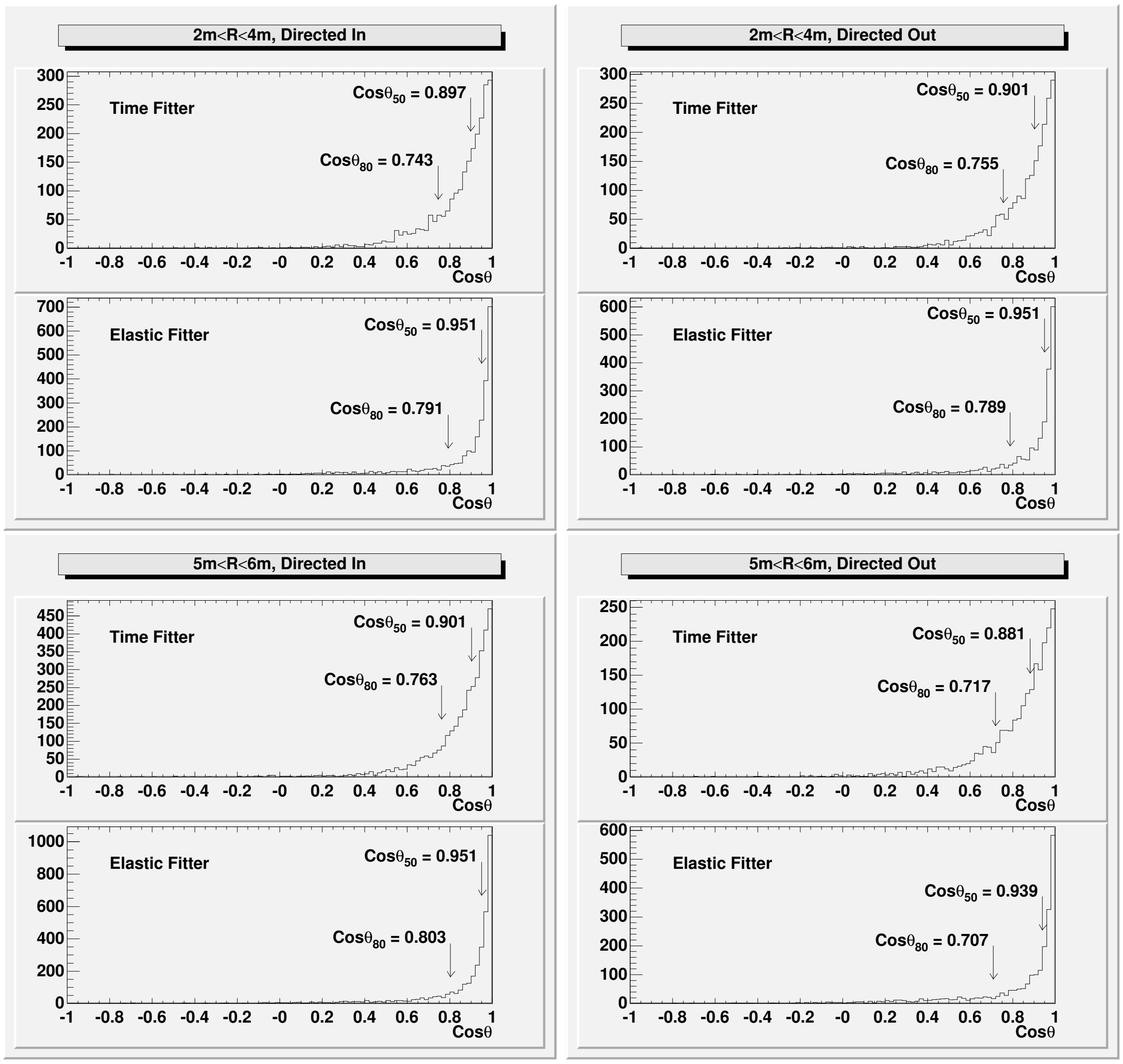

Figure 5.11: The angular distributions are shown for 4 different event locations and directions.

light on the other side. A simulation of 7 MeV electrons was studied to search for a shift. No shift was found for either fitter, even for those events that reconstruct at high radius. The output of the fitter, $\vec{u}_{\rm fit}$, is the best estimate of the direction given that particular fitter. Therefore, there should be no attempt to improve the direction reconstruction in the function $\mathcal{C}$.

What is the source of position-direction dependence at high radius? Simulations were performed to study four factors. First, the effect of the finite position resolution of the fitter was removed by performing the direction fit at the position at which the electron was generated rather than at the reconstructed position. This had a small effect for events at the origin because the distance from the origin to the PMTs is large compared to the finite position resolution. However, at high radius, the position resolution is a significant fraction of the distance from the source to the PMTs.

Second and third, the attenuation in the acrylic and light water were reduced by a factor of 1000. Geometrical effects caused by oblique intersection of the Čerenkov cone and the acrylic vessel will be removed in this case.

Fourth, the refractive index of acrylic was changed to match that of the light water. This will eliminate reflections at the acrylic-water interfaces.

Table 5.4 shows the effect of these changes on the simulations. A comment should be made about event selection for this table. The events were generated between 500 and 590 cm. (The upper limit is to ensure there was no light generated in the acrylic.) A cut was performed on fitted position, $R_{\rm fit} < 700$cm. If the upper limit is set at 600 centimeters, issues of the anticorrelation between reconstructed position and direction become important.

For the simulation with all parameters at default values, the values of $\cos\theta_{50}$ are similar for inward and outward-going events for both fitters. However, there is a small difference in $\cos\theta_{80}$ for the time fitter and a larger difference for the elastic fitter. The value of $\cos\theta_{80}$ and $\cos\theta_{50}$ for the inward-going electrons changes only slightly as the four factors were changed. The values of $\cos\theta_{80}$ for the elastic fitter do come closer to the values for inward-going electrons when the factors are changed. When further, the effect of the chimney is removed by cutting those events with a positive upward component to the reconstructed direction, the values of $\cos\theta_{80}$ for the elastic fitter

Angular Resolution at High Radius					
		Time Fitter		Elastic Fitter	
		$\cos\theta_{80}$	$\cos\theta_{50}$	$\cos\theta_{80}$	$\cos\theta_{50}$
Default	in	0.767	0.901	0.807	0.953
	out	0.727	0.885	**0.739**	0.941
No H_2O atten	in	0.763	0.901	0.801	0.953
	out	0.727	0.887	**0.755**	0.945
No acr atten	in	0.755	0.897	0.795	0.953
	out	0.727	0.883	**0.765**	0.947
perf pos fit	in	0.755	0.897	0.791	0.953
	out	0.727	0.883	**0.769**	0.943
n(acr) = n(H_2O)	in	0.763	0.905	0.791	0.949
	out	0.729	0.887	**0.743**	0.941
All	in	0.745	0.893	0.791	0.951
	out	0.731	0.881	**0.757**	0.945
All and no chimney	in	0.753	0.897	0.803	0.957
	out	0.731	0.879	**0.767**	0.947
		$\pm$ 0.005	$\pm$0.003	$\pm$0.01	$\pm$0.003

Table 5.4: The effect of detector properties on angular resolution at high radius for inward-going and outward-going 7 MeV (kinetic) electrons. The events were generated at a radius between 500 and 590 cm. Inward and outward are defined in the text. The symbols n(acr) and n(H_2O) refer to the refractive index of acrylic and light water. "All" means that all the optical changes were included in one simulation. For the "no chimney" run, the effect of the chimney was eliminated by looking only at events whose z-component of reconstructed direction was negative. The uncertainty in this last row is 1.4 times the uncertainty for all other entries because only half as many events were included.

become quite similar. One effect that could create a small shift has not been considered in detail. This is that the probability of absorption and reflection of photons off the PMTs is a function of the incidence angle of the PMTs. Outward-going events at high radius are more likely to strike the PMTs at large angles than other events and the increase in the probability of reflection at high incidence may skew the hit pattern for these events somewhat.

The attenuation in the acrylic will be measured with approximately 15% uncertainty. A series of simulations was performed to see if changes of this magnitude would contribute an uncertainty in the angular resolution. Simulation of electrons of 7 MeV kinetic energy were performed in which the acrylic attenuation was 0.75, 1.0, 1.25, and 1.5 times the default value. The electrons direction was chosen isotropically and the position was chosen over a sphere of radius 7 meters. Events that reconstructed within the vessel were considered. The values of $\cos\theta_{80}$ and $\cos\theta_{50}$ varied by less than 0.004 for the time fitter and less than 0.01 for the elastic fitter. This will need to be studied again once the optical properties are calibrated and the uncertainties are known. Similar analyses must be done for the uncertainty in light-water attenuation and the uncertainty in the resolution of the position fit.

In the discussion of solar-neutrino analysis in chapter 4, the variables used in the analysis were energy, $\cos\theta_{\text{sun}}$, and radius. The angular distribution is not only a function of radius but also the direction of the event with respect to the radial vector. There is little to be gained by including this information in the solar-neutrino analysis as can be seen from the following statistical argument. Consider a data set with 1000 ES events (approximately 2.5 to 3 year's data) reconstructed within the acrylic vessel. Of these 420 will have a reconstructed radius between 500 and 600 cm. The change in angular distribution was only significant if the angle between the radial vector and the direction was less than 45 degrees. This is only 15% of the 420 events. Therefore, of the 1000 events in the sample, only 63 will have an angular distribution significantly affected by the geometry and optics. Therefore, the statistical improvement in the neutrino analysis from including the position-direction dependence is negligible.

Figure 5.12 summarizes the effect of averaging over directions at a given radius and energy by plotting $\cos\theta_{80}$ for the elastic fitter as a function of energy and radius. The effect of radius is small once the averaging is performed.

5.4 Stability of Monte Carlo Calculation

The discussions in this chapter have assumed that the Monte Carlo accurately describes electron transport in water. The Molière theory does not depend on the exact nature of the cross-section for interactions between the electron and the water as long as that cross-section becomes the Rutherford cross section in the limit of a large scattering angle. There is only one free parameter in the Molière theory and that is the "screening angle" [Be53]. The screening angle is fixed by studying the angular distribution of electrons having traversed thin slabs of material.

While the Molière theory has only one free parameter, there are three parameters used to control the EGS4 code. They are the threshold energies for knock-on-electron and soft-Bremsstrahlung production and the size of the step length for electrons. The thresholds determine whether creation of an electron or photon is treated as a discrete interaction or is considered to be part of the continuous energy loss. The thresholds in the default case are 10 keV for the (kinetic) energy of knock-on electrons and Bremsstrahlung photons. The step length of the electron is chosen such that the electron energy will have decreased by a certain fraction over the step. The default value is 3% energy loss per step in SNOMAN.

Any prediction of the Monte Carlo must not be a function of these three parameters for small changes in parameter value. Simulations were performed with the thresholds altered from their default values. The effect on angular resolution was small, but noticeable. Table 5.5 shows the values of $\cos\theta_{80}$ and $\cos\theta_{50}$ for both fitters for changes in the parameters. The largest change was in $\cos\theta_{80}$ for the elastic fitter when the threshold for discrete Bremsstrahlung and and knock-on electrons was reduced.

The small size of the effect shows the Monte Carlo results are quite stable. Changing the parameters does not change the angular response from the simulation much. This is not a guarantee that the calculations are correct; it is rather a statement that the calculations are being performed

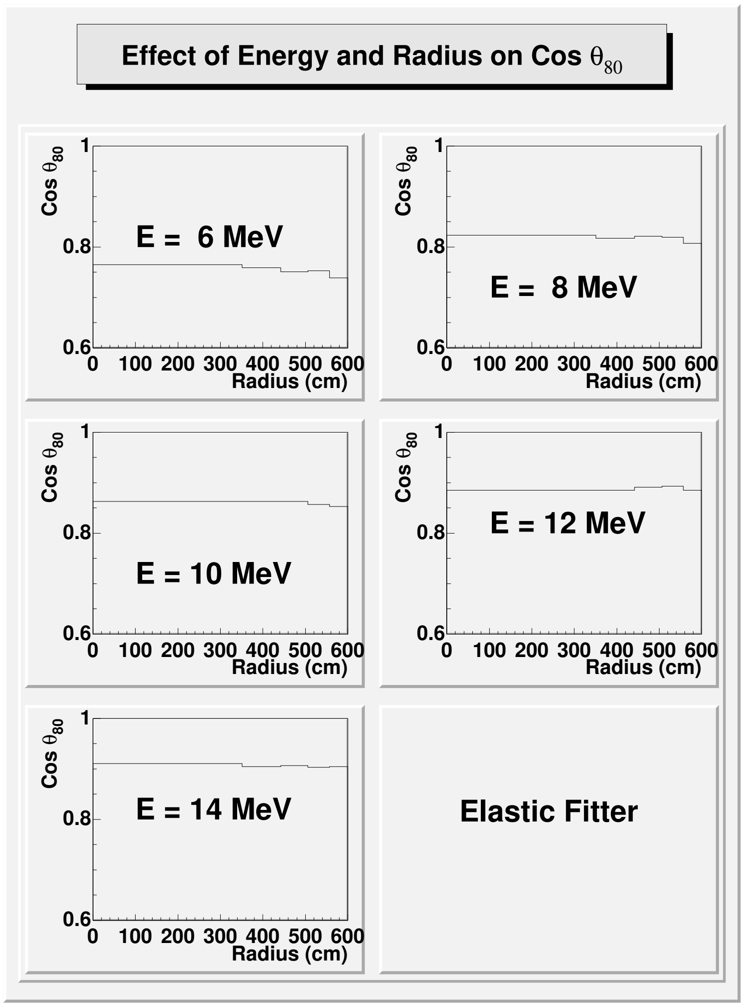

Figure 5.12: The values of $\cos\theta_{80}$ for the elastic fitter are plotted as a function of energy and radius. Note, that while there is a tendency for the angular resolution to worsen at high radius, the effect is small.

Angular Resolution and EGS4 Parameters						
			Time Fitter		Elastic Fitter	
	Default	Test	$\cos\theta_{80}$	$\cos\theta_{50}$	$\cos\theta_{80}$	$\cos\theta_{50}$
all default values			**0.761**	**0.903**	**0.803**	**0.949**
thresholds	10 keV	20 keV	0.767	0.905	0.801	0.953
thresholds	10 keV	5 keV	0.763	0.901	0.789	0.949
step size	3% E loss	1%	0.763	0.903	0.801	0.951
			±0.002	±0.001	±0.003	±0.001

Table 5.5: The effect of parameters used in EGS4 on the angular resolution. The values for all parameters at their default value are shown in bold face. In subsequent rows the parameter changed, its default value, its test value, and the values of $\cos\theta_{80}$ and $\cos\theta_{50}$ are presented. The uncertainties at the bottom of the table are the uncertainty on each measurement in that column.

with parameters that are reasonable. The angular response of the Monte Carlo must be tested. The analysis of solar-neutrino data must consider this as a source of systematic uncertainty.

5.5 Analytic Description of Angular Resolution

The analysis so far has used two simple parameters to estimate the width of the main peak and the size of the tail of the angular distribution plots. This sections describes the angular part of the analytic description of the detector response, $\mathcal{P}$. The analytic function must

- be accurate. Any deviation of the function from the true distribution must be sufficiently small that it has a negligible impact on any subsequent analysis.
- contain relatively few parameters. A description requiring many parameters is no simpler to use than a numerical data table.
- be easily integrable and differentiable.

- be applicable for use with both the elastic and time fitter and for electrons and gamma rays over an energy range from 3 to to 20 MeV.

A candidate function is

$$\mathcal{F}(x \equiv \cos\theta) = N \times \left(e^{a_0(x-1)} + a_1 e^{a_2(x-1)}\right) \tag{5.7}$$

The function assumes that the angular distribution is the sum of two exponential functions. The first determines the shape of the curve near $\cos\theta = 1$. The second determines the size and fall-off of the tail. In this function $a_1 < 1$. N is a normalization factor. The function meets all the requirements.

Figure 5.13 shows the simulation of 7 MeV and 12 MeV electrons at the center of the detector with a fit to equation 5.7 overlaid. At 7 MeV, the values of chi square for $\cos\theta > 0$ are 29 for the time fitter and 109 for the elastic fitter. At 12 MeV the results are 58 and 134. All four values are for 46 degrees of freedom.

The values of chi square for the elastic fitter are large, but this is not necessarily a problem. The analytic function is an approximation. Therefore, if sufficient statistics are accumulated, the approximate function and the histogram will differ by an amount large compared to the uncertainty in the histogram and chi square *must* be large.

What is important is whether use of the approximate function skews the solar neutrino analysis. For this purpose, the analytic function should be compared to a histogram containing approximately the number of ES events in the data sample. The value of chi-square is inversely proportional to the uncertainty squared. The uncertainty in the data is the square root of the number of bin contents. Thus $\chi^2 \propto 1/N$ where N is the total number of counts in the histogram. A five-year data set would have approximately 2000 ES events, only 10% of the content of these histograms. Therefore, the contribution to chi-square from inaccuracies in equation 5.7 is small.

The analytic function was fit to angular distributions for various energies for events distributed throughout the detector. Figure 5.14 shows the functions at 6 energies and 5 radial bins from 0 to 600 cm such that volume contained in each radial bin was equal. Note that the curves for

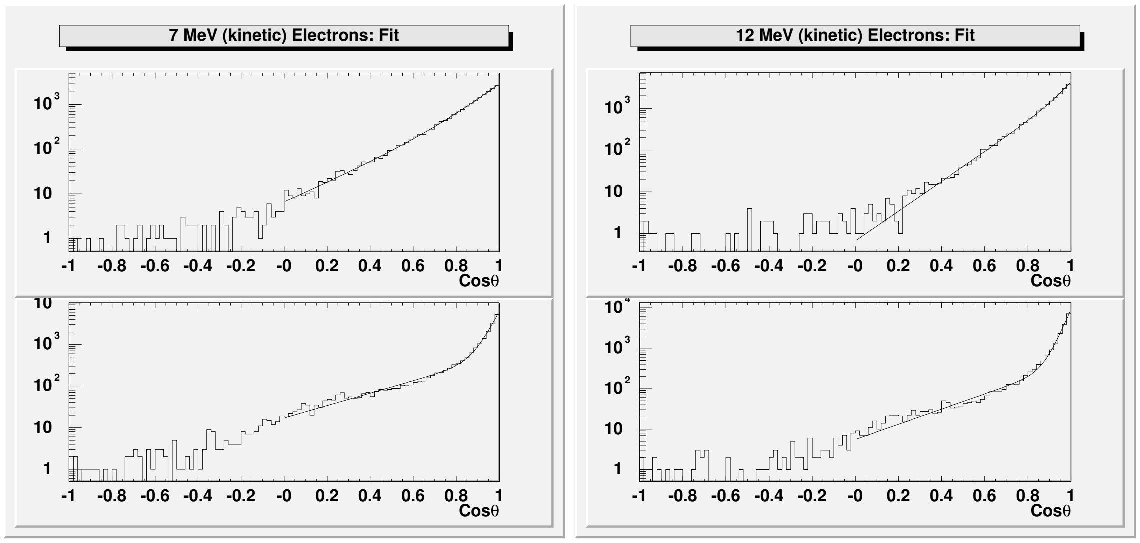

Figure 5.13: The a fit to equation 5.7 for 7 and 12 MeV electrons in the simulation.

the different radial bins are not distinct on the linear plot. Similar curves have been evaluated at electron kinetic energies of 5, 7, 9, 11, and 13 MeV.

It is now possible to construct the angular part of the detector response function. The full response function is $\mathcal{P}(E, \cos\theta_{\text{sun}}, R, \rightarrow E', \cos\theta'_{\text{sun}}, R')$ (equation 4.3). For the electron-scattering signal, $\cos\theta_{\text{sun}} = 1$ to high accuracy. Then the response simplifies to $\mathcal{P}(E, 1, R, \rightarrow E\prime, \cos\theta'_{\text{sun}}, R')$. The discussion on electron energy showed that the energy response and the angular response are not related. Thus the response further simplifies to $\mathcal{P}(E, 1, R, \rightarrow \cos\theta'_{\text{sun}}, R') \cdot \mathcal{P}(E, R, \rightarrow E', R')$. The radial dependence has also been seen to be negligible. Therefore,

$$\mathcal{P} = \mathcal{P}(E, 1 \rightarrow \cos\theta'_{\text{sun}}) \cdot \mathcal{P}(E, R, \rightarrow E', R') \tag{5.8}$$

The values of the parameters for the various energies are shown in table 5.6. This table shows that the parameters change slowly as energy is changed. To obtain values of the angular distribution at intermediate energies, it is necessary only to interpolate between the values of the angular distribution found at the known energies.

Parameters Used in Equation 5.7			
Energy (MeV)	a_0	a_1	a_2
4	21.2	0.178	2.85
5	23.8	0.119	2.94
6	26.3	0.108	3.41
7	28.5	0.084	3.46
8	28.7	0.075	3.63
9	31.0	0.072	4.11
10	30.9	0.063	4.13
11	36.4	0.060	4.59
12	36.4	0.063	4.96
13	37.4	0.055	5.23
14	36.2	0.044	4.86

Table 5.6: The best fit parameters in equation 5.7 for the angular distribution are shown as a function of energy. The electron energy quoted is kinetic energy. The elastic fitter is used.

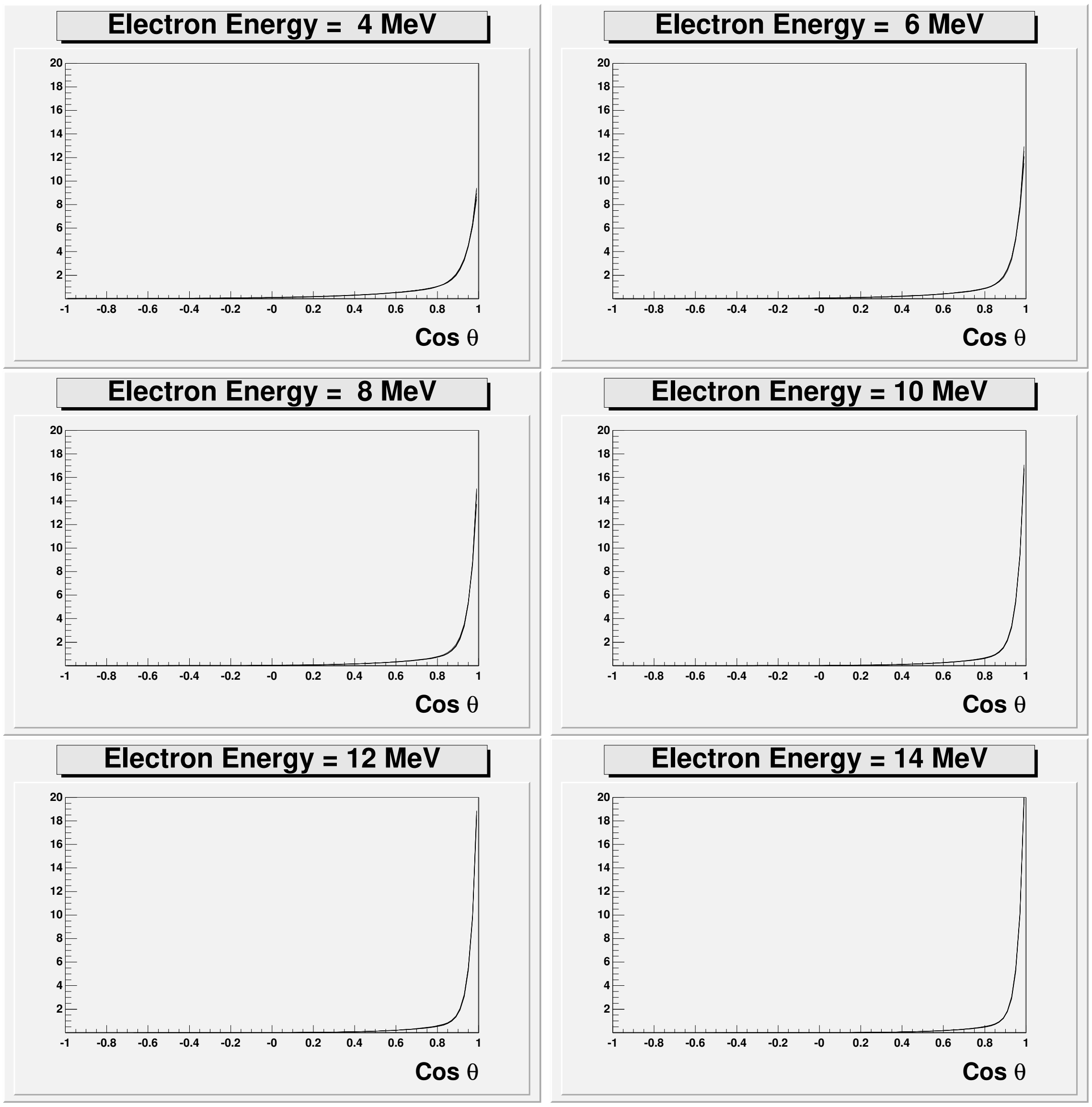

Figure 5.14: The fit to equation 5.7 over the energy range of interest for data from the simulation. The plot for each value of energy contains 5 curves for the radial bins. These curves are identical to high accuracy.

5.6 Summary

The angular resolution of the SNO detector is determined mostly by the multiple scattering of electrons as they travel through water. For 10 MeV electrons (kinetic), the production of Čerenkov light alone gave a value of $\cos\theta_{80}$ (with the time fitter) of 0.843. Including all effects of the detector gave a value of $\cos\theta_{80}$ of 0.831. For electrons with a kinetic energy of 6 MeV, the value of $\cos\theta_{80}$ only including the production of Čerenkovlight was 0.761. Including all effects of the detector changed the value to 0.739.

The optical properties have a small effect on the angular distributions. For the worst-case scenario of outward-going electrons at high radius, the value of $\cos\theta_{80}$ for the elastic fitter changes from 0.739 with acrylic attenuation to 0.765 without acrylic attenuation. There is no significant effect on the time fitter.

The effect of position resolution in the same worst-case scenario of outward-going electrons at high radius is to change the value of $\cos\theta_{80}$ for the elastic fitter on outward-going events from 0.739 (including position resolution) to 0.769 (perfect position resolution).

If all directions are averaged over, there is only a small change in angular resolution with radial position in the detector. The largest effect is for the elastic fitter at low energy. For 6 MeV electrons, the value at $\cos\theta_{80}$ is 0.765 at low radius and 0.739 at high radius. The change in $\cos\theta_{80}$ as a function of radius is 0.03 at 6 MeV and less than 0.02 for higher energies. For the time fitter, the effect is 0.01 at 6 MeV kinetic energy.

The effect of increasing the number of PMTs hit by increasing the efficiency of the PMTs is small. A 20% change in PMT efficiency changes the value of $\cos\theta_{80}$ by approximately 0.01 for both fitters.

The contributions to the uncertainty in angular resolution must be known to determine systematic uncertainties in the extraction of the ES signal. They are presented in table 5.7. The position resolution has a negligible effect compared to other uncertainties because the position resolution can itself be well understood.

Uncertainty in AR from Individual Sources		
Source	Uncertainty in $\cos\theta_{80}$	
	Time Fitter	Elastic Fitter
Soft Brem and δ-ray threshold in EGS	0.005	0.01
Uncertainty in acrylic attenuation	≤ 0.005	≤ 0.01
Parameters in elastic fitter		≤ 0.005

Table 5.7: The uncertainty in the value of $\cos\theta_{80}$ for the time and elastic fitters is shown for the largest sources of uncertainty.

Chapter 6

Verification of the Angular Resolution

This chapter describes a method of verification of the Monte Carlo calculation of the angular distribution for electrons through calibration with the ^{16}N source. The angular resolution of gamma rays is discussed and compared with that for electrons. The method to define the initial direction of a gamma ray is described. A simulation of the calibration is described along with cuts on the data necessary to obtain a good calibration of the angular resolution of 6.13 MeV gamma rays.

6.1 The Angular Resolution of Gamma Rays

A calibration of the angular distribution of electrons using 6.13 MeV gamma rays requires that the angular distribution for the gamma rays be similar to that for electrons. There is good basis to think *a priori* that this would be true. First, because the gamma-ray energy is large compared to the electron rest mass, Compton-scattered (and pair-produced) electrons are directed forward. Thus the Čerenkov light is being generated by an electron (or electrons) whose initial direction is nearly parallel to that of the gamma ray. Also, while the gamma-ray energy can in principle be be shared among many electrons, in the majority of events, one or two electrons carry most of the initial energy. Figure 6.1 shows the fraction of the original 6.13 MeV gamma energy that is transfered to the first and the first two electrons. Those events which converted by Compton scattering are plotted separately from those that converted by pair production. For pair production, the electron-positron pair is created by the gamma ray and thus some of the gamma ray's energy becomes the rest mass of the electron and positron. Because the kinetic energy is plotted, the spike in the pair production plot does not occur at 100% of the total energy, but rather at 83% of the total energy. Also, Compton scattering occurs more frequently than pair production (at this energy) as shown by the relative numbers of events in the two histograms.

The positions at which energy is transfered to electrons is also important because the event reconstruction assumes all the light comes from a point source. Figure 6.2 shows the distance from the gamma-ray source to the position at which energy was transfered to the first electron. This follows an exponential curve as indicated by the fit described in the figure. Also shown is the distance between the positions at which energy was transfered to the first electron and the second electron. (There are many counts in the first bin because pair production is included and in that case the electron and positron are created at the same position.) Because the distance between the first two electrons is almost always small when compared to the speed of light times the timing resolution of the PMTs, the multiple electrons have a small effect on the position reconstruction.

The direct way to show that the angular distribution of gamma rays is qualitatively similar to that of electrons is to perform simulations of gamma rays similar those described earlier for electrons. The results for 6.13 MeV gamma rays at the origin with isotropic direction are shown in figure 6.3. Superimposed is the histogram for 5 MeV electrons. For the time fitter, there is excellent agreement between the angular distribution for 6.13 MeV gamma rays and 5 MeV electrons. There is an interesting feature in the angular resolution for the gamma rays: $\cos\theta_{80}$ for the time fitter is greater than that for the elastic fitter. This was seen too for lower energy electrons. This suggests that light distribution for a gamma ray is somewhat less cone-like than for an electron and thus the energy at which the elastic fitter becomes better than the time fitter is higher for gamma rays than for electrons.

The less cone-like pattern of the Čerenkov light from gamma rays is clear when the angle of the emitted photons relative to the initial gamma direction is histogrammed. Figure 6.4 shows the normalized distributions for 6.13 MeV gamma rays and 5 MeV electrons. While the two

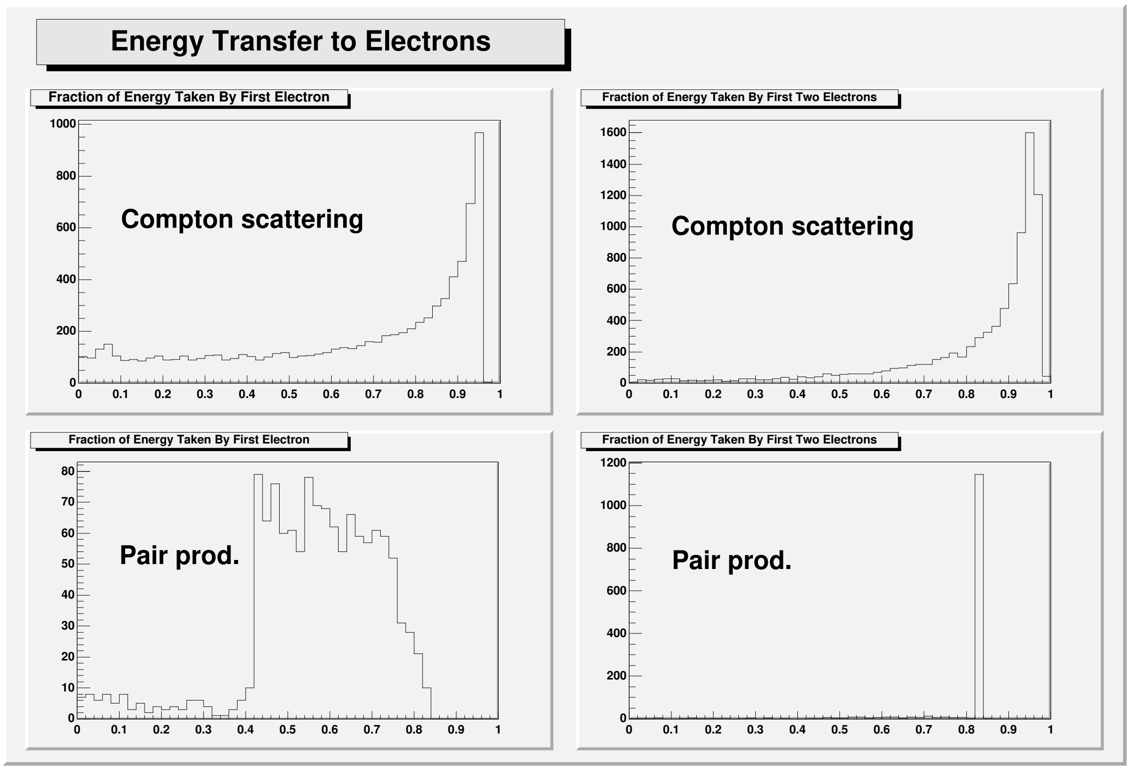

Figure 6.1: The energy transfer to electrons by 6.13 MeV gamma rays. This figure shows that most of the gamma-ray energy is transfered to the first two electrons. The reason for the spike in the pair-production distribution not being at unity is that only kinetic energy is considered for the electron-positron pair created. There is a small tail on the summed-energy plot for pair-production from radiative corrections.

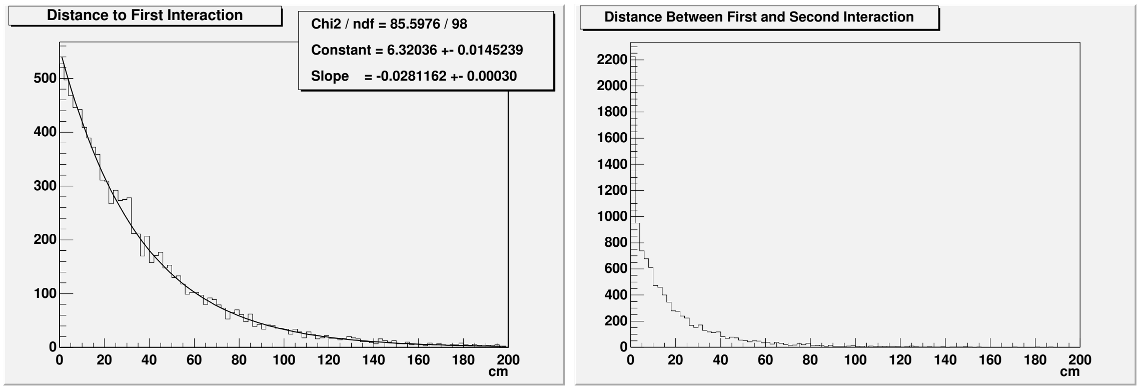

Figure 6.2: The distance from the gamma source to the first interaction is plotted with the distance between the locations at which energy was transferred to the first and second electron. Because the electron and positron in pair-production are created at the same point, there is a large number of counts in the first bin of the second plot.

distributions look similar, there is significantly less light on the cone for gamma rays than electrons.

6.2 Calibrating Angular Resolution With the ^{16}N Source

Calibration with the ^{16}N source requires that the initial direction of the gamma ray be known. Otherwise, it is impossible to define the dot product, $\vec{u} \cdot \vec{u}_{\rm fit}$. The gamma rays are emitted isotropically so the direction of the gamma ray, $\vec{u}$, is unknown. However, $\vec{u}$ can be determined with reasonable accuracy by taking the direction from the source, $\vec{s}$, to the reconstructed vertex, $\vec{x}_{\rm fit}$. Thus the angle θ is now defined by $(\vec{x} - \vec{s}) \cdot \vec{u}_{\rm fit}/|(\vec{x} - \vec{s})|$. If the source is at the center of the detector, $\vec{s} = 0$. Figure 6.5 shows the geometry for the source at the center of the detector.

For this technique to be accurate, the distance from the source to the reconstructed vertex must be large to reduce the effect of the finite position resolution blurring the angular distribution. The magnitude of the component of the reconstructed position perpendicular to the initial gamma-ray direction is plotted in figure 6.6. For events 100, 150 and 200 cm from the source, the distribution in position of figure 6.6 corresponds to the distributions in angle shown in figure 6.7.

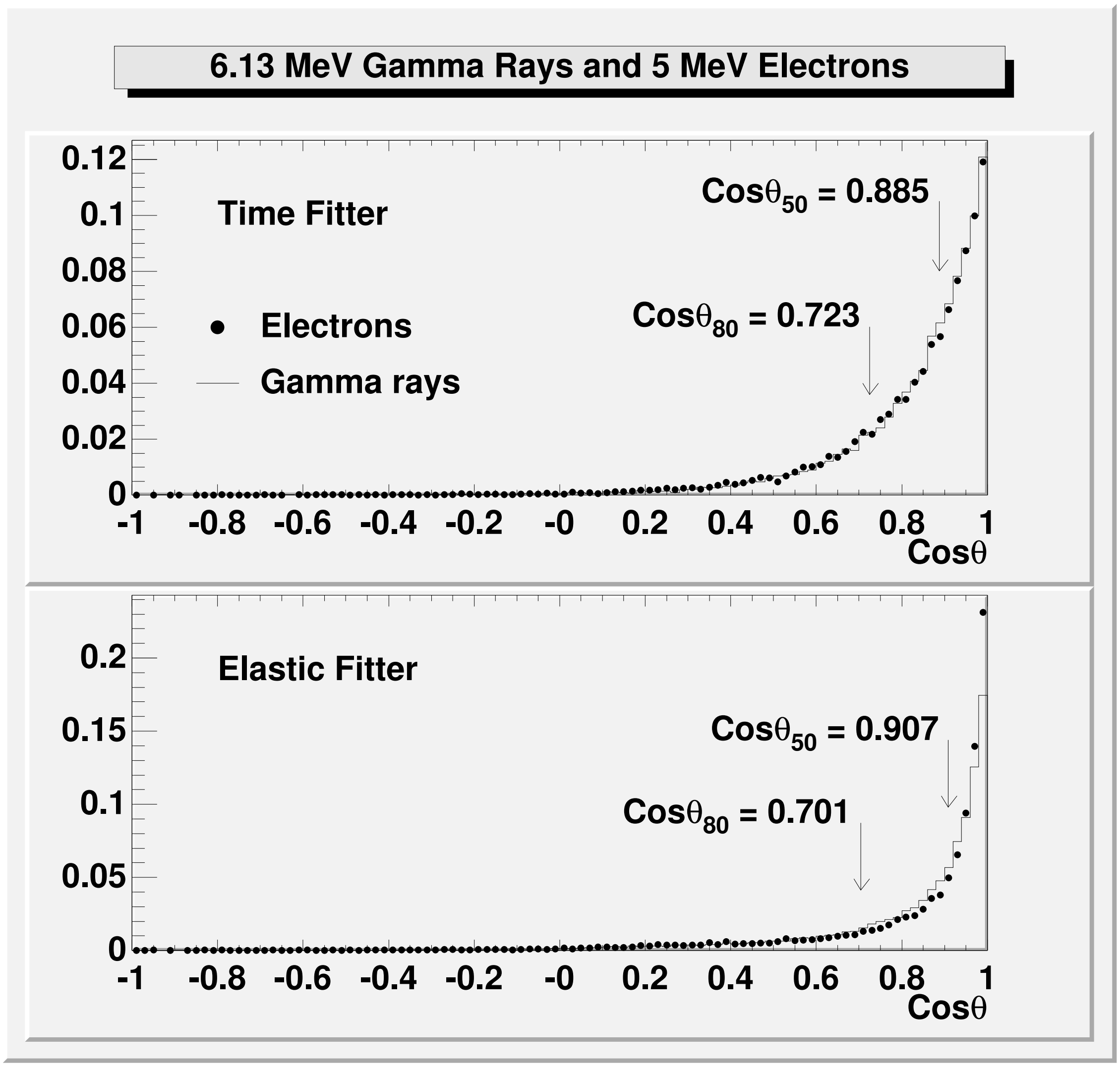

Figure 6.3: The angular distribution is shown for a simulation of 6.13 MeV gamma rays, along with the angular distribution for 5 MeV electrons.

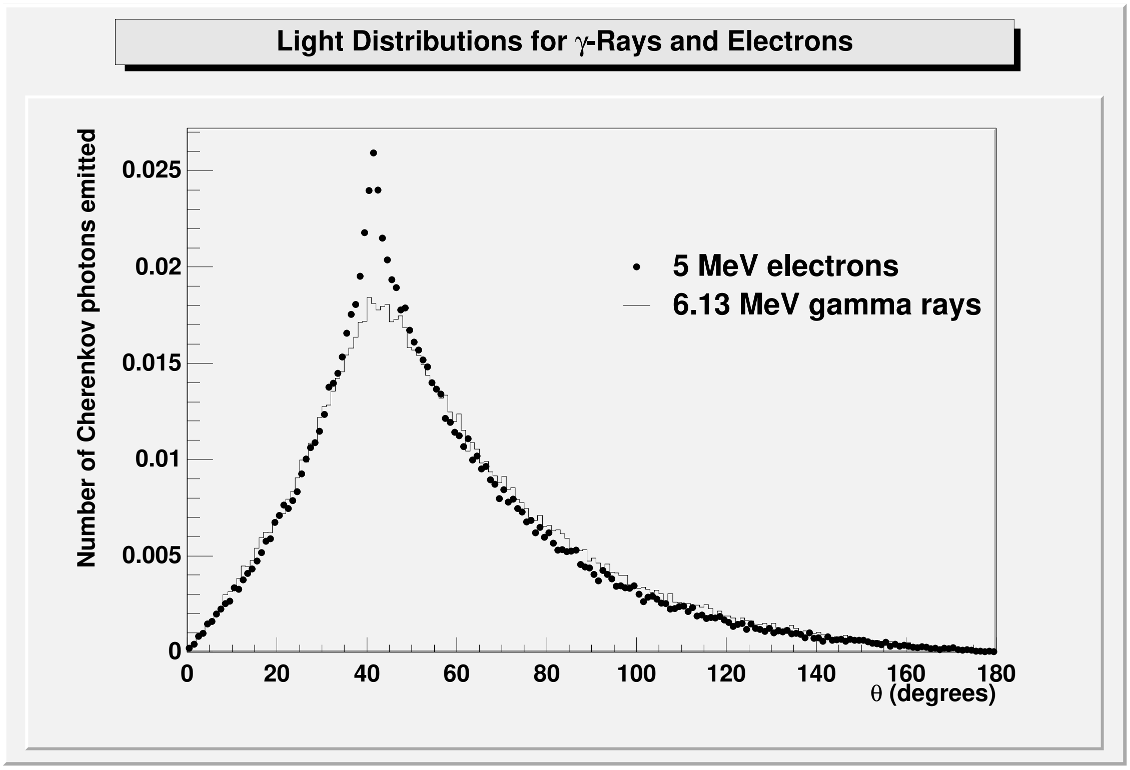

Figure 6.4: The angular distribution of Čerenkov emission is shown for 6.13 MeV gamma rays and 5 MeV electrons. The angle plotted is between the initial direction of the photon and the initial direction of the gamma ray or electron.

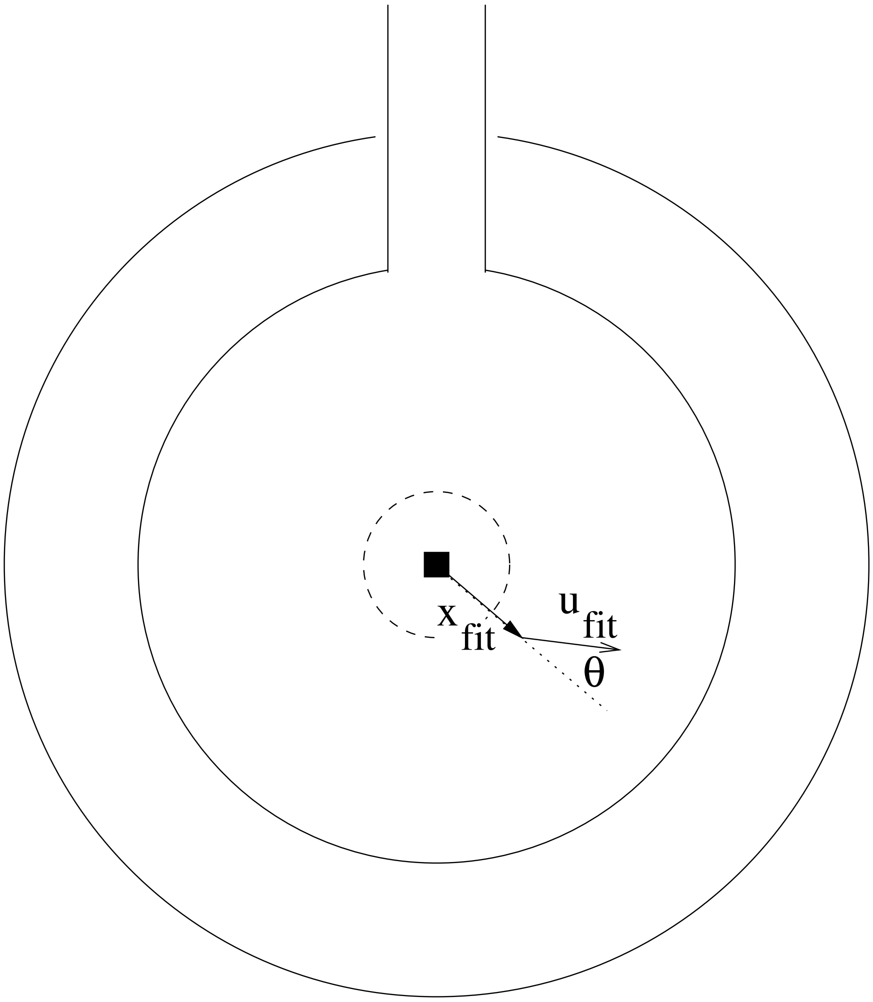

Figure 6.5: A schematic of the ^{16}N calibration at the center of the detector is shown. The dashed circle around the source shows a radius of 150 cm. The reconstructed position and direction are shown as well as the angle θ used for the angular distributions. The figure shows the acrylic vessel and its chimney and the PSUP.

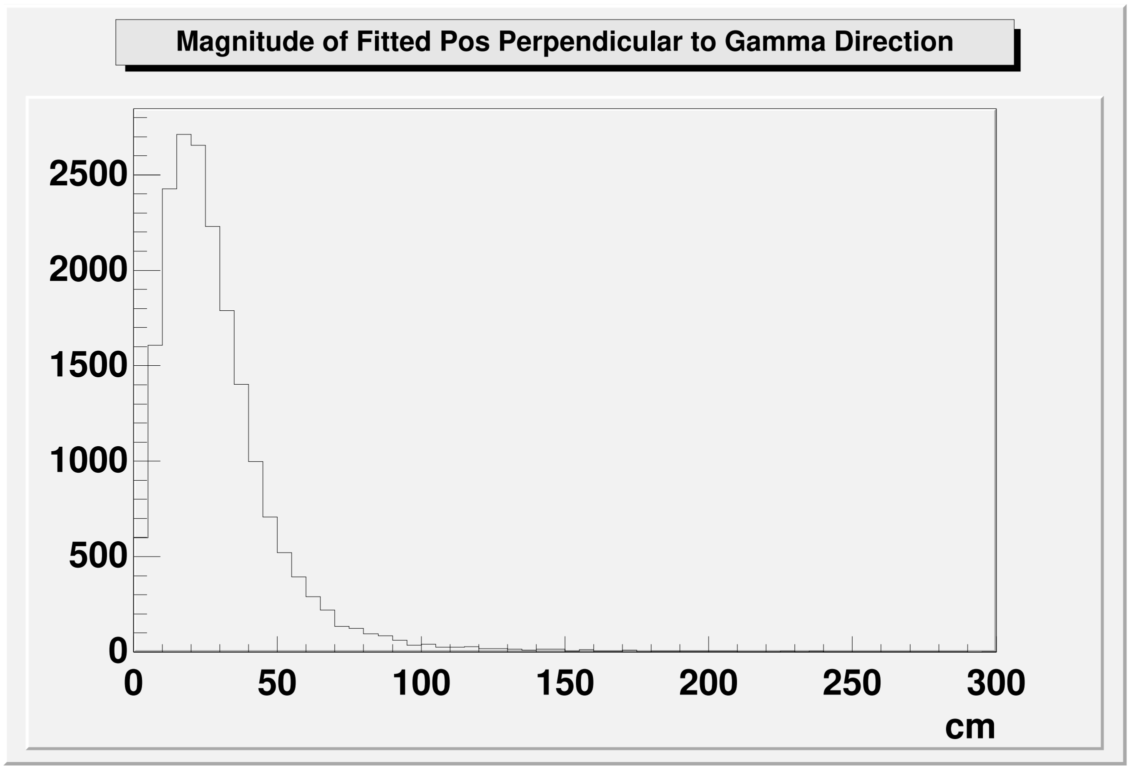

Figure 6.6: The magnitude of the component of reconstructed position perpendicular to the initial gamma-ray direction is shown for the simulation of 6.13 MeV gamma rays at the center of the detector.

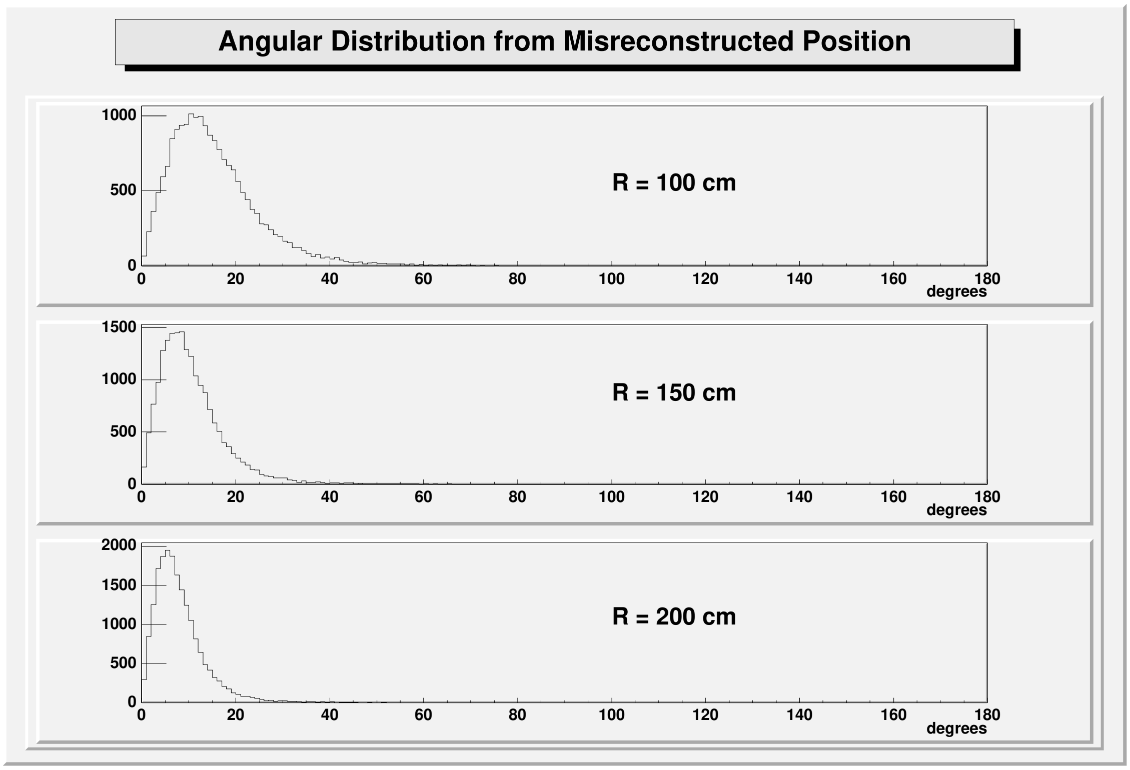

Figure 6.7: The angular distributions resulting from finite position resolution shown in figure 6.6 at three different distances from the source of gamma rays.

The effect of the finite position resolution can be found by performing a convolution of the angular distribution resulting from finite position resolution with the angular resolution of 6.13 MeV gamma rays. For a good calibration of angular resolution the difference between the convoluted spectrum and the angular distribution for 6.13 MeV gamma rays must be small. For the elastic fitter, the result of convolution is $\cos\theta_{80} = 0.633$ at 100 cm, $\cos\theta_{80} = 0.671$ at 150 cm, and $\cos\theta_{80} = 0.683$ at 200 cm. (The value before convolution was 0.701.)

6.2.1 Simulation of Calibration with the ^{16}N Source

A simulation of the ^{16}N source at the center of the detector was performed. This is similar to the simulation of 6.13 MeV gamma rays with the following exceptions: The geometry of the source is properly taken into account; the gamma rays are generated throughout the source gas volume (a cylinder of radius 4.78 cm and height 14.62 cm) and the thin stainless steel can and scintillator are included. As well, the branch resulting in a 7.1 MeV gamma ray is included. (This branch contributes 69 gamma rays for every 1000 6.13 MeV gamma rays.) Included also is the beta decay to the ground state resulting in a trigger, but no gamma ray. (Details of the source geometry and the rate of Bremsstrahlung emission are discussed in section 3.2.2 and in [Ha99].)

The events from the simulation were reconstructed using the time and elastic fitter. The ^{16}N source gives an EXT-ASYNC trigger to the electronics. This defines a start time for the event. (There is an arbitrary offset which is a function of relative timing of the ^{16}N trigger in the electronics and the PMT signals.) Figure 6.8 shows a scatter plot of the distance from the source to the reconstructed position of the events and the reconstructed time of the events. This plot includes all events with NHIT greater than 20. There is a huge majority of events with r_{fit} and t_{fit} linearly related with the reciprocal of the speed of light as the slope. There is a smaller branch with a negative slope which corresponds to events reconstructing on the opposite side of the source relative to the gamma direction. The smaller branch was cut by insisting that $t_\gamma \equiv t_{\text{fit}} - R_{\text{fit}}/c > 118$. (See figure 6.9 for a histogram of t_γ.) Because the gamma source is at the center of the detector, R_{fit} is both the radial position of the reconstructed event in the detector and the distance from the source to the

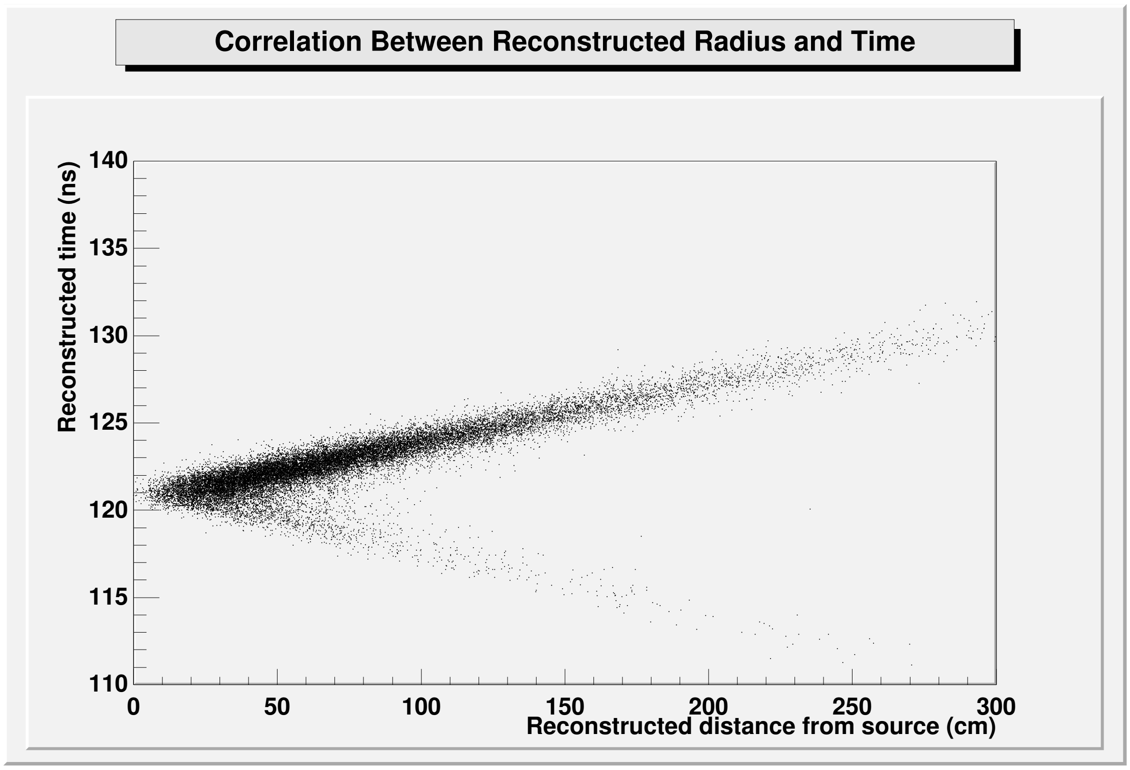

Figure 6.8: The relationship between fitted radius and time is shown. Most events have tightly correlated fits in radius and time. There is a small branch corresponding to events which reconstruct on the opposite side of the source to the direction of the original gamma ray. The offset on the time axis is arbitrary.

reconstructed position. (See figure 6.5.) What is of interest for t_γ is the distance from the source because that is what affects the relative time of the event and the time of the ^{16}N-source trigger.

Angular distributions for the ^{16}N simulations were taken for various cuts on the distance from the source to the reconstructed position of the event. These distributions and a histogram of the distance are shown for the time and elastic fitters in 6.10 and 6.11. As the distance cut was increased the distributions narrowed considerably.

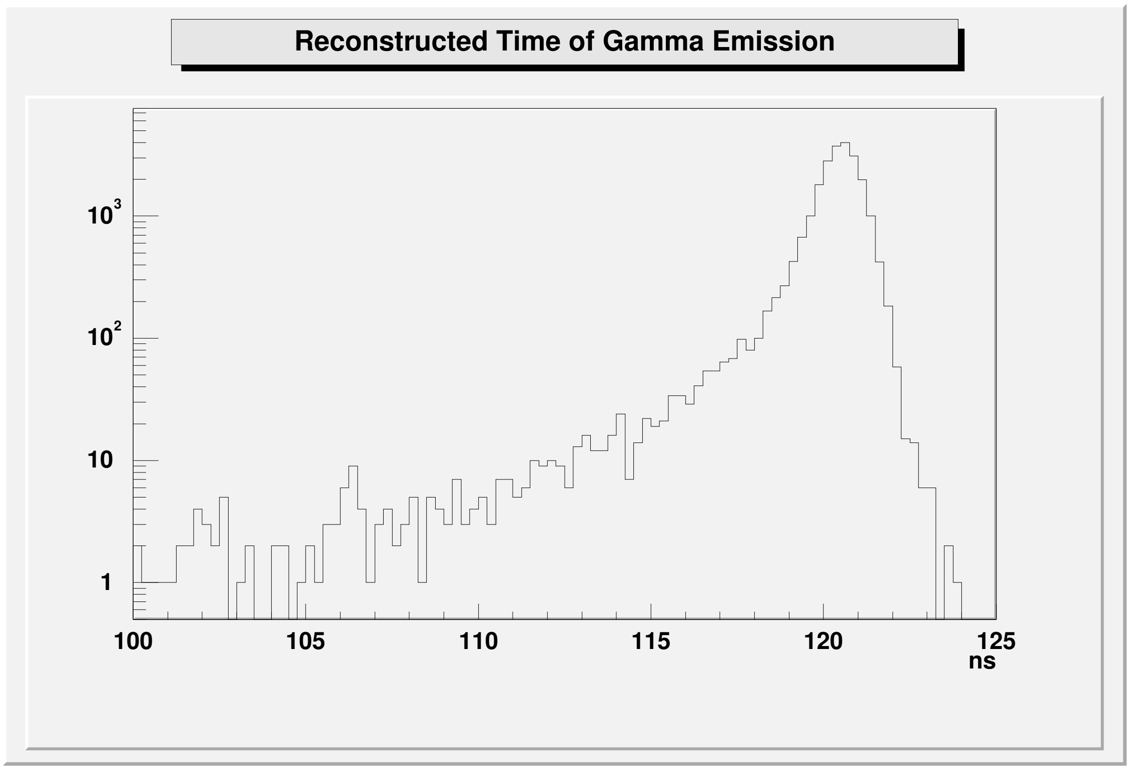

Figure 6.9: The distribution of t_γ for simulation of the ^{16}N calibration. The definition of t_γ is presented in the text.

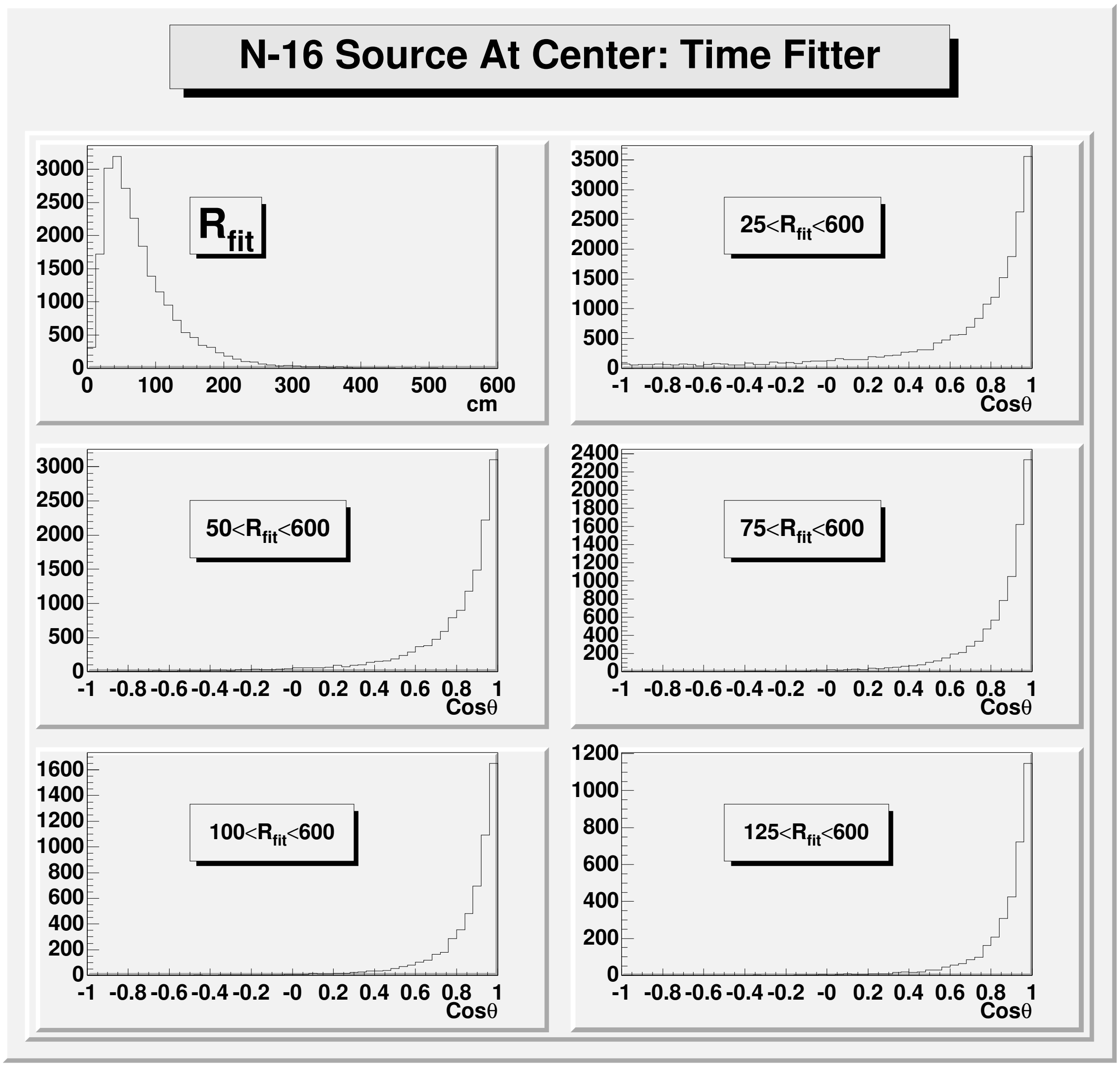

Figure 6.10: The profile of fitted radial position and 5 angular distributions for a simulation of the ^{16}N source at the center of the vessel. The time fitter is used. As the cut on distance from the source to the reconstructed position increases, the angular distributions narrow considerably.

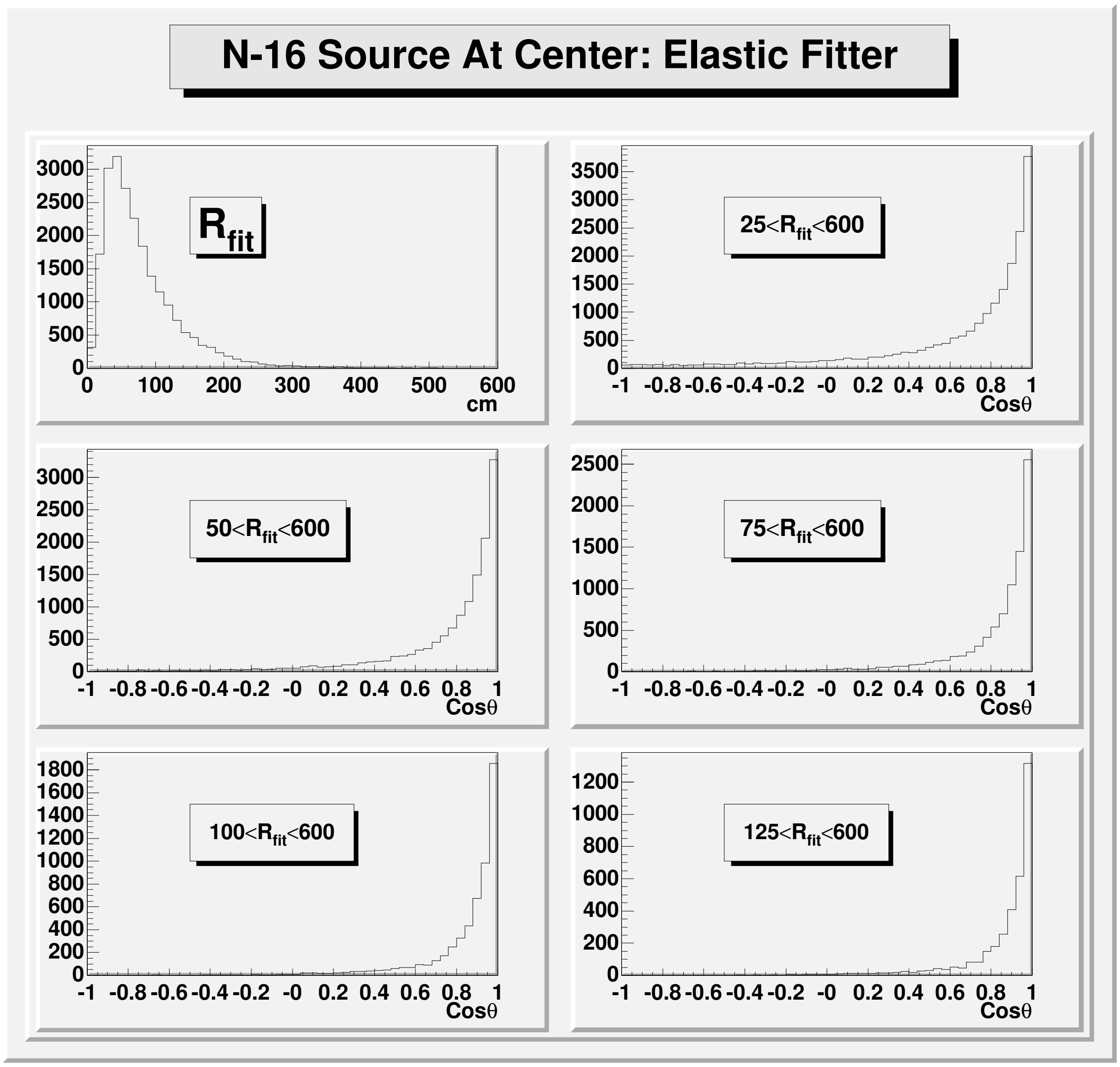

Figure 6.11: The profile of fitted radial position and 5 angular distributions for a simulation of the ^{16}N source at the center of the vessel. The elastic fitter is used. As the cut on distance from the source to the reconstructed position increases, the angular distributions narrow considerably.

6.2.2 Quantitative Comparison of ^{16}N Calibration to Gamma-Ray Simulation

A quantitative comparison was made of the angular distributions as a function of the cut on the distance of the fit from the source and the simulation of 6.13 MeV gamma rays. The following discussions use the notation that the angular distributions for the "^{16}N" events were obtained using $\vec{x}_{\rm fit} \cdot \vec{u}_{\rm fit}/|\vec{x}_{\rm fit}|$ and that the distributions for"gamma-ray" events were obtained using $\vec{u} \cdot \vec{u}_{\rm fit}$.

The values of $\cos\theta_{80}$ and $\cos\theta_{50}$ are plotted for both fitters as a function of radial cut in figure 6.12. As expected, at low radius, the values of $\cos\theta_{80}$ and $\cos\theta_{50}$ are worse than that for the gamma rays. As the cut increases allowing only events that reconstruct farther from the source, the values of $\cos\theta_{80}$ and $\cos\theta_{50}$ improve. But once the cut allows only events reconstructing farther than 100 cm from the source, the angular resolution from the calibration is better than that for gamma rays.

The size of the tail of the angular distributions can also be studied. The size of the tail is defined as the ratio of the number of counts between $-1 < \cos\theta < 0.6$ and the total number of counts in the entire distribution. This was done as a function of radial cut. The ratio is plotted in figure 6.13. The size of the tail is large with a low radial cut because the initial direction of the gamma ray is poorly defined by the reconstructed position. At high radial cuts the size of the tail approaches a constant value. However, this value is much smaller than that of 6.13 MeV gamma rays when the variable plotted was $\vec{u} \cdot \vec{u}_{\rm fit}$. The angular resolution from the calibration appears to be better than it should be.

6.2.3 Why Angular Resolution in the Calibration is so Good

The size of the tail, $\cos\theta_{80}$, and $\cos\theta_{50}$ have a range of values depending on the radial cut used. There are three reasons (apart from using the reconstructed position to determine the gamma-ray direction) why this might be expected. First, the source is of finite size, thus introducing an uncertainty in the gamma-ray direction via the term $\vec{s}$ (the position of the source) which was taken to be uniformly zero in the previous discussion. The source is 9.6 cm in diameter and 14.62 cm high. Thus the maximum distance from the center from which a gamma could originate is 9 cm.

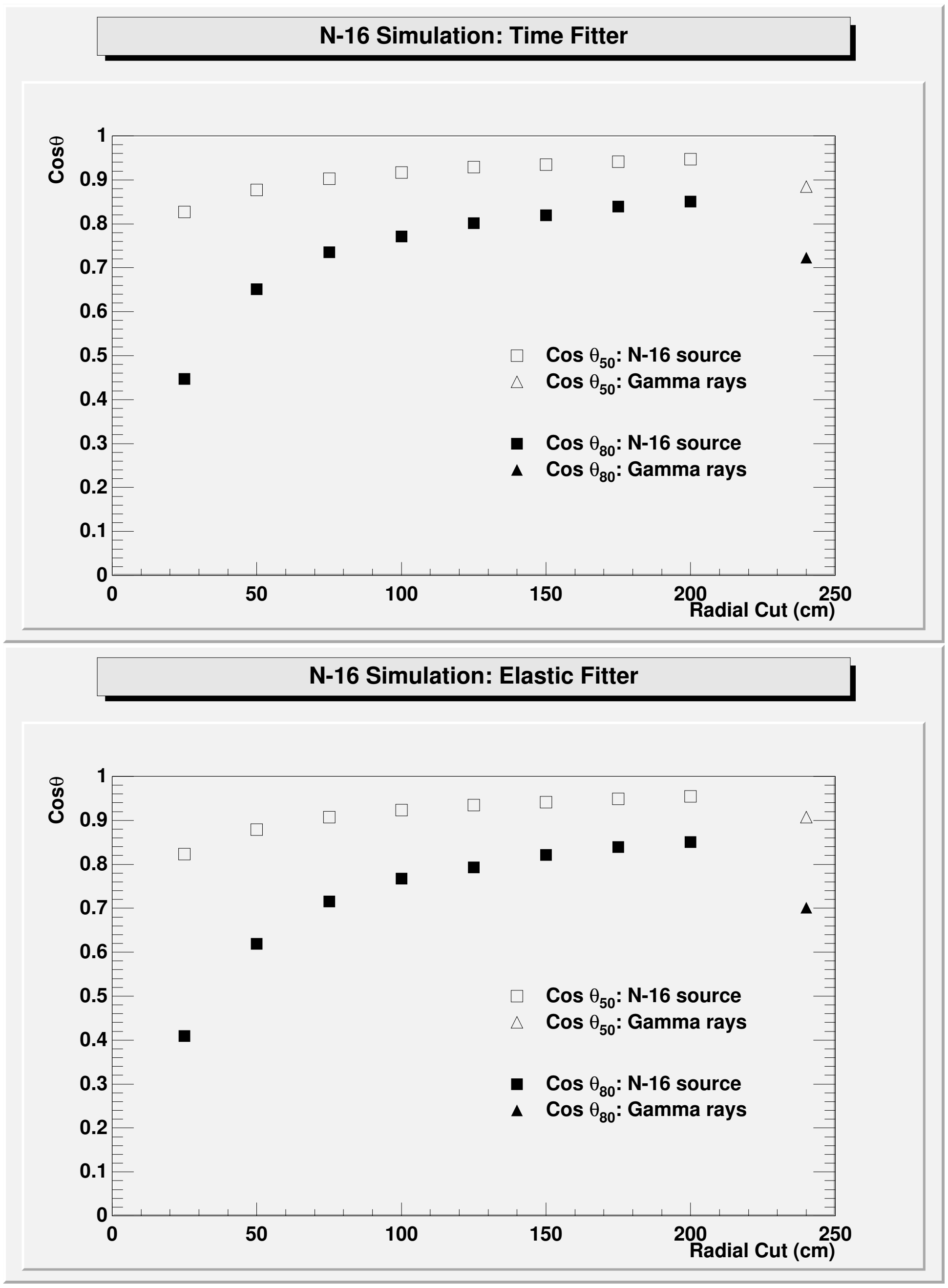

Figure 6.12: The values of $\cos\theta_{80}$ (circles) and $\cos\theta_{50}$ (squares) are shown as a function of radial cut for the ^{16}N source. $\cos\theta_{80}$ and $\cos\theta_{50}$ for 6.13 MeV gamma rays (for which no radial cut was imposed and for which the initial direction of the gamma ray was taken from the Monte Carlo, not reconstructed position) are shown for comparison.

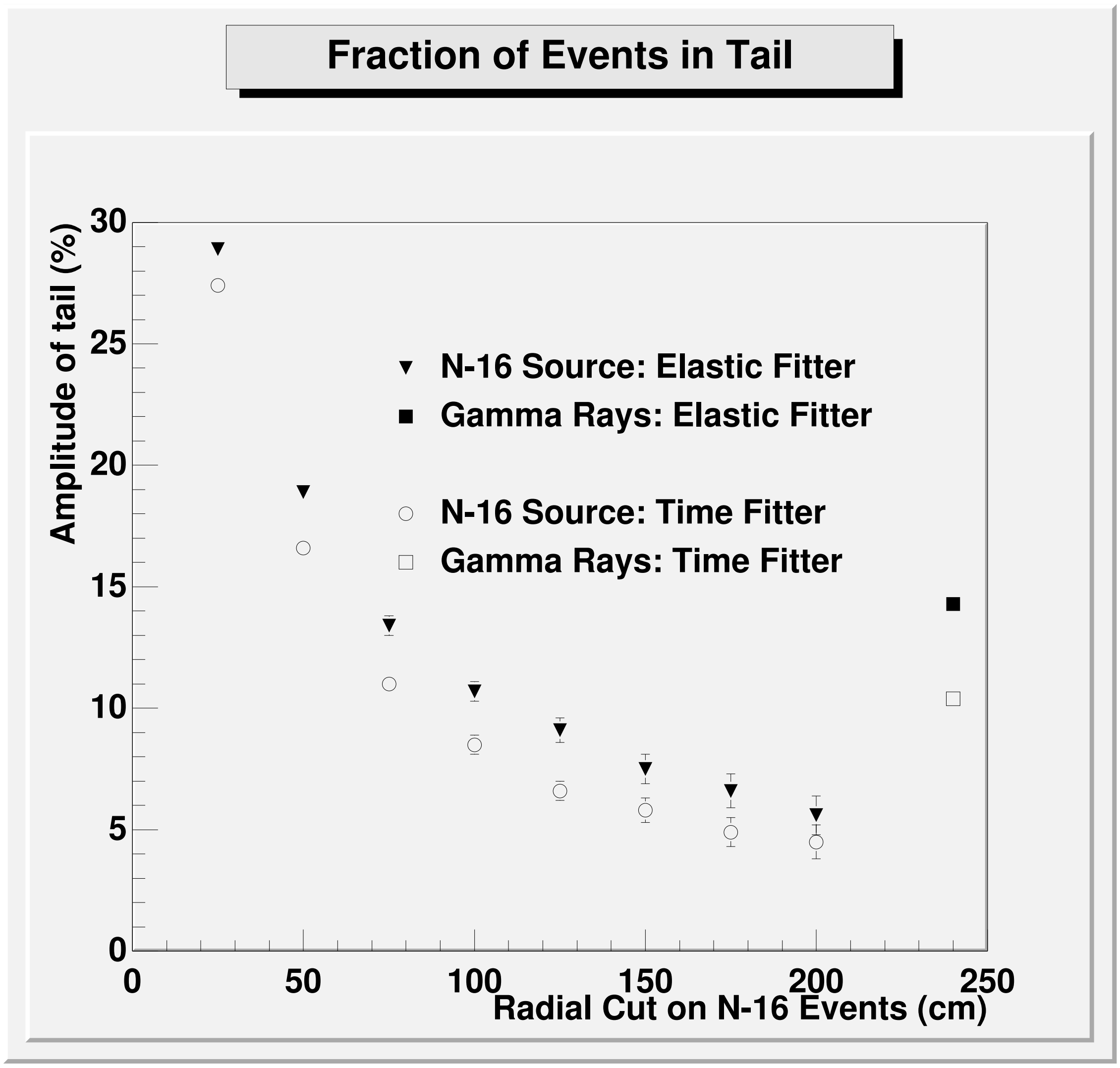

Figure 6.13: The percentage of events in the tail reason of the N-16 angular distribution is plotted as a function of the radial cut imposed. The size of the tail for 6.13 MeV gamma rays (for which no radial cut was imposed and for which the initial direction of the gamma ray was taken from the Monte Carlo, not reconstructed position) is shown on the same plot for comparison.

If a radial cut is imposed at 100 cm, then the maximum angle of deviation is 5.0 degrees. This is negligible compared to both the effect of position resolution and the angular distribution for gamma rays and can be neglected. (It also has the effect of making the angular distribution broader, not narrower.)

The second effect is that the ^{16}N source has two branches of interest: one emits a 6.13 MeV gamma ray and the other a 7.11 MeV gamma ray. For every one-thousand 6.13 MeV gamma rays there will be sixty-nine 7.11 MeV gamma rays. While the strong energy dependence of angular resolution suggests this will contribute to the difference between 6.13 MeV gamma rays and the ^{16}N source, the small size of the admixture causes this to have little effect.

The third difference is caused by the radial cut. There are two classes of events that reconstruct farther from the source than the radial cut: those which genuinely did convert far from the source and those which converted near the source but reconstructed far from the source. This is important because, as discussed in section 5.1.3, events which misreconstruct in position have better angular resolution, on average, than those which reconstruct well in position.

6.2.4 Cuts to Reduce Misreconstructed Events

Cuts must be found to eliminate those events which convert close to the source but reconstruct far from the source. This was studied starting with the ensemble of events that had NHIT > 20. The NHIT distribution for a small sample of events is shown in figure 6.14. (The high-statistics simulations described here cut all events with NHIT < 20 to reduce computational time and disk usage.)

The high-statistics runs were studied with a cut on the distance from the source to the reconstructed position. Distances of 100 cm, 125 cm, 150 cm, 175 cm, and 200 cm were studied. For each cut on reconstructed distance, histograms were plotted of the actual distance from the source at which the gamma ray converted. The position at which the gamma ray converted was found using the following definition. If the gamma ray converted by pair production, the location of the pair production was used as the "real" location of the event, $\vec{x}_{\mathrm{real}}$. If the gamma-ray converted by

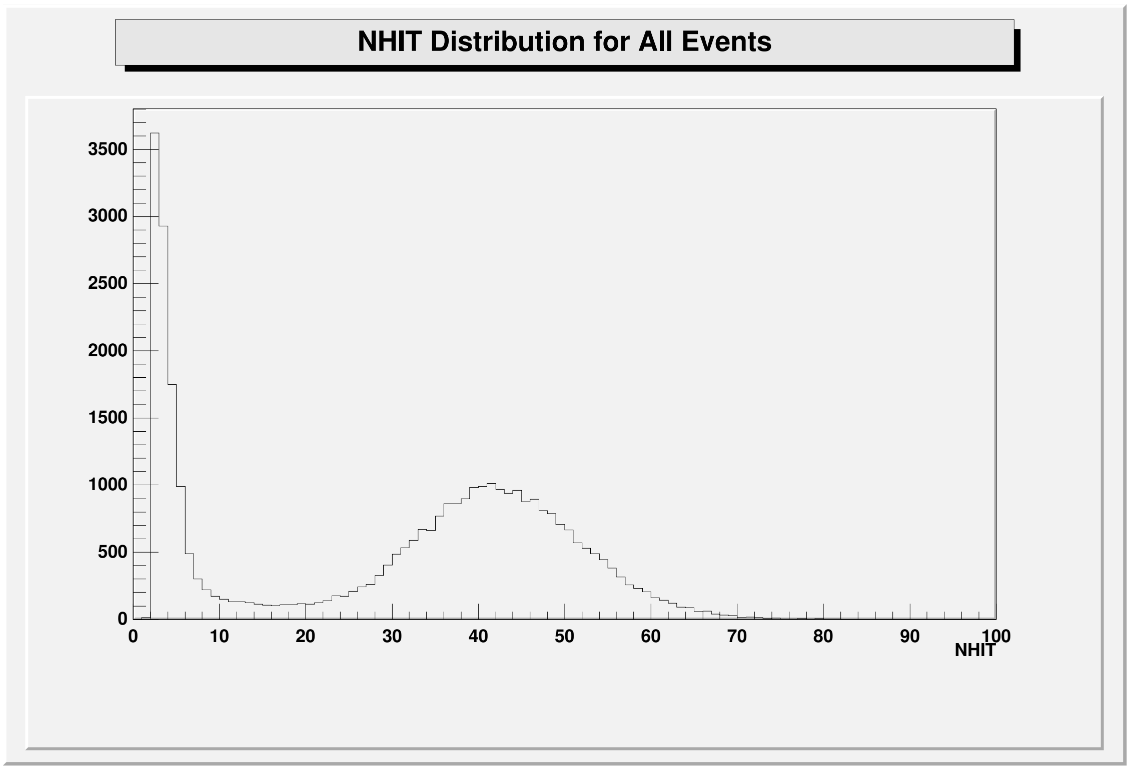

Figure 6.14: The NHIT distribution is shown before application of cuts for a subset of the ^{16}N simulations.

Compton scattering, the location of each scatter, $\vec{x}_\imath$, generating an electron with more than 1 MeV (total) energy was averaged. The average was weighted by the out-going electron energy according to the following formula:

$$\vec{x}_{\text{real}} = \frac{\sum_\imath (E_{tot} - 1)\vec{x}_\imath}{\sum_\imath (E_{tot} - 1)} \tag{6.1}$$

where E_{tot} is measured in MeV. The weights in the average are chosen to approximate the amount of Čerenkov light generated by each electron in the sum.

Figure 6.15 shows histograms of distance from the source to the real position at which the gamma rays converted for different cuts on the reconstructed distance from the source. The most heavily shaded histograms have no cuts imposed on the data. There are many more misreconstructed events than properly reconstructed events. The requirement, $t_\gamma > 118$, (see figure 6.9) removes a small fraction of the events at low radius. The second histogram in figure 6.15 shows the effect of this cut.

The next cut used the fitter itself to determine if an event was likely to be misreconstructed or well-reconstructed. Events which the time fitter badly misreconstructs radially would be expected to have a shallow χ^2 surface as a function of radial position. Because the time fitter produces a covariance matrix when it calculates the fitted position, the uncertainty in radial position, σ_R, can be calculated. This is a direct measure of the shape of the χ^2 surface. A histogram of σ_R is presented in figure 6.16. Events with $\sigma_R > 30$ were rejected. The third histogram in each plot in figure 6.15 includes events which pass this cut and the cut on t_γ.

The final cut on the data was to insist that the events reconstruct in the analysis window with the quad fitter. The lightest histogram for each radial cut in figure 6.15 has all cuts imposed. With all the cuts applied an analysis was made of the angular distributions and values of $\cos\theta_{80}$ and $\cos\theta_{50}$ were extracted. As well, the size of the tails are plotted. The results are shown in figures 6.17, 6.18, and 6.19.

These results are more satisfactory. The size of the tail approaches an asymptotic value as the distance from the source is increased. This value is approximately equal to the size of the tail from simulation of 6.13 MeV gamma rays determined from the distribution of $\vec{u} \cdot \vec{u}_{\text{fit}}$. The values of

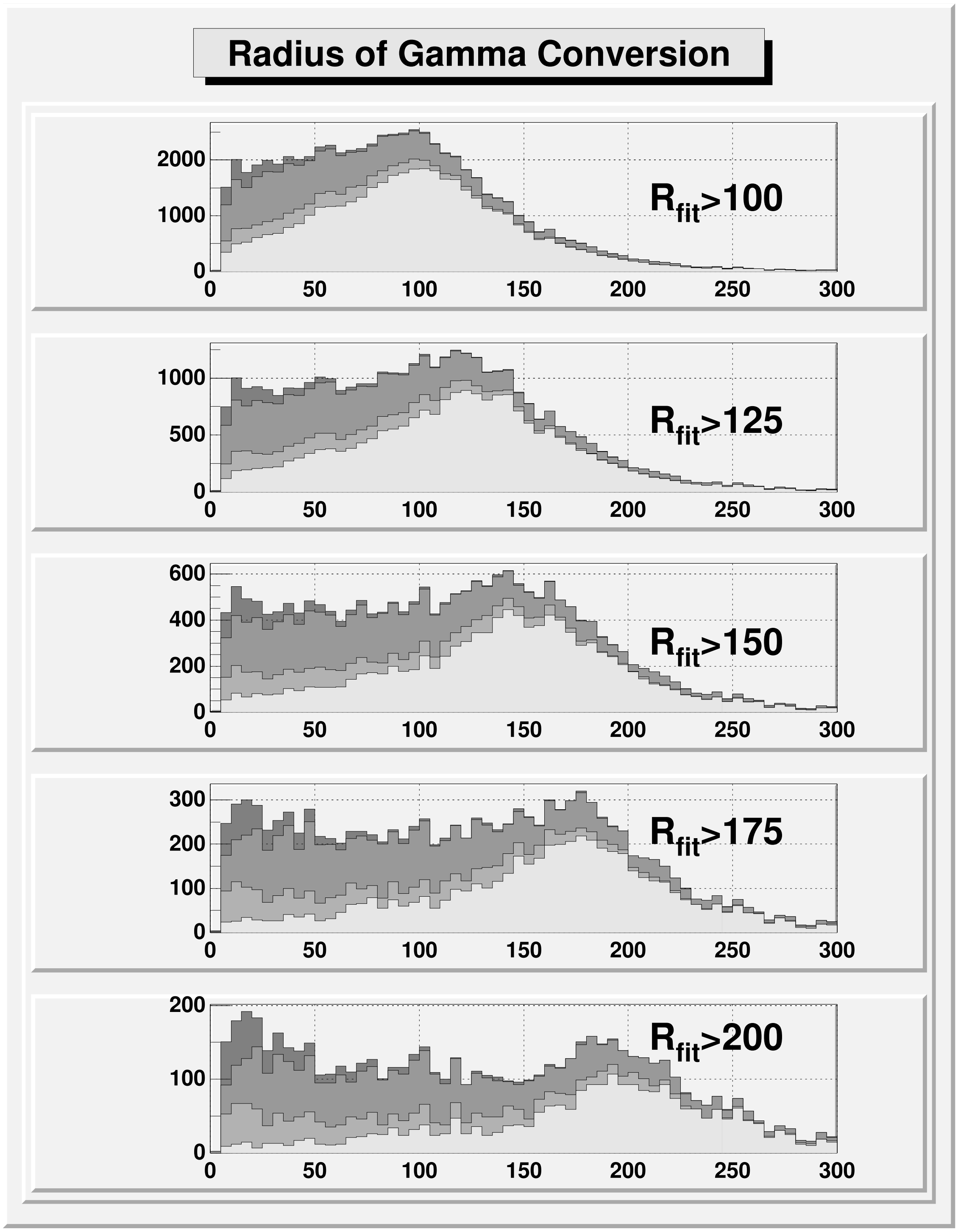

Figure 6.15: The distance between the ^{16}N source and the position at which the gamma ray really converted is histogrammed for events which reconstructed farther than a given distance from the source. The cuts on reconstructed distance, $R_{\rm fit}$, are shown on each plot. The most heavily shaded histogram has no cuts on the data. The next darkest histogram has the cut on t_γ imposed. The third histogram is for events which also passed the cut on σ_R. The lightest histogram is for events which also reconstructed farther than the given distance from the source with the quad fitter.

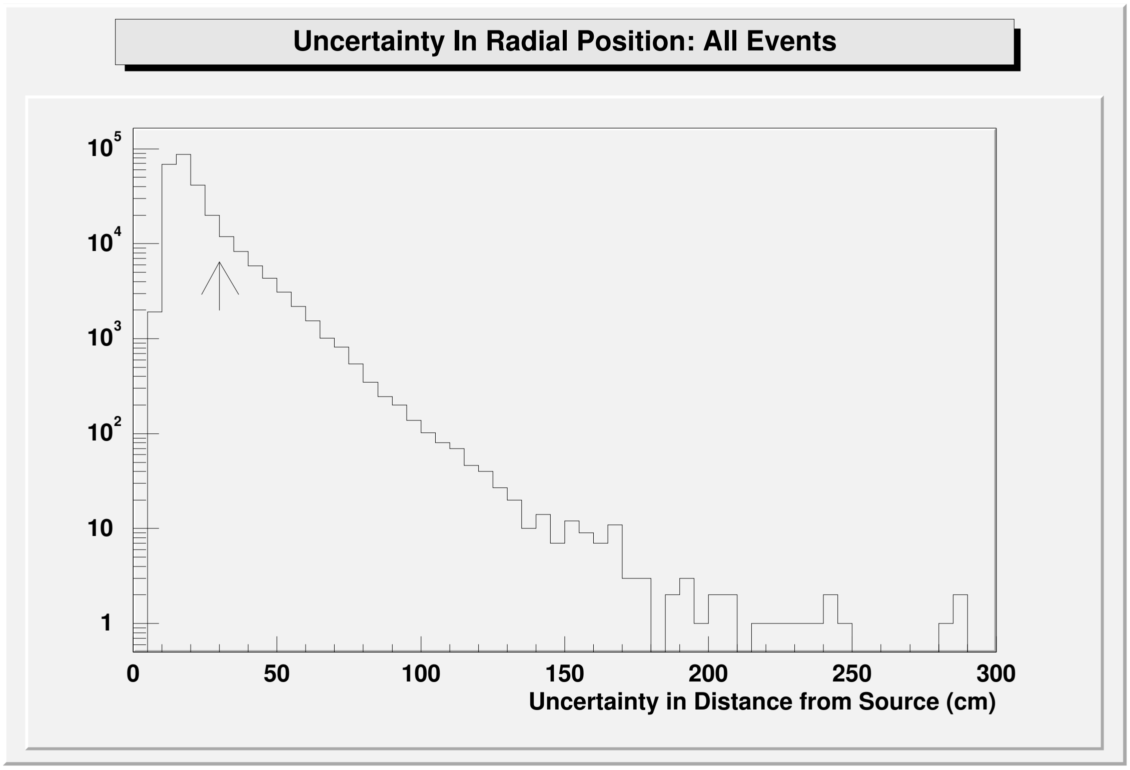

Figure 6.16: The uncertainty in the radial fit position from the time fitter. The arrow at 30 cm indicates where the cut was made on the data. This histogram was made for all events with NHIT > 20 before the application of any cuts.

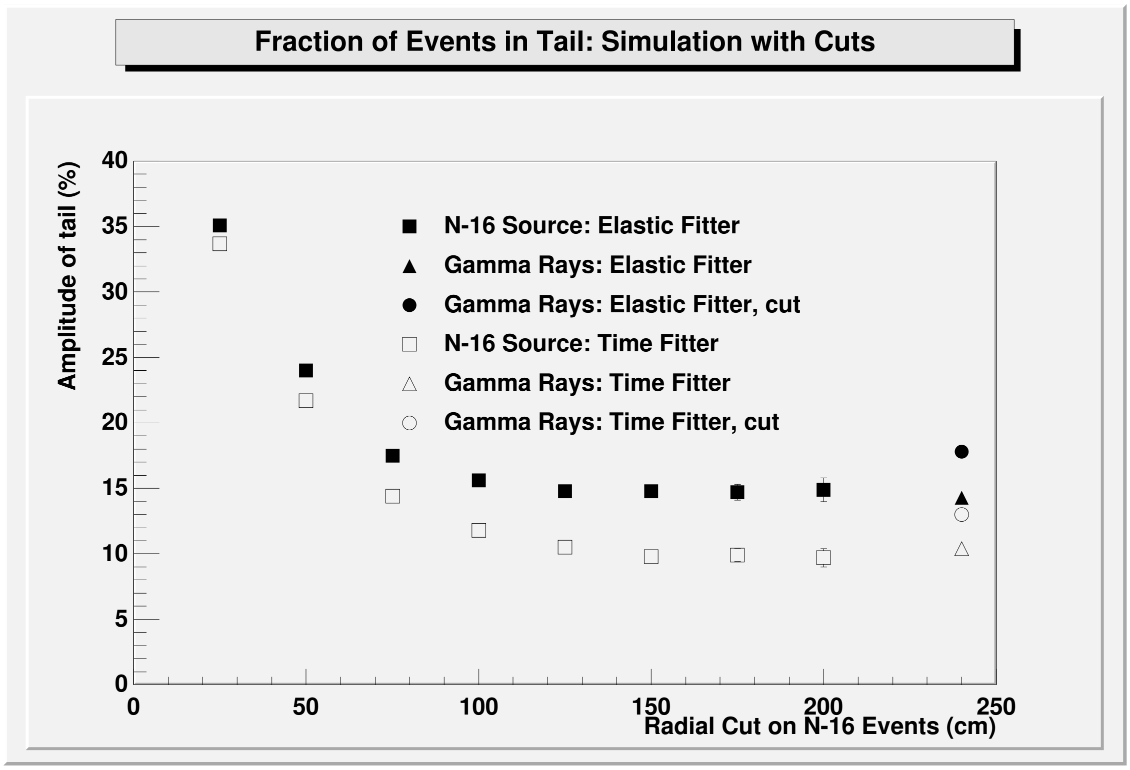

Figure 6.17: The size of the tail as a function of radial cut for data that has been passed through the cuts on σ_R, NHIT, and t_γ, and the quad fitter. The points for "cut" 6.13 MeV gamma rays refers to the gamma rays which have passed the cut on σ_R. (See section 6.2.5.)

$\cos\theta_{80}$ and $\cos\theta_{50}$ agree much better with that for the simulation of gamma rays as well.

6.2.5 The Cut on σ_R and Gamma Rays and Electrons

To remove misreconstructed events, a series of three cuts was imposed on the data. The most important cut was to reject events with σ_R greater than 30. The effect of this cut on 6.13 MeV gamma rays and 7 MeV electrons was studied. For both gamma rays and electrons, the particles were generated with isotropic directions at the center of the detector. The usual histograms of $\vec{u} \cdot \vec{u}_{\rm fit}$ were made for both the elastic and time fitter for those events which reconstructed within 600 cm of the origin. Histograms were also made of $\vec{u} \cdot \vec{u}_{\rm fit}$ for those events that had $\sigma_R < 30$.

Figure 6.20 shows the result for 6.13 MeV gamma rays. The behavior is as expected. The effect

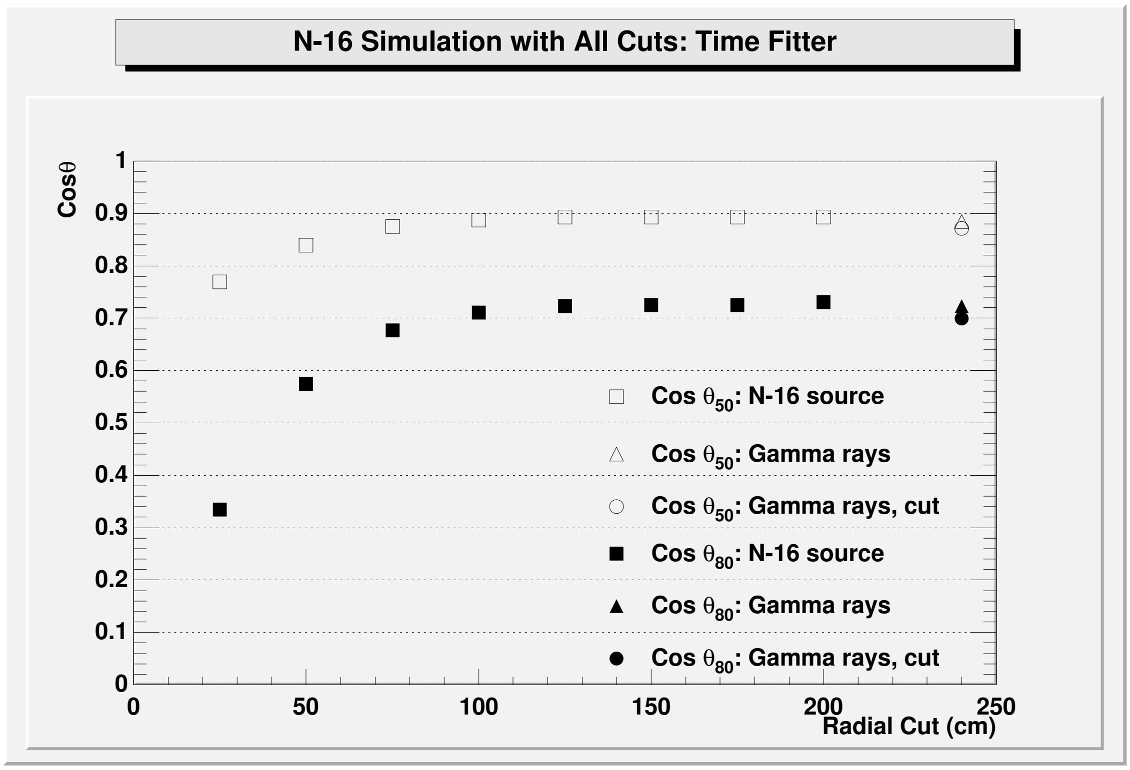

Figure 6.18: The angular resolution as a function of radial cut for data that has been passed through the cuts on σ_R, NHIT, and t_γ, and the quad fitter. The time fitter is used. The points for "cut" 6.13 MeV gamma rays refers to the gamma rays which have passed the cut on σ_R. (See section 6.2.5.)

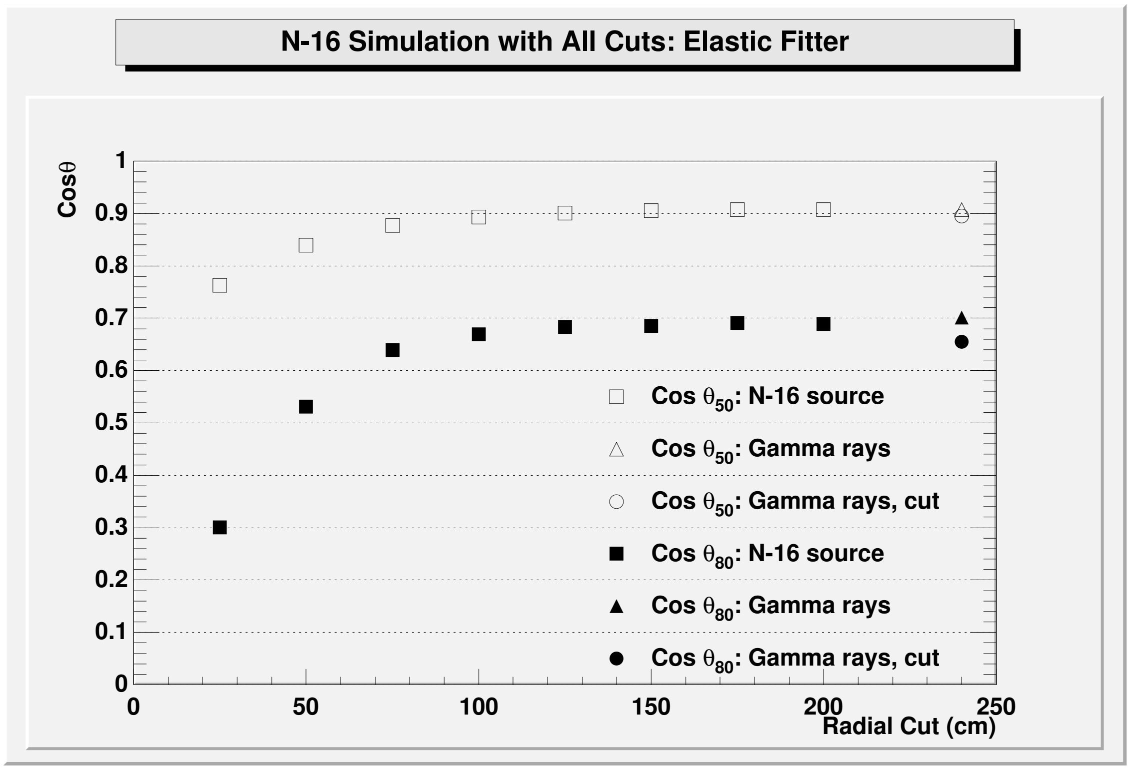

Figure 6.19: The angular resolution as a function of radial cut for data that has been passed through the cuts on σ_R, NHIT, and t_γ. The elastic fitter is used. The points for "cut" 6.13 MeV gamma rays refers to the gamma rays which have passed the cut on σ_R. (See section 6.2.5.)

σ_R **and 6.13 MeV** γ **rays and 7 MeV** e^-					
		Time Fitter		Elastic Fitter	
		$\cos\theta_{80}$	$\cos\theta_{50}$	$\cos\theta_{80}$	$\cos\theta_{50}$
γ rays	uncut	0.723	0.885	0.697	0.907
	cut	0.699	0.871	0.665	0.895
electrons	uncut	0.759	0.903	0.797	0.951
	cut	0.737	0.887	0.765	0.947

Table 6.1: The values of $\cos\theta_{80}$ and $\cos\theta_{50}$ are shown for simulations of 6.13 MeV gamma rays and 7 MeV (kinetic) electrons before and after the cut on σ_R. The values before application of the cuts may be slightly different than previous values because a new simulation was performed.

of the cut is largest near $\cos\theta = 1$. The cut removes those events which have poor radial position reconstruction and these events have, on average, excellent angular resolution. There are 19411 events before cuts and 15586 after cuts. The cut removes 19.7% of events.

The angular distributions for 7 MeV electrons are shown in figure 6.21. The effect of the cut on the reconstruction of electrons is clear in figure 6.22. The cut has largest relative effect on events which reconstruct poorly. There are 19709 events before the cut and 16069 events after the cut. The cut removes 18.5% of events. The value of $\cos\theta_{80}$ and $\cos\theta_{50}$ are shown in table 6.1 for both 6.13 MeV gamma rays and 7 MeV electrons. The largest change is 0.032. The cut on σ_R causes a small change on the angular resolution of gamma rays and electrons.

The impact of the cuts on the fraction of events in the tail of the distribution is larger than the effect on $\cos\theta_{80}$ and $\cos\theta_{50}$. The reason is that the cuts leave the tail undisturbed while removing events from the forward part of the distribution. Thus the size of the tail for 6.13 MeV gamma rays increases from 14.3% of the distribution to 17.8% for the elastic fitter and from 10.4% to 13.0% for the time fitter.

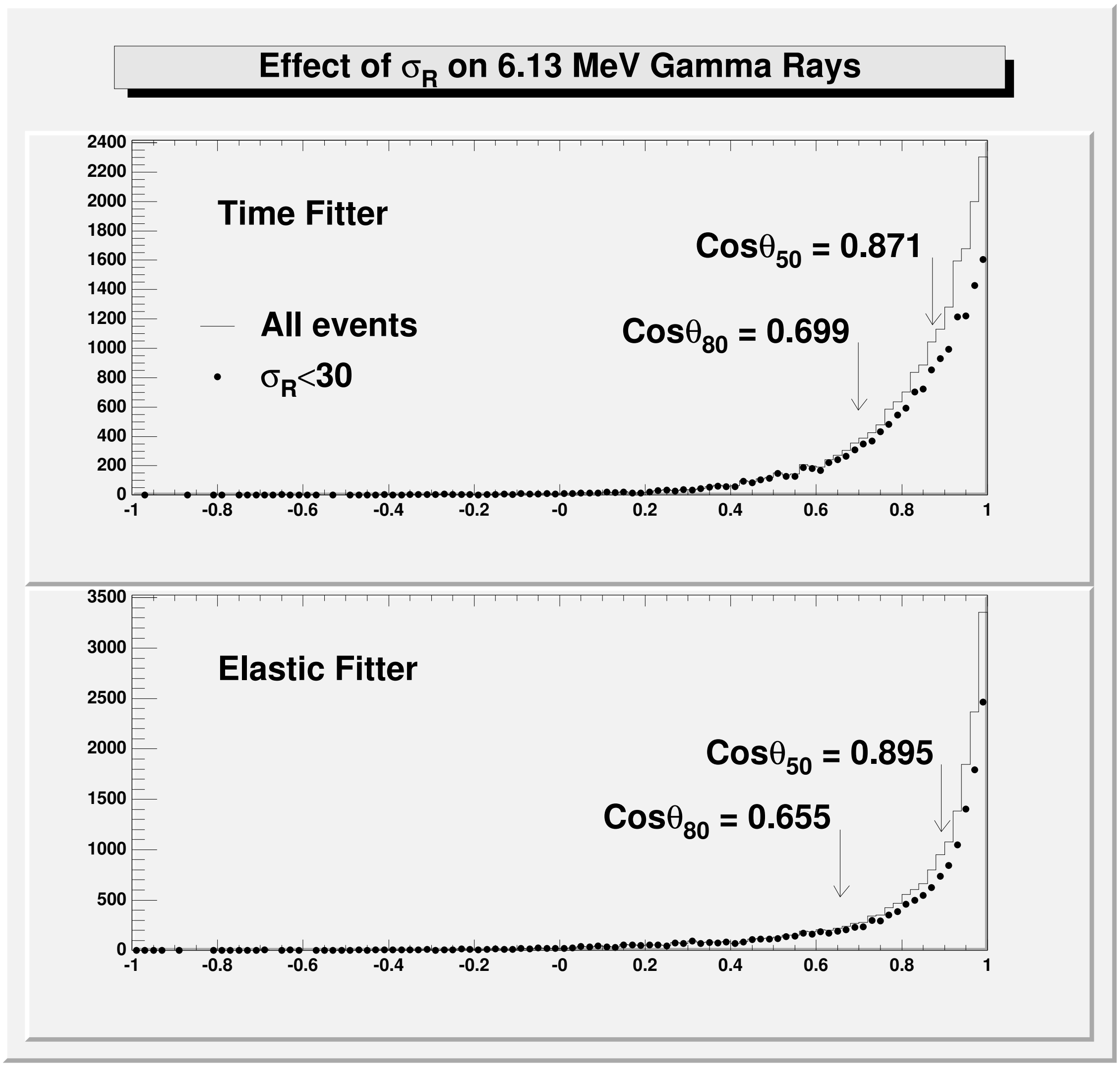

Figure 6.20: Effect of cut on σ_R on 6.13 MeV gamma rays is shown. The solid histogram shows the angular distribution before application of the cut. The points show the histogram after the cuts. The values of $\cos\theta_{80}$ and $\cos\theta_{50}$ shown here are for the histogram after the application of the cut.

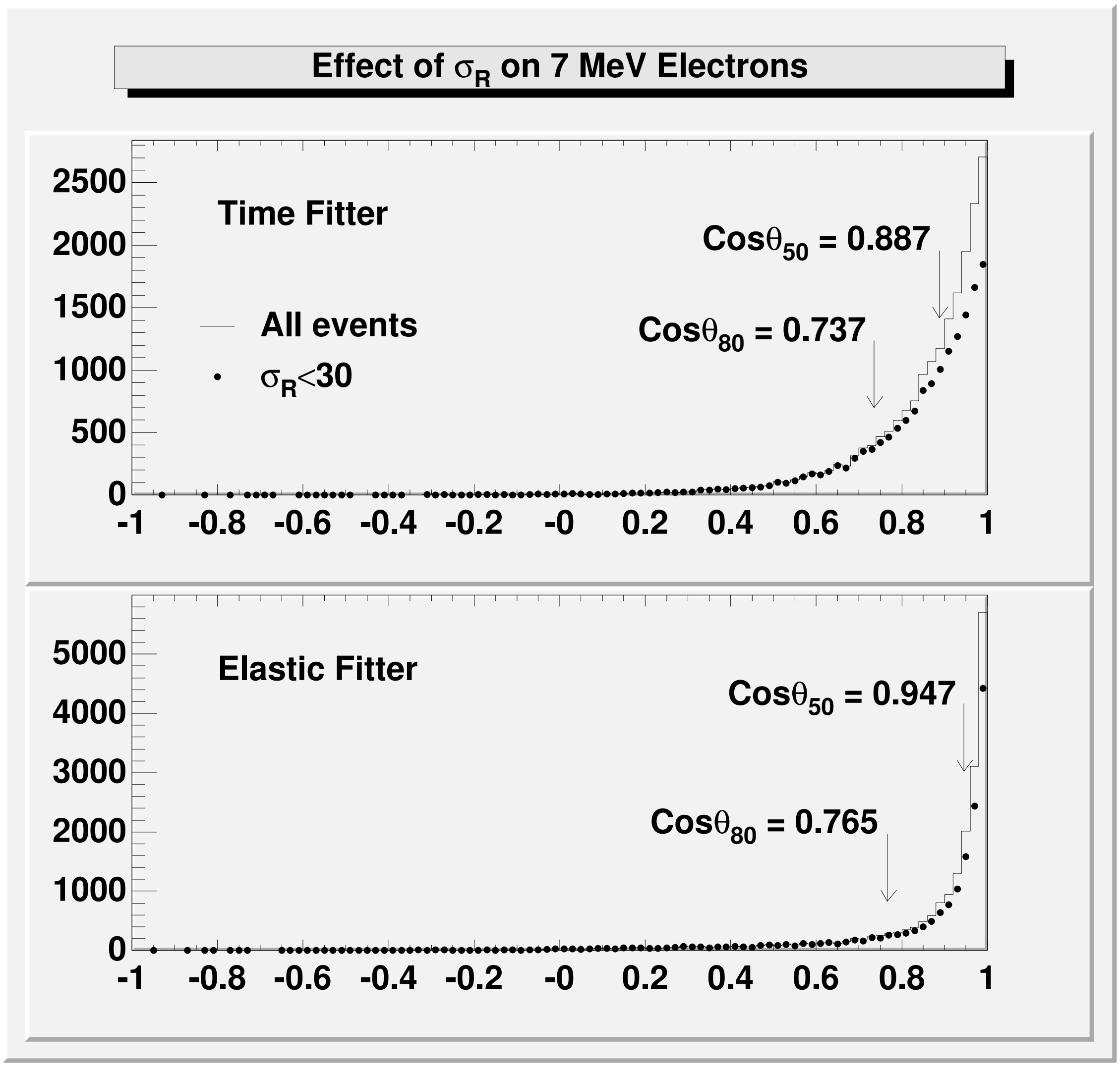

Figure 6.21: Effect of cut on σ_R on 7 MeV electrons is shown. The solid histogram shows the angular distribution before application of the cut. The points show the histogram after the cuts. The values of $\cos\theta_{80}$ and $\cos\theta_{50}$ shown here are for the histogram after the application of the cut.

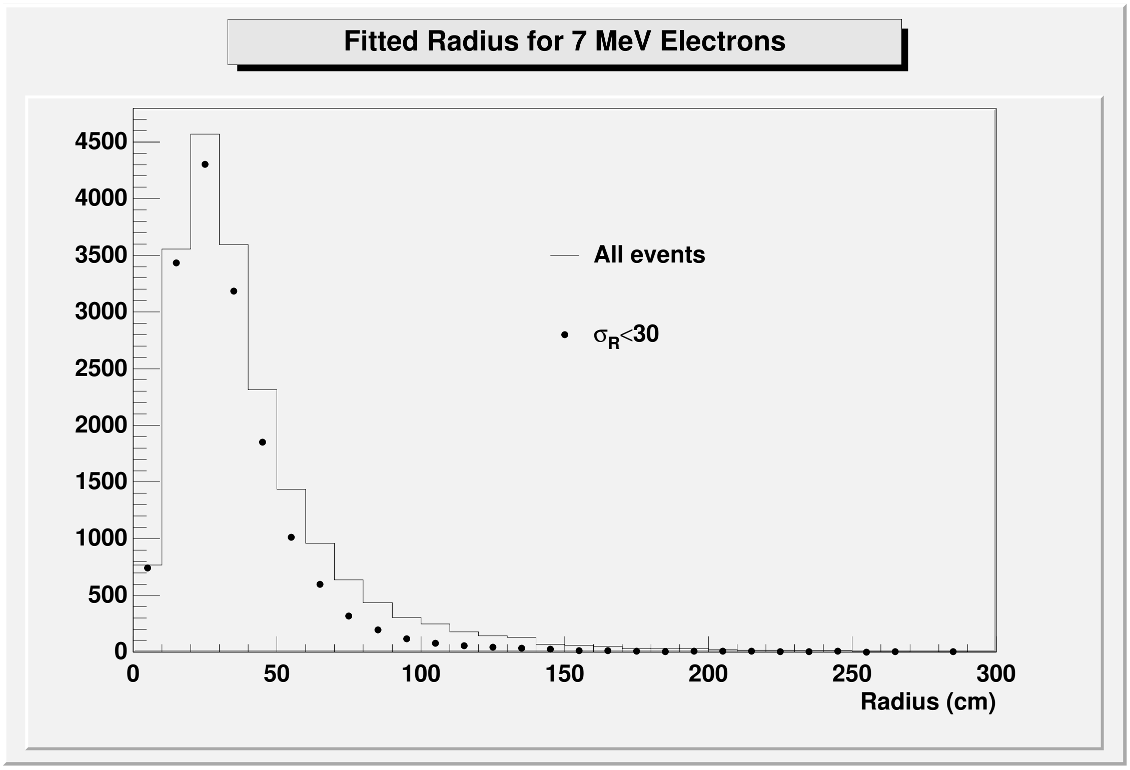

Figure 6.22: Effect of cut on σ_R on the position reconstruction of 7 MeV electrons is shown. The solid histogram shows the distribution of reconstructed radius application of the cut. The points show the distribution after the cuts. The electrons were generated at the origin.

6.2.6 Detailed Study of events Passing all Cuts

The cuts imposed removed most, but not all, of the events from ^{16}N simulation which really converted at low radius. The effects of finite position resolution perpendicular to the direction of the gamma ray worsening the angular resolution and the anticorrelation improving the resolution are still present. The agreement between the calibration and the simulation of 6.13 MeV gamma rays must be understood.

To study the effect of the finite position resolution perpendicular to the gamma-ray direction broadening the angular distribution, the angle between the vector from the source to the reconstructed position and the vector from the source to the position at which the gamma ray converted was calculated for each event. This angle, ξ, is plotted against $R_{\mathrm{real}} \equiv |\vec{x}_{\mathrm{real}}|$ for events which reconstruct farther than 175 cm from the source. All cuts were applied. The result is shown as a scatter plot in figure 6.23.

The scatter plot in figure 6.23 is divided into 9 regions. The bottom right corner contains the events desired. Those events have a small angle ξ and reconstructed radially correctly. The angular distributions for the 9 regions are shown in figure 6.24. (The angular distributions are laid out to match the regions in figure 6.23; the top left histogram of figure 6.24 corresponds to the top left region of figure 6.23 and so on.)

Three important points are clear from the figure. First, at larger values of ξ in figure 6.24, the distributions become broader; second, at lower values of R_{real} the distributions become narrower; and third, there are many events which have $R_{\mathrm{real}} < 150$: 1891 of 4633 events in total.

The value of $\cos\theta_{80}$ for the elastic fitter for each region is shown in table 6.2. The first point is that the good events (those with $R_{\mathrm{real}} > 175$ and $\xi < 10$ degrees) have a value of $\cos\theta_{80}$ of 0.601 which is unlike that for the 6.13 MeV gamma rays (0.701) shown in figure 6.3. The value of $\cos\theta_{80}$ for all events in the simulation reconstructing with $R_{\mathrm{real}} > 150$ and $\xi < 20$ is 0.621 (using the elastic fitter). This is still much less than the value for 6.13 MeV gamma rays.

To understand these low values of $\cos\theta_{80}$ from the simulation of ^{16}N calibration, all events which converted farther than 175 cm from the source (according to the definition of $\vec{x}_{\mathrm{real}}$) were

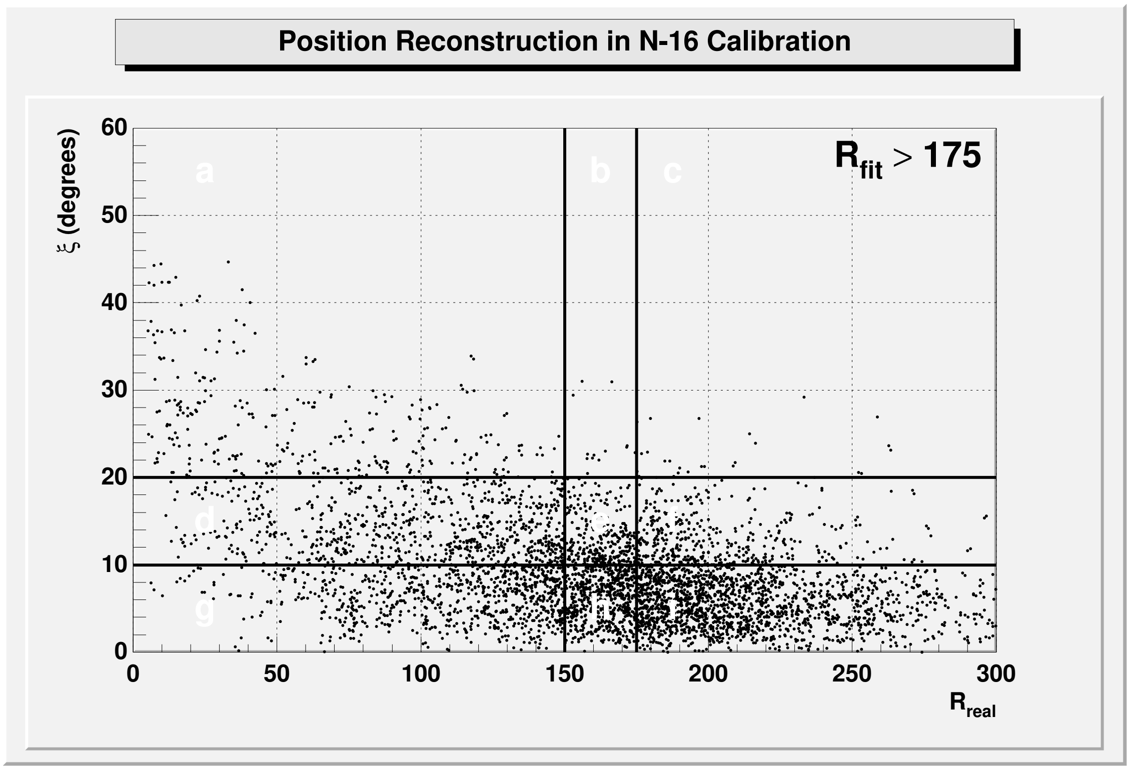

Figure 6.23: The position resolution for ^{16}N calibration is shown. The variable on the y axis is the angle, ξ, the angle between the vector from the source to the reconstructed position and the vector from the source to the real position of gamma conversion. The variable plotted on the x axis is the distance from the source at which the gamma really converted. This figure comprises events which reconstructed (after all cuts) more than 175 cm from the source. The solid lines divide the plot into the 9 regions discussed in the text.

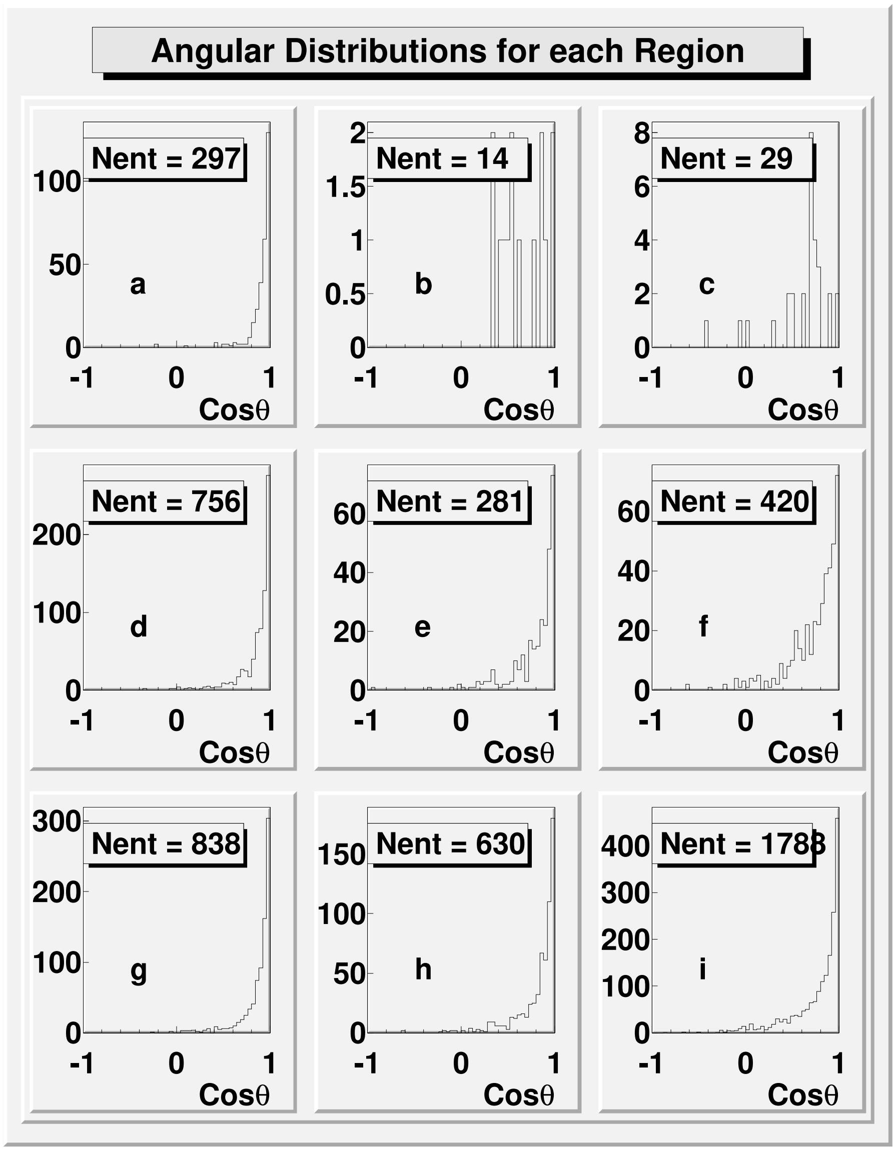

Figure 6.24: Angular distributions are shown for events in the different regions in figure 6.23. All events reconstructed farther than 175 cm from the source and had all cuts to reduce misreconstruction applied. The nine plots are labelled to to correspond to the 9 regions in figure 6.23. The number of entries in each region is noted on the histograms.

$\cos\theta_{80}$ **for the regions of figure 6.23**			
	$R_{\text{real}} < 150$	$150 < r_{\text{real}} < 175$	$R_{\text{real}} > 175$
$\xi > 20$	a .875 (297)	b .429 (14)	c .461 (29)
$10 < \xi < 20$	d .781 (756)	e .665 (281)	f .547 (420)
$\xi < 10$	g .805 (838)	h .691 (630)	i .601 (1788)

Table 6.2: The value of $\cos\theta_{80}$ is shown for the elastic fitter for the 9 regions of figure 6.23. In brackets is shown the number of events in that region. Recall that the value of $\cos\theta_{80}$ for 6.13 MeV gamma rays shown in figure 6.3 is 0.701. The labels (a through i) correspond to the regions in figure 6.23.

considered without regard to the radius of reconstruction. A histogram was made of the angular distribution. It is shown in figure 6.25. The angular resolution for these events ($\cos\theta_{80}$ for the elastic fitter is 0.643) is worse for these events than for the simulation of 6.13 MeV gamma rays because of the effect of the finite position resolution in determining the initial direction of the gamma ray. However, because no radial cut is imposed on the reconstruction, the effect of the anti-correlation is not present.

The angular resolution of events from ^{16}N simulation which *convert* far from the source is still better than the angular resolution for events which both convert and reconstruct far from the source. This can be explained by considering the events which really did convert farther than 175 cm from the source but reconstruct closer than 175 cm from the source or are eliminated from the sample either by the cut on σ_R or by the quad fitter reconstruction. These events either misreconstruct in radius or, at least, are poorly constrained in radius. Thus, they can be expected to have excellent angular resolution and, indeed, they do. These events have $\cos\theta_{80} = 0.803$ for both fitters. Therefore, the reason the events which reconstruct well in radius and ξ and pass all cuts have poor angular resolution (on average) is that the events from high radius which the cuts remove have excellent angular resolution on average.

There are two conclusions from this analysis. First, the angular distribution measured in the ^{16}N

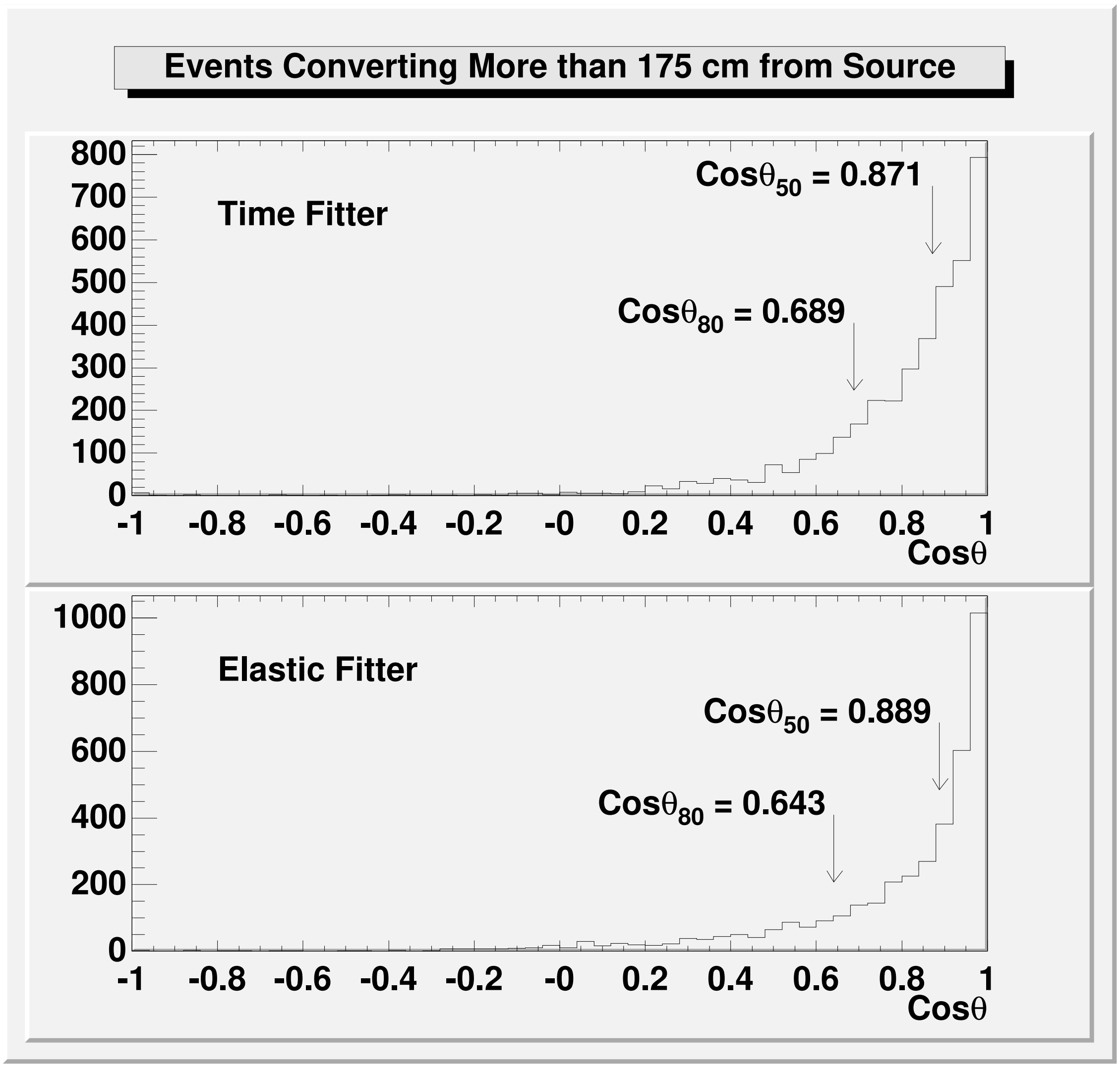

Figure 6.25: Angular distributions are shown for those events which convert farther than 175 cm from the ^{16}N source. The angular distribution is found using the reconstructed position to give the initial direction of the gamma ray. The values of $\cos\theta_{80}$ shown are, therefore, less than the corresponding values for the simulation of 6.13 MeV gamma rays shown in figure 6.3.

calibration is dependent on two factors: the angular resolution of the SNO detector to gamma rays and position resolution of the reconstruction. Second, the success of this calibration will depend on how well the position reconstruction is understood.

Position resolution has two components: the resolution perpendicular to the direction of the gamma ray which broadens the angular resolution and resolution parallel to the direction of the gamma rays which, in conjunction with a cut on reconstructed distance from the source, narrows the angular distribution.

The effect of the position resolution perpendicular to the direction can be understood in the calibration if the values of $\cos\theta_{80}$ and $\cos\theta_{50}$ agree with the Monte Carlo, not only at high radius, but also at low radius, because the position resolution perpendicular to the gamma ray direction dominates the width of the angular distribution at low radius.

Understanding the position resolution in the radial direction can be accomplished by studying the radial distribution of events. Figure 6.26 shows the radial distribution of reconstruction and conversion for the simulation of the ^{16}N calibration. The radial distribution of reconstruction has more events at large radius than the distribution for conversion, as expected. In the real calibration, the position at which the gamma rays converted will not be available. However, the radial distribution for the conversion is based upon well-understood Compton-scattering and pair-production interaction lengths and the electron densities in the various components of the source and the heavy water. Thus, the distribution of the radius at which the gamma rays convert need be calculated only once.

The radial distributions of reconstructed position from the simulation and the calibration must be compared carefully. Because the underlying distributions for Compton scattering and pair-production are well known, any discrepancy between calibration and Monte Carlo is an indication of misunderstanding of the position resolution of the fitter. In the case where the position resolution is on order of the radiation length in water (36 cm) or larger, the position resolution plays a key role in determining the radial distribution and it is therefore possible to extract meaningful information about the position resolution. If the position resolution is much smaller than the radiation length in

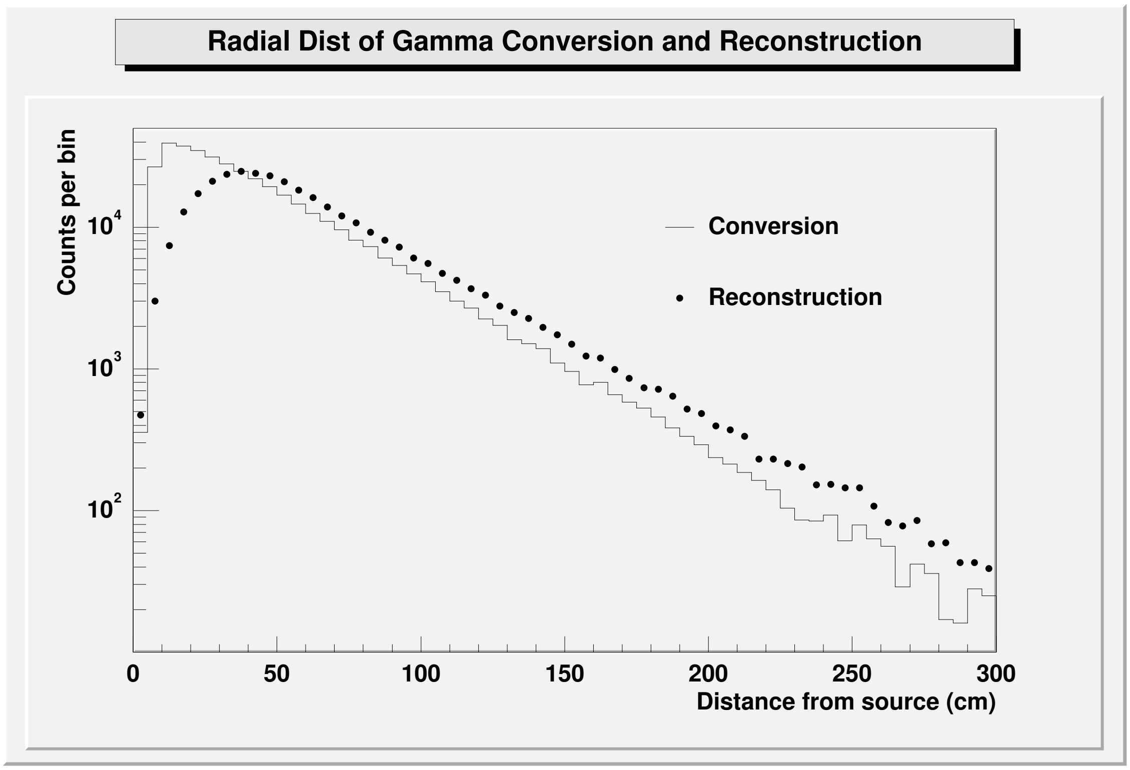

Figure 6.26: The distribution of radial position of the conversion and reconstruction of events for the simulation of the ^{16}N calibration. Both histograms are for the same number of events.

water, then the fitter reconstructs accurately and the position reconstruction will be less important to the calibration of angular resolution.

The radial distribution of events must be studied carefully after the application of each cut necessary to remove misreconstructed events to ensure that the cuts affect the data as expected.

Statistically, it is possible to measure the position resolution. Inspection of figure 6.26 shows that there are over 100 counts per (5 cm wide) bin up to distances of 250 cm from the source. This was for a simulation of 800000 ^{16}N decays. This many decays can be accumulated in approximately 45 minutes running time. Therefore, with a run a few hours long, it will be possible to get over 1000 counts in each radial bin of interest. This will allow precise comparison of the distributions form the simulation and calibration.

6.2.7 Summary of Analysis Plan

Data for several hours running with the ^{16}N source should be taken to ensure there are adequate statistics for events that reconstruct at high radius. The data must first be used to understand the energy scale and energy resolution of the detector and to set the absolute PMT efficiencies in the Monte Carlo as described in section 4.1. Once this is done, high-statistics simulations must be performed. The calibration data and the simulation can then be analyzed using exactly the same codes. The events (both calibration and simulation) must be reconstructed using the time, elastic, and quad fitters.

The radial distribution of events for the simulation and the calibration must be compared. The distributions must be normalized to an equal number of triggers for calibration and simulation. The cuts must then be applied individually to the events to ensure that the radial profile in both the simulation and the calibration behave similarly. Angular distributions must then be made for the events with all cuts imposed. The angular distributions must be plotted as a function of radial cut on the reconstruction to ensure that the values of $\cos\theta_{80}$ and $\cos\theta_{50}$ behave similarly for calibration and simulation.

The systematic uncertainty in the angular resolution of gamma rays caused by uncertainty in the radial distribution of events can be estimated. If, in the calibration, there is an excess of events at high radius compared to the simulation, then those extra events at high radius, being misreconstructed in position can be expected to have excellent angular resolution, similar to the events in regions a,d, and g of figures 6.23. The angular distribution for these events is known from figure 6.24. This angular distribution, scaled to the number of excess events at high radius in the calibration, can be subtracted from the measured angular distribution. This corrected distribution can be compared with the uncorrected angular distribution from calibration. The difference in $\cos\theta_{80}$ and $\cos\theta_{50}$ from these two distributions can then be taken as an upper limit on the systematic uncertainty from misunderstanding the radial distribution.

The comparison of simulation to calibration is not simply a comparison of angular distributions. It is simultaneously a comparison of the behavior of the reconstruction of position and direction. The best-fit values of the optical calibration will have been used as inputs to the Monte Carlo. However, theses values will have uncertainties. If varying the optical parameters in the Monte Carlo yields a better global fit to optical and ^{16}N calibration, then further analysis and optical calibration must be performed to determine if there is a systematic difference between the optical and ^{16}N calibration or if the difference becomes insignificant as increasing statistically accurate calibrations are made.

The calibration can be used to extract information about the angular resolution for gamma rays. The (small) discrepancies between the Monte Carlo and the calibration can be used as an indication of the systematic error in the angular resolution for gamma rays. If the discrepancy is small, or statistically insignificant, then the process is complete. If the discrepancy is statistically significant or large enough to affect the analysis of the electron-scattering signal (see next chapter) then further investigation and calibration must take place to understand the origin of the discrepancy.

6.3 Extensions to the Calibration of Angular Resolution

The procedure described in this chapter forms the core of the calibration of angular resolution. There are two extensions to give more information. First, the angular resolution was shown to be different for outward-going electrons at high radius than for electrons in other geometries. This can be tested by running the ^{16}N source approximately 350 cm off center. It is then possible to study angular resolution for events near the acrylic.

Secondly, and more importantly, angular resolution is strongly dependent on energy. The high-energy gamma-ray source ($E_\gamma = 19.8$ MeV) discussed in chapter 3 should be used to confirm that the angular resolution scales with energy as the Monte Carlo predicts. Both of these extensions can use the techniques developed in this chapter.

6.4 An Air Volume Underneath the Gamma-Ray source

If misreconstruction of events limits the accuracy of the calibration then one possibility is to install a hollow cylinder on the bottom of the ^{16}N source. This cylinder would give gamma rays a free travel path in one direction away from the source. An analysis would be performed on the gamma rays that reconstruct below the end of the cylinder. The design of such a cylinder is difficult because of size and weight constraints imposed by other calibration hardware. Such a source is being considered [He98].

6.5 Relating the Angular Resolution of Gamma Rays to Electrons

The specific objective is the extraction of the electron-scattering signal. The information learned about the angular resolution of gamma rays must be applied to electrons.

The uncertainty in the angular resolution for electrons will depend on all the effects of the fitter, uncertainty in the Monte Carlo parameters, and uncertainty in optical constants derived from the optical and ^{16}N calibrations. Simulations of electrons must be performed with these parameters varied within the ranges allowed by the optical, ^{16}N, and high-energy gamma-ray sources. The careful comparison of the ^{16}N calibration and the Monte Carlo can provide valuable information leading to an accurate estimate of the uncertainty in angular resolution for electrons.

Chapter 7

Extraction of the Electron-Scattering Signal From the Data

This chapter turns to step 4 in the analysis: extracting physics information from the data. It will deal with a narrower range of issues than that required for a full analysis; only those parts which most affect the ES signal will be considered. As well, the analysis presented will only consider one variable, $\cos\theta_{\rm sun}$, in detail. The chapter will include information about other systematic effects in the extraction of the ES signal and ES/CC ratio.

7.1 One-Dimensional Subtraction

This section presents the simplest analysis of the extraction of the ES signal. In the discussion certain parameters are given concrete values. This is to illustrate the concept under discussion; it is not a statement that this particular parameter is the best choice in a global analysis. After the procedure has been illustrated with concrete values, the effect of choice of these parameters on the total uncertainty is discussed more generally.

7.1.1 The Subtraction and Statistical Uncertainty

A one-dimensional subtraction analysis of the angular distribution of events with respect to the sun is the simplest possible extraction of the signal. The spectrum is similar to that of figure 3.3. The fitter used was the elastic fitter. The data are shown in figure 7.1.

The analysis is performed by fitting a straight line, $y = a + bx$, to the data in the region $-1 < \cos\theta < 0.72$. The fit (and all subsequent fits in this chapter) was performed with the Root [BR96] implementation of the Minuit function minimization and error analysis code [JR94]. The data were converted from units of counts per bin to counts per $\cos\theta$. The fit result was $a = 1890 \pm 33$, $b = -403 \pm 66$, and $\sigma^2_{ab} = 287$. The fit, after correction for bin width, is shown with a dashed line. The straight line is then extrapolated to the region $0.8 < \cos\theta < 1$, where the ES signal is large. This is also shown as a dashed line. The area under the extrapolation, the background, $\mathcal{B}'$ is

$$\mathcal{B}' = \int_X^1 (a + bx) = a(1 - X) + b(1 - X^2)/2 \tag{7.1}$$

With $X = 0.8$, $\mathcal{B}' = 337$. The uncertainty on $\mathcal{B}'$ is given by $\sigma_{\mathcal{B}'}$.

$$\begin{aligned}
\sigma^2_{\mathcal{B}'} &= \sigma^2_a \left(\frac{\partial \mathcal{B}'}{\partial a}\right)^2 + \sigma^2_b \left(\frac{\partial \mathcal{B}'}{\partial b}\right)^2 + 2\sigma^2_{ab} \left(\frac{\partial \mathcal{B}'}{\partial a}\right)\left(\frac{\partial \mathcal{B}'}{\partial b}\right) \\
&= 48 + 145 + 20 \\
\sigma_{\mathcal{B}'} &= 15
\end{aligned}$$

The total area of the data in the region above $\cos\theta_{\mathrm{sun}} = 0.8$ and found to be 578 with an uncertainty of 24. Therefore, the measured signal is 241 ± 28. The uncertainty is 11%. For comparison, there were 265 ES events in the region of interest input to the analysis.

It is now necessary to correct for the inclusion of the tail of the ES signal skewing the fit. To do so, it is necessary to take the information gleaned about the peak and extrapolate that to the tail using a high-statistics simulation of the ES signal. (The angular distribution from this is shown in figure 7.2.) The ES angular distribution can be normalized to match the area in the peak from the analysis above. The size and shape of the tail is then known. It is possible to subtract this

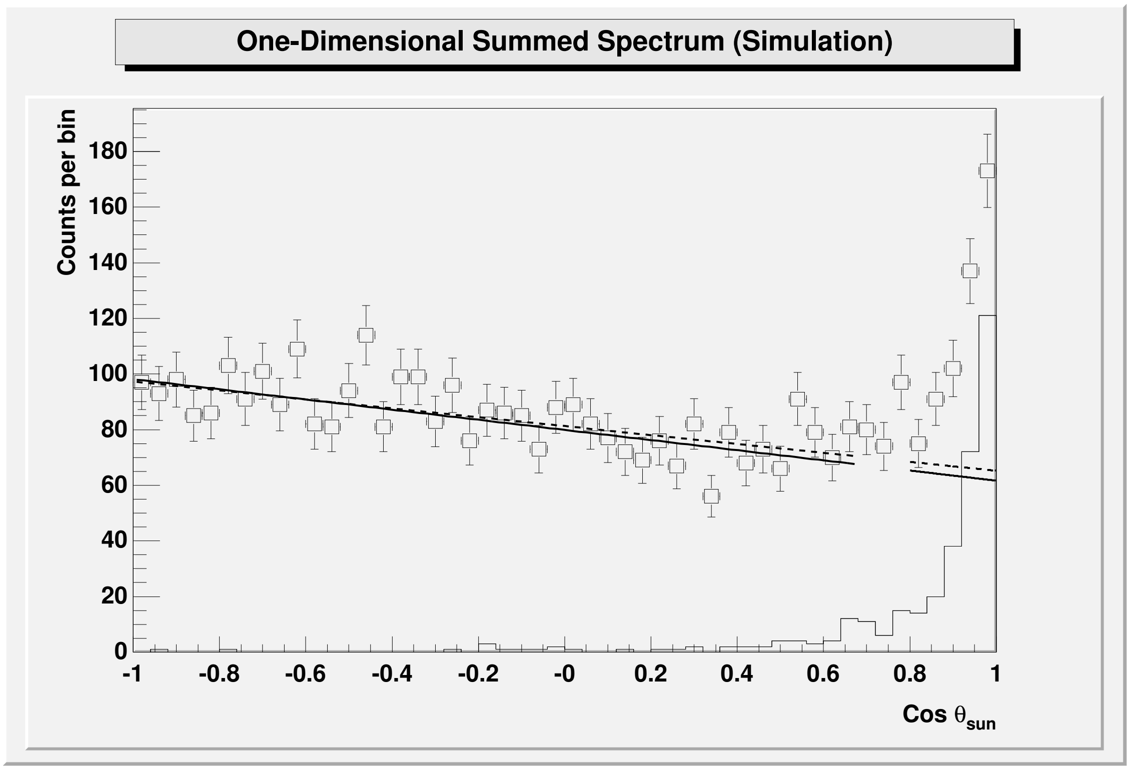

Figure 7.1: The subtraction analysis using the elastic fitter. The squares are a sum of the angular distributions for CC, ES, NC, and ^{208}Tl in the heavy water. Threshold of 45 hits is imposed. The dashed line is a fit to the data on the region $-1 < \cos\theta < 0.72$ before correction for the effect of the ES tail. It is extrapolated into the peak region to show the background. The corresponding lines after correction for the ES tail are shown as solid lines. The histogram is the ES signal that was generated by the Monte Carlo.

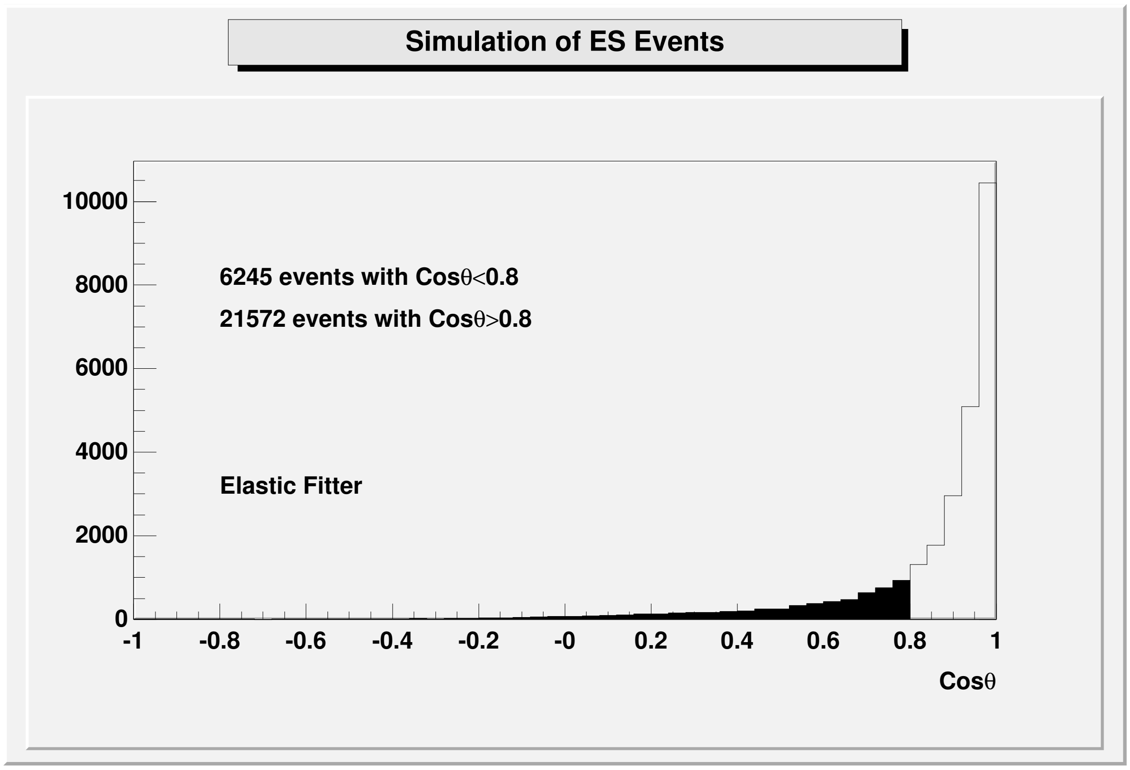

Figure 7.2: The angular distribution from a high-statistics simulation of ES is shown for those events which reconstruct in the heavy-water volume and have NHIT > 45. This histogram is used to correct the number of ES events for those withcos $\theta < 0.8$.

tail from the data and reperform the fit. The result of this is shown in solid lines on figure 7.1. The background is now $\mathcal{B} = 318 \pm 15$. This gives 261 ± 28 ES events above $\cos\theta_{\mathrm{sun}} = 0.8$. The statistical uncertainty is 11% and does not include the systematic uncertainty in subtracting the ES tail from the background region.

For comparison, the same analysis was done using the time fitter. Figure 7.3 shows the data. Because the time fitter's angular resolution is less precise than the elastic fitter, the background was only be estimated from $-1 < \cos\theta < 0.6$ and the peak is integrated over $0.68 < \cos\theta < 1$. After correction for the tail of the ES signal, the background is $\mathcal{B} = 508 \pm 26$ and the total area of the peak is 828 ± 29. Thus there are 320 ± 39 ES events in the peak compared to 296 that went in. The statistical uncertainty is 12%, which is slightly larger than the value of 11% for the elastic fitter.

(Close inspection of the figures shows that the data, except for the ES signal, are the same in the two fitters. This is indeed so. There is negligible difference in the slope of the CC signal using the elastic and time fitter. Using identical inputs for CC, NC, and backgrounds allows for easier comparison of the extraction of ES with the elastic and time fitters.)

7.1.2 Correction for the Threshold in $\cos\theta_{\mathbf{sun}}$

The correction for the threshold in $\cos\theta_{\text{sun}}$ must be made. The size of the correction was calculated using the Monte Carlo. Of 27826 ES events with NHIT > 45 that reconstructed inside the vessel, there were 6245 with $-1 < \cos\theta < 0.8$ and 21572 with $0.8 < \cos\theta < 1.0$. Thus the ES rate must be multiplied by $1/0.775$. The angular distribution from the simulation is shown in figure 7.2. The integral of this distribution is shown in figure 7.4. The 261 ± 28 counts in the peak become 336 ± 36 (statistical uncertainty only) in the entire angular range.

The parameters which define the peak region and the background-determination region chosen in this discussion are nearly optimal. The statistical uncertainties depend only weakly on the region in which the peak area is determined. For the elastic fitter, the statistical uncertainty drops from 11% to 10% if the peak is determined on $\cos\theta_{\text{sun}} > 0.84$. However, the correction for the cutoff is much larger. Measuring the peak in the region $\cos\theta_{\text{sun}} > 0.76$ increases the statistical uncertainty from 11% to 11.5%.

7.2 Fitting To An Analytic Function

The subtraction analysis is not completely satisfactory. Extending the fit to include the entire angular distribution is the most complete one-dimensional analysis.

The first step is to use equation 5.7 (here labelled $\mathcal{ES}$), a function of $\cos\theta_{\text{sun}}$ and three parameters, $\vec{a}$, to fit the high-statistics ES spectrum of figure 7.2. When this is done, the best-fit parameters are $a_0 = 19.5 \pm 0.4$, $a_1 = 0.114 \pm 0.006$, and $a_2 = 3.23 \pm 0.9$. The fit was performed over the region $0 < \cos\theta < 1$. There were 28173 entries in the histogram. The value of χ^2 was 54.6

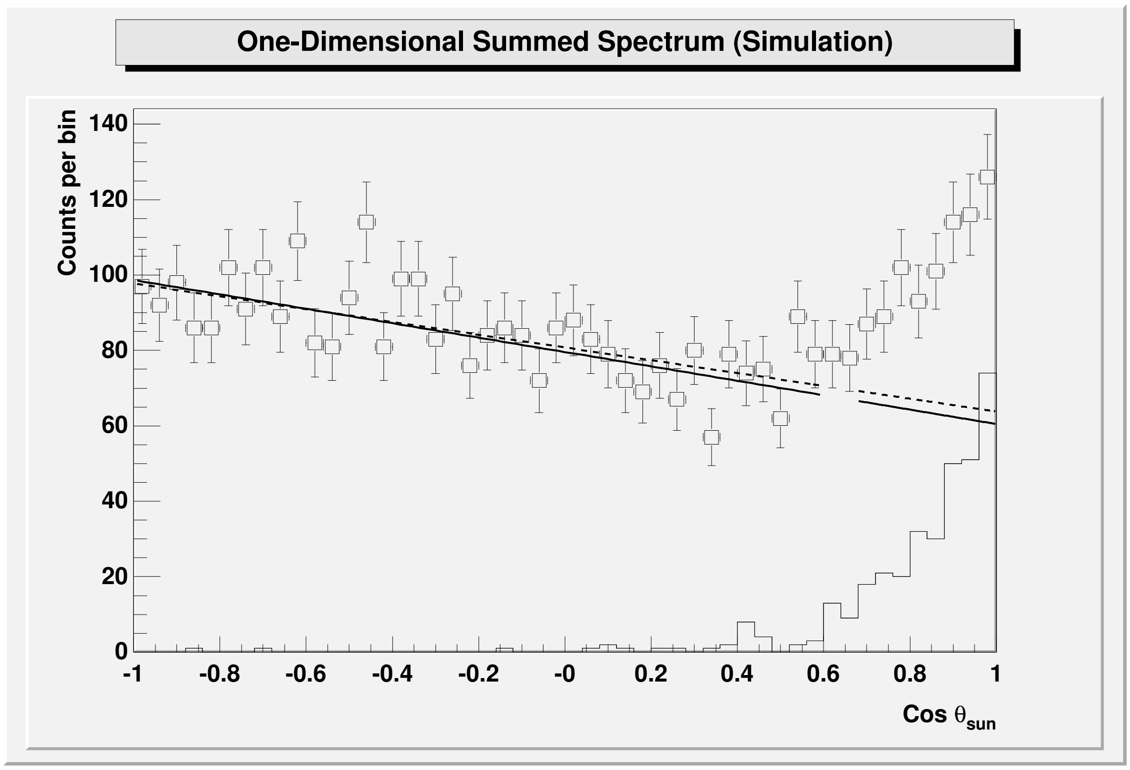

Figure 7.3: The subtraction analysis using the time fitter. The squares are a sum of the angular distributions for CC, ES, NC, and ^{208}Tl in the heavy water. Threshold of 45 hits is imposed. The dashed line is a fit to the data on the region $-1 < \cos\theta < 0.6$ before correction for the tail of the ES signal. It is extrapolated into the peak region above 0.68. The solid lines are the corresponding lines after correction for the ES tail. The histogram is the ES signal that was generated by the Monte Carlo.

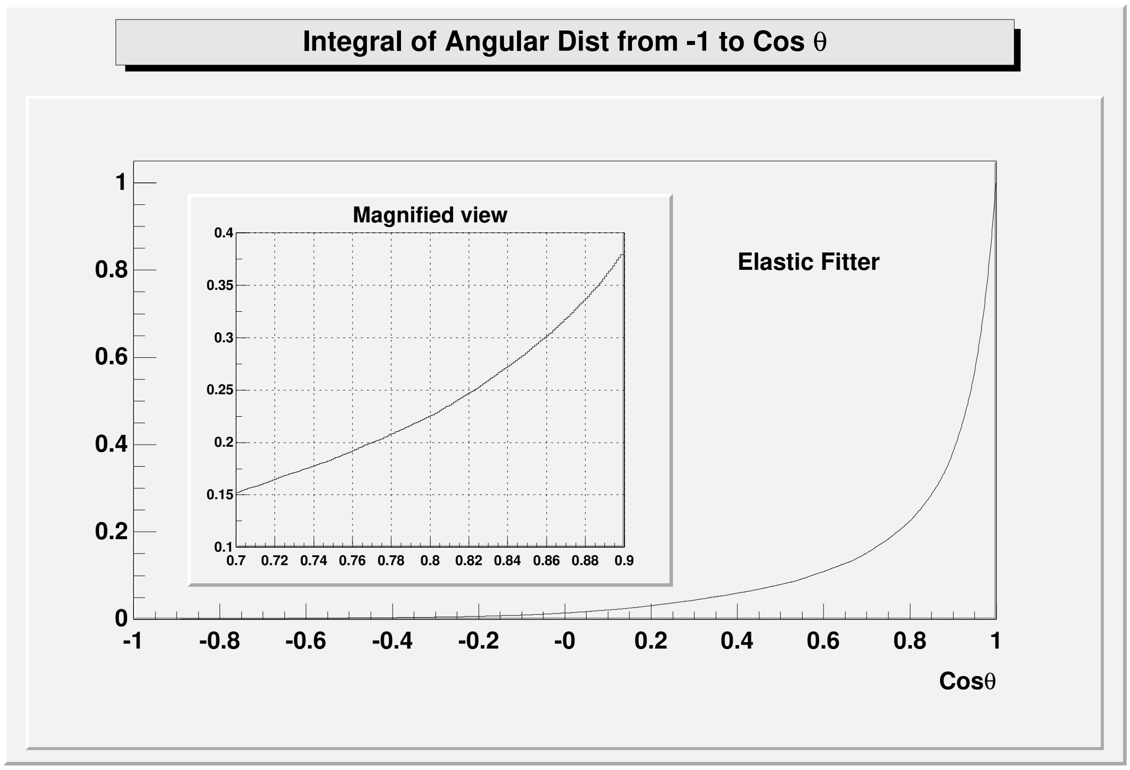

Figure 7.4: The integral of the angular distribution shown in figure 7.2 with a magnified view for $0.7 < \cos\theta < 0.9$.

for 21 degrees of freedom.

The simulation of the one-year data set was fit to the following function:

$$y(\cos\theta_{\rm sun};\vec{b},\vec{a}) = b_1 \times \frac{1}{2}(1-\frac{\cos\theta_{\rm sun}}{3}) + b_2 \times \frac{1}{2} + b_3 \times \mathcal{ES}(\cos\theta_{\rm sun},\vec{a}) \tag{7.2}$$

The parameters, $\vec{b}$ were allowed to vary to minimize the following χ^2:

$$\chi^2 = \sum_i \frac{[y(\cos\theta_{\rm sun};\vec{b},\vec{a}) - y_i]^2}{\sigma_i^2} \tag{7.3}$$

where i is the index of the bins of the histogram. The result of the fit is shown in figure 7.5. The value of χ^2 is 47.4 for 47 degrees of freedom. The number of ES events from the fit is 335 ± 34. For comparison, 347 were input in the histogram. This is a 10% statistical uncertainty.

7.3 Fitting to a Histogram from the Monte Carlo

The most accurate way to analyze the data is to compare to Monte Carlo simulations. The fit was performed by comparing the data to the same linear functions for CC, NC and background signals and to a histogram for the ES signal. The histogram describing this is the histogram shown in figure 7.2. (The histogram was normalized before the fit was performed.) The result is shown in figure 7.6

The size of the ES signal from the fit was 325 ± 33. This, like the fit to the analytic function has a 10% statistical uncertainty.

7.4 Systematic Uncertainty from the Angular Resolution

The uncertainty in angular resolution will contribute uncertainty to the extraction of the ES signal. The most convenient analysis in which to study the uncertainty in angular resolution is in the fits to the analytic function. The behavior of the fit was studied as the parameters, $\vec{a}$, describing the angular distribution are changed.

One important point to consider while studying the systematic uncertainty is that the data points nearest $\cos\theta_{\rm sun} = 1$ drive the ES amplitude in the fit. Consider the case in which a_2 is

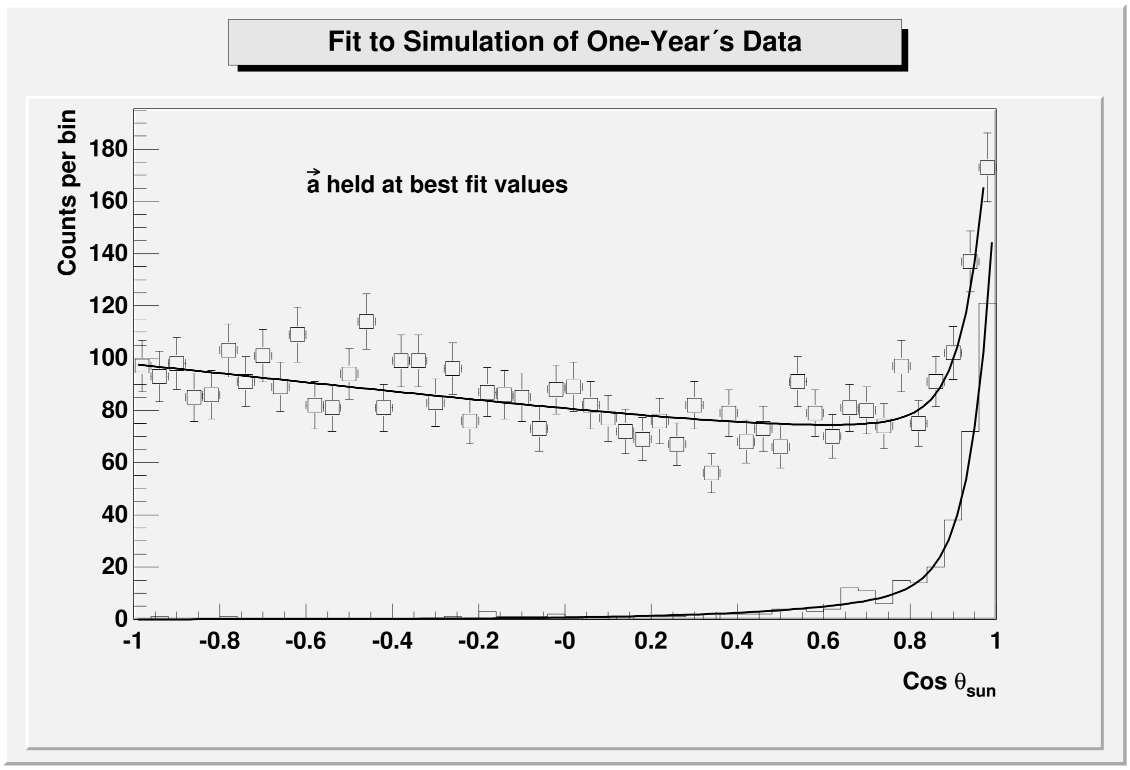

Figure 7.5: Fit to the full angular distribution with angular resolution parameters fixed at true values. The data to which the fit is performed is plotted with open squares. The ES component is shown as the histogram. The top curve is the result of the fit. The bottom curve is the ES component to the top curve.

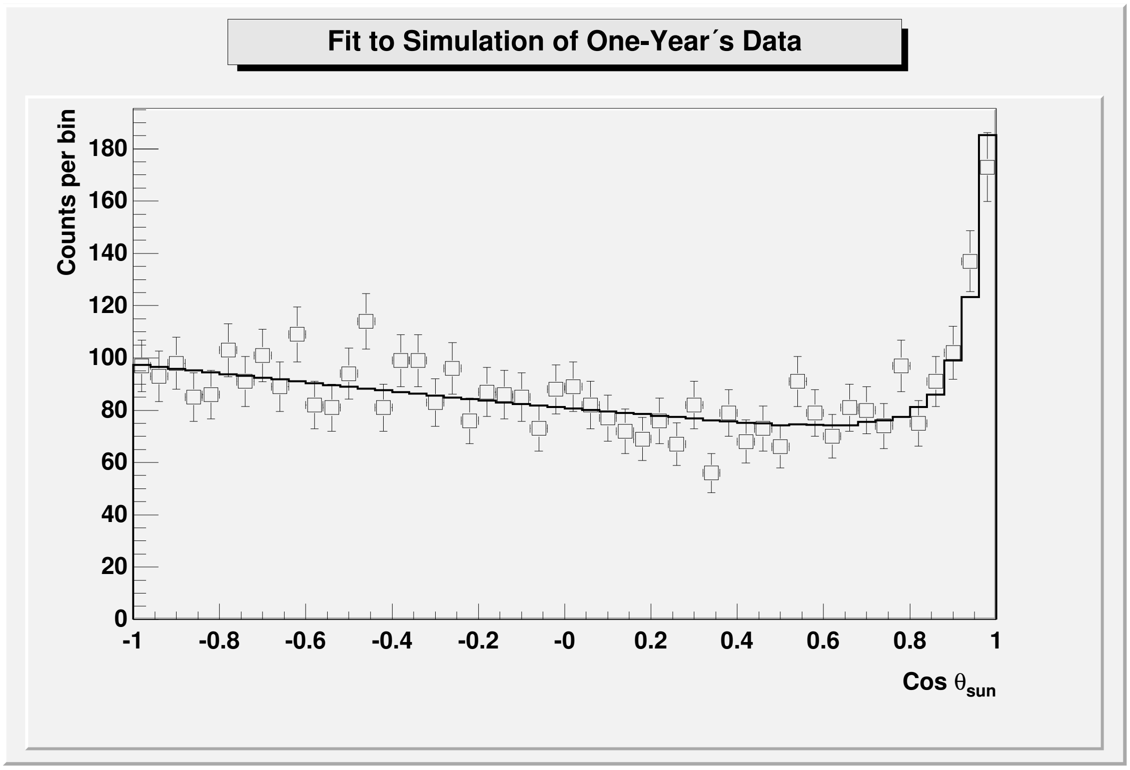

Figure 7.6: Fit to the full angular distribution with the ES signal taken from the high-statistics Monte Carlo. The data to which the fit is performed is plotted with open squares. The fit is shown as a histogram.

increased. In this case, the tail of the function is a larger fraction of the total area. The main peak is thus a smaller fraction of the total area. Then the amplitude of the ES signal in the fit must be increased to match the data near the peak.

The method used to estimate the systematic uncertainty is the following. A value for the uncertainty in $\cos\theta_{80}$, 0.02, was chosen. The parameters in the analytic function were varied independently to determine what variation in $\vec{a}$ caused a shift in $\cos\theta_{80}$ equal to 0.02, the assumed uncertainty in $\cos\theta_{80}$. These three parameter sets will then be used in the ES extraction to determine the change in the fitted number of ES events. This will then be the uncertainty in the ES signal from uncertainty in angular resolution of 0.02. Once the uncertainty in $\cos\theta_{80}$ is evaluated, the uncertainty in the ES extraction can be determined.

For the best-fit values of $\vec{a}$, the value of $\cos\theta_{80}$ is 0.770. The "standard change" in $\cos\theta_{80}$ is taken to be 0.02. To obtain $\cos\theta_{80} = 0.75$, the value of a_1 had to be shifted from 19.5 to 22.8. The result of the fit for the number of ES events is decreases by 4 to 331. This is a -1.2% change.

The value of a_2 had to be changed from 0.114 to 0.130 to change $\cos\theta_{80}$ from 0.77 to 0.75. The result of the fit using this value of a_2 is 348 ES events. This is 13 events more than the 335 with best-fit parameters $\vec{a}$ and is a 4% change in the ES signal.

The value of a_3 had to be changed from 3.23 to 3.05. The result of the fit was 344 ES events, or 9 more than the 345 in the best-fit case. This is a 2.6% shift. Figure 7.7 shows the function with the best-fit parameters and with the variation in each parameter.

These three cases raise the question of which uncertainty to use. The best-case scenario is that the source of the uncertainty is in the main peak of the ES distribution and then the systematic uncertainty in the ES signal for an uncertainty in $\cos\theta_{80}$ of 0.02 is approximately 1%. In the worst case, the uncertainty is entirely due to a_2 and the systematic uncertainty becomes 4%.

Stated differently, the ES extraction is more sensitive to the tail of the angular distribution than to the width of the main peak. The reason that the main peak is less important is the following. Increasing the co-efficient in the first exponent has two effects that tend to cancel. First, by reducing the number of events in the main peak, it increases the relative importance of the tail.

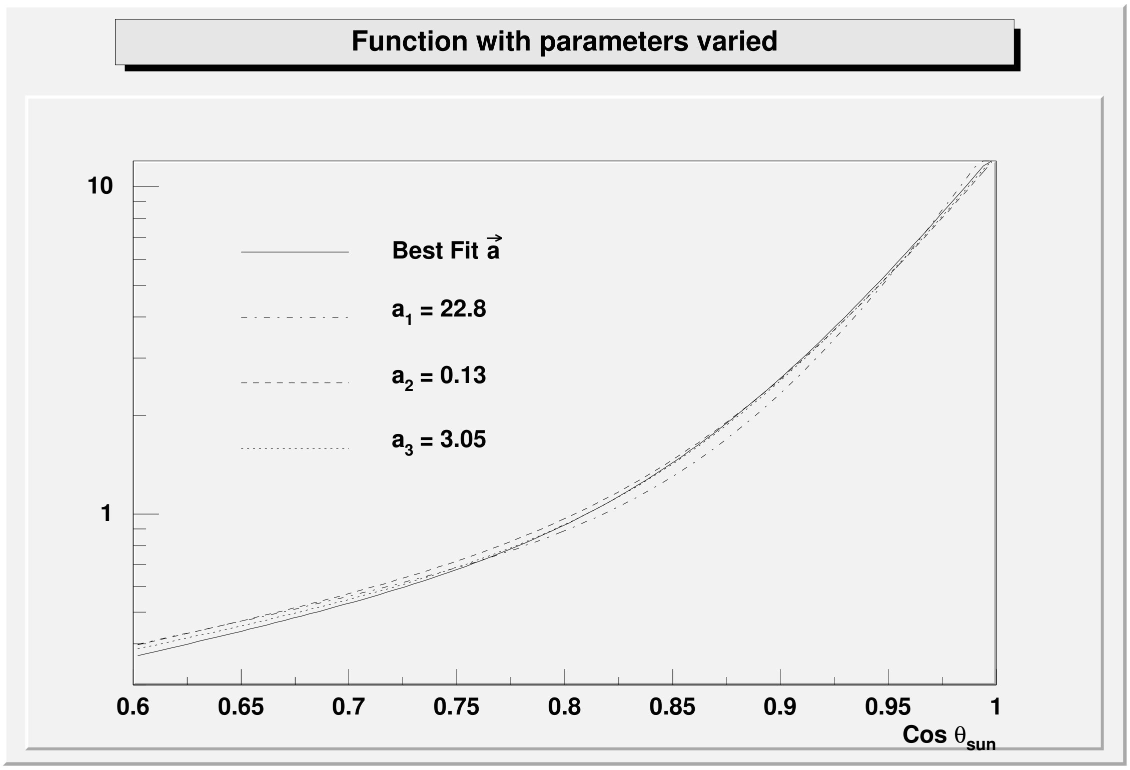

Figure 7.7: The analytic function for fitting the ES spectrum is shown with the default parameters and with each parameter varied individually as noted in the figure.

Because the amplitude of the ES signal in the fit is driven by the data nearest $\cos\theta_{\text{sun}} = 1$, the number of ES events is overestimated. But second, the number of counts between 0.84 and 0.92 is underestimated by the function. The overestimate of the number events between -1 and 0.8 is compensated for by the underestimate between 0.8 and 0.92.

The value of $\cos\theta_{50}$ was found for each set of parameters. When a_1 was varied, $\cos\theta_{50}$ was 0.938. When a_2 was varied it was 0.931. Therefore, $\cos\theta_{50}$ has limited utility in determining which of the three systematic uncertainties should be used. A conservative approach is to use the worst-case scenario and assume that an uncertainty in $\cos\theta_{80}$ of 0.02 corresponds gives a 4% systematic uncertainty in the ES amplitude.

Given the relation between an uncertainty in $\cos\theta_{80}$ and an uncertainty in the ES extraction, it is possible to quantify the effect of the various factors described in chapter 5. The uncertainty in the acrylic attenuation contributes an uncertainty in $\cos\theta_{80}$ of approximately 0.01. Changing the threshold for soft-Bremsstrahlung production and delta-ray production in the Monte Carlo, changed $\cos\theta_{80}$ by 0.01 also. These were the two largest effects. There were other optical effects that affected the uncertainty of $\cos\theta_{80}$ at the level of 0.005. Thus the uncertainty in $\cos\theta_{80}$ given all the factors considered in chapter 5 is ≤ 0.02. Thus a 4% systematic uncertainty in the ES signal arising from angular resolution is a conservative, but realistic, estimate.

7.5 Other Systematic Uncertainties

There are other sources of systematic uncertainty that can be divided into two main groups: detector-induced systematics and theoretical systematics. Detector-induced systematics are uncertainties caused by uncertainty in the knowledge of the detector. Theoretical uncertainties are those caused by uncertainty in theoretical inputs to the analysis. The theoretical uncertainties here are for measuring the ES/CC ratio, not just extracting the ES spectrum

7.5.1 Theoretical Systematics

The most important theoretical systematic is the uncertainty in the absolute CC cross section which is approximately 5% [KN94], as discussed in chapter 2. The radiative corrections are small compared to this. The uncertainty in the absolute ES cross section is much smaller. After the radiative corrections discussed in chapter 2, the remaining uncertainty is less than 1% [BKS95]. The shape of the neutrino spectrum is uncertain and contributes 2% uncertainty to the ES/CC ratio. This was found by calculating the reaction rates for the best fit and $\pm 3\sigma$ neutrino spectra presented in chapter 2.

If the neutrino spectrum is significantly different than the predicted ^{8}B spectrum, it is still possible to obtain model-independent information about neutrino oscillations by comparing the ES and CC rates. This method, due to Villante, Fiorentini and Lisi [VFL99], was developed in the context of comparing the ES rate in the Super-Kamiokande experiment to the CC rate in SNO and works for an arbitrary neutrino spectrum in the energy range from approximately 5 to 15 MeV.

This method is appealing because if there is oscillation of electron neutrinos into sterile neutrinos and muon or tau neutrinos, the shape of the total non-sterile neutrino spectrum at the earth would be distorted.

The crux of the method lies in setting a different energy threshold for the ES rate and the CC measurement. If the analysis threshold for studying the ES events is approximately 1.7 MeV greater than for the CC events, and given approximately equal energy resolution for the ES events (in Super-Kamiokande or SNO) and the CC events, then the sensitivity to *neutrinos* is approximately equal for both the ES and CC reactions. While the authors do not comment on the numerical value of 1.7 MeV for the difference in thresholds, it is likely related to the difference between the neutrino energy and the peak of the electron-recoil energy spectrumfor the CC reaction. The Q-value for the CC reaction is 1.44 MeV and the peak in the electron-recoil spectrum is peaked slightly below the neutrino energy less the Q-value. Figure 2.5 shows that the electron recoil spectrum for an 8 MeV neutrino is peaked at almost exactly 1.7 MeV less than the neutrino energy.

While this method will allow model-independent analysis even in the presence of oscillation to sterile neutrinos, it has limitations for comparing the ES to CC ratio within SNO because setting the threshold for ES analysis 1.7 MeV above that for the CC analysis will significantly reduce the event rate as can be seen by studying the recoil-electron energy spectra for the ES reaction in figure 2.6.

The approach discussed below assumes that the same threshold is used for the ES and CC reactions. This minimizes the experimental systematic uncertainties, but requires that the uncertainty in the ^{8}B-neutrino spectral shape be considered.

7.5.2 Detector Systematics

The uncertainty in the absolute energy scale of the SNO detector can affect the result because the data is analyzed above a certain NHIT threshold. The absolute energy scale can be determined through the calibrations within an uncertainty of approximately 0.1 MeV at an energy threshold of about 5 MeV. However, when taking the ratio of the ES to CC rates, the effect is reduced because the same threshold is applied to both signals. Thus if 45 NHIT corresponds to a higher energy than assumed in the calibration, *both* the ES and CC rates will be underestimated. (Even if the thresholds for analysis are slightly different, there is still some cancellation.)

A simple calculation was used to quantify this effect. The interaction rates and energy spectra were taken from equations 2.28 and 2.29. The spectra were convoluted with an approximate detector energy response, a Gaussian with a 1-σ width at 10 MeV (σ_{10}) of 12%, and $\sigma(E) = \sigma_{10} \times (E/10)^{1/2}$. No MSW effects were included. These spectra can be used to estimate the uncertainty from misunderstanding the energy threshold. If the analysis threshold is thought to be 5 MeV, and is in fact 4.9 MeV, then the CC rate will be over-estimated by 1.4% and the ES rate will be over-estimated by 2.5%. However the ratio changes by only 0.9%. If the threshold were in fact 5.1 MeV, then the CC rate would be under-estimated by 1.8%; the ES rate by 3.3%; but the ratio by only 1.8%. Thus the systematic error from the uncertainty in the energy threshold is less than 2%.

Similar calculations were performed to study the effect on uncertainty in the energy resolution. The effect was found to be less than 2%.

As discussed in the text, some events which did occur in the heavy water will misreconstruct outside the volume of heavy water. For ES events this matters less than for CC events as there will be ES events from the light water which misreconstruct inside the heavy water. (Because the light from events in the light water does not necessarily need to pass through the acrylic vessel, some light water events will have a greater NHIT than events in the heavy water. This shifts the energy spectrum of the events in light water and thus there will not be exactly a one-to-one correspondence between light-water events which misreconstruct in the heavy water and heavy-water events which mis-reconstruct in the light water.) However, for the CC signal, there are only events in the heavy water and some of these will misreconstruct.

7.6 Summary of Systematic Uncertainties

The systematic effects considered in this work are presented in table 7.1. Systematic effects dealing with the extraction of the CC signal, except for the effect of the energy threshold have not been discussed.

The total systematic uncertainty is dominated by two entries: the CC cross section and the angular resolution. These two terms alone would contribute a 6.4% systematic uncertainty. The statistical uncertainty for the extraction of the ES signal for a simulation of a one-year data set was 10%. Thus the total uncertainty for a one-year data set is approximately $\sqrt{10^2 + 7^2} = 12\%$. For a two-year data set the total uncertainty is approximately 10%; for a three-year data-set, 9%. These calculations are approximate because the systematic uncertainties, particularly in the CC cross section are likely not Gaussian-distributed.

Summary of Systematic Uncertainties	
Theoretical	
Absolute Neutrino Flux	**0**
Absolute CC cross Section	$\leq 5\%$
Absolute ES cross section	$< 1\%$
Shape of ^{8}B spectrum (no sterile ν)	2%
Experimental	
Angular resolution	$\leq 4\%$
Energy threshold	$\leq 2\%$
Energy Resolution	$\leq 2\%$
Position resolution and Radial Cut	?
Total	$\leq 7\%$

Table 7.1: A summary table of systematic uncertainties for the extraction of the ES signal and comparison with the CC signal. Uncertainties relating to the extraction of the CC signal (except for the effect of energy threshold) have not been considered. The total was found by a sum in quadrature.

Chapter 8

Data

This chapter discusses commissioning and early calibration data of the SNO detector.

8.1 Airfill Calibrations

Airfill is the term used to describe the detector with no water in front of the photomultipliers. The airfill calibrations were performed with two sources: the laserball and the ^{16}N source. The laserball calibrations allowed the discriminator thresholds and relative timing to be measured for each PMT. They are described in [Fo98].

The occupancy of a PMT is the number of times it detected a photon and generated a pulse above discriminator threshold. It can be measured in many ways. Occupancies are the first pass examination of whether a PMT and its associated electronics channel are working. The occupancies described here were measured with the ^{16}N source at the center of the detector. There are 9456 inward-pointing PMTs. Figure 8.1 shows a histogram of the occupancies. There are 1179 PMTs with zero occupancy. (The majority of these channels had been deliberately disconnected for maintenance.) There are very few PMTs with an occupancy between 1 and 50. The majority of the PMTs lie in a wide peak between an occupancy of 50 and 250. A PMT is defined to be "on" if it had an occupancy greater than 50. Otherwise it was defined as "off". (The large width of the distribution is due to the variation in discriminator thresholds at this early stage of commissioning.)

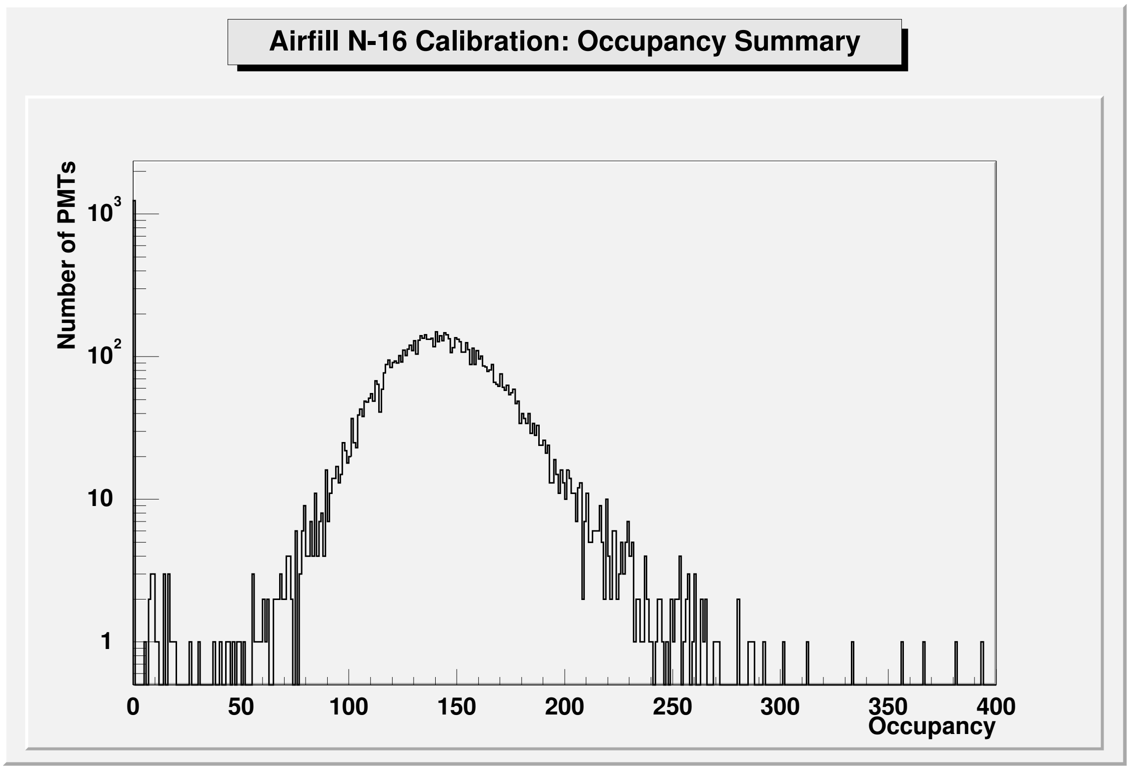

Figure 8.1: A histogram of occupancy for the ^{16}N run. There are 1179 PMT with no signals during the run, most of which were deliberately disconnected for repair.

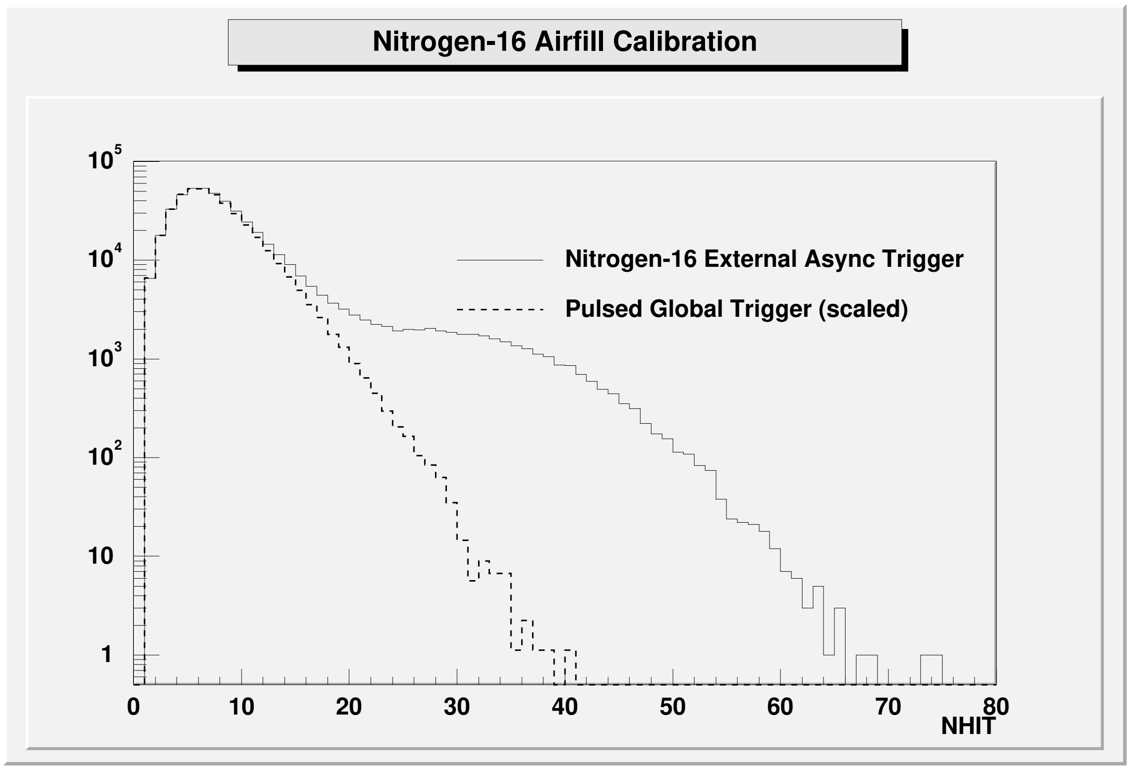

Figure 8.2: NHIT spectra for ^{16}N airfill calibration. The pulsed global trigger histogram has been scaled such that the integrated number of counts between 1 and 6 hits is equal for the two histograms.

For gamma rays from ^{16}N to produce light in the detector, the gamma rays must convert in the acrylic vessel (or in the PMT glass). The electrons will create Čerenkov light as they travel in the acrylic (or glass). Figure 8.2 shows the distribution of NHIT for ^{16}N events. The figure also shows the NHIT spectrum for pulsed-global-trigger (PGT) events from the same run. The PGT spectrum is scaled such that the total number of events yielding 1 to 6 hits is equal for the two spectra. (PGT events are those in which the detector is triggered independent of any physics process or calibration in the detector. It gives a random sample of the detector.)

At low values of NHIT, the external-asynchronous data should look similar to the PGT data for two reasons. First, the branch of ^{16}N beta decay to the ground state of ^{16}O will not create a gamma ray but will generate an EXT-ASYNC trigger. These events are exactly identical to PGT events. Second, 6.13 MeV gamma rays have a small probability of interacting in the acrylic, so most ^{16}N decays that do produce gamma rays will not generate any light visible to the PMTs. (In a simulation of 10000 6.13 MeV gamma rays, only 953 interacted in the acrylic vessel.)

PMT signals in a PGT event come from inherent noise in the PMTs or from light within the detector. The most important light source is alpha scintillation in air [BMW97, Bi64]. The ^{222}Rn concentration in the air of Creighton mine is approximately 1 to 3 pCi/L. A concentration of 1 pCi contributes 0.037 ^{222}Rn decays per 400 ns in the volume enclosed by the PSUP. (400 ns is the approximate time during which each channel accepts signals in one event.) This implies that 3.7% of PGT events will contain light from radon decay. Neglecting this light from the alpha decays it is possible to estimate the mean noise rate in the PMTs from this data. The mean value of the PGT histogram is 8.0. There are 8277 PMTs with non-zero occupancy. The mean number of PMTs per event, $\bar{n}$ can be related to the mean noise rate, $\bar{N}$ in counts per second with

$$\bar{n} = \bar{N} \times 8277 \times 400 \times 10^{-9} \tag{8.1}$$

where 400×10^{-9} is the length of the time window for accepting signals within an event. This gives $\bar{N} = 2400$. This is an upper limit because the alpha scintillation in air has been neglected.

To obtain the NHIT spectrum of EXT-ASYNC events for which a gamma ray did in fact interact in the acrylic vessel, the scaled NHIT distribution from PGT events was subtracted from that of the EXT-ASYNC events. There will still be PMT signals from noise included in this NHIT distribution and to perform a comparison with the Monte Carlo, it is necessary to take them into account.

To accomplish this a simulation was run in which the PMT noise rate was zero. For better comparison with the actual calibration, the PMTs with zero occupancy in the calibration were discarded from the analysis of the simulation. Furthermore, the PMT discriminator thresholds were set to 0.5 photoelectrons to better match those in the detector [Fo98].

One can convolute the NHIT spectrum from the Monte Carlo with the PGT spectrum to obtain a spectrum for comparison with the data. The spectrum before convolution is shown in figure 8.3.

The simulation substantially underestimates the number of PMTs hit. Figure 8.4 shows a comparison of the NHIT spectra for the data and the Monte Carlo convoluted with the PGT spectrum.

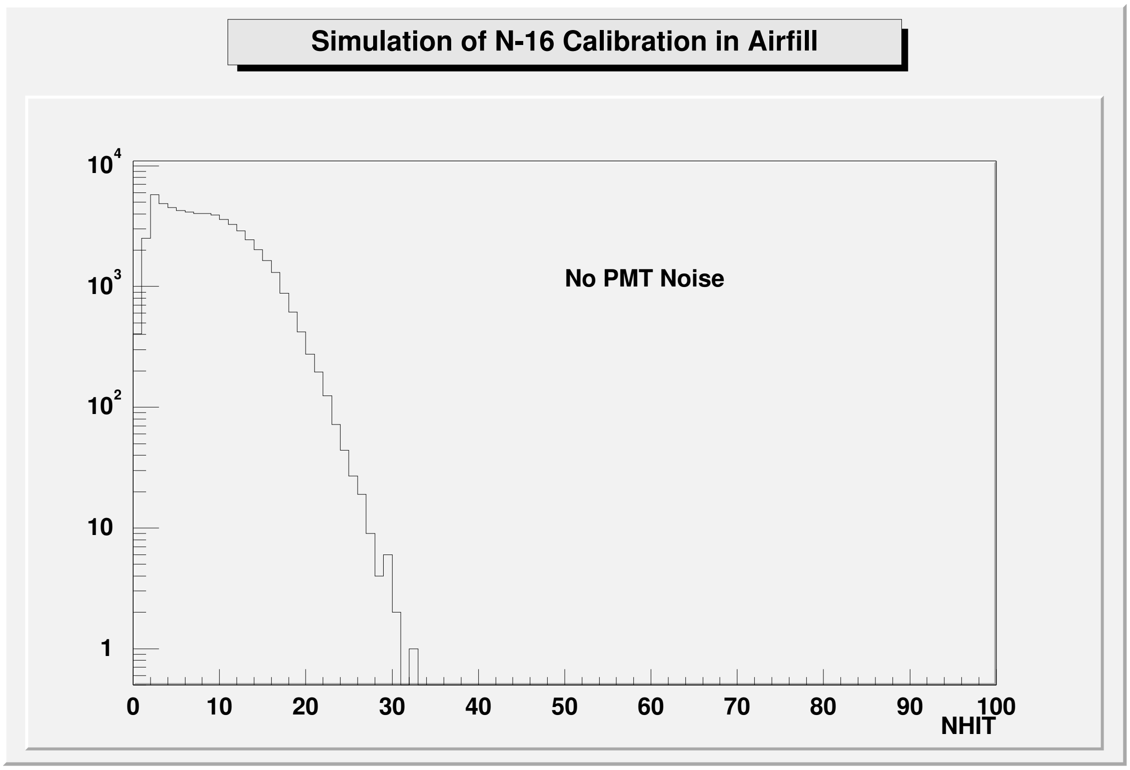

Figure 8.3: NHIT spectrum for simulation of ^{16}N airfill calibration.

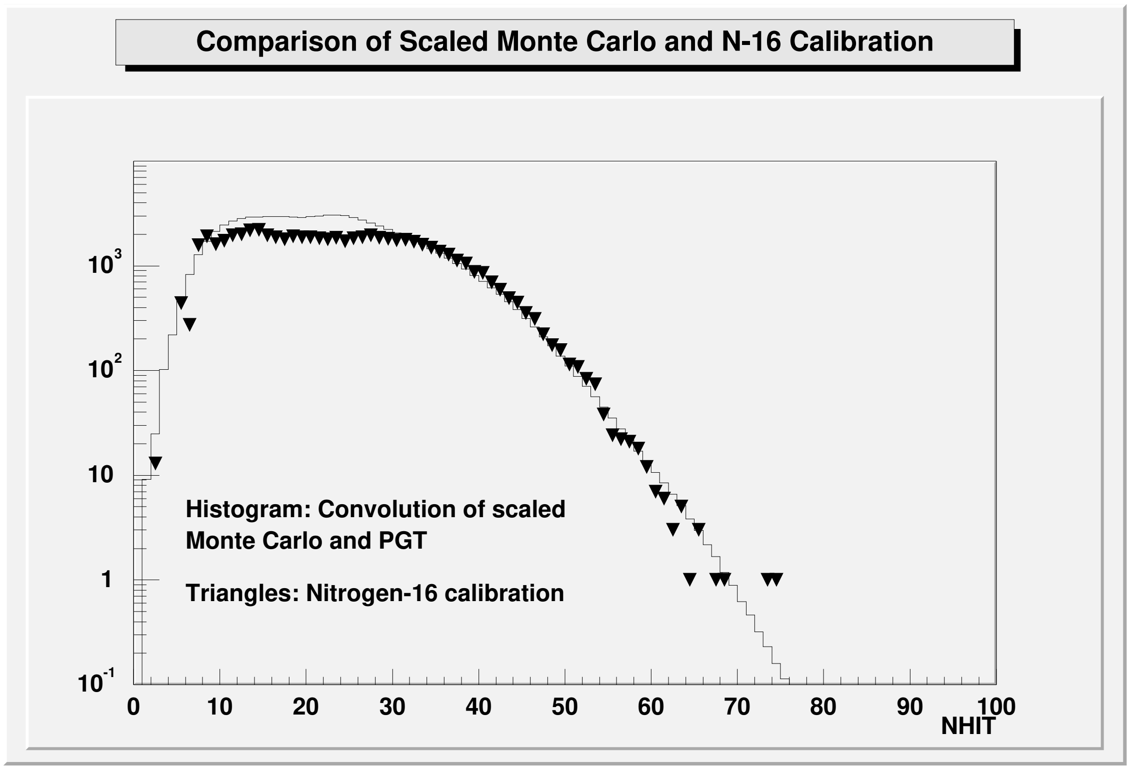

Figure 8.4: Comparison of the NHIT spectra for the ^{16}N data and the Monte Carlo convoluted with the PGT spectrum. The ^{16}N events have had their NHIT value increased by a factor of 1.9.

However, the value of NHIT from the Monte Carlo was scaled by a factor of 1.9 to better agree with the data.

A hypothesis for the source of this discrepancy can be found in the optics of the acrylic-air interface. In the simulation, this interface is optically smooth. In reality it is known that there are several optical "defects". The acrylic vessel was made of individual panels, whose thickness varied by 1/8 of an inch. At the bonds between panels, the vessel was sanded to have a smooth transition from one thickness to the next; however, the transition does distort the optics. Also, there are many locations on the vessel where it was necessary to roughen the surface of the vessel for construction purposes, particularly near bonds. These areas were sanded with polishing paper to aid quality-control inspections, but an attempt was not made to produce an optically perfect surface. Even away from the bond areas there are some optical imperfections at the surface of the acrylic that are easily visible to the eye. These imperfections were not polished because they do not cause stress on the vessel and did not impede inspection of the bonds.

Why might optical effects at the acrylic-air interface be expected to have a large effect? According to the simulation much of the Čerenkov light is totally internally reflected and thus never has the opportunity to leave the vessel and reach a PMT. The refractive index of acrylic is 1.5. This leads to a critical angle of 41.8 degrees. An electron traveling in acrylic emits light at a Čerenkov angle of 48 degrees (as $\beta \rightarrow 1$). Thus photons emitted on the Čerenkov cone by electrons traveling normal to the acrylic-air interface are totally internally reflected. They are subsequently absorbed in the acrylic in the simulation. In reality these photons encounter surface optical defects which allow them to "leak out" of the acrylic.

(The effect is important only for airfill. With water surrounding the acrylic, the more closely matched indices of refraction reduces the effect of surface defects. As well the angle for total internal reflection changes to 62 degrees.)

The shift in NHIT of 90% was studied more carefully to ensure it is plausible. The uncertainty in the 90% shift is considered first. A small number of PMTs have been tested with a calibrated light source to obtain a 3% accuracy on the absolute efficiency. Given uncertainty in the collection efficiency of the reflectors around each PMT and uncertainty in the optics at the air-glass interface, 10% is the largest plausible uncertainty in the absolute PMT/reflector efficiency. The charge threshold used in the Monte Carlo was 0.5 photo-electrons which was chosen to match as best as possible the average threshold in the detector [Fo98]. There is some uncertainty in this threshold which contributes approximately 10% to the uncertainty in the mean NHIT. These two uncertainties do not approach the 90% needed to match data and Monte Carlo.

Simulations were run with a similar light generation with the detector empty and with the detector full. The light source followed a Čerenkov frequency spectrum with the same directional pattern as the light emitted from the simulation of 6.13 MeV gamma rays. To obtain the direction of emission of each Čerenkov photon, a simulation was performed with 6.13 MeV gamma rays at the origin directed directly down towards the vessel (at airfill). The z-component of the direction of

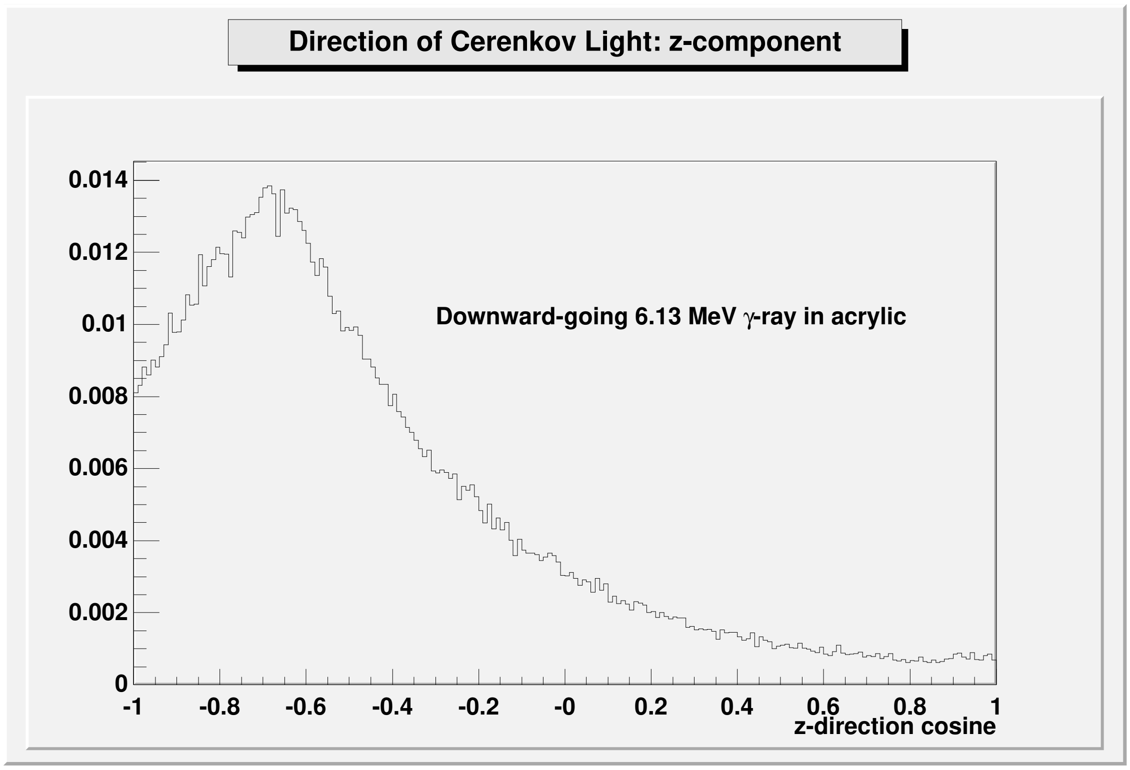

Figure 8.5: The z-direction cosine for the direction of Čerenkov light for a downward-going gamma-ray in the acrylic. The original direction of travel is plotted for all photons regardless of whether they caused a PMT hit.

every Čerenkov photon created in the vessel was histogrammed. The result is shown in figure 8.5.

The simulations for an empty and a filled detector were performed in which light was generated with a z-direction chosen from the distribution of figure 8.5 and a Čerenkov frequency spectrum. The light was generated inside the acrylic at the bottom of the vessel. For the case of the air-acrylic optics, 1736 of 500000 photons generated a signal in a PMT. For the case of the water-acrylic optics, 4092 of 500000 photons caused a PMT hit. (The absolute efficiency is not relevant: it depends very strongly on the range of frequencies of the Čerenkov photons because the acrylic is almost totally absorbing above a certain frequency [Fo98]. Including these photons in the range in the simulation changes nothing about the photons detected but substantially reduces efficiency. The same parameters were used for the two simulations to ensure consistency.) Because the reduction from acrylic-air to acrylic-water is a factor of 2.4, there is room to account for the 90% shift in NHIT.

If the reason for extra light does in fact lie in the acrylic-air optics, one would expect to see evidence of that in the distribution of light for the Monte Carlo and the data. When looking at the light distribution it is necessary to determine the direction of the event. The elastic fitter should not be used because it fits the event to a cone. Unusual optics will cause the light distribution to look unlike a cone. The time fitter's algorithm is a better choice, but it too may be skewed by the unusual optics. A more robust choice is to use the unit vector pointing from the source location to the fitted vertex as the direction. A histogram is then made of the angle between this direction vector and the vector between the vertex and the PMT hits. There is still one correction to be made. The vertices for the events do not lie exactly on the acrylic vessel. A histogram of the radial fit position is shown in figure 8.6. The peak in the distribution is at a radius slightly larger than the radius of the acrylic vessel. This is an example of "fitter pull" discussed in section 5.1.2. However, the light generated must have come from the acrylic. Therefore, to make the histogram of the angular distribution of PMT hits, the vertex position was moved radially to lie on the vessel. (Both Monte Carlo and data had this correction applied.) As well, a cut was imposed such that only those events whose radial position (before adjustment) was between 500 and 750 cm were included. The figures show that there is clearly more backward light in the data than in the Monte Carlo.

There is agreement between the histograms at low angles. In fact, the histogram for the Monte Carlo was scaled such that the number of counts in the first 10 bins in both histograms was equal. Nonetheless, the agreement is intriguing and a series of gamma ray simulations was performed to investigate the cause of this agreement. When the known location of interaction from the Monte Carlo was used, there were far fewer PMTs at low angle and the agreement between data and Monte Carlo at low angles was lost.

When the distribution was made using the reconstructed position shifted radially to lie on the acrylic vessel, the Monte Carlo agreed with the data. Thus, the dominant effect in the shape of this

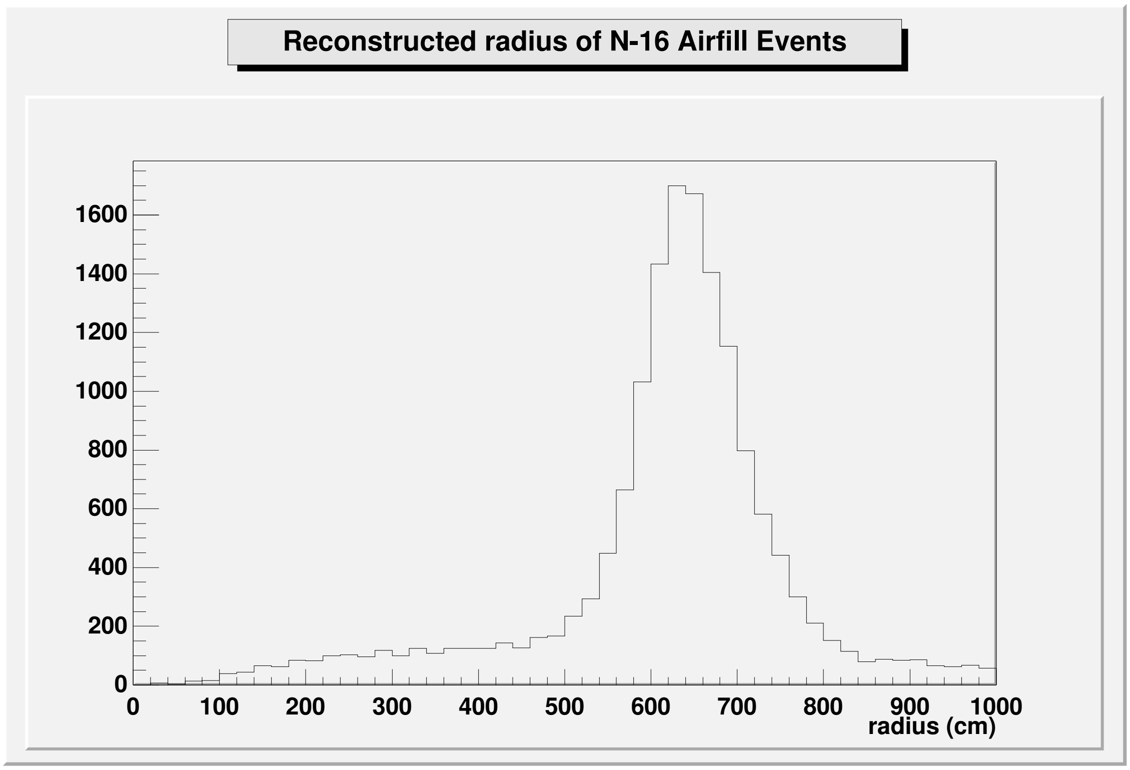

Figure 8.6: Reconstructed radial position of airfill ^{16}N events. The radius of the acrylic is 600 cm.

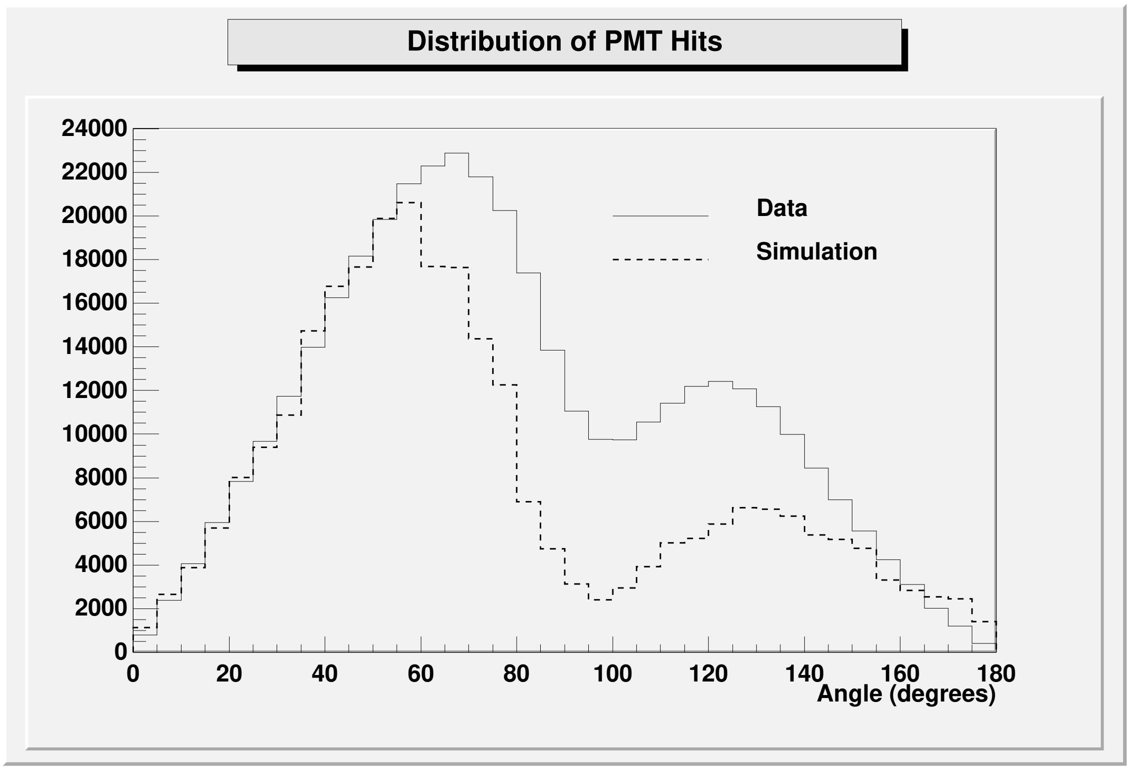

Figure 8.7: The angular distribution of PMT hits for ^{16}N airfill calibration is shown for data and for simulation. The histogram from the simulation has been scaled so the integrated number of counts in the first ten bins of the two histograms is the same. The cut-off from total internal reflection is much larger in the simulation than in the data. As well the data has much more backward going light.

histogram at low angles is the position resolution perpendicular to the radial direction. There is no justification for saying that the agreement gives meaningful information about multiple scattering or the angular distribution of photons emitted in the acrylic. The utility of figure 8.7 is in showing that there is more backward-going light in the data than in the simulation.

Even with this extra light it is possible to fit a direction to each event. As in the case where individual PMT hits were studied, the angular distribution of events was calculated assuming the vertex was at a radius of 600 cm, that is to say events were put on the vessel. (This correction was used in the simulation as well.) Only the time fitter was used to obtain an angular distribution. It is shown in figure 8.8. The terrible agreement is expected given the radically different distributions of PMT hits in the data and simulation. The angular resolution for the data is much worse.

The optical properties of the acrylic-air interface make this result unusable for a calibration of angular resolution. When the detector is filled the importance of the optics at the boundary of the acrylic will matter less because the indices of refraction of acrylic and water are much more closely matched than acrylic and air. Also, when the detector is full, the light generation is not entirely in the acrylic, but mostly in the water and light generated in the water cannot be trapped by total internal reflection in the acrylic unless the photon scatters in the acrylic.

A collaborator at the University of Oxford has studied the optics of the acrylic and the acrylic-air interface in detail [Mc99]. His explanation includes two factors: some diffuse transmission at the acrylic-air interface and reducing the attenuation of long-wavelength light in the acrylic. Reducing the attenuation increases, on average, the number of times a photon strikes the acrylic-air interface, thus increasing the probability of escape.

8.2 Partial Fill Running

8.2.1 Event Rates and Gamma Fluxes

A run was taken at partial fill with the surface of the heavy water -228 cm below the equator of the vessel. There was no calibration source, the detector was triggered on NHIT and ESUM. The

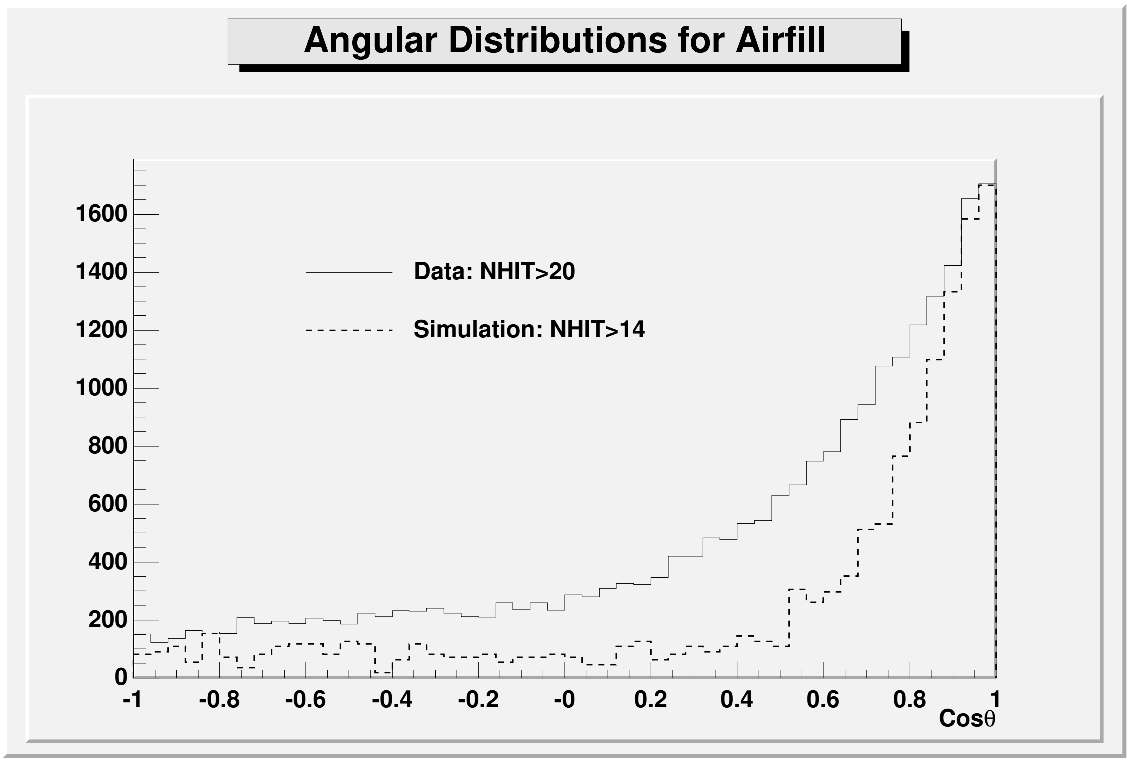

Figure 8.8: The angular distribution of airfill ^{16}N calibration. The time fitter is used and a cut is imposed that accepts events with NHIT > 20. The analysis of the simulation accepts events with NHIT > 14 to account for the differences in the NHIT spectra between the data and the simulation. The value of $\cos\theta$ is found by taking the dot product of the vector from the source to the reconstructed position and the direction vector.

Gamma Flux in Cavity		
Energy (MeV)	Flux ($h^{-1}cm^{-2}$)	Error (%)
0-1	246	10
1-2	291	10
2-3	34	10
3-4	0.88	10
4-5	5.8×10^{-3}	12
5-6	1.4×10^{-3}	23
6-7	6.1×10^{-4}	21
7-8	1.3×10^{-4}	30
8-9	0	?

Table 8.1: The gamma flux in the SNO cavity as measured in [ICD$^+$97].

principal source of events was gamma rays from the cavity. The gamma rays interact in the water producing Čerenkov light. There are two critical differences between this situation and that for ^{16}N calibration at partial fill. First, the gamma rays do not come from a localized source and, second, they have a continuous and broad energy distribution. The flux as a function of energy has been measured and is presented in table 8.1 [ICD$^+$97]. An analysis of partial fill data has two goals: to ensure that the fitting algorithms work properly and to measure the gamma flux.

The NHIT spectrum is shown in figure 8.9. This commissioning data have been passed through a filter to remove background events caused by "non-physics" sources. These sources include PMT flashers (events in which the PMT acts as a light source) and electrical breakdown. There are no other cuts on the data, other than NHIT > 40.

The spectrum is approximately log-linear. This makes interpretation difficult because the histogram for the case of a large number of events producing a low mean NHIT per event looks identical to that for a smaller number of events producing a greater mean NHIT. More precisely, if

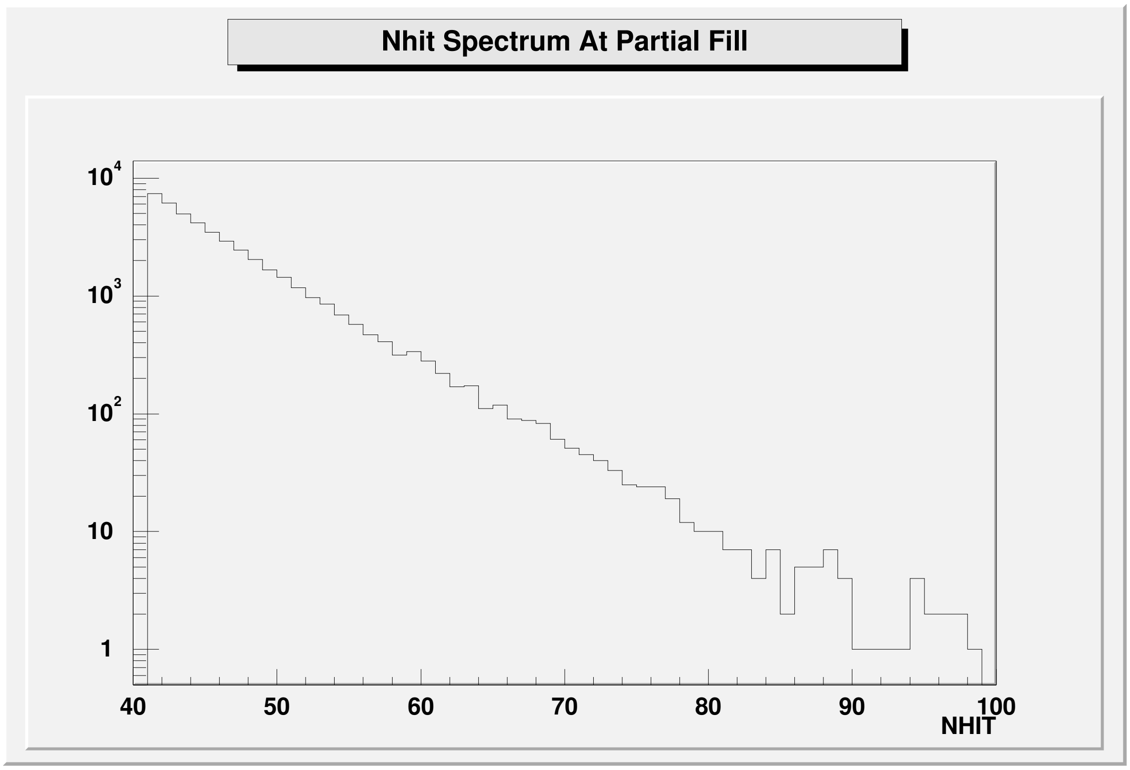

Figure 8.9: The NHIT spectrum is shown from a partial fill run. There is no calibration source. The data have been passed through a filter identifying non-physics backgrounds.

the NHIT distribution follows the function

$$f(\text{NHIT}) = Ne^{-a\times \text{NHIT}} \tag{8.2}$$

where N is a measure of the rate at which events occur, then the number of counts above a certain threshold, NCUT, is

$$\frac{N}{a}e^{-a\times \text{NCUT}} \tag{8.3}$$

Thus from the NHIT spectrum alone it is not possible to untangle the event rate and the mean NHIT per event. The event rate is interesting because that indicates the flux of high energy gamma rays in the SNO cavity. These gamma arrays can contribute a background to the neutrino signal if sufficient numbers of them penetrate the light water shielding and convert in front of the PMTs. Comparison with the Monte Carlo will be used to study the data.

The air-water interface changes event reconstruction. The basic technique for finding the position of an event is to minimize the χ^2 just like the time fitter. However, the transit time for light from the hypothesized position of the event to the hit PMTs must be calculated differently. Three methods are considered. The first method is to ignore the interface and calculate the transit times for photons from the hypothesized vertex to the hit PMTs with the speed of the photons being c/n.

The second method is to assume that light travels in straight lines from the hypothesized vertex to the hit PMTs but calculate the time of flight of the photon with the appropriate speed along the path. Figure 8.10 shows 4 straight-line paths. Path "a" from position p1 starts under water and strikes a PMT above water. Thus the travel time for light to the PMT is calculated using c/n as the speed of light for the solid portion of the path and c for the dashed part. For path "b", the entire path is under water and "c" is used as the speed. For path "c" which starts at position p2 above the water and ends at a PMT above the water, c is used as the speed of light along the entire path. For path "d", c is taken as the speed of light over the part of the path shown as a dashed line and c/n is used for that part of the path shown as a solid line.

The third method is the same as the second method except for path "d". The third method assumes that light is, in reality, generated in water. Therefore, for path "d", the transit time is calculated using c/n for the entire path.

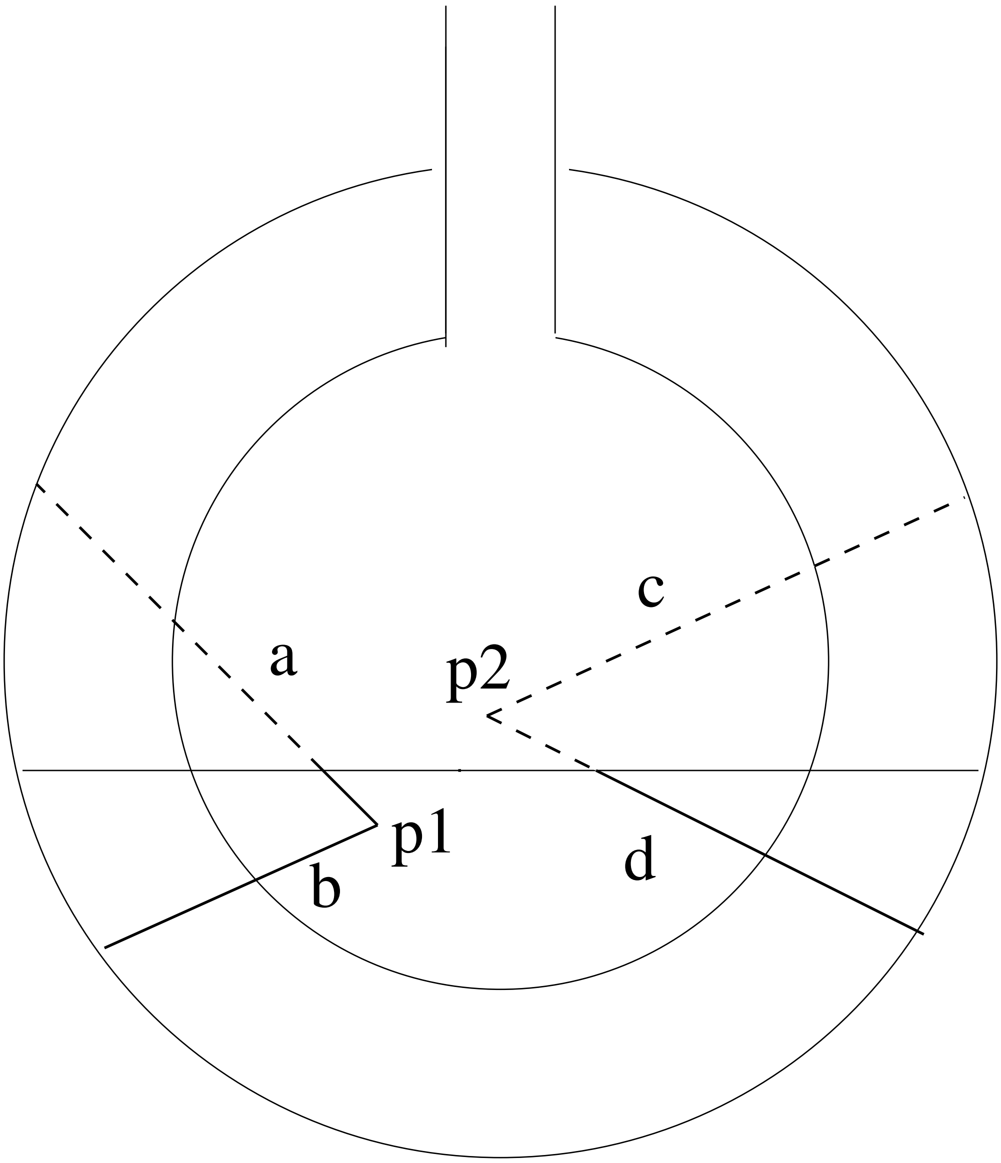

Figure 8.10: Four optical paths are shown at partial fill. The horizontal line indicates the water level. A discussion of the paths is presented in the text.

The z-profiles of the reconstructed positions are shown in figure 8.11. The cuts imposed on the data was NHIT > 40 and $\rho_{\rm fit}\left(\equiv\sqrt{x_{\rm fit}^2+y_{\rm fit}^2}\right) < 400$cm. (The cylindrical cut ensures that only a small number of events converting in the acrylic above the water enter the analysis.) For the first method which assumes a fully-filled detector, the profile is clearly non-physical. A large number of events reconstruct above the water level because the PMTs above the water drive the fit upwards because the transit time for those PMTs is calculated incorrectly. The second method yields a reasonable profile, although the tail extending above the water is quite broad. The third method gives only slightly different results than the second method. Approximately 3% more events pass the reconstruction and these events are near the water surface. The difference between the second and third method for events which reconstruct under the water is small because the time of flight for the light generated under water is the same. In the discussion that follows the reconstruction uses the second method.

8.2.2 Individual Events

The air-water interface will introduce effects in the data that will not be present when the detector is filled. Nonetheless, a study of individual events, and in particular, the behavior of the direction-fitting algorithms on these events is useful. For these events, the vertices were reconstructed with the time fitter and the directions were reconstructed with both the time and elastic fitters. All events discussed in this section are from run number 1698.

Plots were made of individual events. These "target plots" view the event from the vertex of the fit. The "forward" plot shows the forward hit PMTs as seen when facing along the direction of the event. The "backward" plot shows the backward hit PMTs as viewed when facing opposite the direction of the event. The circles show 30, 60 and 90 degrees. Therefore the 90-degree circles for the forward and backward plot are the same. The angle between the direction of view and the PMT is indicated by the radial position of the marker on the plot. The fitted-direction vector is not enough to completely define a co-ordinate system. While the polar angle is defined the azimuthal angle is not. The component of the vector $(1,0,0)$ that is perpendicular to the direction vector

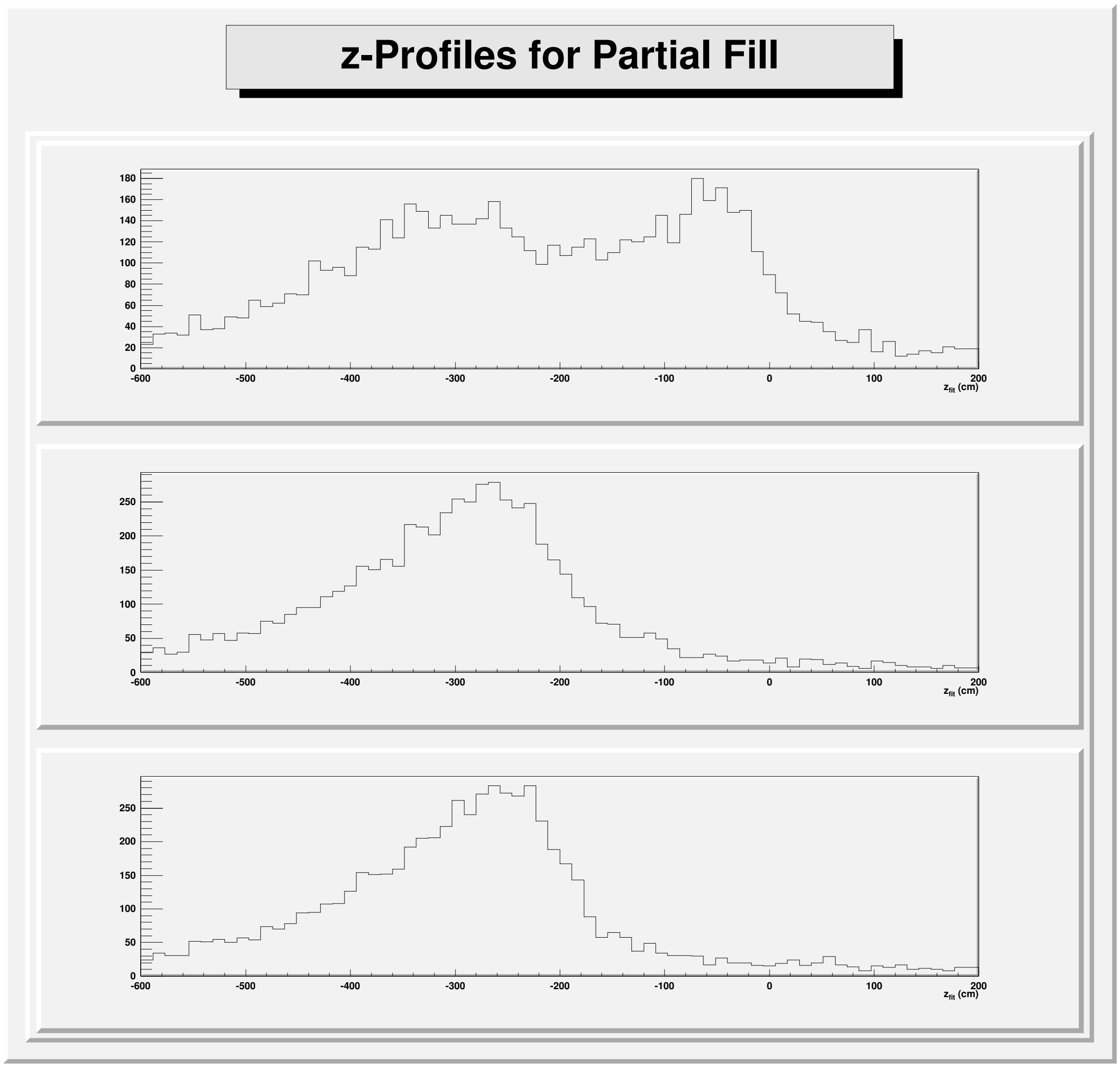

Figure 8.11: The z-profile of reconstructed events at partial fill. The level of the heavy water is -228 cm. The top plot is for a fitter assuming the entire detector was filled. The middle plot assumes a straight-line path between the vertex and PMT but corrects the travel time of light along the path to account for the two indices of refraction. The bottom plot assumes for PMTs under water that the entire path is in water. The three methods are fully described in the text.

was found. This vector defined the zero of azimuthal angle. Thus the zero of azimuthal angle was consistent within any event, but varied from event to event because the direction vector changed.

To illustrate the meaning of the target plots, an event in a hypothetical two-dimensional detector is shown in figure 8.12. The vertex of the event is at $\vec{v}$ and the direction is given by $\vec{d}$. The target plot (now one-dimensional) is shown in the same figure. The PMTs are labelled in both plots to show the correspondence. This figure is not to scale.

At partial fill, the Čerenkov light will be distorted by the water surface. However for downward-going gamma rays, this effect will be minimal. The event with global trigger identification (GTID) 2065 (figure 8.13 shows a beautiful Čerenkov cone. Some of the in-time PMT hits are near the water surface and the photons from the vertex to these PMTs may have been reflected at the water surface. The z-component of the direction from the elastic fitter is -0.66 which corresponds to an angle of 48 degrees relative to the negative z-axis. Thus a Čerenkov cone (half-angle 41 degrees) is entirely beneath the water, but just barely. The data reflect this. The in-time PMTs (solid squares on the target plot) are clustered between $\theta = 30$ and $\theta = 60$. The hit pattern for the elastic fitter is shifted slightly compared to the time fitter causing more of the in-time PMTs to lie near $\theta = 41$ degrees. The rectangular projection of all the PMT hit positions is also shown. (This is a projection of the sphere of PMTs onto a Cartesian plot with "latitude" and "longitude" plotted as for maps.) On this plot, the Čerenkov ring is also evident.

If an event meets the surface at near-grazing incidence, the effect of the water surface will be large. Such an event is also found in figure 8.13. Event 3885 has almost all the hit PMTs clustered in a small region near the water surface.

Such an event would have a considerable amount of light reflected by the water surface. The time-fitted direction points straight at the cluster. The elastic fitter tries to put this cluster on the ring. It succeeds, but there is no good information to discern where on the ring to put the cluster of hit PMTs. The fitter "guesses". Thus the elastic fit direction is not reliable here. However, the elastic fitter does succeed in finding a direction for which most of the PMTs do lie on the fitted cone. While this does not necessarily represent the physics of the event, numerically the fitter works.

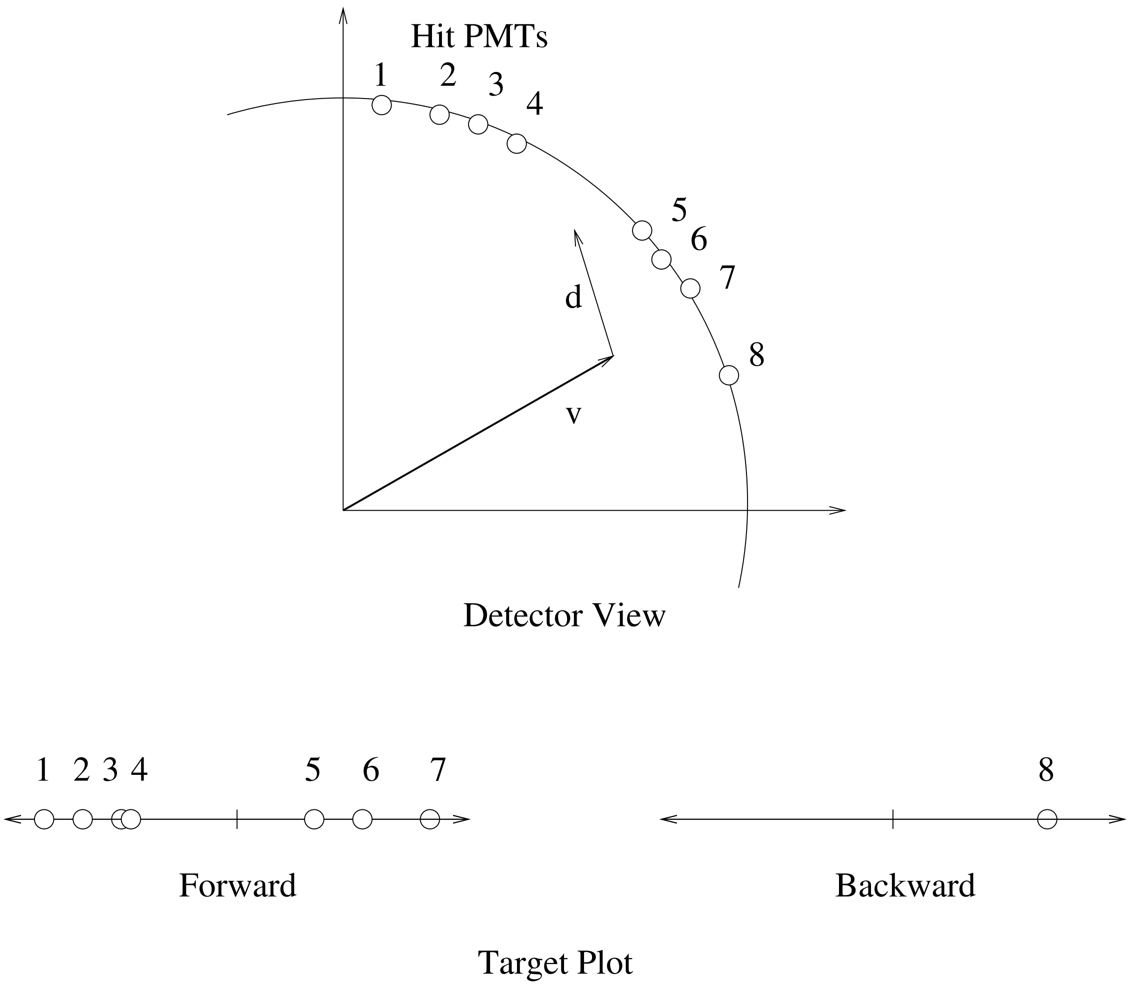

Figure 8.12: A schematic example of a target plot for a two-dimensional detector. The view of the detector is shown on top with 8 PMTs hit. The event vertex is shown with $\vec{v}$ and the direction is shown with $\vec{d}$. The target plots underneath show the 8 PMTs as seen from the event vertex looking along the fit direction. Because the detector is two-dimensional, the target plots are one dimensional. This figure is not to scale.

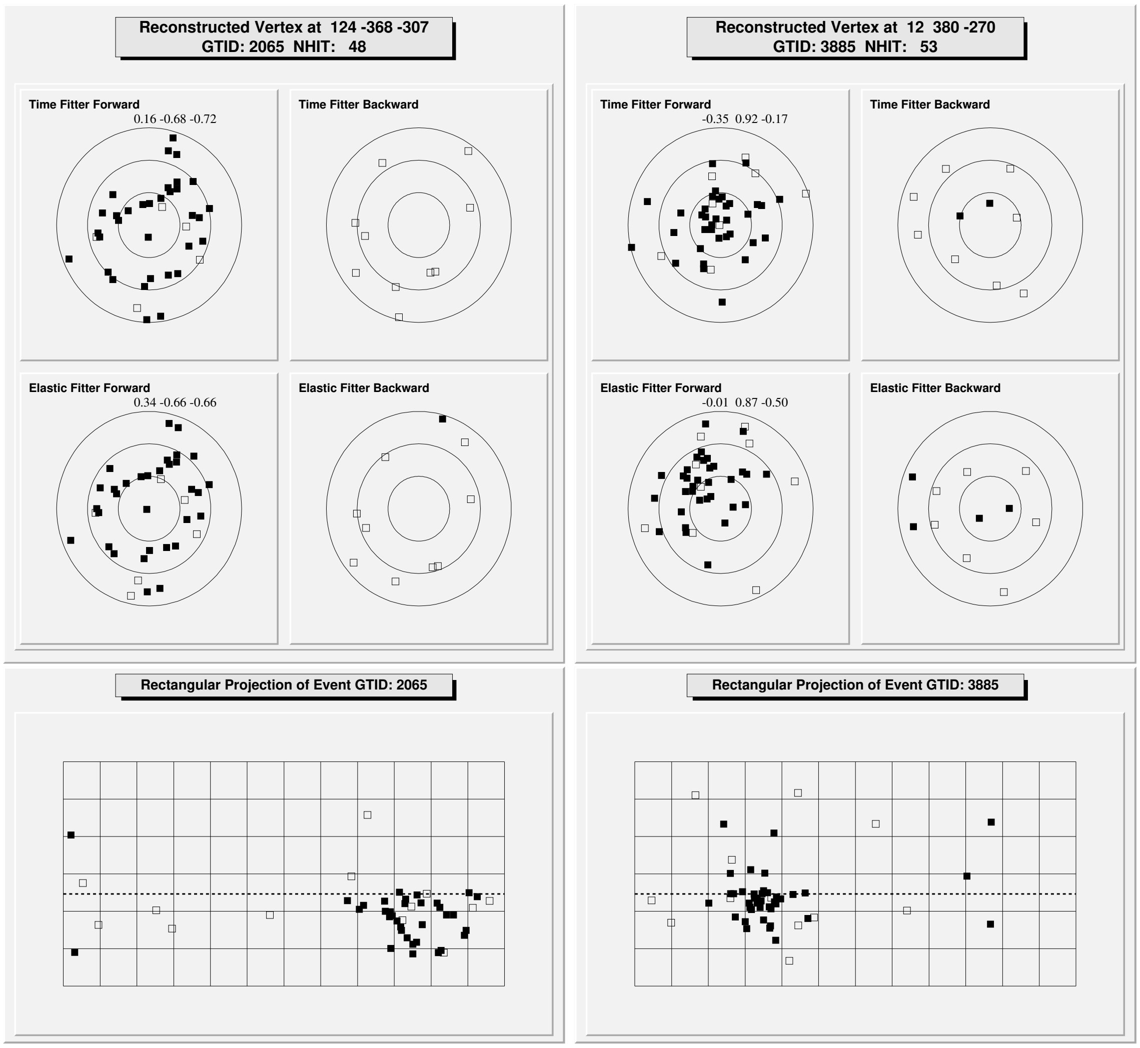

Figure 8.13: Events 2065 and 3885 of run 1698. The "target plots" show the projections of PMTs as viewed from the reconstructed vertex. Each circle represents 30 degrees angle from the fitted direction. The outer ring in both the forward and backward plot represents 90 degrees. The bottom plot is a rectangular projection of the SNO detector. The water level is indicated with the heavy dashed line. In-time PMT hits are shown by solid squares while out-of-time hits are shown with hollow squares. The position (in cm) at which the event reconstructed is noted in the title of the plot. The direction cosines in the x-, y-, and z-directions are noted for each fitter on the forward plot.

There are some events in which the PMT hits seem almost random, yet the fitter is able to deduce a pattern. Event 4168 (figure 8.14) is one such event. The target plots shows that the fitter does find a cone-like pattern to this event. This plot shows also the importance of rejecting out-of-time hits from the direction fit. The ring structure would be lost if in-time and out-of-time hits were not plotted with different symbols. Again, the elastic fitter shifts the direction to better represent a cone.

Event 4588 (figure 8.14) is one that was probably affected by the water surface. This is indicated by an absence of ring-like symmetry in the PMT hits and the proximity of the PMT hits to the water surface. The large clump of PMTs in the middle of the ring may well have been the result of light reflected from the surface. The elastic fitter has shifted the direction of the fit by 22 degrees relative to the time fitter to better put the PMT hits on the cone. Numerically, the elastic fitter behaved properly for this fit.

Summaries of the entire run can be derived from the data. First, the dot products between directions of the elastic and time fit for each event can be taken. Figure 8.15 shows a histogram of this. Second a histogram was made (8.16) of the angle between the fit direction and the PMTs for all in-time PMTs in all events. It is clear that the elastic fitter is capable of putting more PMTs on the Čerenkov cone than the time fitter.

These summaries include all events including those which have interacted significantly with the surface. To study more typical SNO events, a cut was made to accept only events with a z-component if direction less than -0.707, within 45 degrees of straight down. Figure 8.17 shows the angle to the in-time hit PMTs from these events. It closely resembles the plots for all events.

The properties of the elastic and time fitters have been examined at partial fill. The elastic fitter adjusted the direction of the event to maximize the amount of light on the Čerenkov cone. For events in which the water-air interface affected the optics, this does not give the best fitted direction. Nonetheless, it shows that numerically, the elastic fitter is behaving as expected.

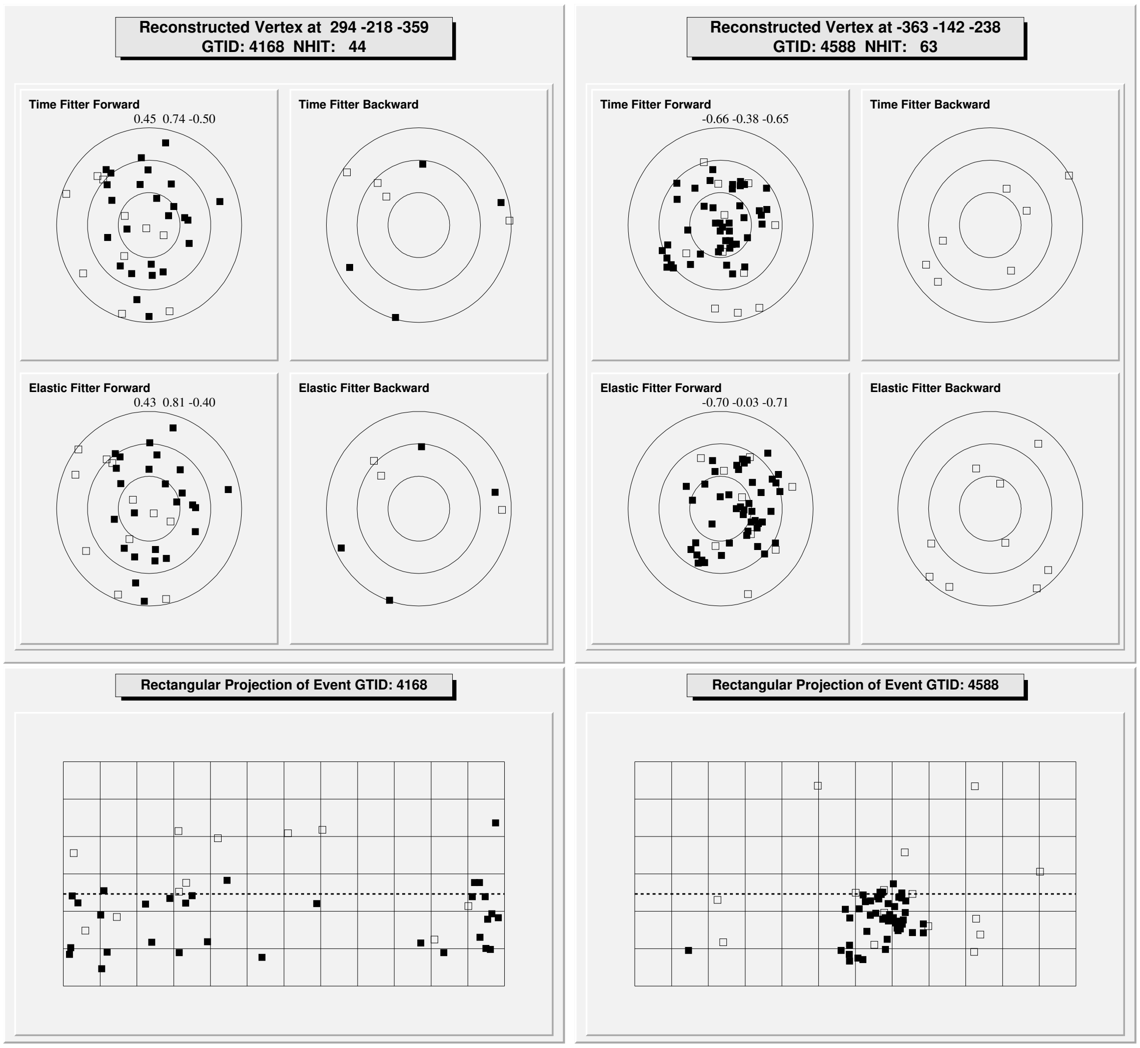

Figure 8.14: Events 4168 and 4588 of run 1698. The "target plots" show the projections of PMTs as viewed from the reconstructed vertex. Each circle represents 30 degrees angle from the fitted direction. The outer ring in both the forward and backward plot represents 90 degrees. The bottom plot is a rectangular projection of the SNO detector. The water level is indicated with the heavy dashed line. In-time PMT hits are shown by solid squares while out-of-time hits are shown with hollow squares. The position (in cm) at which the event reconstructed is noted in the title of the plot. The direction cosines in the x-, y-, and z-directions are noted for each fitter on the forward plot.

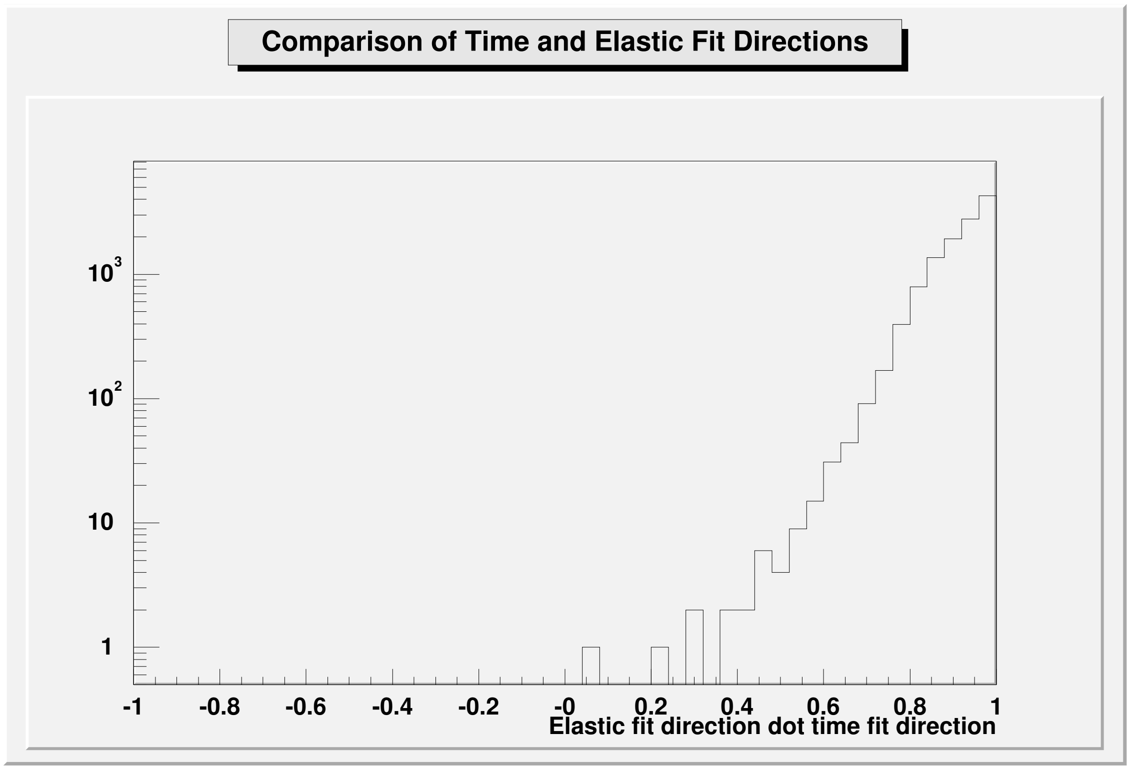

Figure 8.15: The dot product between the fitted direction for the time fitter and elastic fitter is histogrammed. For events to be included in the histogram the reconstructed position had to lie below the water level (-228 cm) but above -500 cm and have $\sqrt{x^2+y^2} < 400$.

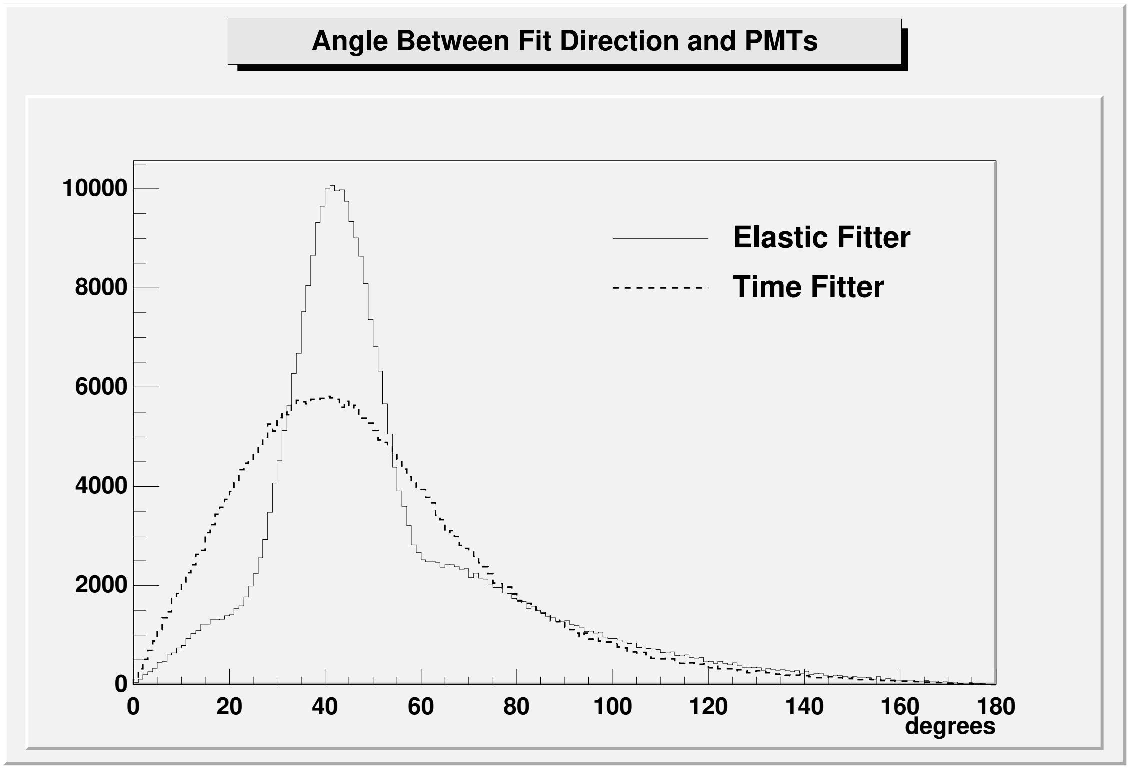

Figure 8.16: The angle between the fitted direction and the vector to the in-time PMTs in the events is histogrammed for the time and elastic fitter. The histogram is summed over all events subject to the same reconstruction cuts as the previous figure.

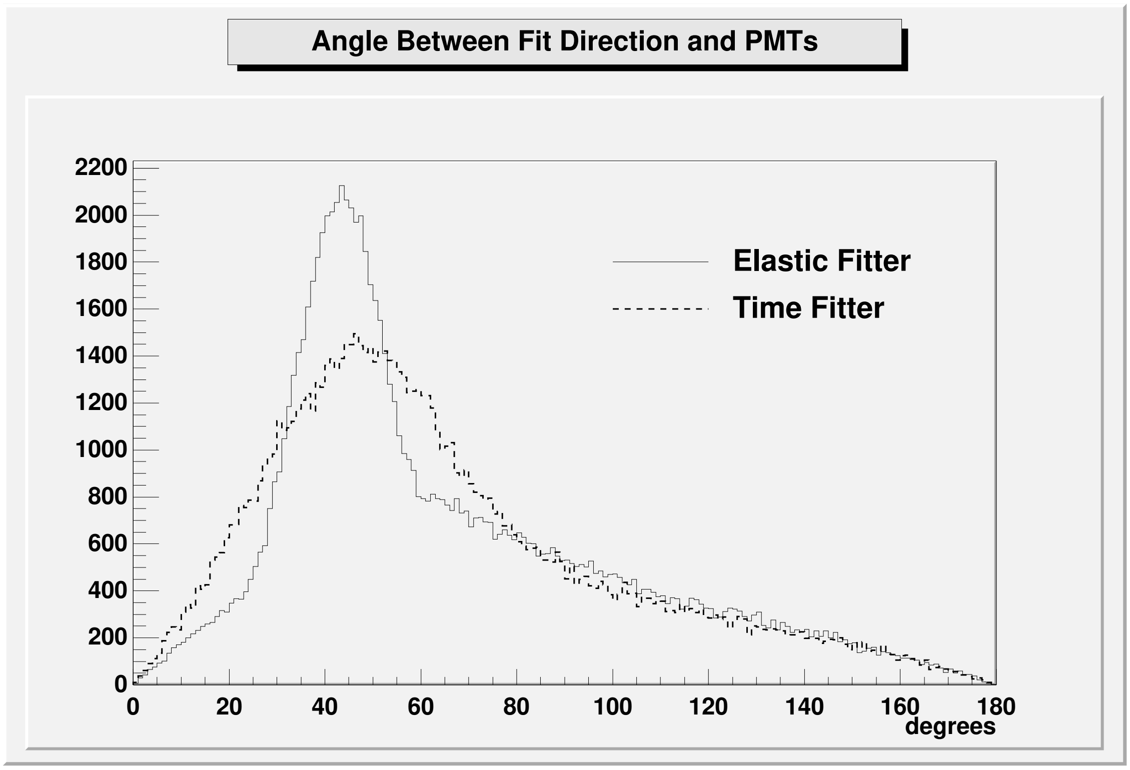

Figure 8.17: The angle between the fitted direction and the vector to the in-time PMTs in the events is histogrammed for the time and elastic fitter. Only events directed within 45 degrees of straight down were considered. The position cuts were as in the figures above.

8.3 Summary

The air-fill and partial fill stages were important for commissioning of the detector and the calibration systems. The analysis of the partial-fill data gave a demonstration that, numerically at least, the elastic fitter succeeds in fitting a cone to the PMT hit pattern. However, apart from this, it was not possible to use the air-fill and partial fill data to study either the angular resolution of the detector or the ES signal which have been discussed in the previous chapters.

Chapter 9

Conclusions

The angular resolution of SNO and the extraction of the electron scattering signal have been considered. Several conclusions can be drawn from the analysis.

The angular resolution of gamma rays can be measured and compared with Monte Carlo Calculations. The calibration scheme described in chapter 6 will yield the angular resolution for 6.13 MeV gamma rays. It will allow the values of $\cos\theta_{80}$ and $\cos\theta_{50}$ to be verified with precision on order of 0.01 if the position resolution is as expected. The analysis requires knowledge of the events which misreconstruct in position. The position resolution can be tested using the gamma-ray calibration data.

The angular resolution of 6.13 MeV gamma rays yields information about electrons. A detailed comparison of the angular resolution of gamma rays in the simulation and Monte Carlo yields information about the uncertainty in angular resolution of gamma rays and the sources of the uncertainty. Monte Carlo simulations of electrons performed by varying the parameters affecting angular resolution within ranges allowed by optical and gamma-ray calibration will give a quantitative estimate of the effect these sources of uncertainty have on electrons.

The uncertainty of extraction of the ES signal is dominated by statistical uncertainty. Unless the calibration of angular resolution with the ^{16}N source shows a large discrepancy between calibration and Monte Carlo, the statistical uncertainty will be larger than the systematic uncertainty in the first 2 or 3 years of data taking.

Choice of reconstruction algorithm affects the statistical accuracy of the result. The elastic fitter algorithm with its better angular resolution yields a smaller statistical uncertainty in the ES extraction than the time fitter algorithm. It should be used for neutrino analysis. The systematic uncertainty from elastic fitter may be slightly larger than the time fitter but not enough to overcome the statistical advantage of using it.

The elastic fitter should be run with several parameter sets. The elastic fitter relies on a series of parameters to control its minimizations. While operating values of these parameters can be deduced from the mathematics of the fit, it is important to ensure that the angular distribution from the calibration is not affected by parameter choice.

The elastic fitter was shown to work on data at partial fill. The discussion of individual events and the histogram of directions to the PMTs for all events shows that the elastic fitter is capable of determining an orientation of a cone that maximizes the number of PMT hits on or near the cone, even in the non-optimal circumstance of partial fill.

The angular distributions for both the elastic fitter and time fitter do not have a systematic bias. While the angular distributions for gamma rays and electrons can be broad, there is no systematic shift in the reconstructed direction of the events. Thus, for a choice of fitter, the output of the reconstruction, $\vec{u}_{\rm fit}$ is the best estimate of the event direction and no second order corrections are required in the function, $\mathcal{C}$, to improve the reconstruction of direction.

One year of data will be sufficient to make a strong statement about neutrino oscillations by comparing the ES and CC rates if the electron-neutrino survival probability

is as small as predicted in the large-angle MSW solution. How much data will be required depends on exactly what the neutrino oscillation parameters are. The large-angle scenario shows a 45% effect in the ratio of ES to CC. Statistically, this is approximately a 4.5σ effect for a one-year data sample. Including systematic effects reduces the size of the effect to 3.7σ.

Two to three years of data will be required to make a strong statement about neutrino oscillations by comparing the ES and CC rates if the electron-neutrino survival probability is similar to that for the small-angle MSW solution. The small-angle scenario shows a 20% effect in the ratio of ES to CC, smaller than the large-angle case because the surviving electron neutrinos have, on average, a higher energy than in the large angle case. This results in more CC events becase the CC cross section increases with energy. Statistically, this is approximately a 3σ effect for a two-year data sample. Including systematic effects reduces the significance to 2σ.

Appendix A

Some Specific Parts of the Detector

This appendix describes some detector components in detail, all of which were developed or implemented by the author. The parts described are components of the mechanism for deployment of calibration sources, known as the manipulator, designed and built by many members of the Queen's University SNO group. The purpose of the manipulator is to move calibration sources on two perpendicular planes within the acrylic vessel and vertically up and down in 7 locations between the acrylic vessel and the PSUP.

Calibration sources are moved with a rope-and-pulley system that uses either one-rope for vertical motion or three ropes for motion in a plane. The layout of the manipulator is shown in figure A.1. As well the manipulator system needs to control the calibration-source umbilicals (bundles of electrical and gas lines, depending on the source) from the deck to the manipulator carriage. A weight is bolted under the carriage and the sources can easily be attached to and removed from a flange on the weight.

Manipulator motion with one rope is vertically up and down. The umbilical acts as a *follower*; its length is controlled such that it follows the motion of the carriage with minimal effect on that motion. In three rope motion the carriage is moved with the side ropes and the central rope and the umbilical are followers.

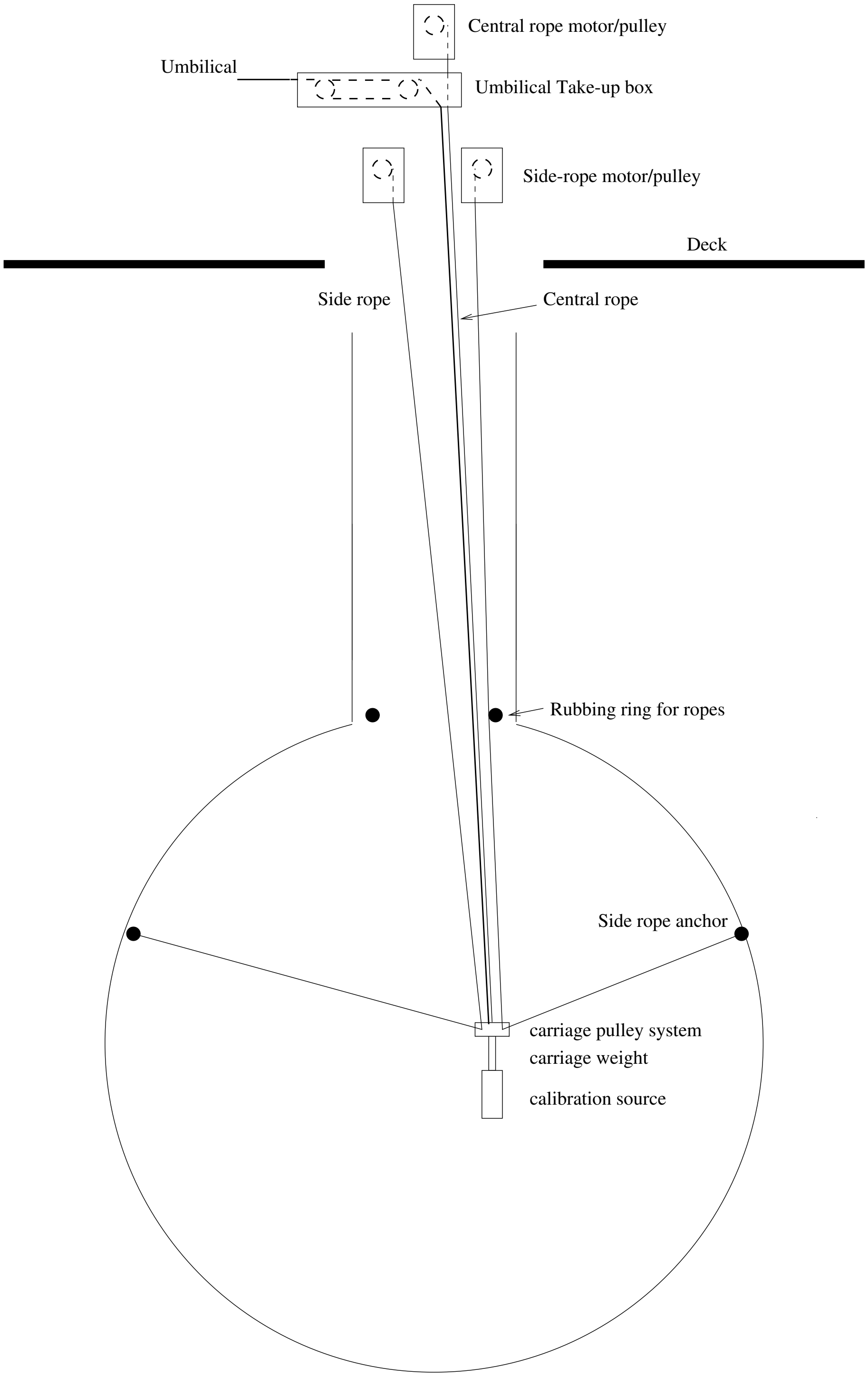

Figure A.1: The manipulator system is shown deploying a source in three-rope mode.

A.1 Location of The Acrylic Vessel

A.1.1 Requirements

In three-rope mode, the manipulator uses ropes attached to both the deck and to the vessel. Since the vessel is hung on ropes attached to the deck, the position of the vessel relative to the deck is not fixed. This imposes two requirements. First, the rope-and-pulley system must have the ability to slacken or tighten the ropes quickly, without human or computer-controlled intervention should the vessel move. This is accomplished by having the ropes wound around a set of pulleys on a spring. The stretch on the spring is normally kept such that a sudden motion of the vessel of up to 8 inches can be accommodated by motion of the springs. (Seismic events can move the vessel. It is important that SNO hardware be protected from such occurrences.)

The second requirement is that the location of the vessel be known for accurate placement of calibration sources within the vessel because the side ropes are attached at one end to the vessel and at the other end to the (fixed) deck.

A separate system of ropes, called *sense ropes*, is used to measure the location of the top of the vessel chimney. Seven such ropes are attached at one end to the deck and at the other end to the top flange of the acrylic vessel. The rope at the end on the deck is wound around a coil on a retraction mechanism. A 10-turn potentiometer is attached to the axle of the retraction mechanism allowing a measurement of the length of the rope. Figure A.2 shows the sense-rope system. From these 7 lengths the position and orientation of the neck of the acrylic vessel can found. Assuming rigidity of the vessel, the location of the side-rope attachments can be calculated thus allowing accurate control of rope lengths. (The hardware for the snouts was developed by several members of the Queen's University group.)

A.1.2 Installation and Calibration

On top of the neck of the acrylic vessel is a stainless-steel flange. On this flange are three mounts for attachment blocks for the 7 sense ropes. Three ropes are attached to block one and 2 ropes are

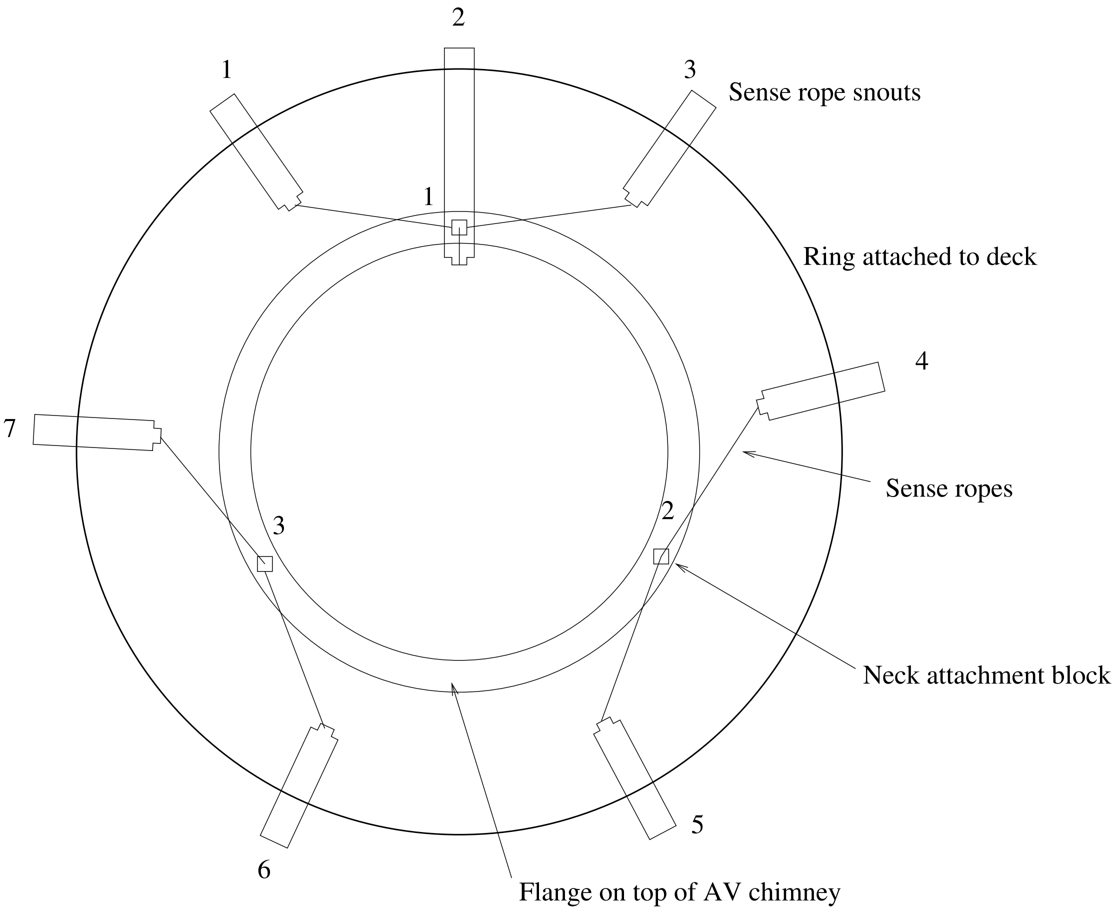

Figure A.2: A schematic top view of the sense-rope system is shown. The figure is not to scale. The neck attachment blocks are numbered 1 to 3 on the inside; the snouts are numbered 1 to 7 on the outside of the figure. The snouts are approximately 50 cm above the neck-attachment blocks.

Sense-Rope Geometry			
Neck Attachment Blocks			
1	-17.02	-86.51	1288.35
2	-64.93	58.95	1288.15
3	84.94	27.41	1288.12
Snouts			
1	25.96	-106.10	1337.32
2	-14.19	-77.97	1336.87
3	-62.82	-88.57	1337.03
4	-105.17	-30.28	1337.19
5	-45.73	99.75	1337.69
6	78.43	74.62	1337.94
7	110.49	-10.96	1337.14

Table A.1: The location of the 7 snouts and 3 neck-attachment blocks of the sense-rope system at time of survey. All dimensions are in centimeters. The origin is chosen such that were the vessel exactly according to the drawings, the origin would be at the center of the vessel.

attached to each of blocks two and three. During installation each rope was strung through its *snout* on the deck and knotted through the blocks. The blocks were then bolted onto the mounts on the flange. The location of the seven snouts and three blocks was found from a survey performed with a theodolite. The survey was difficult because the rope holes on the snouts and on the attachment blocks were large ($\simeq 4$ mm) and rounded to prevent fraying of the sense ropes. The location of the snouts and top blocks at time of survey is shown in table A.1.

The survey alone is not adequate. During installation, a calibration was performed of the change in voltage of the potentiometer for a given change in rope length. Also, once the ropes were attached the voltage on the potentiometer was read. This coupled with the surveyed position of the blocks and snouts gave a full calibration of the sense ropes. It also reduced an important systematic error. The survey was imprecise on the order of 1 or 2 millimeters. However, measurements of change in position of the acrylic-vessel neck are determined entirely by change in the rope lengths. Thus an uncertainty in the absolute rope lengths does not affect the measured change in position of the vessel neck. The absolute location of the vessel is found once from the survey and the location at any future time is found from the change in position relative to that surveyed location.

A.1.3 Real-Time Monitoring of the Neck

Real-time monitoring of the acrylic vessel neck is performed in the manipulator-control program, MANIP. MANIP is a custom-written C++ program that runs on an Intel Pentium computer under DOS. The principal authors of MANIP are P. J. Harvey and T. J. Radcliffe. All parts of the code related to the acrylic vessel were written by the author.

All hardware used by the manipulator is polled in a loop that takes less than 8 milliseconds of real time including time spent in calculations to process the information. In this loop the acrylic vessel is polled. The polling of the acrylic vessel involves

- reading the ADC values for all sense ropes and converting them to a length in centimeters,
- calculating the location of the attachment blocks for the sense ropes and the center of the vessel and the rotation of the vessel,
- calculating the location of the attachment blocks for the side ropes of the manipulator, and
- writing the results to an interface for use by the rest of the program.

The first step is straight-forward. The reading of the low-level hardware (ADCs etc) will be discussed later. The second step is complicated. There are 7 ropes but the motion of a rigid body is completely described by 6 quantities: 3 angles in a rotation matrix and a translation. Thus, there is extra information for error checking. Also, the problem is non-linear. One can either linearize the problem and get an approximate solution or do a non-linear solution.

A.1.4 Methods To Locate the Neck

A.1.4.1 Non-Linear Fitting

A non-linear fitting technique is well-suited to this problem. The function minimized is a chi-square formed by the summing the squares of the residuals in the lengths of the sense ropes. The residuals are calculated by determining the sense-rope lengths from the hypothesized position and rotation of the vessel and subtracting the measured rope length. Because the expected motion of the vessel is small compared to the characteristic dimension of the vessel, the fitting algorithm is given an initial guess which is the location and rotation found by the survey at installation of the system.

A.1.4.2 A Matrix solution of the Linearized Problem

The other methods involve approximating the problem to a linear one. Consider the equations for the 7 ropes, r_0 to r_6. Define the unit vector, $\hat{r}_\imath$, as the unit vector pointing along the length of the $\imath^{\text{th}}$rope from the snout to the surveyed attachment position. Also define $(x_\jmath, y_\jmath, z_\jmath)$ as the location of the $\jmath^{\text{th}}$ neck attachment block. In the linearization, it is assumed that if rope $\imath$ lengthens by l centimeters then the position of the attachment block moves l centimeters in the direction defined by $\hat{r}_\imath$. If the ropes were orthogonal, then the calculation does not require matrix solution. For ropes that are not orthogonal, a matrix solution is required. The unit vectors, $\hat{x}$, $\hat{y}$, and $\hat{z}$ are the usual Cartesian basis.

$$\begin{pmatrix} \hat{x}\cdot\hat{r}_0 & \hat{y}\cdot\hat{r}_0 & \hat{z}\cdot\hat{r}_0 & & & & & & \\ \hat{x}\cdot\hat{r}_1 & \hat{y}\cdot\hat{r}_1 & \hat{z}\cdot\hat{r}_1 & & & & & & \\ \hat{x}\cdot\hat{r}_2 & \hat{y}\cdot\hat{r}_2 & \hat{z}\cdot\hat{r}_2 & & & & & & \\ & & & \hat{x}\cdot\hat{r}_3 & \hat{y}\cdot\hat{r}_3 & \hat{z}\cdot\hat{r}_3 & & & \\ & & & \hat{x}\cdot\hat{r}_4 & \hat{y}\cdot\hat{r}_4 & \hat{z}\cdot\hat{r}_4 & & & \\ & & & & & & \hat{x}\cdot\hat{r}_5 & \hat{y}\cdot\hat{r}_5 & \hat{z}\cdot\hat{r}_5 \\ & & & & & & \hat{x}\cdot\hat{r}_6 & \hat{y}\cdot\hat{r}_6 & \hat{z}\cdot\hat{r}_6 \end{pmatrix} \begin{pmatrix} \Delta x_0 \\ \Delta y_0 \\ \Delta z_0 \\ \Delta x_1 \\ \Delta y_1 \\ \Delta z_1 \\ \Delta x_2 \\ \Delta y_2 \\ \Delta z_2 \end{pmatrix} = \begin{pmatrix} \Delta L_0 \\ \Delta L_1 \\ \Delta L_2 \\ \Delta L_3 \\ \Delta L_4 \\ \Delta L_5 \\ \Delta L_6 \end{pmatrix} \tag{A.1}$$

This is not sufficient. Using this approach has taken away the non-linearity, but we have a system with 9 parameters to find instead of 6. The rigidity constraints must be included. Consider the following two-dimensional argument.

$$\sqrt{(x_0 - x_1)^2 + (y_0 - y_1)^2} = L_{01} \tag{A.2}$$

$$\sqrt{(x_0 + \Delta x_0 - x_1 - \Delta x_1)^2 + (y_0 + \Delta y_0 - y_1 - \Delta y_1)^2} = L_{01} \tag{A.3}$$

$$\sqrt{(X + \Delta_x)^2 + (Y + \Delta_y)^2} = L_{01} \tag{A.4}$$

where $X = x_0 - x_1$, $Y = \cdots$, $\Delta_x = \Delta x_0 - \Delta x_1$, $\Delta_y = \cdots$. Then

$$X^2 + 2X\Delta_x + \Delta_x^2 + Y^2 + 2Y\Delta_y + \Delta_y^2 = L_{01} \tag{A.5}$$

which can be expanded to include the third dimension and linearized to

$$2X\Delta_x + 2Y\Delta_y + 2Z\Delta_z = 0 \tag{A.6}$$

This gives a total of 10 equations. For a matrix solution to be guaranteed to work, one must be dropped. It can be used as a check after the fact.

To increase accuracy, it is possible to then define new set of directions based on the position just calculated. The process can be iterated until the desired accuracy is achieved. For small motions, the iterative procedure will converge. Thus one has eliminated non-linearity at the expense of many iterations.

A.1.4.3 Simplified Matrix Solution

There is a simplification of this method. One can solve for the location of the three neck attachment blocks separately. The first block can be found using the three ropes attached to it. The second block can be located using the fixed length between the first and second block and the two ropes attached to the second block. Similarly the third point can be found. A check can then be performed to ensure that the distance between the second block and the third block is constant within some margin of error. The prime advantage of the simplification is computational speed. The largest matrix to solve is 3×3.

A.1.4.4 Linear Solution Using Derivatives

There is another, computationally faster, approach that will work over a narrower range of motion. (This algorithm was suggested by Aksel Hallin [Ha98].) The position and orientation of the neck are expressed as a function of 6 variables, $\vec{\xi}$: 3 positions and 3 angles. Similar to the non-linear case, the rope lengths are calculated as a function of the parameters. Then derivatives can be calculated numerically, $\frac{\partial L_i}{\partial \xi_j}$, where ξ_j represents one of the six variables. These derivatives can be written in a 7×6 matrix, M, with elements $M_{ij} = \frac{\partial L_i}{\partial \xi_j}$.

For small motions, one can write

$$\Delta\vec{L} = M\Delta\vec{\xi} \tag{A.7}$$

In fact, the required quantity is $\vec{\xi}$ and $\Delta\vec{L}$ is measured. Therefore, one row of the matrix is eliminated and then the matrix is inverted. The location and orientation of the neck can then be found with

$$\Delta\vec{L} = \mathcal{M}\Delta\vec{\xi} \tag{A.8}$$

where $\mathcal{M}$is the inverse of M after one row has been removed from M. What makes this approach so fast is that the matrix, $\mathcal{M}$, need only be calculated once at program startup. The calculation within the polling loop is much reduced.

A.1.5 Implementation of Methods

Implementing the non-linear fitting is done using the Numerical Recipes [PTV+92] routine, `mrqmin`, with modification in error handling. The calculation is performed every poll cycle. The method is acceptably fast although it is the slowest of the implemented methods. The method is accurate.

The full linearized matrix solution discussed in section A.1.4.2 was not implemented. At an off-site test stand at Queen's University the simplified matrix solution (section A.1.4.3) was implemented. This method worked accurately on the test stand but not on site. The reason is a change in geometry. On site, this method feeds a large uncertainty into the y-location of the first attachment block, because the rope vectors, $\vec{r}_i$ for the three ropes attached to the first block all have small y-components. (On the test stand, snout 2 was radially farther inward giving a reasonable y-component for the second rope.) This inaccuracy is then propagated to the other two points because the simplified algorithm uses the first block position to calculate the second and third.

The linearized method with derivatives (section A.1.4.4) is implemented on site. It is the fastest method. The acrylic-vessel class in the MANIP program allows any one of the three methods to be used and it is possible to switch between methods without restarting the program. All methods produce a measure of error. For the fit, it is the chi-square. For the simplified linearization it is the change in distance between the second and third blocks, which should be zero for a rigid body. For the method using derivatives, a check is made on the unused rope length to ensure it agrees with the calculation. If a poll, by whatever method, passes, calculations of all parameters needed by the manipulator are performed and the success is logged. If a poll fails the parameters from the last good poll are kept and the failure is logged. The number of good and bad polls is continuously available to the user. During normal operation all polls are successful.

A.1.6 Testing The Neck Location Algorithm

A test was performed in which the neck of the acrylic vessel was pushed. It was first pushed and held in the x-direction and then allowed to swing. The oscillation was forced for a few cycles and then allowed to subside. This was then repeated in the y-direction. The raw ADC data from the sense ropes were recorded. This data was then replayed into all three algorithms implemented on site (the non-linear fitting described in A.1.4.1, the simplified matrix solution in section A.1.4.3, and the method using derivatives described in section A.1.4.4). Thus all three algorithms were tested on identical data. The fit and the derivatives method agreed exactly in their determination of the three attachment block positions. Figure A.3 shows the y-position for the first neck attachment block. The disagreement between the simplified-matrix solution and the other two methods is evident.

A.2 Control and Reading of Low-Level Hardware

The low-level hardware is the equipment which directly measures some physical property. For the manipulator this includes the potentiometers and ADCs on the sense ropes, the loadcells and ADCs for measuring rope tension, and the shaft encoders for measuring rotation of the pulleys, switches and gauges for the nitrogen laser, and other devices. The MANIP program had the following requirements for low-level hardware:

- It must be possible to remove and add low-level devices without recompiling the code.
- The code controlling the hardware must be extensible to include new types of hardware.
- Most importantly, the commands to access the hardware must be independent of the nature of the hardware used.

Object-oriented programming allows the last two requirements to be met. All classes for controlling low-level hardware are derived from one base class, `HWIO`. The base class has four public methods which perform the fundamental tasks. They are `unsigned int read()`, `void write(unsigned int)`, `void on(void)`, and `void off(void)`. (Integers are 16-bits long in DOS.) These methods

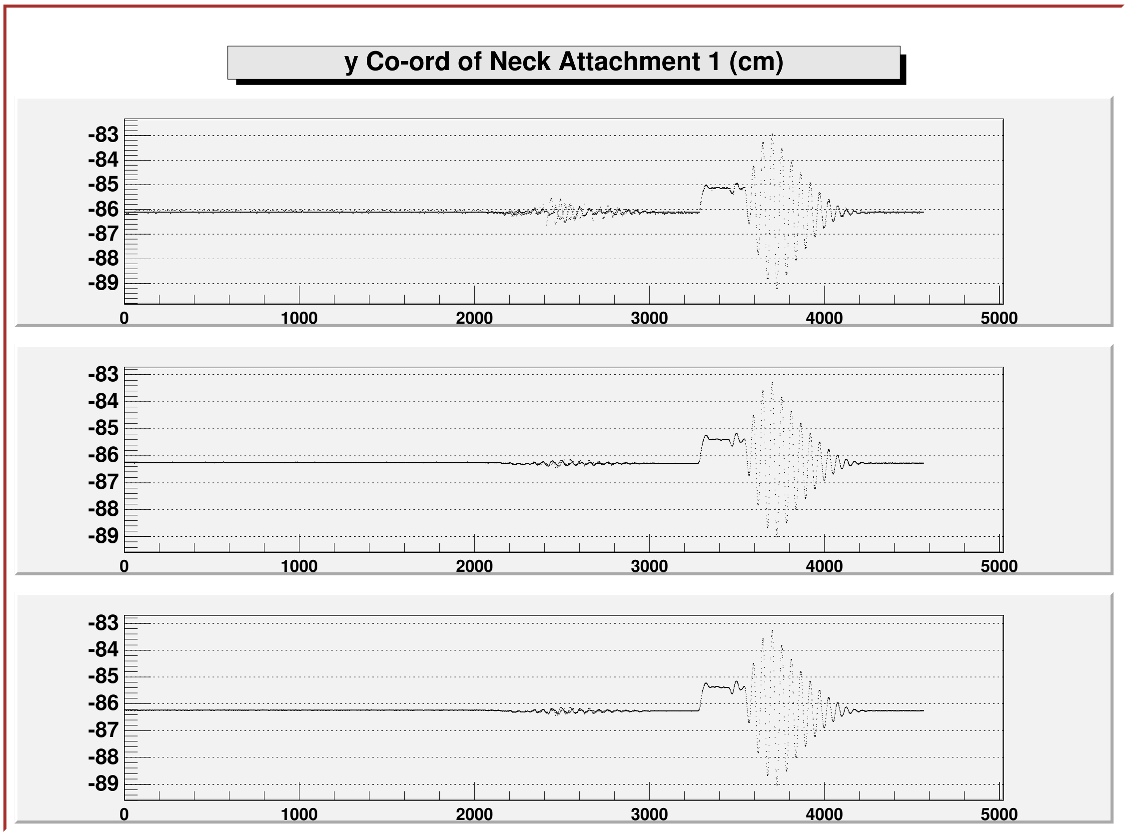

Figure A.3: The y-component of neck-attachment block 1 for the test of the position sensing system is shown for all three algorithms. The top plot shows the position as found using the matrix solution one attachment point at a time; the second plot shows the method with derivatives; the third using non-linear fitting. Note that the top plot is shifted in y by 0.2 cm. The top plot is noisier near 2500 when the vessel was oscillated in the x-direction. The variable plotted on the x-axis is an index of the data points. Only one point in 10 was kept so the data spans 46000 polls, or approximately 240 seconds. Starting at data point 2200, the vessel was pushed in the x-direction. Note that the bottom two plots are very stable. The top plot shows significant noise. Starting at approximately data point 3200, the vessel was pushed and held in the y-direction. Starting at approximately data point 3600 the vessel was rocked in the y-direction.

in the base class check that the particular object is in fact able to carry out this instruction. If so, it calls a virtual method which does the actual work. Because the method is virtual, the method from the derived class will be used. This guarantees that the user of an `HWIO`-derived class need know nothing about the derived class.

For example, the length of the sense ropes used in the acrylic-vessel polling is found by reading the voltage from a 10-turn potentiometer with an ADC which produces binary-coded decimal output. The code to read this ADC calls the method `read()` for the appropriate `HWIO`-derived object. This call to `HWIO::read()`, checks that it is permissible to try to read this hardware and then calls the virtual function `read1()`. Because `read1()` is virtual, the version of `read1` that gets called is that in the class `HWBCDIO`. Thus the correct reading is performed.

Bibliography

[AAB+98] E. G. Adelberger, S. M. Austin, J. N. Bahcall, *et al.*, Rev. Mod. Phys. **12345** (1998).

[Ba89] J. N. Bahcall, *Neutrino Astrophysics*, Cambridge University Press (1989).

[Ba97] J. N. Bahcall, Phys. Rev. C **56**, 3391 (1997).

[BDH+92] T. Bowles, P. Doe, A. Hime, R. Robertson, T. Spencer, P. Thornewell, J. Wilhelmy, and J. Wilkerson, *Neutral Current Detection in the Sudbury Neutrino Observatory*, Los Alamos National Laboratory (1992).

[Be53] H. A. Bethe, Phys. Rev. **89**, 1256 (1953).

[Be86] H. A. Bethe, Phys. Rev. Lett. **56**, 1305 (1986).

[Bi64] J. B. Birks, *The Theory and Practice of Scintillation Counting*, Pergamon Press (1964).

[BK98] J. N. Bahcall and P. I. Krastev, Phys. Lett. B **436**, 243 (1998).

[BKS95] J. N. Bahcall, M. Kamionkowski, and A. Sirlin, Phys. Rev. D **51**, 6146 (1995).

[BKS98] J. N. Bahcall, P. I. Krastev, and A. Yu. Smirnov, "Where do we stand with solar neutrino oscillations?", submitted to Phys. Rev. D (1998).

[BL96] J. N. Bahcall and E. Lisi, Phys. Rev. D **54**, 5417 (1996).

[BLA+96] J. N. Bahcall, E. Lisi, D. E. Alburger, L. D. Braeckeleer, S. Freedman, and J. Napolitano, Phys. Rev. C **54**, 411 (1996).

[BMW97] S. D. Biller, M. E. Moorhead, and D. L. Wark, "Addendum to: Simulations of SNO during an air or partial fill", SNO-STR-97-011-A (1997).

[BP98] J. N. Bahcall, S. Basu, and M. H. Pinsonneault, "How uncertain are solar neutrino predictions?", Phys. Lett. B, accepted for publication (1998).

[BPW95] J. N. Bahcall, M. H. Pinsonneault, and G. J. Wasserburg, Rev. Mod. Phys. **67**, 781 (1995).

[Br95] S. Brice, "The elastic fitter", SNO-STR-95-040 (1995).

[BR96] R. Brun and F. Rademakers, http://root.cern.ch and Nucl. Instr. and Meth. in Phys. Res. A **389** (1996).

[BTM98] A. S. Brun, S. Turck-Chièze, and P. Morel, Astrophys. J. **506** (1998), to appear.

[CB83] E. D. Commins and P. H. Bucksbaum, *Weak Interactions of Leptons and Quarks*, Cambridge University Press (1983).

[CDD+98] B. T. Cleveland, T. Daily, R. Davis, Jr., J. R. Distel, K. Lande, C. K. Lee, P. S. Wildenhain, and J. Ullman, Astrophys. J. **496**, 505 (1998).

[Ce] Cernlib, *http://www.cern.ch/*, European Laboratory for Particle Physics.

[Ch85] H. H. Chen, Phys. Rev. Lett. **55**, 1534 (1985).

[DGJ+96] G. Doucas, S. Gill, N. Jelley, L. McGarry, M. Moorhead, N. Tanner, and C. Waltham, Nucl. Instr. and Meth. in Phys. Res. A **370**, 579 (1996).

[Dr99] M. Dragowski, *Sudbury Neutrino Observatory Energy Calibration using Gamma Ray Sources*, PhD thesis, Oregon State University (1999).

[Ew+87] G. T. Ewan *et al.*, *Sudbury Neutrino Observatory Proposal*, SNO-87-12 (1987).

[FED+83] B. Filippone, A. Elwyn, C. Davids, and D. Koetke, Phys. Rev. C **28**, 2222 (1983).

[FLM+97] G. Fogli, E. Lisi, D. Montanino, and G. Scioscia, Phys. Rev. D **56**, 4365 (1997).

[Fo98] R. J. Ford, *Calibration of SNO for the Detection of ^8B Neutrinos*, PhD thesis, Queen's University at Kingston (1998).

[GA92] GALLEX Collaboration: P. Anselmann *et al.*, Phys. Lett. B **285**, 376 (1992).

[GA96] GALLEX Collaboration: W. Hampel *et al.*, Phys. Lett. B **388**, 384 (1996).

[GA97] GALLEX Collaboration: W. Hampel, ITP Conference on Solar Neutrinos: News about SNUs **http://www.itp.ucsb.edu/online/snu/** (1997).

[GK76] D. Garber and R. Kinsey, *Neutron Cross Sections Volume II, Curves*, Brookhaven National Laboratory (1976).

[Ha98] A. Hallin, private communication (1998).

[Ha99] A. Hamer, *Energy Calibration of SNO or the measurement of the charged-current Neutrino Reaction*, PhD thesis, Queen's University at Kingston (1999).

[He98] J. Hewett, private communication (1998).

[HL97] N. Hata and P. Langacker, Phys. Rev. D **56**, 6107 (1997).

[HR85] W. Hampel and L. Remsberg, Phys. Rev. C **31**, 667 (1985).

[HR96] K. M. Heeger and R. Robertson, Phys. Rev. Lett. **77**, 3720 (1996).

[ICD+97] M. P. Isaac, Y. Chan, M. Dragowski, D. Hurley, K. Lesko, M. Moorhead, E. Norman, D. Cluff, D. Hallman, J. Heise, and P. Jagam, "High energy gamma-ray measurements in the sno cavity", SNO-STR-97-009 (1997).

[Ja75] J. D. Jackson, *Classical Electrodynamics*, John Wiley & Sons, second edition (1975).

[JFH+96] C. J. Jillings, R. J. Ford, A. L. Hallin, P. J. Harvey, R. W. MacLeod, H. B. Mak, P. Skensved, and R. L. Stevenson, Nucl. Instr. and Meth. in Phys. Res. A **373**, 421 (1996).

[JR94] F. James and M. Roos, *MINUIT, Function Minimization and Error Analysis*, CERN Program Library Office, CERN-IT Division, CERN, CH-1211, Geneva 21, Switzerland, http://www.cern.ch (1994).

[Ka96] Kamiokande Collaboration: Y. Fukuda *et al.*, Phys. Rev. Lett. **77**, 1683 (1996).

[KN94] K. Kubodera and S. Nozawa, Int. J. of Mod. Phys. E **3** (1994).

[Ko98] Y. Koshio, *Study of Solar Neutrinos at Super Kamiokande*, PhD thesis, University of Tokyo (1998).

[KP89] T. K. Kuo and J. Pantaleone, Rev. Mod. Phys. **61**, 937 (1989).

[Mc99] N. K. McCauley, private communication (1999).

[Mo48] G. Moli'ere, Z. Naturforsch. a **3**, 78 (1948).

[MS85] S. P. Mikheyev and A. Yu. Smirnov, Sov. J. Nucl. Phys. **42**, 913 (1985).

[NHR85] W. R. Nelson, H. Hirayama, and D. W. O. Rogers, *The EGS4 Code System*, Stanford Linear Accelerator Center (SLAC-Report-265 1985).

[NSWG96] A. J. Noble and the SNO Water Group, *Sudbury Neutrino Observatory Water Systems review*, SNO-96-60 (1996).

[Pa86] S. J. Parke, Phys. Rev. Lett. **57**, 1275 (1986).

[Pa94] The Particle Data Group, Phys. Rev. D **50** (1994).

[Pa98] The Particle Data Group, The European Physical Journal C **3** (1998).

[Po98] A. W. P. Poon, *Energy Calibration of the Sudbury Neutrino Observatory Using Monoenergetic Gamma-Ray Sources*, PhD thesis, Univeristy of British Columbia (1998).

[PTV$^+$92] W. H. Press, S. A. Teukolsky, W. T. Vetterling, and B. P. Flannery, *Numerical Recipes in C*, Cambridge University Press, second edition (1992).

[SA94] SAGE Collaboration: J. N. Abdurashitov *et al.*, Phys. Lett. B **328**, 234 (1994).

[SA97] SAGE Collaboration: V. Gavrin, ITP Conference on Solar Neutrinos: News about SNUs **http://www.itp.ucsb.edu/online/snu/** (1997).

[Sc63] W. T. Scott, Rev. Mod. Phys. **35**, 231 (1963).

[Su98a] The Super-Kamiokande Collaboration: Y. Fukuda *et al.*, Phys. Rev. D **999** (1998), submitted.

[Su98b] The Super-Kamiokande Collaboration: Y. Fukuda *et al.*, Phys. Rev. Lett. **81**, 1158 (1998).

[Su98c] The Super-Kamiokande Collaboration: Y. Fukuda *et al.*, Phys. Rev. Lett. **81** (1998), to appear.

[SW98] J. Simpson and J.-X. Wang, "Determination of NC/CC ratio and CC shape during the pure D_2O stage", SNO-STR-98-002 (1998).

[TDF$^+$93] S. Turck-Chièze, W. Dappen, E. Fossat, J. Provost, E.Schatzman, and D. Vignaud, Phys. Rep. **230**, 57 (1993).

[To98] I. Towner, Phys. Rev. C **58**, 1288 (1998).

[To99] Totsuka, *notes taken by the author at the American Physical Society Centennial Meeting, Atlanta, Georgia*, (1999).

[VFL99] F. Villante, G. Fiorentini, and E. Lisi, Phys. Rev. D **58** (1999).

[Wo78] L. Wolfenstein, Phys. Rev. D **17**, 2369 (1978).

[YHH82] S. Ying, W. Haxton, and E. Henley, Phys. Rev. C **45**, 1992 (1982).

Vitae

Name:	Christopher James Jillings
Place and Year of birth:	Regina, Saskatchewan, Canada, 1968
Education:	Ph.D, Experimental High Energy Physics
	Queen's University, Kingston, Ontario, 1999
	Master of Science, Physics
	Queen's University, Kingston, Ontario, 1993
	Bachelor of Science with Honours in Physics
	McGill University, Montreal, Quebec, 1990
Experience:	Teaching and Research Assistant (Physics Department)
	Queen's University, Sept 1990 - Oct 1992 and Sept 1994 - July 1999
	Secondary School Teacher
	Gdynia Senior High Schools No 3, Gdynia, Poland, Jan 1993 - June 1994
	NSERC Summer Student
	University of Regina, May 1988 - Aug 1988 and May 1989 - Aug 1989
Awards:	Ontario Graduate Scholarship, 1991, 1995-1997
	Queen's Graduate Fellowship, 1994
	Queen's Graduate Award, 1994, 1995, 1996, 1997